Interaction of waves in a two-layer density stratified fluid

by

Mohammad-Reza Alam

Master of Science in Mechanical Engineering (2005)
Massachusetts Institute of Technology, Cambridge, MA, USA

Master of Science in Applied Mechanics (2003)
Bachelor of Science in Mechanical Engineering (2001)
Sharif University of Technology, Tehran, Iran

Submitted to the Department of Mechanical Engineering
in partial fulfillment of the requirements for the degree of

Doctor of Philosophy

at the

MASSACHUSETTS INSTITUTE OF TECHNOLOGY

September 2008

Author .....
Department of Mechanical Engineering
June 30, 2008

Certified by .....
Dick K.P. Yue
Philip J. Solondz Professor of Engineering,
Professor of Mechanical and Ocean Engineering
Thesis Supervisor

Certified by .....
Yuming Liu
Principal Research Scientist
Thesis Supervisor

Accepted by .....
Lallit Anand
Chairman, Departmental Committee on Graduate Students

Interaction of waves in a two-layer density stratified fluid

by

Mohammad-Reza Alam

Submitted to the Department of Mechanical Engineering
on June 30, 2008, in partial fulfillment of the
requirements for the degree of
Doctor of Philosophy

Abstract

In the first part of this thesis, the mechanisms of nonlinear resonant interaction of surface-interfacial waves with a rippled bottom in a two-layer density stratified fluid in two dimensions is investigated via perturbation analyses and direct simulation. Three classes of Bragg resonances are found to exist if the nonlinear interactions up to third order in the wave/ripple steepness are considered. At second order, class I Bragg resonance occurs involving two surface and/or internal waves and one bottom ripple component. At third order, class II and III Bragg resonances occur involving resonant interactions of four wave/ripple components. A powerful high-order spectral (HOS) method for nonlinear gravity wave dynamics in a homogeneous fluid is extended to the case of a two-layer fluid over non-uniform bottom. The method is capable of capturing the nonlinear interactions among large number of surface/interfacial wave mode and bottom ripple components up to an arbitrary high order. As an illustration of the usefulness of the numerical method a somewhat complicated problem involving many wave/bottom components is considered and it is shown that the ensuing multiple (near) resonant interactions result in the generation of multiple new transmitted/reflected waves that fill a broad wavenumber band eventually leading to loss of order and chaotic motion.

In the second part of this thesis, Resonance between waves of an oscillating/translating disturbance in two-layer density stratified fluids is studied. Waves in homogeneous fluid are known to be non-resonant at the second order. Many seas and oceans, however, are weakly stratified. Here it is shown that in the presence of stratification triad resonance between ship-generated waves can occur. For the more general problem and as an independent validation, the HOS is extended to consider the effect of the current and an oscillating submerged singularity. Direct simulation results compare well with analytical predictions in the near- and far-fields and offer a powerful tool for practical problems with general time-dependent motions/interactions of one or more bodies.

Thesis Supervisor: Dick K.P. Yue
Title: Philip J. Solondz Professor of Engineering,
Professor of Mechanical and Ocean Engineering

Thesis Supervisor: Yuming Liu
Title: Principal Research Scientist

Acknowledgments

There are people in your life who help you; help you a lot. They help you solve your problems, write your papers, overcome issues, calm you down when angry and frustrated, ... I always use the best adjectives I know to acknowledge them: "great, amazing, wonderful, ...". But there are a few people in your life who *shape your life*. Shape your thoughts, your feelings. They open new doors for you, redefine concepts of joy, beauty, life. When I want to thank these people I feel the language lacks powerful enough adjectives.

Professor Yue and Doctor Liu indeed reshaped my outlook on the world. I would like to sincerely thank them both for all new doors they opened to my life. Professor Yue is a true sample of a very patient and nice adviser, and Dr. Liu has been, and is, one of my best friends and instructors here at MIT. A very special thanks goes to them. I am also grateful to Professor Triantaphyllos Akylas, Professor Chiang C. Mei and Professor George Haller for all I learnt from them. I would like to thank all my friends for making my PhD course of study not only an amazing educational opportunity, but also a memorable friendship period.

I would like to dedicate this thesis to my parents,

Fazlollah Alam & Seddighe Basiti-Yazdi

whose unbelievable endurance, unconditional love, and untouchable devotion have been monumental; for their never-ending support, patience, understanding and for being my life long educators. It is because of you, and the way in which you raised me that I have been allowed to make it this far in life. I am really indebted to you for all the good spirit you gifted me, and all the joy you placed in my life.

Thank you again,

Contents

List of Figures

List of Tables

Introduction

The discovery of internal waves goes back to the late nineteenth century, when Fridtjof Nansen observed the drift of the vessel "Farm" while exploring the Arctic ocean between 1893-1896 (see Nansen, 1969). The phenomenon was then explained by Ekman (1904): "sailing vessels may encounter serious impedance in fiords if the water column is stratified".

Internal waves are commonly observed in stratified media such as the ocean and the atmosphere. Mountain waves or lee waves and mixing and circulation of the air layers are related to existence and propagation of internal waves in the atmosphere. In the ocean, seas and lakes, where stratification is typical due to the variation of salinity and temperature in the vertical direction, internal waves influence sediment transport, acoustic propagation, optical clarity, radar observations, deep ocean mixing, surface wave dissipation, marine structure designs, and life of many organisms like phytoplanktons (see Harris, 1986). They are also considered as a possible reason for the dead-water phenomenon causing drowning of swimmers in lakes (see Maas & van Haren, 2004).

Although the dynamics of internal wave propagation is relatively well understood (see for example Baines, 1997), *how they are generated* is yet unclear. The generation of internal waves is mainly attributed to the relaxation of internal hydraulic flows and interactions of current with topographies and surface waves (see Farmer & Armi, 1999). Nonlinear interaction between surface waves and bottom topography, specially in nearshore areas, is a likely mechanism for generation of internal waves that has gotten scant little attention so far and is the subject of this paper.

In the study of internal wave propagation in a two-layer density stratified fluid, three dimensionless numbers are relevant: nonlinearity ratio, aspect ratio (shallowness), and depth ratio. Based on the relative order of magnitude of these numbers, a number of models such as KdV equation, intermediate long wave equation and Benjamin-Ono equation are

developed to describe the dynamics of internal waves (see Choi & Camassa, 1996, 1999). Some of these models can be extended to the multi-layer stratified fluid (see Choi, 2000).

Ball (1964) was the first who studied nonlinear interactions between surface and interfacial waves. He considered a resonant triad formed by two surface wave components and one internal wave component, and showed that an internal wave can be generated by extracting energy from surface waves through the second-order triad resonant interaction. Hill & Foda (1996) next studied both theoretically and experimentally a resonant triad consisting of a single surface wave component and two internal wave component in two dimensions. Under the assumptions that the amplitude and wavelength of the surface wave is much larger than those of the internal waves, they showed that the amplitude of the resonant wave modulates in time, but does not grow exponentially. They also found that the addition of a small viscose damping to the lower layer causes the resonant wave to grow exponentially. Hill & Foda (1998), Jamali (1998) and Jamali *et al.* (2003) studied this problem in three dimensions with further relaxation in the wavelength assumption. Jamali *et al.* (2003) explained the source of discrepancy (algebraic) between Jamali (1998) and Hill & Foda (1998). Hill (2004) extended the study of second-order triad resonance to third-order quartet resonance. He showed that the evolution of resonant wave amplitude can be casted in terms of Jacobian elliptic functions. He showed that the truncation at the second order would "significantly overestimate the maximum resonant wave amplitude".

Wave motion in a periodic environment has been of significant interest in past few decades due to its applications from small scale quantum and solid state physics to large scale ocean wave dynamics. For the problem of a surface wave traveling in a region with undulated bottom, wave reflection is greatly amplified when the wavelength of the surface wave is twice of that of the bottom ripples, due to the effect of Bragg Resonance rooting in solid state physics. Owing to its importance in the formation of nearshore sandbars and the evolution of ocean wavefield in littoral zones, Bragg resonant interactions of surface waves with bottom undulations in a homogeneous fluid have been studied extensively. Davies (1982) used a regular perturbation analysis to investigate the second-order Bragg resonance phenomenon. His solution is unbounded when the number of bottom ripples increases indefinitely. To overcome this difficulty, Mei (1985) invoked a multiple-scale method to derive a uniformly convergent solution for interacting wave components. Kirby (1986) obtained a similar solution by extending the mild slope equation to include the effect of fast

bottom undulations. By including higher-order interactions, Liu & Yue (1998) generalized the second-order Bragg resonance to third-order quartet resonant interactions of waves and bottom ripples. For the propagation of water waves over a random bathymetry, the localization phenomenon was first observed in the laboratory experiments by Belzons *et al.* (1988) and then investigated theoretically by Mei *et al.* (2005).

In a two-layer density stratified fluid, the study on nonlinear interactions of surface/interfacial waves with bottom undulations is quite limited despite its relevance to the generation of internal waves and equally importance in the development of coastal processes. McKee (1996) extended the modified mild slope equation of Kirby (1986) to a two-layer fluid and investigated the second-order resonant interaction among a surface incident wave, an internal wave, and a sinusoidal bottom undulation. Unlike in an one-layer fluid, the Bragg resonance generated wave in a two-layer fluid can be reflected or transmitted in a surface or internal mode. Generalization of such (second-order) Bragg resonance to higher order in a two-layer fluid has not yet been pursued. Chen & Liu (1996) studied the localization phenomenon of internal waves traveling over a random bathymetry under the rigid-lid assumption.

The theme of first two chapters of this work is to generalize the understanding of Bragg resonant interactions of surface wave with bottom undulations in a one-layer fluid to a two-layer fluid including both second-order triad and third-order quartet Bragg resonances. Such Bragg resonances may play an important role in the generation mechanism and propagation of internal waves specially in nearshore and estuary areas where stratification layers are relatively shallow and comparable in depth.

In chapter one a detailed analysis of the conditions is given for generalized Bragg resonances for nonlinear interactions of surface/internal waves with bottom ripples up to third order in the wave/ripple steepness. Specifically, under the class I Bragg resonance condition, a second-order resonant triad can be formed with an incident wave, a bottom ripple component, and a resonance generated wave. The resonance generated wave has the same frequency as the incident wave. Depending on the wavenumbers of the incident wave and bottom ripples, the generated wave can be a surface or internal wave travelling in the same or opposite direction as the incident wave. For steep waves and bottom ripples, quartet resonances can occur when the third-order free-surface and bottom nonlinearities are included. Specifically, two types of resonant quartets can be formed. One involves two free wave components and two bottom ripple component, and the other involves three wave

components and one bottom component. For convenience in description, the former/latter is called class II/III Bragg resonance. Class II resonance is similar to class I in nature except there are two bottom ripple components participating in the resonance. In a class III resonant quartet, in general, two of three wave components can be considered as the incident waves, and the third one is then regarded as the generated wave. Unlike class I and II resonances, the frequency of the generated wave (due to class III resonance) is the sum or difference of the frequencies of the two incident waves. As in class I and II resonance, the generated wave may be reflected or transmitted in a surface or internal mode depending on the wavenumber combination of incident waves and bottom ripples. For class III Bragg resonance, twelve different cases can be observed.

To understand the basic mechanism and characteristics of the resonances, we perform a theoretical analysis of the nonlinear interaction problem involving surface/internal/bottom waves. For class I resonance, regular perturbation techniques are invoked to study the growth near the resonance. However when the number of ripples goes to infinity, regular perturbation predicts infinite growth and violates the energy conservation. Basically as observed for homogeneous fluid, regular perturbation fails to predict strong reflection/transmission. To overcome this difficulty, the multiple scales method is utilized to study the strong reflection/transmission for class I Bragg reosnance. For class II and III Bragg resonances, regular perturbation analysis although tedious is still doable. Weak third order resonance, therefore, is studied via regular perturbation and thereafter discussion is presented.

As the order of nonlinearity and the number of wave and bottom ripple components increase, perturbation terms soon become algebraically too complicated to be handled analytically. For a realistic situations involving a spectrum of incident wave and bottom ripples, it is thus necessary to develop and apply a reliable and efficient numerical simulation, which is the subject of chapter two.

Although chapter one gives basic information for various resonance cases and weak resonance amplitude growth, it fails for higher nonlinearity where the analytical approach gets too tedious to be accomplished. Furthermore, in real life, the surface/interface and the bottom spectrum consists of much more than a few wave-numbers causing simultaneous multiple interactions between different components. Include to this the partial resonance that occurs close to the exact resonance-condition (detuning cases), it is appear that the

analysis fails to predict these all. The advantage of a time-efficient robust numerical algorithm is that it simulates the ocean independent of the degree of the complexity.

In chapter two a powerful high-order spectral method (HOS) originally developed for nonlinear wave-wave and wave-body interaction by Dommermuth & Yue (1987) is adopted to a two-layer density stratified setup. HOS is the extension of Zakharov (1968) mode coupling idea in a direct computational approach. This method computationally accounts for nonlinear interaction up to an arbitrary specified order M is wave steepness, and a large number of free wave modes, say $N = O(1000)$ per horizontal dimension, are typically used in nonlinear simulations. Each of the latter wave components is free in that it is subject to its own evolution equation. By using the fast transform techniques, the computational effort is only linearly proportional the total number of modes N and the order M. The convergence with N and M is shown to be exponentially fast. The HOS method has been tested extensively and compared to experiments and other weakly and fully nonlinear predictions for wave-wave interactions in two and three dimensions (Dommermuth & Yue, 1987). The method has been generalized to include the presence of atmospheric forcing (Dommermuth & Yue, 1988), long-short waves (J. Zhang & Yue, 1993), finite depth and depth variations (Liu & Yue, 1998), variable current (Wu, 2004) and fixed and moving submerged bodies (Y. Liu & Yue, 1992; Q. Zhu & Triantafyllou, 1999).

The two-layer version of HOS including the Boundary Value Problem Solver and the numerical integrator is validated using an exact initial condition. We use Newton's iterative algorithm to find the steady wave solutions to the Laplace's equation. Furthermore it is found that this iterative approach converges to an exact solitary wave solution given the solution of KdV equation as its approximate initial guess.

Component reconstruction has been well studied and widely used in signal processing using many different approaches such as filtering or wavelets. However, most of the time the basic assumption in electromagnetic signal processing is that the frequencies of components are far different from each other, which is not valid in the wave tank. To reconstruct components of the final mixture of surface waves with close wave-numbers, a finite length window of data is approximated with the least-square algorithm and then averaged over the entire domain using Galerking method. The result shows substantial advancement over existing methods specially when perturbation exists on the data measurement.

The numerical results section starts with the validation of known analytical results. By

increasing the nonlinearity we show that the HOS predication fails analytical perturbation results. Numerical results show a shift in the resonance frequency and a change in the amplitude of the resonant wave at the resonance frequency. This discrepancy increases in higher order resonances (Class II and Class III). We then consider the multiple resonance. The multiple resonance occur when more than three wave-components participate in the resonance. We show in this case, that in a short time the behavior can be predicted by superposition of known low-order resonance cases, while in the long time, energy distributes almost evenly over all frequencies and no more order can be observed. we then seek the order in higher spaces and show that the motion is not random, it is chaotic.

Organization of chapter three is as follows: section 1 is the formulation of HOS for two-layer fluid. In section 2 we invoke the Newton iterative algorithm to find exact nonlinear initial condition to be used to verify the accuracy of our HOS boundary value problem (BVP) solver and time integrator. Section 3 discusses our proposed method to reconstruct elementary waves out of a mixture of waves. section 4 is the implementation and convergence test and last section, section 5, deals with numerical results from verification of theoretical results of chapter one to new phenomena happening due to nonlinearity which are out of scope of chapter one results.

In chapter three the linear problem of wave generation and propagation by a submerged disturbance that is steadily translating and its strength is sinusoidally oscillating in time is considered analytically and numerically in a two-layer density stratified fluid. Understanding of waves due to the motion of a submerged body has many practical applications from non-acoustic detection of underwater vehicles, to seakeeping and wave load calculations on moored/floating offshore structures. In stratified waters and particularly in littoral zones, it can help understanding of generation of internal gravity waves (Pramanik, 1974). Inversely, density stratification hence ocean-body composition can be found from the wake pattern behind a moving object (see Avital & Miloh, 1999, 1994).

Kelvin (1905) was the first who published an analytical paper on the problem of the ship wave. He considered a singular disturbance moving with a constant velocity in an infinitely deep homogeneous water and shows the famous "herring bone pattern"' of the ship wake which are confined between two lines of angle $19^o\ 28''$. Later Havelock (1908) extends Kelvin's theory to the finite depth case where he shows as the Froude number increases toward unity, the angle rises sharply toward $\pi/2$ but both transverse and divergent waves

exist. If the Frude number exceeds the unity, the transverse waves disappear and half angle slowly decreases from $\pi/2$ (see Havelock, 1964). waves generated by a uniformly moving source is similar to Cherenkov Radiations in electromagnetic physics [1](Gorodtsov, 1993). The linear two-dimensional problem of far field waves of an oscillating and translating disturbance first studied by Haskind (1954).

Two-layer density stratified flow past a submerged obstacle is a classic subject (see the monograph by Baines, 1997, where the rigid-lid assumption has been employed). With a free surface and infinitely deep lower layer Voitsenya (1958) derived the complex potential for a pulsating source and vortex. For the same setup, Hudimac (1961) showed that a moving ship generates similar-shaped internal waves besides the surface Kelvin waves. He pointed out that for speeds less than a critical speed, the internal ship wave consists of both transverse and divergent waves, while above that critical speed, only divergent wave persists. (see also Crapper, 1967; Sharman & Wurtele, 1983). In three dimension, the internal wake is usually narrower and much longer than the surface kelvin wake (Avital & Miloh, 1999; Wei *et al.*, 2003, 2005). For a two semi-infinite fluids, Lu & Chwang (2005) derived analytical expressions for the three dimensional interfacial waves due to a fundamental singularity. They consider three cases: upper and lower inviscid, and either or lower are viscous. They use linearized kinematic and dynamic boundary condition on the interface and Laplace's equation for the inviscid fluid and steady Oseen's equation for viscous fluid. In a special case of the general problem considered here, if the disturbance is a steadily moving/oscillating pressure distribution on the interface, Pramanik (1974) gives the integral form solution (in terms of inverse Fourier transform) of the initial value problem and studies a couple of limiting cases. A brief energy discussion is given in Gorodtsov (1993) where cases of homogeneous density and uniform stratification is considered.

The problem of wave generation in a continuous stratification is interesting enough even in the absence of the free surface effect. Mowbray & Rarity (1967) considered two-dimensional internal waves generated by an oscillating cylinder in a constant Brunt-Vaisala stratified fluid, and, showed internal waves can be generated if the frequency of excitation ω_0 is less than the Brunt-Vaisala frequency N. They also showed that the maximum amplitude of internal waves occur along lines with angle $\theta = \sin^{-1}(\pm\omega_0/N)$ measured with respect to the horizontal axis. Later Stevenson & Thomas (1969) included the translational motion

[1]http://en.wikipedia.org/wiki/Cherenkov-radiation

to the oscillating cylinder.

Mielke (1986) considered the continuous stratification case. The literature on this subject is divided into two categories: 1- symmetric steady flow past the symmetric obstacle, and, 2- flows with a train of waves downstream. Sha & Vanden-Broeck (1993) consider the first problem by solving the integro-differential equation numerically. They observed two types of behavior: broad horizontally hump or an overhanging of the waves. Forbes (1989)Generalizes his one-layer paper (see Forbes, 1988) to two layer with a free surface. Experiments of Melville & Helfrich (1987) shows good agreement between KdV and eKdV solutions.

In chapter three, the general problem of an oscillatory singularity which is steadily translating in a two-layer density stratified fluid is considered. The number of waves in the far field is a function of ratio of depths, ratio of densities, Froude number and the frequency of oscillation of the disturbance. Based on these four variables, four, six or eight distinct free waves can be seen at the far field. Similar to homogeneous fluid, for slow enough speed/oscillation, waves can propagate in front of the ship. However, the number of distinct waves in front of the ship increase as the number of stratified layers increases. Green's function is derived in a two-layer stratified fluid setup for the source located in the upper/lower layer. To verify the analytical results and to develop an efficient method for the general problem of accelerating/variable strength disturbance, an algorithm based on spectral method is invoked. The numerical effort of this algorithm is linearly proportional to the number of free wave-modes in the domain of interest. Cross validation of numerical-analytical results are performed both in the far-field and the near-field. Green's function in three dimension is given for the general case.

In chapter four, the second order (triad) resonance between ship waves in a two-layer density stratified fluid is considered analytically and numerically. A steadily translating and sinusoidally oscillating singularity in a homogeneous fluid is known to generate four unsteady waves and one co-moving wave, as seen in the ship frame of reference. Each pair of these waves, although may satisfy the resonance condition with a third free wave, can not exchange energy and hence no new wave can be formed (D′yachenko & Zakharov, 1994). However, if stratification is taken into account, as is the case in many open seas, oceans and lakes, resonance triads with non-zero amplitudes may form: two surface wave and one internal wave or two internal waves and one surface wave are possible candidates for such

a resonance. Here we show that the existence of line of the sudden density change (i.e. the thermocline) along with second order nonlinearity can play a significant role in optical (non-acoustic) detection of underwater/surface vehicles.

In a two-layer density stratified fluid, Ball (1964) showed that two oppositely traveling surface waves can resonate an internal wave. Later on, Wen (1995*a*); Hill & Foda (1996) and Jamali *et al.* (2003) showed that similar triad resonance may occur between two oppositely traveling internal waves and one surface wave. To close the second order problem in a two-layer setup, chapter one and two of this thesis took into account the effect of topography (Bragg resonance) and further consider third order analysis, where Bragg resonance is between three free waves and a bottom topography components.

Motivated by the need for the determination of the trace of ships and submarines in strong stratified waters such as littoral zones of warm seas and oceans, here the second order problem of interaction between waves generated by an oscillatory singularity that steadily translates in a two-layer density stratified fluid is considered. Depending on the ratio of depths and densities of fluid layers, Froude number and the frequency of oscillation of the disturbance, linear theory predicts up to eight distinct free waves at the farfield of the object. Two out of these eight waves, that only exist if the source speed and frequency is small enough, advance ahead of the source and the rest trail the ship.

General formulation of the problem is given followed by a kinematic analysis based on the dispersion relation. The resonance condition can be obtained from the kinematic analysis solely and is discusses. For the growth rate and resonant wave, however, the amplitude of disturbance waves need to be determined.

Although exact resonance condition is only satisfied at a finite number of condition, countless near-resonance cases are possible; some with the possibility of generating high amplitude near-resonance waves. To develop an efficient numerical scheme for the general problem of accelerating/variable strength disturbance that take into account all resonance and near-resonance interactions a spectral-based algorithm is developed in §4. The algorithm is the extension of a high-order spectral method originally developed to simulate nonlinear gravity wave-wave interactions (Dommermuth & Yue, 1987). The numerical effort of this algorithm is linearly proportional to the number of free wave-modes in the domain of simulation. Cross validation of numerical-analytical results are performed.

Chapter 1

Bragg resonance of waves in a two-layer fluid propagating over bottom ripples: Perturbation analysis

1.1 Introduction

In this chapter the resonant interactions of waves in a two-layer density stratified fluid travelling over bottom undulations is considered. The problem is similar to the case of a homogeneous fluid, in that waves are modified, i.e., exchange energy, as they travel over and interact with the nonuniform bottom topography. Unlike the case of a homogeneous fluid, however, in a two-layer fluid, there are two free-wave solutions at a given frequency: a surface-mode and an internal-mode solution. Of great interest is when they - along with the bottom topography - satisfy the so called Bragg condition where the rate of energy exchange is maximum. When an incident wave hitting the rippled region satisfies this condition the resonant wave can now be a reflected/transmitted surface/internal mode wave. Bragg resonance in stratified fluids can affect the development of the wave spectrum in the coastal regions and continental shelves (e.g. Ball, 1964), modify the shore-parallel sandbars (e.g. Heathershaw & Davies, 1985) and may explain the generation of internal waves (considered, for instance, by Grue, 2005; Nycander, 2006).

In the simpler case of a homogeneous fluid, the interaction of surface waves with bottom undulations has been studied extensively, owing to its importance in the formation of near-shore sandbars and the evolution of ocean wave-field in littoral zones. Davies (1982) used regular perturbation analysis to find the amplitude growth rate of the resonant wave at and near the resonance. His solution becomes unbounded when the number of bottom ripples increases indefinitely. To overcome this, Mei (1985) invoked a multiple-scale analysis to derive a uniformly convergent solution for the interacting wave components. Kirby (1986) gave a similar solution by extending the mild slope equation to include the effect of fast bottom undulations. By including higher-order interactions, Liu & Yue (1998) generalized the second-order Bragg resonance to include third-order quartet resonant interactions of waves and bottom ripples.

In the absence of bottom non-uniformity, the dynamics of internal wave propagation is relatively well understood (see for example the monograph by Baines, 1997), although their generation mechanisms is still a subject of active research (see, e.g., Farmer & Armi, 1999). The nonlinear resonant interactions between surface and interfacial waves was studied by Ball (1964) who considered a resonant triad formed by two surface mode wave components and one internal mode wave component. Later, Wen (1995*a*) (also see Hill & Foda, 1996, 1998; Jamali, 1998; Jamali *et al.*, 2003) showed that resonance may occur between two internal mode waves and one surface mode wave.

In the presence of the bottom topography, McKee (1996) extended the modified mild slope equation of Kirby (1986) to a two-layer fluid and investigated the second-order resonant interaction among a surface incident wave, an internal wave, and a sinusoidal bottom undulation. Over a random bathymetry Chen & Liu (1996) studied the localization of internal waves under the rigid-lid assumption.

The objective of this chapter is to consider the general nonlinear resonance interactions involving surface and internal waves in two-layer density stratified fluid travelling over a wavy bottom. Of special interest are the higher order (generalized) Bragg resonances that may play an important role especially in near-shore and estuary areas where stratification layers are relatively shallow and comparable in depth.

In §1.2 an analysis of the conditions is provided for generalized Bragg resonances for nonlinear interactions of surface/internal waves with bottom ripples up to third order in the wave/ripple steepness. At second order, class I Bragg resonance condition obtains wherein

a resonant triad can be formed with an incident wave, a bottom ripple component, and a resonance generated wave. The resonance generated wave has the same frequency as the incident wave. Depending on the wave numbers of the incident wave and bottom ripples, the generated wave can be a surface or internal mode wave travelling in the same or opposite direction as the incident wave. The various triad combinations are enumerated and categorized schematically in Feynman-diagram-like representations. For steep waves and bottom ripples, (generalized) Bragg resonances at third order may be important involving quartet interactions among free-surface/internal and bottom modes. Specifically, two types of resonant quartets can be formed. One involves two free wave components (surface or internal mode) and two bottom ripple components, and the other involves three propagating wave components (surface or internal mode) and one bottom component. For convenience in description, and following existing convention for one-layer fluid (see Liu & Yue, 1998), the former/latter is called class II/III Bragg resonance. Class II resonance is similar to class I in characteristic except there are now two bottom ripple components participating in the resonance. In class III Bragg resonance, for the resonant quartet, two of the three propagating wave components can in general be considered as incident waves, and the third one is then regarded as the resonance generated wave. Unlike class I and II resonances, the frequency of this generated wave equals the sum or difference of the frequencies of the two incident waves. As in class I and II resonances, the generated wave may be reflected or transmitted and may be surface or internal mode depending on the wavenumber combination of the incident waves and bottom ripples. For class III Bragg resonance, a total of 48 different cases are enumerated.

To understand the mechanisms and characteristics of the resonances, perturbation analyses of these cases are performed. For class I resonance, in §1.3, a regular perturbation technique is used to obtain the (initial) growth near the resonance. As the number of ripples (or interaction distance) increases indefinitely, regular perturbation becomes invalid and fails to predict strong Bragg reflection/transmission. To overcome this difficulty, a multiple-scale analysis is utilized in §1.4 to study strong reflection/transmission for class I Bragg resonance.

For class II and III Bragg resonances, the algebra involved in the regular perturbation analyses is quite cumbersome. These are presented and discussed in §1.5. For strong resonant interactions, multiple-scale analyses similar to that in §1.4 are needed. While

the formulation of such analyses is in principle obtained, the analyses themselves quickly become algebraically complicated/intractable and are not pursued here.

In practice, the surface/internal mode waves and bottom undulations in general may contain many components. Depending on the steepnesses and the size of the interacting domain, multiple resonances at different orders may obtain. The analytic results in this chapter provide a basis for understanding these nonlinear interactions. For useful quantitative predictions of the surface/internal wave environment, one needs to resort to effective direct numerical simulations. This is the subject of the next chapter.

1.2 Resonance condition

1.2.1 Statement of the problem

Consider a two-layer fluid with incident wave(s) propagating over non-uniform bottom topography, subject to the condition of relatively mild surface/interface/bottom wave slopes. Of basic interests here are the conditions involving the incident wave and bottom topology wavenumbers for given fluid layer depths and density ratios for which (generalized) Bragg resonant interactions obtain.

Governing equations

A Cartesian coordinate system is defined with x-axis on the mean free surface and z-axis positive upward. Let's consider a two-layer density stratified fluid where the upper and lower fluid layers have respectively mean depths h_u and h_ℓ, and fluid densities ρ_u and ρ_ℓ (subscripts u and ℓ hereafter denote quantities associated with the upper and lower fluid layers, respectively). The two-layer fluid rests on a rippled horizontal bottom given by $z = -h_u - h_\ell + \eta_b$ where η_b is the elevation of the bottom undulation measured from mean bottom depth (see figure 1-1).

Assume that the fluids in both layers are homogeneous, incompressible, immiscible and inviscid so that the fluid motion is irrotational. The effect of surface tension is neglected. The flow in each layer is described by a velocity potential, $\phi_u(x, z, t)$ and $\phi_\ell(x, z, t)$. The

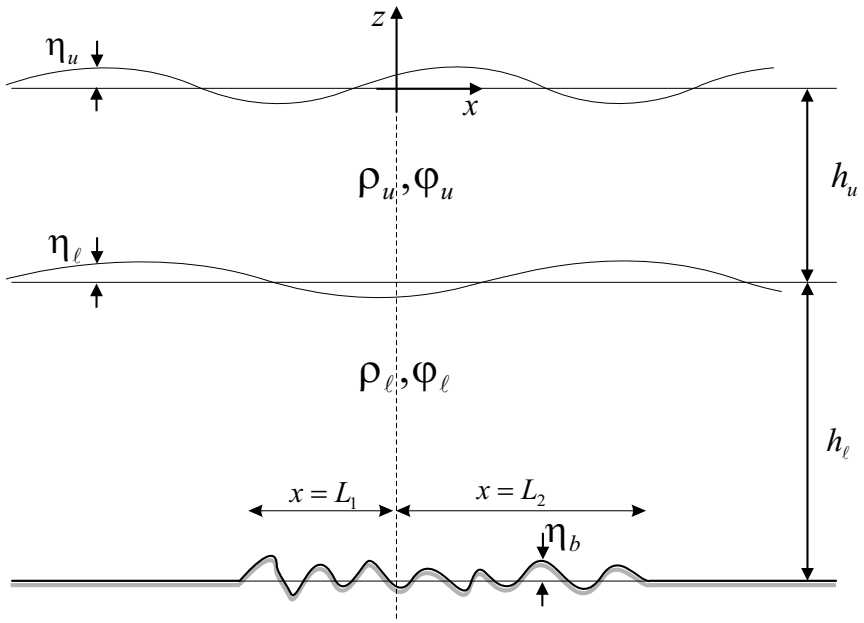

Figure 1-1: Definition sketch of waves on a two-layer fluid over a rippled bottom.

nonlinear equations governing the potential flow in the two-layer fluid are:

$$\nabla^2\phi_u = 0 \qquad -h_u + \eta_\ell < z < \eta_u \tag{1.2.1a}$$

$$\nabla^2\phi_\ell = 0 \qquad -h_u - h_\ell + \eta_b < z < -h_u + \eta_\ell \tag{1.2.1b}$$

$$\phi_{u,tt} + g\phi_{u,z} + (\partial_t + 1/2\ \phi_{u,x}\partial_x + 1/2\ \phi_{u,z}\partial_z)(\nabla\phi_u \cdot \nabla\phi_u) = 0 \qquad z = \eta_u \tag{1.2.1c}$$

$$g\eta_u + \phi_{u,t} + 1/2\ (\nabla\phi_u \cdot \nabla\phi_u) = 0 \qquad z = \eta_u \tag{1.2.1d}$$

$$\begin{aligned}\mathcal{R}\{&\phi_{u,tt} + g\phi_{u,z} + 1/2\ (\nabla\phi_u \cdot \nabla\phi_u)_{,t} \\ &+\eta_{\ell,t}[\phi_{u,t} + 1/2\ (\nabla\phi_u \cdot \nabla\phi_u)]_{,z} - g\eta_{\ell,x}\phi_{u,x}\} \\ -\{&\phi_{\ell,tt} + g\phi_{\ell,z} + 1/2\ (\nabla\phi_\ell \cdot \nabla\phi_\ell)_{,t} \\ &+\eta_{\ell,t}[\phi_{\ell,t} + 1/2\ (\nabla\phi_\ell \cdot \nabla\phi_\ell)]_{,z} - g\eta_{\ell,x}\phi_{\ell,x}\} = 0 \qquad z = -h_u + \eta_\ell\end{aligned} \tag{1.2.1e}$$

$$\eta_{\ell,t} + \eta_{\ell,x}\phi_{u,x} - \phi_{u,z} = 0 \qquad z = -h_u + \eta_\ell \tag{1.2.1f}$$

$$\eta_{\ell,t} + \eta_{\ell,x}\phi_{\ell,x} - \phi_{\ell,z} = 0 \qquad z = -h_u + \eta_\ell \tag{1.2.1g}$$

$$\eta_{b,x}\phi_{\ell,x} - \phi_{\ell,z} = 0 \qquad z = -h_u - h_\ell + \eta_b \tag{1.2.1h}$$

where $\mathcal{R} \equiv \rho_u/\rho_\ell$ is the density ratio, $\eta_u(x,t)$ and $\eta_\ell(x,t)$ are the elevations of the free-surface and the interface respectively, and g is the gravity acceleration.

Regular perturbation expansion

For small surface η_u and interfacial η_ℓ waves over a mildly varying bottom topography η_b, the velocity potentials (ϕ_u and ϕ_ℓ) and the wave elevations (η_u and η_ℓ) are expanded in perturbation series with respect to a small parameter ϵ that measures the wave/bottom steepnesses which are assumed, for simplicity, to be of the same order:

$$\phi_u = \epsilon\phi_u^{(1)} + \epsilon^2\phi_u^{(2)} + O(\epsilon^3)\ , \tag{1.2.2a}$$

$$\phi_\ell = \epsilon\phi_\ell^{(1)} + \epsilon^2\phi_\ell^{(2)} + O(\epsilon^3)\ , \tag{1.2.2b}$$

$$\eta_u = \epsilon\eta_u^{(1)} + \epsilon^2\eta_u^{(2)} + O(\epsilon^3)\ , \tag{1.2.2c}$$

$$\eta_\ell = \epsilon\eta_\ell^{(1)} + \epsilon^2\eta_\ell^{(2)} + O(\epsilon^3)\ . \tag{1.2.2d}$$

Substituting (1.2.2) into (1.2.1), expanding the quantities on the free surface, interface, and bottom in Taylor series with respect to the respective mean positions, and collecting terms at each order $m = 1, 2, \ldots$, it obtains:

$$\nabla^2\phi_u^{(m)} = 0 \qquad -h_u < z < 0 \tag{1.2.3a}$$

$$\nabla^2\phi_\ell^{(m)} = 0 \qquad -h_u - h_\ell < z < -h_u \tag{1.2.3b}$$

$$\phi_{u,tt}^{(m)} + g\phi_{u,z}^{(m)} = f_1^{(m)} \qquad z = 0 \tag{1.2.3c}$$

$$g\eta_u^{(m)} + \phi_{u,t}^{(m)} = f_2^{(m)} \qquad z = 0 \tag{1.2.3d}$$

$$\mathcal{R}(\phi_{u,tt}^{(m)} + g\phi_{u,z}^{(m)}) - (\phi_{\ell,tt}^{(m)} + g\phi_{\ell,z}^{(m)}) = f_3^{(m)} \qquad z = -h_u \tag{1.2.3e}$$

$$\phi_{u,z}^{(m)} - \phi_{\ell,z}^{(m)} = f_4^{(m)} \qquad z = -h_u \tag{1.2.3f}$$

$$\eta_{\ell,t}^{(m)} - \phi_{u,z}^{(m)} = f_5^{(m)} \qquad z = -h_u \tag{1.2.3g}$$

$$\phi_{\ell,z}^{(m)} = f_6^{(m)} \qquad z = -(h_u + h_\ell). \tag{1.2.3h}$$

where $f_j^{(1)} = 0$ for $j = 1, \ldots, 6$, and $f_j^{(m)}$, $m \geq 2$, $j = 1, \ldots, 6$, are functions of lower order quantities. In a regular perturbation, the linear equation systems (1.2.3) are solved successively to higher order starting from m=1.

Linear solution

At m=1, (1.2.3) is homogeneous, and the eigen solution representing a free propagating wave, can be written as (see Lamb, 1932)

$$\eta_u^{(1)} = a\cos(kx-\omega t) \tag{1.2.4a}$$

$$\eta_\ell^{(1)} = b\cos(kx-\omega t) \tag{1.2.4b}$$

$$\phi_u^{(1)} = (A\cosh kz + B\sinh kz)\sin(kx-\omega t) \tag{1.2.4c}$$

$$\phi_\ell^{(1)} = C\cosh k(z+h_u+h_\ell)\sin(kx-\omega t) \tag{1.2.4d}$$

where ω and k represent the frequency and wavenumber of the wave, respectively. The coefficients a and b are the amplitudes of waves on the surface and the interface, and are related by

$$\frac{b}{a} = \cosh kh_u - \frac{gk}{\omega^2}\sinh kh_u \ . \tag{1.2.5}$$

In terms of a and b, the coefficients A, B and C are given by

$$A = \frac{ga}{\omega}, \quad B = \frac{\omega a}{k}, \quad C = \frac{\omega b}{k\sinh kh_\ell} \ . \tag{1.2.6}$$

In (1.2.4), ω and k satisfy the dispersion relation:

$$\mathcal{D}(k,\omega) \equiv \omega^4(\mathcal{R}+\coth kh_u\coth kh_\ell) - \omega^2 gk(\coth kh_u+\coth kh_\ell) + g^2k^2(1-\mathcal{R}) = 0. \tag{1.2.7}$$

For a given ω, (1.2.7) possesses two pairs of real roots for the wavenumber k (Ball, 1964). The variation of these roots as a function of the frequency is sketched in figure 1-2, which hereafter is referred to as Ball's diagram. In figure 1-2, the steeper(milder)-sloped pair of branches with smaller(greater) $|k|$ for given ω is referred to as the surface(internal) mode. A surface-mode (or an internal-mode) wave is a freely propagating wave that has a surface elevation *and* an interface elevation. Therefore, for example, the interface elevation of a surface-mode wave i.e. equation 1.2.4b when ω, k are associated with a surface-mode wave which is the inner branch of the Ball's diagram. The qualitative difference between the surface and internal modes can be seen more readily by considering the case of weak stratification ($\mathcal{R}$ close to 1): the sign of b/a in (1.2.5) is positive(negative) for the surface(internal) mode, and therefore the phases of the surface elevation $\eta_u^{(1)}$ and the interfacial elevation $\eta_\ell^{(1)}$

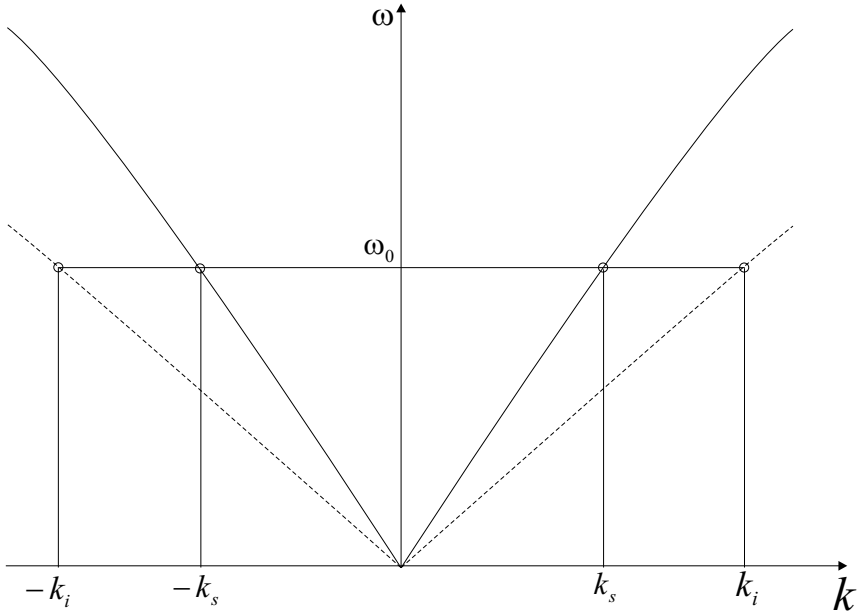

Figure 1-2: Sketch of the dispersion relation for wavenumber k and frequency ω of a free wave in a two-layer fluid. Dashed lines correspond to the internal mode, and the solid lines correspond to the surface mode.

are the same(π radian different); also the free surface wave amplitude a is greater(smaller) than that of the lower surface (interface) amplitude b. As the density ratio $\mathcal{R}$ varies from 0 to 1, the surface-mode branch does not change much while the internal-mode branch moves from the vicinity of the surface-mode branch (as $\mathcal{R} \to 0$) towards the wavenumber axis (as $\mathcal{R} \to 1$).

1.2.2 Class I Bragg resonance

Consider a right-going incident wave of frequency ω and wavenumber k propagating over a rippled bottom with the elevation given by

$$\eta_b(x) = d\sin(k_b x) \tag{1.2.8}$$

where d and k_b are respectively the amplitude and wavenumber of the bottom undulations. The incident wave can be either a surface mode or internal mode given by (1.2.4).

At the second order ($m = 2$), the inhomogeneous terms $f_j^{(2)}$, $j = 1, \ldots, 6$, take the form:

$$f_1^{(2)} = -\eta_u^{(1)} \phi_{u,ztt}^{(1)} - g\eta_u^{(1)} \phi_{u,zz}^{(1)} - (\nabla\phi_u^{(1)}.\nabla\phi_u^{(1)})_{,t} \tag{1.2.9a}$$

$$f_2^{(2)} = -\eta_u^{(1)} \phi_{u,zt}^{(1)} - \frac{1}{2}(\nabla\phi_u^{(1)}.\nabla\phi_u^{(1)}) \tag{1.2.9b}$$

$$\begin{aligned} f_3^{(2)} = {} & [(\eta_\ell^{(1)} \phi_{\ell,zt}^{(1)})_{,t} - g(\eta_\ell^{(1)} \phi_{\ell,x}^{(1)})_{,x} + \frac{1}{2}(\nabla\phi_\ell^{(1)}.\nabla\phi_\ell^{(1)})_{,t}] \\ & -\mathcal{R}\ [(\eta_\ell^{(1)} \phi_{u,zt}^{(1)})_{,t} - g(\eta_\ell^{(1)} \phi_{u,x}^{(1)})_{,x} + \frac{1}{2}(\nabla\phi_u^{(1)}.\nabla\phi_u^{(1)})_{,t}] \end{aligned} \tag{1.2.9c}$$

$$f_4^{(2)} = [\eta_\ell^{(1)}(\phi_u^{(1)} - \phi_\ell^{(1)})_{,x}]_{,x} \tag{1.2.9d}$$

$$f_5^{(2)} = -(\eta_\ell^{(1)} \phi_{u,x}^{(1)})_{,x} \tag{1.2.9e}$$

$$f_6^{(2)} = (\eta_b \phi_{\ell,x}^{(1)})_{,x} \tag{1.2.9f}$$

Substituting (1.2.4) and (1.2.8) into (1.2.9) shows that $f_6^{(2)}$ contains a term with a factor of $\sin[(k \pm k_b)x - \omega t]$, which is associated with the interaction of a surface/internal mode wave and bottom ripples. If $k \pm k_b$ and ω satisfy the dispersion relation, i.e.,

$$\left.\begin{aligned} \mathcal{D}(k_r, \omega) = 0 \\ k_r = k \pm k_b \end{aligned}\right\}, \tag{1.2.10}$$

where the subscript r denotes the resonant wave, the interaction term is secular and the second-order interaction becomes resonant. As a result, a free propagating wave of wavenumber k_r and frequency ω is generated. The surface (η_u) and interfacial (η_ℓ) elevations of this wave are determined from (1.2.3) (with m=2) to be:

$$\eta_u^{(2)}, \eta_\ell^{(2)} \propto t \sin(k_r x - \omega t) \tag{1.2.11}$$

for a long uniformly-rippled bottom. Under this condition, (1.2.11) shows that the amplitude of the generated wave grows indefinitely over time.

As in a one-layer fluid (e.g. Liu & Yue, 1998), (1.2.10) is called the class I Bragg condition. For a given incident wave (or bottom ripples) wavenumber, the requisite wavenumber of bottom ripples (or incident wave) for class I resonance can be derived directly from figure 1-2. For convenience, the wavenumber of the incident wave is denoted generally as k and k is written as k_s (k_i) if it is a surface(internal)-mode wave. For k=k_s, class I resonance happens if $k_b = k_i - k_s$, $k_b = 2k_s$ or $k_b = k_s + k_i$. On the other hand, for k=k_i, class I

resonance obtains if $k_b = k_i - k_s$, $k_b = 2k_i$ or $k_b = k_s + k_i$.

Interaction of waves with bottom topography in some aspects resembles the interaction of particles in quantum electrodynamics (QED) where Feynman diagrams are commonly used to schematically represent the different interaction processes. In the present context, the use of Feynman-like diagrams to represent the resonant interactions is found to be even more intuitive (for another use of such diagrams in a related context, see Hasselmann, 1966). Figure 1-3-left shows the use of this schematic representation to illustrate all six cases of class I Bragg resonance. In each diagram, a surface-mode, an internal-mode and an undulatory bottom component is depicted respectively by a solid, dash and a wavy line. The directions of each of the incident, reflected, and transmitted waves are indicated by arrows. In all diagrams it is assumed that the incident wave always comes from the far left. Since only one frequency (i.e. ω) participates in class I Bragg resonance the resonance condition can be written solely in terms of wavenumbers. This condition is given immediately below each corresponding diagram in figure 1-3. The interpretation of these diagrams is direct and straightforward. For example, in the left (class I) column, the second diagram represents a class I Bragg resonance between an incident surface-mode wave and the wavy bottom. If the wavenumber of the wavy bottom satisfies $k_b = k_s + k_i$, where each of k_i and k_s and the frequency ω satisfy the dispersion relation, then the resonant wave will be a reflected (i.e. left-going) internal-mode wave with the wavenumber k_i. Part of the incident wave with the wavenumber k_s continues to travel to the right without change as indicated by the solid arrow (labelled k_s) going to the right.

These six cases can be classified into three groups based on whether the energy exchange happens between two different modes (i.e. a surface-mode wave gives its energy to an internal-mode wave or vice versa) or between similar modes, and if the resonant wave is a transmitted or a reflected wave. Based on this, the six cases of class I Bragg resonance can be grouped into the following: (i) inter-modes in transmission, $S_c \xrightarrow{k_b} I_T$ and $I_c \xrightarrow{k_b} S_T$; (ii) inter-modes in reflection, $S_c \xrightarrow{k_b} I_R$ and $I_c \xrightarrow{k_b} S_R$; and (iii) same-mode in reflection, $S_c \xrightarrow{k_b} S_R$ and $I_c \xrightarrow{k_b} I_R$. In the above, S and I stand for surface-mode and internal-mode repectively, and, subscripts c, R and T denote incident, reflected and transmitted waves respectively. For (i)/(ii), energy exchange occurs between surface mode and internal mode of waves that travel in the same/opposite direction. For (iii), energy exchange occurs in the same mode of waves travelling in the opposite direction. Case (iii) is the direct extension

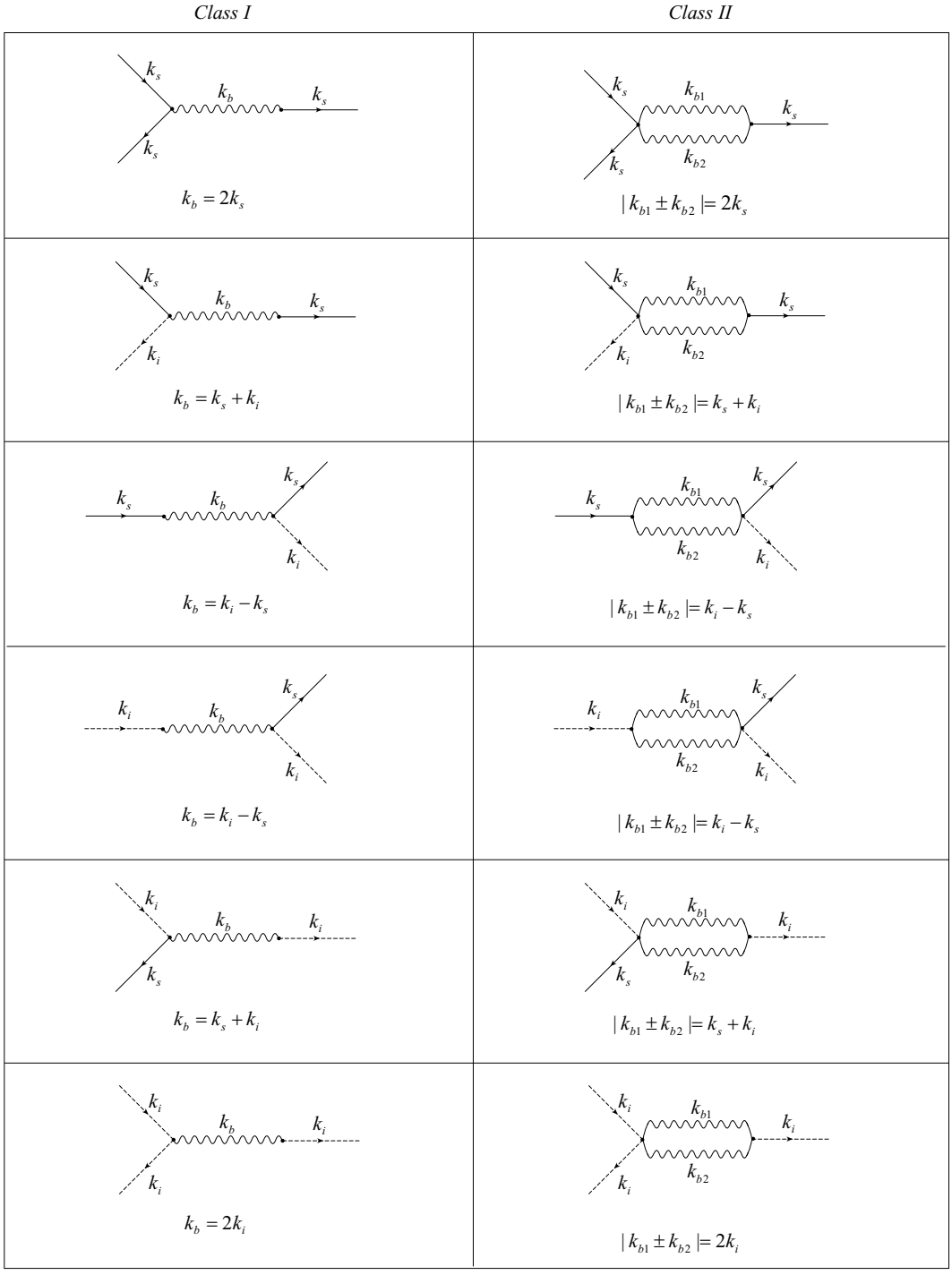

Figure 1-3: Feynman diagram representations of class I (left) and II (right) Bragg resonance conditions in a two-layer fluid. The solid/dash/wavy line represents surface/internal/bottom wave components. Arrows indicate the direction of wave propagation.

of the result in a one-layer fluid (see Liu & Yue, 1998) to a two-layer fluid.

1.2.3 Class II Bragg resonance

As expected, resonance interactions occur also at third-order (m=3) involving quartets of propagating/bottom modes. These belong to two broad types: one consisting of two free wave and two bottom ripple components; and the other three wave components and one bottom component. As in the case of Bragg scattering in a one-layer fluid (Liu & Yue, 1998), the resonance associated with the former/latter quartet wave-bottom interaction is denoted as class II/III Bragg resonance.

To illustrate the class II Bragg resonance condition, consider a bottom elevation is given by the superposition of two ripple components of wavenumbers k_{b1} and k_{b2}. Upon carrying out the perturbation analysis to the third order (with (1.2.4) as the first-order solution), it is obtained that the bottom forcing $f_6^{(3)}$ in (1.2.3) contains terms proportional to $\sin[(k \pm 2k_{b1})x - \omega t]$, $\sin[(k \pm 2k_{b2})x - \omega t]$, and $\sin[(k \pm k_{b1} \pm k_{b2})x - \omega t]$. Class II Bragg resonance occurs whenever the wavenumber $k \pm 2k_{b1}$ or $k \pm 2k_{b2}$ or $k \pm k_{b1} \pm k_{b2}$ and the frequency ω satisfy the dispersion relation (1.2.7). Thus, in general form, the class II Bragg resonance condition can be expressed as:

$$\left.\begin{aligned} \mathcal{D}(k_r, \omega) &= 0 \\ k_r &= k \pm k_{b1} \pm k_{b2} \end{aligned}\right\} . \tag{1.2.12}$$

The class II resonance condition (1.2.12) is identical to the class I resonance condition (1.2.10) if k_b in (1.2.10) is replaced by the super- or sub-harmonic combination of the two bottom ripple components $k_{b1} \pm k_{b2}$. Class II resonance is thus a direct extension of class I resonance to the third order. Like class I, there are also six cases of class II resonance, which are schematically illustrated in the right column of figure 1-3. Finally, note that class II resonance may also obtain when the bottom contains only one ripple component, given from (1.2.12) by setting k_{b1}=k_{b2}.

1.2.4 Class III Bragg resonance

In class III Bragg resonance, the resonant quartet is composed of three travelling waves and one bottom ripple component. To obtain this resonance condition, consider the general

case involving two incident waves of wavenumbers, k_1 and k_2, and frequencies, ω_1 and ω_2. Without loss of generality, assume $k_1 > |k_2| > 0$. Starting with the linear solution for the two free wave components and carrying out the perturbation analysis in (1.2.3) to the third order, it is obtained that the inhomogeneous terms, $f_j^{(3)}$, j=1, ..., 6, contain terms proportional to $\sin[(2k_1 \pm k_b)x - 2\omega_1 t]$, $\sin[(2k_2 \pm k_b)x - 2\omega_2 t]$, and $\sin[(k_1 \pm k_2 \pm k_b)x - (\omega_1 \pm \omega_2)t]$. If the combined wavenumber and frequency in any of these forcing terms satisfy the dispersion relation, the associated wave-bottom interaction becomes resonant and a third free wave component is generated by the resonance. The condition for class III Bragg resonance can be written in the following general form:

$$\left.\begin{aligned} \mathcal{D}(k_r, \omega_r) = 0 \\ k_r = k_1 \pm k_2 \pm k_b, \quad \omega_r = \omega_1 \pm \omega_2 \end{aligned}\right\} \tag{1.2.13}$$

in which k_r and ω_r represent the wavenumber and frequency of the resonant generated wave.

Due to the involvement of three free propagating waves, combinations of wave components in class III resonance are more complicated than those in class II resonance. Figure 1-4 shows schematic representations of all possible wave-ripple combinations satisfying the class III resonance condition (1.2.13). In Figure 1-4, the resonant wave is indicated by the subscript "r" which has frequency of either $\omega_1 + \omega_2$ (corresponding to + superscript) or $\omega_1 - \omega_2$ (corresponding to − superscript), and it can be either a surface-mode wave or an internal-mode wave indicated respectively by an additional subscript s or i. As an illustration, consider the first case of figure 1-4. This case represents four possible interactions between two surface-mode waves (k_{s1}, k_{s2}) that results in a transmitted surface-mode wave (k_{rs}). The resonant generated surface-mode wave with wavenumber k_{rs} can have two possible frequencies: (1) $\omega_1 + \omega_2$, and therefore is denoted by k_{rs}^+, i.e., $\mathcal{D}(k_{rs}^+, \omega_1 + \omega_2) = 0$; or (2) $\omega_1 - \omega_2$, hence denoted by k_{rs}^- with $\mathcal{D}(k_{rs}^-, \omega_1 - \omega_2) = 0$. If two incident waves travel in the same direction (from the left to the right), then only right-arrows have to be picked up for the correct representation. In this case, there are two bottom wavenumbers that can cause the incident wave to resonate a new wave: if $k_b = k_{rs}^+ - (k_{s1} + k_{s2})$ or $k_b = k_{s1} - k_{s2} - k_{rs}^-$. If two incident waves travel in opposite directions, assume k_{s1} moves rightward and k_{s2} moves leftward, hence left arrows on k_{s2} lines must be chosen. In this case a transmitted surface-mode wave can be generated if $k_b = k_{rs}^+ - (k_{s1} - k_{s2})$ or $k_b = k_{s1} + k_{s2} - k_{rs}^-$. Note that although the resonant wave can have a positive or negative wavenumber in 1.2.13, for

Class III

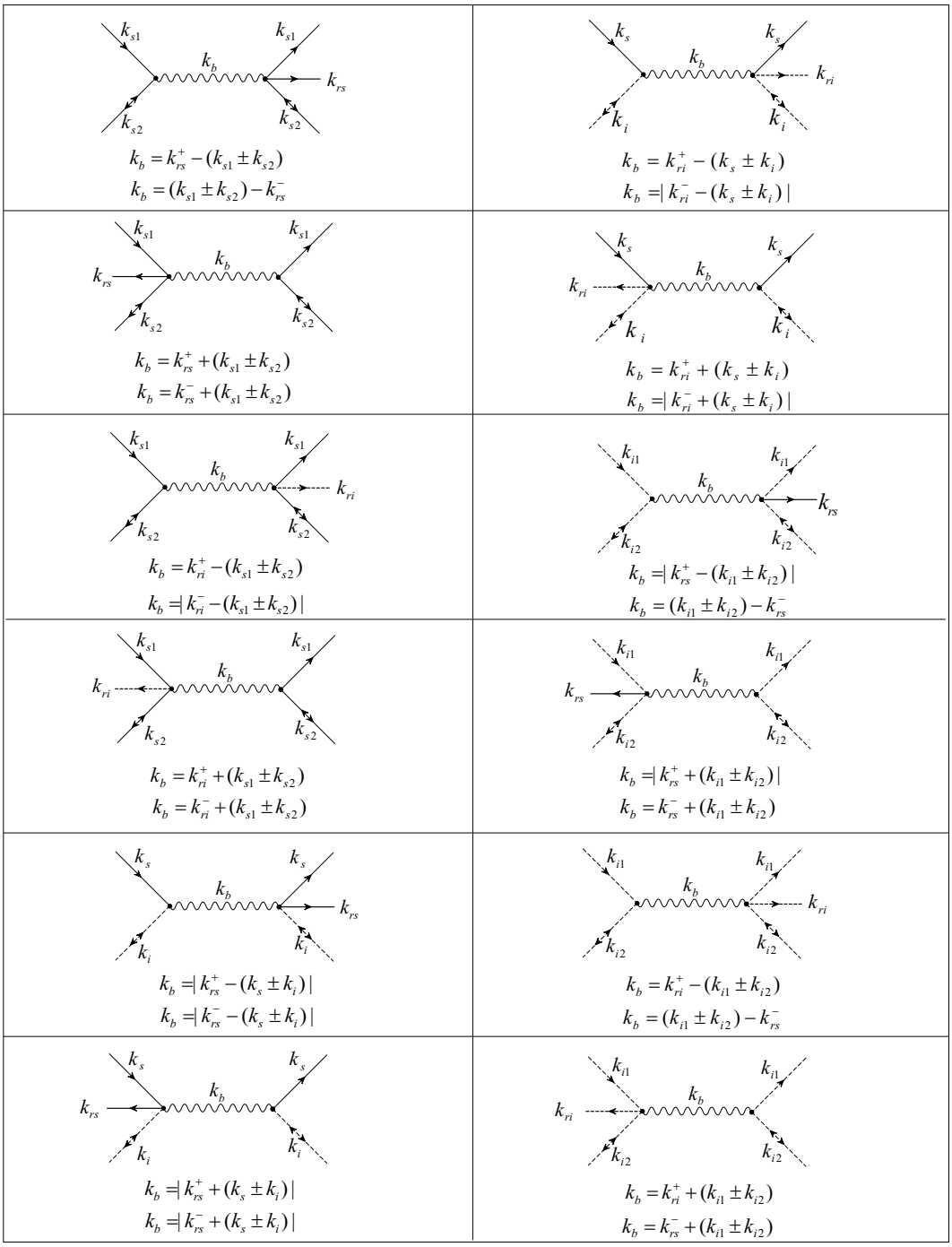

Figure 1-4: Feynman diagram representations of class III Bragg resonance conditions in a two-layer fluid. The solid/dash/wavy line represents surface/internal/bottom wave components. Arrows indicate the direction of wave propagation. Each diagram shows four cases. The line with double-sided arrow shows two cases when a right (left) going wave gives another right (left) going wave on the other side of the ripples.

clarity in the diagrams in figure 1-4, wavenumbers are always given as positive and the wave direction is indicated by the arrow.

As before, the resonance cases in figure 1-4 can be classified in terms of the energy exchange among surface/internal wave modes and propagation direction of the resonance generated wave. There are four such categories: (i) inter-modes in transmission $S_{c1}+S_{c2} \xrightarrow{k_b} I_T$, $I_c + S_c \xrightarrow{k_b} S_T$, $I_c + S_c \xrightarrow{k_b} I_T$, and $I_{c1} + I_{c2} \xrightarrow{k_b} S_t$; (ii) inter-modes in reflection, $S_{c1} + S_{c2} \xrightarrow{k_b} I_R$, $I_c + S_c \xrightarrow{k_b} S_R$, $I_c + S_c \xrightarrow{k_b} I_R$, and $I_{c1} + I_{c2} \xrightarrow{k_b} S_R$; (iii) same-mode in reflection, $S_{c1} + S_{c2} \xrightarrow{k_b} S_R$ and $I_{c1} + I_{c2} \xrightarrow{k_b} I_R$; and (iv) same-mode in transmission, $S_{c1} + S_{c2} \xrightarrow{k_b} S_T$ and $I_{c1} + I_{c2} \xrightarrow{k_b} I_T$. One notes that in the above, (i) and (ii) are unique for a two-layer fluid, while (iii) and (iv) are a direct extension of class III resonances in a one-layer fluid (Liu & Yue, 1998).

1.3 Regular perturbation analysis for class I Bragg resonance

A regular perturbation analysis is performed here to solve the second-order wave-bottom interaction problem in a two-layer fluid. Consider the general case where a single surface-mode or internal-mode incident wave in a two-layer fluid propagates over a finite patch of periodic ripples on an otherwise uniform depth shown (figure 1-1). Following the approach of Davies (1982) who obtained a solution for the class I Bragg resonance in a one-layer fluid, here the perturbed boundary-value problems (1.2.3) is solved to the second-order (m=2).

At m=1, the solution for a right-going incident wave is (1.2.4). At m=2, only $f_6^{(2)}$ is associated with the interaction of the incident wave and the bottom ripples while the other inhomogeneous terms $f_j^{(2)}$, j=1, ..., 5, represent the self-interaction of the incident wave. Therefore to find the solution associated with class I resonance, only the effect of $f_6^{(2)}$ is needed to be considered. The system of equations (1.2.3) with $f_6^{(2)} \neq 0$ (and $f_j^{(2)}$=0, j=1, ..., 5) can be solved using Fourier transform to yield the second-order potentials in the upper and lower layers in terms of Fourier integrals:

$$\phi_u^{(2)}(x,z,t) = \frac{1}{\sqrt{2\pi}} \int_{-\infty}^{\infty} \{[A_{u1}(\xi)\cosh(\xi z) + B_{u1}(\xi)\sinh(\xi z)]\cos(\omega t) + [A_{u2}(\xi)\cosh(\xi z) + B_{u2}(\xi)\sinh(\xi z)]\sin(\omega t)\} e^{-\mathrm{i}\xi x} \mathrm{d}\xi \ , \quad (1.3.14)$$

$$\phi_\ell^{(2)}(x,z,t) = \frac{1}{\sqrt{2\pi}} \int_{-\infty}^{\infty} \{[A_{\ell 1}(\xi)\cosh(\xi z) + B_{\ell 1}(\xi)\sinh(\xi z)]\cos(\omega t) + [A_{\ell 2}(\xi)\cosh(\xi z) + B_{\ell 2}(\xi)\sinh(\xi z)]\sin(\omega t)\} e^{-\mathrm{i}\xi x} \mathrm{d}\xi \ , \quad (1.3.15)$$

where

$$A_{uj}(\xi) = \frac{g\omega^2\Lambda_j(\xi)}{\sqrt{2\pi}\tilde{D}(\xi,\omega)} , \quad B_{uj} = \frac{\omega^2}{g\xi}A_{uj}(\xi) , \quad A_{\ell j} = A_{uj}(\xi)\hat{A} , \quad B_{\ell j} = B_{uj}(\xi)\hat{B} \quad (1.3.16)$$

for j=1 and 2. The coefficients $\Lambda_1(\xi)$, $\Lambda_2(\xi)$, $\tilde{D}$, $\hat{A}$, and $\hat{B}$ are defined by:

$$\Lambda(\xi,t) \equiv \Lambda_1(\xi)\cos(\omega t) + \Lambda_2(\xi)\sin(\omega t) = \int_{-\infty}^{\infty}\left[\eta_{b,x}\phi^{(1)}_{\ell,x} - \eta_b\phi^{(1)}_{\ell,zz}\right]_{z=-h_u-h_\ell} e^{\mathrm{i}\xi x}\mathrm{d}x , \quad (1.3.17)$$

$$\tilde{D}(\xi,\omega) = \mathcal{D}(\xi,\omega)\sinh\xi h_u \sinh\xi h_\ell , \quad (1.3.18)$$

$$\hat{A} = 1 + \frac{\omega^4 - g^2\xi^2}{2g\xi\omega^2}(1-\mathcal{R})\sinh 2\xi h_u , \quad (1.3.19)$$

$$\hat{B} = 1 - \frac{\omega^4 - g^2\xi^2}{2\omega^4}(1-\mathcal{R})(1-\cosh 2\xi h_u) . \quad (1.3.20)$$

The integrals in (1.3.14) and (1.3.15) can be evaluated by contour integration in terms of their residues in the complex plane. The integrand in (1.3.14) or (1.3.15) has four poles on the real axis ξ_j, j=1,...,4, and an infinite numbers of poles on the imaginary axis, which correspond respectively to the real and imaginary solutions of the dispersion relation $\mathcal{D}(\xi,\omega)$=0 for a given ω. Specifically, among ξ_j, j=1,...,4, two of them are k_s and $-k_s$ representing surface modes and the other two are k_i and $-k_i$ representing internal modes. The contribution from the poles at ξ_j, j=1,...,4, represent propagating waves while those from poles on the imaginary axis represents evanescent waves. Upon (properly) indenting the contour in the complex plane and imposing the radiation condition (e.g. Davies, 1982), it obtains:

$$\phi^{(2)}_u(x,z,t) = \frac{\mathrm{i}\omega^2}{2}\sum_{\xi=k_s,k_i}\alpha(\xi)\left(g\cosh\xi z + \frac{\omega^2}{\xi}\sinh\xi z\right)\gamma^{\pm}(\xi,x,t) , \quad (1.3.21)$$

$$\phi^{(2)}_\ell(x,z,t) = \frac{\mathrm{i}\omega^2}{2}\sum_{\xi=k_s,k_i}\alpha(\xi)\left(g\hat{A}\cosh\xi z + \frac{\omega^2\hat{B}}{\xi}\sinh\xi z\right)\gamma^{\pm}(\xi,x,t) , \quad (1.3.22)$$

$$\eta^{(2)}_u(x,t) = -\frac{\mathrm{i}\omega^2}{2}\sum_{\xi=k_s,k_i}\alpha(\xi)\frac{\mathrm{d}}{\mathrm{d}t}\,\gamma^{\pm}(\xi,x,t) , \quad (1.3.23)$$

$$\eta^{(2)}_\ell(x,t) = -\frac{\mathrm{i}\omega^2}{2}\sum_{\xi=k_s,k_i}\alpha(\xi)\left(\cosh\xi h_u - \frac{g\xi}{\omega^2}\sinh\xi h_u\right)\frac{\mathrm{d}}{\mathrm{d}t}\gamma^{\pm}(\xi,x,t) , \quad (1.3.24)$$

as $x \to \pm\infty$, in which

$$\alpha(\xi) = \left(\frac{\mathrm{d}\tilde{D}}{\mathrm{d}\xi}\right)^{-1} , \tag{1.3.25}$$

$$\gamma^{\pm}(\xi, x, t) = [\Lambda_1(\xi) \mp \mathrm{i}\Lambda_2(\xi)]\mathrm{e}^{-\mathrm{i}(\xi x \mp \omega t)} - [\Lambda_1(-\xi) \pm \mathrm{i}\Lambda_2(-\xi)]\mathrm{e}^{\mathrm{i}(\xi x \mp \omega t)} \ . \tag{1.3.26}$$

For specificity, consider a right-going surface (or internal) incident wave with a wave number $k{=}k_s$ (or k_i) and frequency ω, propagating over a patch of bottom undulations, consisting of M_b ripples in the region $x{=}\pm L$, given by $\eta_b{=}d\sin(k_b x)$ for $|x| \le L$ and $\eta_b{=}0$ for $|x| > L$, where $L{=}M_b\pi/k_b$. From (1.3.17), it obtains $\Lambda_1(\xi)$ and $\Lambda_2(\xi)$. The elevations of the reflected and transmitted surface and internal waves are determined from (1.3.23) and (1.3.24):

$$\eta_u^{(2)}(x,t) = \omega^4\alpha(k_s)\beta_s^R(k_s,k)\cos(k_s x + \omega t) + \omega^4\alpha(k_i)\beta_s^R(k_i,k)\cos(k_i x + \omega t) \ , \tag{1.3.27}$$

$$\eta_\ell^{(2)}(x,t) = \omega^4\alpha(k_s)\beta_i^R(k_s,k)\cos(k_s x + \omega t) + \omega^4\alpha(k_i)\beta_i^R(k_i,k)\cos(k_i x + \omega t) \ , \tag{1.3.28}$$

as $x \to -\infty$, and

$$\eta_u^{(2)}(x,t) = \omega^4\alpha(k_s)\beta_s^T(k_s,k)\cos(k_s x - \omega t) + \omega^4\alpha(k_i)\beta_s^T(k_i,k)\cos(k_i x - \omega t) \ , \tag{1.3.29}$$

$$\eta_\ell^{(2)}(x,t) = \omega^4\alpha(k_s)\beta_i^T(k_s,k)\cos(k_s x - \omega t) + \omega^4\alpha(k_i)\beta_i^T(k_i,k)\sin(k_i x - \omega t) \ , \tag{1.3.30}$$

as $x \to +\infty$, where

$$\beta_i^{R,T}(\xi,k) = \beta_s^{R,T}(\xi,k)\lambda(\xi) \ , \qquad \lambda(\xi) = \cosh\xi h_u - \frac{g\xi}{\omega^2}\sinh\xi h_u \ , \tag{1.3.31}$$

$$\beta_s^R(\xi,k) = (-1)^{m+1}\frac{2ad\xi k_b\lambda(k)\sin(k+\xi)L}{[(k+\xi)^2 - k_b^2]\sinh kh_\ell} \ , \tag{1.3.32}$$

$$\beta_s^T(\xi,k) = (-1)^{m+1}\frac{2ad\xi k_b\lambda(k)\sin(k-\xi)L}{[(k-\xi)^2 - k_b^2]\sinh kh_\ell} \ . \tag{1.3.33}$$

This solution shows that regardless of whether the incident wave is a surface or internal mode, both surface and internal modes are present in the reflected and transmitted waves. Reflection and transmission coefficients are defined as R_{pq} and T_{pq}, where p and q represent respectively the mode of the incident wave and the resonant wave, with p, $q = s$ or i denoting surface or internal mode waves respectively. Thus, $R_{ss} \equiv A_s^R/a, R_{si} \equiv A_i^R/a$ and $T_{si} \equiv A_i^T/a$; and $R_{is} \equiv A_s^R/b, R_{ii} \equiv A_i^R/b$ and $T_{is} \equiv A_s^T/b$; where A_s^R and A_s^T are

respectively the amplitudes of the reflected and transmitted surface mode waves on the free surface; and A_i^R and A_i^T respectively those of the reflected and transmitted internal mode waves on the interface. From (1.3.27) to (1.3.30), it is clear that A_s^R=$\omega^4\alpha(k_s)\beta_s^R(k_s,k)$, A_i^R=$\omega^4\alpha(k_i)\beta_i^R(k_i,k)$, A_s^T=$\omega^4\alpha(k_s)\beta_s^T(k_s,k)$, and A_i^T=$\omega^4\alpha(k_i)\beta_i^T(k_i,k)$.

Under the class I Bragg condition, one of the reflected/transmitted surface/internal wave components is significantly amplified, as evidenced by vanishing of the denominator of β_s^R in (1.3.32) or β_s^T in (1.3.33). For the six cases of class I resonances, the reflection or transmission coefficient of the resonance generated wave at the exact resonance condition is determined to be:

$$R_{ss} = \frac{M_b \pi d \omega^4 \alpha(k_s)\lambda(k_s)}{2\sinh k_s h_\ell}\,, \qquad \text{for} \qquad k=k_s,\ k_b=2k_s\ ; \tag{1.3.34}$$

$$R_{si} = \frac{M_b \pi d \omega^4 \alpha(k_i)\lambda(k_s)}{\sinh k_s h_\ell}\cdot\frac{k_i}{k_i+k_s}\,, \qquad \text{for} \qquad k=k_s,\ k_b=k_s+k_i\ ; \tag{1.3.35}$$

$$T_{si} = \frac{M_b \pi d \omega^4 \alpha(k_i)\lambda(k_s)}{\sinh k_s h_\ell}\cdot\frac{k_i}{k_i-k_s}\,, \qquad \text{for} \qquad k=k_s,\ k_b=k_i-k_s\ ; \tag{1.3.36}$$

$$R_{ii} = \frac{M_b \pi d \omega^4 \alpha(k_i)}{2\sinh k_i h_\ell}\,, \qquad \text{for} \qquad k=k_i,\ k_b=2k_i\ ; \tag{1.3.37}$$

$$R_{is} = \frac{M_b \pi d \omega^4 \alpha(k_s)}{\sinh k_i h_\ell}\cdot\frac{k_s}{k_i+k_s}\,, \qquad \text{for} \qquad k=k_i,\ k_b=k_s+k_i\ ; \tag{1.3.38}$$

$$T_{is} = \frac{M_b \pi d \omega^4 \alpha(k_s)}{\sinh k_i h_\ell}\cdot\frac{k_s}{k_i-k_s}\,, \qquad \text{for} \qquad k=k_i,\ k_b=k_i-k_s\ . \tag{1.3.39}$$

Our analysis is general for any density ratio $\mathcal{R}$. Before looking at ocean values of $\mathcal{R}$, it is of some interest to look at the perturbation theory predictions for a broader range of density ratios. In addition to theoretical interest, these are useful for comparisons with other experimental (Melville & Helfrich, 1987, for example uses $\mathcal{R}=0.85$) and computational (Dias & Vanden-Broeck, 2003, for example uses $\mathcal{R}$=0.4,0.5) studies of density stratified phenomena, for applications such as two-layer tanks (Veletsos & Shivakumar, 1993), and motion of dilute mud on the ocean floor (Jamali *et al.*, 2003).

Figure 1-5 shows the variation of the maximum amplitude of the resonance generated wave under the exact class I Bragg condition as a function of $\mathcal{R}$ for three different dimensionless frequencies $\omega^2 h_u/g$=0.25,0.0625 and 0.0025. For an upper layer depth of $h_u = 5\ m$, say, these correspond to waves of periods T=9,18 and 90 seconds respectively. The behaviors of R_{ss}, R_{is} and T_{is} are similar for different dimensionless frequencies. The reflection coefficient of surface mode wave R_{ss} increases as $\mathcal{R}$ increases and approaches a finite num-

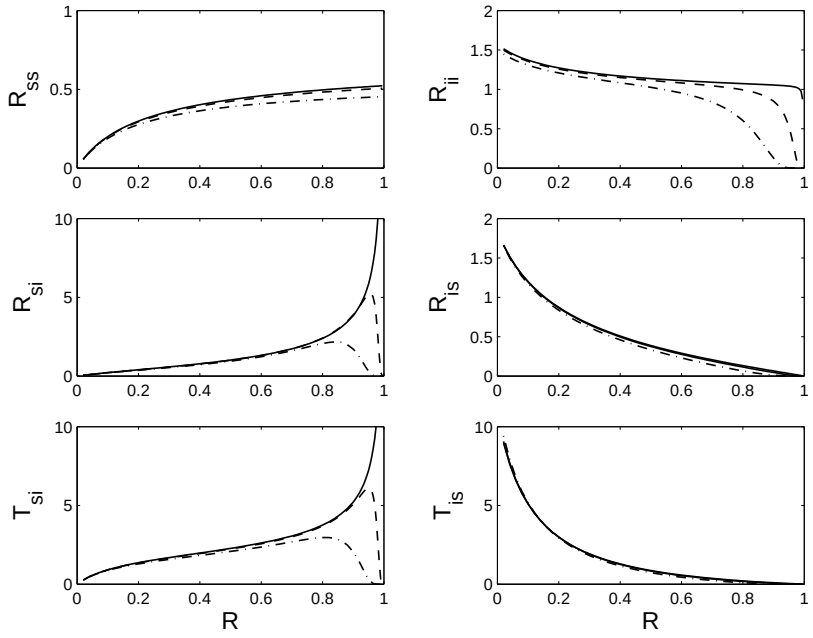

Figure 1-5: Variations of the reflection and transmission coefficients of the resonance generated wave under the exact class I Bragg resonance condition as a function of density ratio $\mathcal{R}$. d/h_ℓ=0.1, M_b=20, h_ℓ/h_u=0.5 and $\omega^2 h_u/g$=0.25, (– · –); $\omega^2 h_u/g$=0.0625, (- - -); $\omega^2 h_u/g$=0.0025 (——).

ber as $\mathcal{R} \to 1$, as in the case of a homogeneous fluid. Conversely, R_{is} and T_{is} decrease as $\mathcal{R}$ increases and vanish at the limit of $\mathcal{R} \to 1$. Coefficients R_{si} and T_{si} behave similarly. For a relative low frequency surface mode incident wave, R_{si} and T_{si} always increase as $\mathcal{R}$ increases and go unbounded as $\mathcal{R} \to 1$. For incident waves of higher frequencies, however, the increases in R_{si} and T_{si} stop at an extremum point and then decay to zero. For the resonant reflection of an internal mode waves due to an internal mode incident wave, R_{ii} decreases with the increase of $\mathcal{R}$ and may reach a finite value in the limit of $\mathcal{R} \to 1$.

Figure 1-5 shows that the results can behave qualitatively quite differently for $1 - \mathcal{R} \sim O(1)$ or not. To illustrate some features of the former, we show in Figure 1-6 all six cases of class I resonance as a function of relative wavenumber $2k_s/k_b$ for a fixed incident wave frequency, where k_s is the wavenumber of the surface-mode wave for this frequency. For each resonance case, in general, the reflection or transmission coefficient of the resonant surface or internal wave obtains its maximum value at exact resonance (given by (1.3.34) - (1.3.39)) and decreases away from the resonance in an oscillatory manner. The surface wave has higher energy than the internal wave of the same height, therefore coefficients R_{si}, T_{si} are generally greater than their internal counter-part R_{is}, T_{is}.

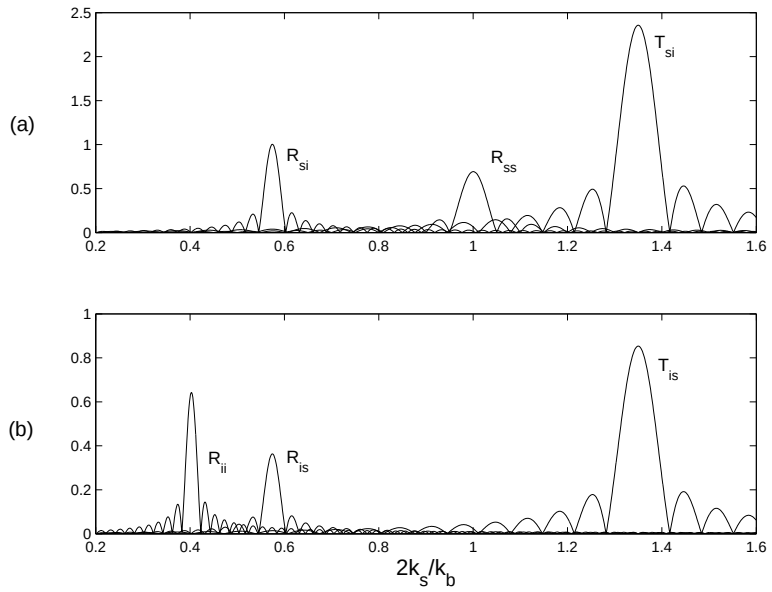

Figure 1-6: Reflection and transmission coefficients of the resonance generated wave in the neighborhood of class I Bargg resonance as a function of relative wavenumber $2k_s/k_b$ for: (a) a surface mode, and (b) an internal mode incident wave. $\mathcal{R}$=0.5, h_ℓ/h_u=1, $\omega^2 h_u/g$=0.2, d/h_ℓ=0.1, and M_b=20. For surface-mode incident waves (k=k_s), R_{si}, R_{ss}, and T_{si} associated respectively with class I resonances exactly satisfied at $2k_s/k_b$=0.575, 1.000, and 1.350, are shown in figure 1-6a. For internal-mode incident waves (k=k_i), R_{ii}, R_{is}, and T_{is} associated respectively with class I resonances exactly satisfied at $2k_s/k_b$=0.403, 0.575 and 1.350, are shown in figure 1-6b.

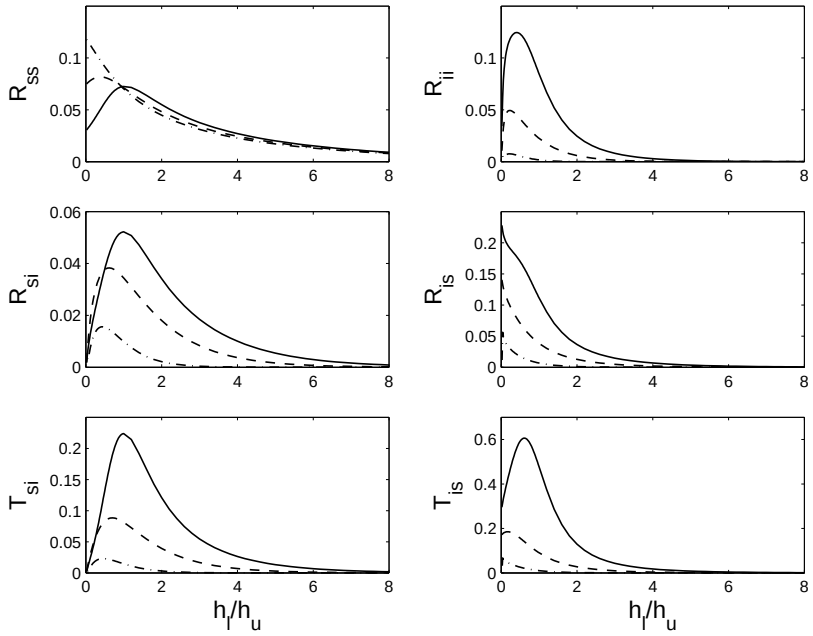

Figure 1-7: Variations of the reflection and transmission coefficients of the resonance generated wave under the exact class I Bragg resonance condition as a function of the depth ratio h_ℓ/h_u. d/h_u=0.01, $\omega^2 h_u/g$=0.16, M_b=20 and $\mathcal{R}$=0.2 (——), $\mathcal{R}$=0.5 (- - -), $\mathcal{R}$=0.8 (– · –)

Unlike $\mathcal{R}$, in a realistic environment, h_ℓ/h_u vary over a wide range. Figure 1-7 shows the dependence on the depth ratio. Relative to figure 1-5, the dependence is generally more varied with changing h_ℓ/h_u. For large increasing values of h_ℓ/h_u, class I Bragg resonance is generally weak and decreasing. Near $h_\ell/h_u \sim O(1)$, however, the resonance is strongly amplified, obtaining a maximum amplitude in the transmission/reflection coefficients in many cases. As $\mathcal{R}$ increases towards unity, this maximum occurs at lower values of h_ℓ/h_u and may eventually obtain only in the limit of $h_\ell/h_u = 0$.

We now turn to realistic ocean stratification of $1 - \mathcal{R} \ll 1$. The coefficients R_{is} and T_{is} decrease as $\mathcal{R}$ increases and vanish at the limit of $\mathcal{R} \to 1$ (see figure 1-5). In this limit a unit amplitude incident internal wave has zero energy, and hence can not excite a finite amplitude surface mode wave. From figure 1-5 we see that even with weak stratification, R_{ss} can differ from that for homogeneous fluid. This is discussed in an example in §5.1. Figure 1-5 also shows that for a relatively low frequency incident surface mode wave, R_{si} and T_{si} increase indefinitely in the limit of $1 - \mathcal{R} \ll 1$. These strong resonances are shown to offer possible mechanisms for the generation of high frequency internal waves in seas and lakes (§5.3). The underlying mechanism of R_{ii} reflection is the direct extension of Bragg resonance in a homogeneous fluid. It is seen that R_{ii} may remain finite as $\mathcal{R} \to 1$, which may explain the reflection of internal waves on continental shelves.

An interesting limiting case is when $\mathcal{R} \ll 1$, corresponding to the case of a very light upper fluid over a heavy lower fluid. In this limit, the dispersion relation of each of the two layers becomes independent of the other (and also independent of $\mathcal{R}$), and reduces to a homogeneous fluid dispersion relation. The ratio of the "natural frequencies" of the upper and lower layers is now only a function of the layer depths h_ℓ, h_u, and when $h_\ell/h_u = 1$, these frequencies are equal. For example consider an incident internal-mode wave. This incident wave acts like an external forcing to the upper layer with a frequency equal to the natural frequency of the upper layer, consequently the amplitude of the upper layer wave increases indefinitely near $h_\ell/h_u = 1$ as can be seen on the right column of figure 1-8. When the incident wave is a surface-mode wave (figure 1-8, left column), a similar behavior obtains close to $h_\ell/h_u = 1$. The surface mode excites the interface, and the interface interacts with the bottom to generates a reflected wave with the same frequency as the natural frequency of the upper/lower layers.

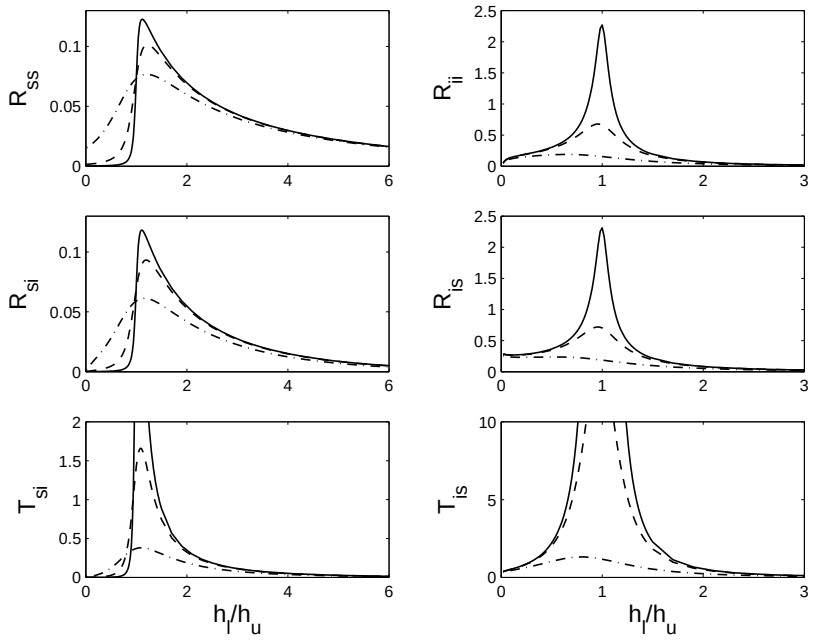

Figure 1-8: Variations of the reflection and transmission coefficients in class I Bragg resonance as a function of the depth ratio h_ℓ/h_u for small $\mathcal{R}$. d/h_u=0.01, $\omega^2 h_u/g$=0.16, M_b=20 and $\mathcal{R}$=0.001 (——), $\mathcal{R}$=0.01 (- - -), $\mathcal{R}$=0.1(– · –)

1.4 Multiple-scale analysis for class I Bragg resonance

The regular perturbation solution derived in the preceding section is valid only for resonant interactions bounded in their growth spatially by the length of the bottom topography. The reflection and transmission coefficients of the resonant wave predicted by (1.3.34) to (1.3.39) increase linearly with the number of bottom ripples M_b (or, equivalently, the length of the bottom patch $2L$), violates energy conservation and is clearly invalid for $M_b, L \to \infty$. To obtain a uniformly valid solution, a multiple-scale analysis of class I Bragg resonance is applied here following the approach of Mei (1985). The objective is to obtain and elucidate the solution for the resonance cases presented in §1.2.

1.4.1 Formulation

Consider the interaction of a surface/internal wave with bottom ripples in the neighborhood of class I Bragg resonance. Let's introduce slow variables $\bar{x} = \epsilon x$ and $\bar{t} = \epsilon t$, and make multiple-scale expansions for the potentials in the two fluid layers:

$$\phi_u = \epsilon\phi_u^{(1)} + \epsilon^2\phi_u^{(2)} + O(\epsilon^3) \qquad \text{and} \qquad \phi_\ell = \epsilon\phi_\ell^{(1)} + \epsilon^2\phi_\ell^{(2)} + O(\epsilon^3) \tag{1.4.40}$$

where $\phi_u^{(1)}$, $\phi_\ell^{(1)}$, $\phi_u^{(2)}$, and $\phi_\ell^{(2)}$ are all functions of fast variables x, z, and t, and slow variables $\bar{x}$ and $\bar{t}$. For class I Bragg resonance, assume that the amplitude of the resonance generated wave is of the same order as the incident wave, and write:

$$\eta_u = \epsilon A(\bar{x},\bar{t})\mathrm{e}^{\mathrm{i}\theta} + \epsilon A^r(\bar{x},\bar{t})\mathrm{e}^{\mathrm{i}\theta^r} + c.c. \equiv \epsilon\zeta_u \tag{1.4.41a}$$

$$\eta_\ell = \epsilon\lambda A(\bar{x},\bar{t})\mathrm{e}^{\mathrm{i}\theta} + \epsilon\lambda^r A^r(\bar{x},\bar{t})\mathrm{e}^{\mathrm{i}\theta^r} + c.c. \equiv \epsilon\zeta_\ell \tag{1.4.41b}$$

$$\eta_b = \epsilon d\sin(k_b x) \equiv \epsilon\zeta_b \tag{1.4.41c}$$

where A and A^r are respectively the complex amplitudes of the incident and resonance-generated waves on the free surface, $\theta = kx - \omega t$, $\theta^r = k^r x - \omega t$, $\lambda = \cosh(kh_u) - (gk/\omega^2)\sinh(kh_u)$ and $\lambda^r = \cosh(k^r h_u) - (gk^r/\omega^2)\sinh(k^r h_u)$. Here k and ω are the wavenumber and frequency of the (right-going) incident wave. In this section, k^r is the wavenumber of the resonance-generated wave given by the class I Bragg resonance condition: $k^r{=}k \pm k_b$. If $k^r{=}k_s$ (or k_i), the resonance-generated wave is a transmitted surface (or internal) mode wave. If $k^r{=}{-}k_s$ (or $-k_i$), the resonance-generated wave is a reflected surface (or internal) mode wave. For a somewhat simpler expression of the solution, without loss of generality, consider the rippled bottom located in the region $0 \le x \le 2L$ in this section.

For such a triad wave system, the first-order potentials are:

$$\phi_u^{(1)} = \psi_{1u}\mathrm{e}^{\mathrm{i}\theta} + \psi_{1u}^r\mathrm{e}^{\mathrm{i}\theta^r} + c.c. \qquad \text{and} \qquad \phi_\ell^{(1)} = \psi_{1\ell}\mathrm{e}^{\mathrm{i}\theta} + \psi_{1\ell}^r\mathrm{e}^{\mathrm{i}\theta^r} + c.c. \tag{1.4.42}$$

where $\psi_{1u}{=}\ F(z)A(\bar{x},\bar{t})$, $\psi_{1u}^r{=}F^r(z)A^r(\bar{x},\bar{t})$, $\psi_{1\ell}{=}\ G(z)A(\bar{x},\bar{t})$, and $\psi_{1\ell}^r{=}\ G^r(z)A^r(\bar{x},\bar{t})$ with (see equation 1.2.4)

$$F(z) = -\mathrm{i}\frac{g}{\omega}\left(\cosh kz + \frac{\omega^2}{gk}\sinh kz\right), \qquad F^r(z) = -\mathrm{i}\frac{g}{\omega}\left(\cosh k^r z + \frac{\omega^2}{gk^r}\sinh k^r z\right),$$
$$G(z) = -\frac{\mathrm{i}\omega\lambda}{k}\frac{\cosh[k(z+h_u+h_\ell)]}{\sinh(kh_\ell)}, \qquad G^r(z) = -\frac{\mathrm{i}\omega\lambda^r}{k^r}\frac{\cosh[k^r(z+h_u+h_\ell)]}{\sinh(k^r h_\ell)}.$$

At $O(\epsilon^2)$, the following system of equations is obtained:

$$\phi^{(2)}_{u,xx} + \phi^{(2)}_{u,zz} = -2\phi^{(1)}_{u,x\bar{x}} \qquad -h_u < z < 0 \qquad (1.4.43a)$$

$$\phi^{(2)}_{\ell,xx} + \phi^{(2)}_{\ell,zz} = -2\phi^{(1)}_{\ell,x\bar{x}} \qquad -h_u - h_\ell < z < -h_u \qquad (1.4.43b)$$

$$\phi^{(2)}_{u,tt} + g\phi^{(2)}_{u,z} = -2\phi^{(1)}_{u,t\bar{t}} \qquad z = 0 \qquad (1.4.43c)$$

$$\phi^{(2)}_{u,z} = \zeta_{\ell,\bar{t}} + \zeta_{\ell,x}\phi^{(1)}_{u,x} + \zeta_\ell \phi^{(1)}_{u,xx} \qquad z = -h_u \qquad (1.4.43d)$$

$$\phi^{(2)}_{\ell,z} = \zeta_{\ell,\bar{t}} + \zeta_{\ell,x}\phi^{(1)}_{\ell,x} + \zeta_\ell \phi^{(1)}_{\ell,xx} \qquad z = -h_u \qquad (1.4.43e)$$

$$\mathcal{R}(\phi^{(2)}_{u,tt} + g\phi^{(2)}_{u,z}) - (\phi^{(2)}_{\ell,tt} + g\phi^{(2)}_{\ell,z}) = -2\mathcal{R}\phi^{(1)}_{u,t\bar{t}} + 2\phi^{(1)}_{\ell,t\bar{t}} \qquad z = -h_u \qquad (1.4.43f)$$

$$\phi^{(2)}_{\ell,z} = \zeta_{b,x}\phi^{(1)}_{\ell,x} + \zeta_b \phi^{(1)}_{\ell,xx} \qquad z = -h_u - h_\ell \qquad (1.4.43g)$$

Upon substitution of $\phi^{(1)}_u$, $\phi^{(1)}_\ell$, and ζ_b, it is clear that (1.4.43) contains inhomogeneous terms proportional to $\mathrm{e}^{\mathrm{i}\theta}$ and $\mathrm{e}^{\mathrm{i}\theta^r}$; thus, $\phi^{(2)}$ takes a form similar to $\phi^{(1)}$ in (1.4.42). After applying the solvability condition for $\phi^{(2)}$, a set of coupled partial differential equations governing the evolution of A and A^r is obtained :

$$A_{,\bar{t}} + C_g A_{,\bar{x}} + \mathcal{M}A^r = 0\,, \qquad \text{and} \qquad (1.4.44)$$

$$A^r_{,\bar{t}} + C^r_g A^r_{,\bar{x}} + \mathcal{N}A = 0\,, \qquad (1.4.45)$$

where:

$$\begin{aligned}
\mathcal{M} = \quad & \omega^3 d\lambda\lambda^r k \sinh kh_\ell / (2\mathcal{R}gk \sinh kh_\ell - 3\mathcal{R}\lambda gk \sinh kh_\ell \ \cosh kh_u + 3\mathcal{R}\lambda\omega^2 \sinh kh_\ell \ \sinh kh_u \\
& + \mathcal{R}g\lambda^2 k \sinh kh_\ell + 3\omega^2\lambda^2 \cosh kh_\ell - g\lambda^2 k \sinh kh_\ell)/(2 \sinh kh_\ell \ \sinh k^r h_\ell) \\
\mathcal{N} = \quad & \omega^3 d\lambda\lambda^r k^r \sinh k^r h_\ell / (2\mathcal{R}gk^r \sinh k^r h_\ell - 3\mathcal{R}\lambda^r gk^r \sinh k^r h_\ell \ \cosh k^r h_u \\
& + 3\mathcal{R}\lambda^r\omega^2 \sinh k^r h_\ell \ \sinh k^r h_u + \mathcal{R}g\lambda^{r2}k^r \sinh k^r h_\ell + 3\omega^2\lambda^{r2} \cosh k^r h_\ell \\
& - g\lambda^{r2}k^r \sinh k^r h_\ell)/(2 \sinh kh_\ell \ \sinh k^r h_\ell)
\end{aligned}$$

Combining (1.4.44) and (1.4.45), two decoupled partial differential equations for A and A^r are obtained:

$$\left[\frac{\partial^2}{\partial\bar{t}^2} + C_g C^r_g \frac{\partial^2}{\partial\bar{x}^2} + (C_g + C^r_g)\frac{\partial^2}{\partial\bar{x}\partial\bar{t}} - \mathcal{M}\mathcal{N}\right] \left\{ \begin{array}{c} A \\ A^r \end{array} \right\} = 0\,. \qquad (1.4.46)$$

where C_g and C_g^r are the group velocities of the incident and resonance-generated waves, respectively. In the following, the focus will be on long-scale variations only, and, for clarity, all overbars in x and t are omitted hereafter in this section.

1.4.2 Perfect Tuning case

For the steady solution, A and A^r are independent of t, and (1.4.46) becomes

$$\left(\frac{\partial^2}{\partial x^2} - \frac{\mathcal{M}\mathcal{N}}{C_g C_g^r}\right) \left\{ \begin{array}{c} A \\ A^r \end{array} \right\} = 0 \; . \tag{1.4.47}$$

For the case where the resonance-generated wave is a transmitted wave (i.e. k^r=k_s or k_i), it can be shown that $\kappa^2 \equiv -\mathcal{M}\mathcal{N}/(C_g C_g^r) > 0$. In this case, the general solution to (1.4.47) takes the form:

$$A(x) = C_1 \sin(\kappa x) + C_2 \cos(\kappa x) \; , \qquad A^r(x) = C_3 \sin(\kappa x) + C_4 \cos(\kappa x) \tag{1.4.48}$$

where C_j, j=1, . . . , 4, are the unknown constants. If the resonant wave is a transmitted wave, the boundary conditions are: $A^T(x) = A^r(x)$=0 and $A(x)$=a at x=0, where a is the amplitude of the incident wave. From these boundary conditions, together with either (1.4.44) or (1.4.45), the four unknown constants C_j, j=1, . . . , 4, can be solved. The final solution for A and A^T is:

$$A(x) = a \cos(\kappa x) \; , \qquad A^T(x) = -\frac{\mathcal{N}}{\kappa C_g^r} a \sin(\kappa x) \; . \tag{1.4.49}$$

From conservation of wave action, as in the one fluid case (cf. Mei *et al.*, 2005, equation 3.1.17), the following relation can be shown to obtain:

$$\left(\frac{\mathcal{N}}{\kappa C_g^r}\right)^2 = \frac{\mathcal{N} C_g}{\mathcal{M} C_g^r} = \frac{[\mathcal{R} + \lambda^2(1-\mathcal{R})] C_g}{[\mathcal{R} + \lambda^{r2}(1-\mathcal{R})] C_g^r} \tag{1.4.50}$$

Therefore, the solution for the amplitude of the resonance-generated wave in (1.4.49) can also be expressed as:

$$|A^T(x)| = \left\{ \frac{[\mathcal{R} + \lambda^2(1-\mathcal{R})] C_g}{[\mathcal{R} + \lambda^{r2}(1-\mathcal{R})] C_g^r} \right\}^{1/2} a \, |\sin(\kappa x)| \; . \tag{1.4.51}$$

Numerical evaluation of the dimensionless modulation wavenumber $\kappa^* = \kappa/(dkk^r)$ shows that κ^* increases as kh_u, kh_ℓ or $\mathcal{R}$ decreases. This indicates that the modulation in $A^r(x)$ occurs more rapidly for stronger wave-bottom interactions. Also κ varies linearly with the bottom topography amplitude.

For the case where the resonance-generated wave is reflected (i.e. $k^r{=}{-}k_s$ or $-k_i$), it can be shown that $-\mathcal{MN}/(C_g C_g^r) < 0$. Therefore by defining $\kappa^2 = \mathcal{MN}/(C_g C_g^r)$ the general solution to (1.4.47) takes the form:

$$A(x) = C_1 \sinh(\kappa x) + C_2 \cosh(\kappa x)\ , \qquad A^R(x) = C_3 \sinh(\kappa x) + C_4 \cosh(\kappa x) \quad (1.4.52)$$

The boundary conditions are: $A^R(x){=}0$ at $x{=}2L$ and $A(x){=}a$ at $x{=}0$. Using these boundary conditions and either (1.4.44) or (1.4.45), the four unknown coefficients can be solved and finally for A and A^R it obtaines:

$$A(x) = a\frac{\cosh\kappa(2L-x)}{\cosh 2\kappa L} \quad (1.4.53)$$

$$A^R(x) = a\frac{\mathcal{N}}{\kappa C_g^r}\frac{\sinh\kappa(2L-x)}{\cosh 2\kappa L} \quad (1.4.54)$$

It is to be noted that in the special case of one fluid, the above results reduce directly to (3.5) and (3.6) of Mei (1985).

For a very long bottom patch of periodic ripples, the problem (away from the edges of the patch) can be cast in terms of the time evolution of a wave traveling over a periodic domain of bottom ripples. In this case, the governing equations are still (1.4.46) with the x dependencies dropped. If the resonant wave is a transmitted wave, sinusoidal modulation occurs in time. With the initial conditions $A(t){=}a$ and $A^T(t){=}0$ at $t{=}0$,

$$A(t) = a\cos(\kappa^t t), \qquad |A^T(t)| = a\left[\frac{\mathcal{R}+\lambda^2(1-\mathcal{R})}{\mathcal{R}+\lambda^r(1-\mathcal{R})}\right]^{1/2}|\sin(\kappa^t t)| \quad (1.4.55)$$

where $\kappa^t{=}(-\mathcal{MN})^{1/2}$.

It is now possible to relate $A^T(t)$ in (1.4.55) to $A^T(x)$ in (1.4.51) in terms of group velocity. In the special cases of same-mode resonance interactions, or in the case of a homogeneous fluid (Liu & Yue, 1998), the group velocity of the resonant wave, C_g^r, is the same as the group velocity of the incident wave, C_g, and $A^T(t)$ and $A^T(x)$ are related by the single group velocity $t = x/C_g$, as in the classical relationship between the spatial/temporal

evolution of a single wave train (eg Gaster, 1962). In the general case, $C_g \neq C_g^r$, and, from (1.4.46), it can be readily shown that $A^T(x)$ in (1.4.51) is related to $A^T(t)$ in (1.4.55) by a factor of $(C_g/C_g^r)^{1/2}$ and the relation $t{=}x/(C_g C_g^r)^{1/2}$.

1.4.3 Detuned case

Assume that the incident wave has a wavenumber of $k + \epsilon K$ and a frequency $\omega + \epsilon\Omega$, where $\mathcal{D}(k,\omega) = 0$ and $\Omega{=}C_g K$. On the rippled bottom region ($0 \leq x \leq 2L$), let

$$(A, A^r) = a[F(x), F^r(x)]\mathrm{e}^{-\mathrm{i}\Omega t} \; . \tag{1.4.56}$$

Substitution of the above into (1.4.46) gives the differential equations for F and F^r:

$$\left[\frac{\partial^2}{\partial x^2} - \mathrm{i}\Omega\left(\frac{1}{C_g} + \frac{1}{C_g^r}\right)\frac{\partial}{\partial x} - \frac{\Omega^2 + \mathcal{M}\mathcal{N}}{C_g C_g^r}\right]\left\{\begin{array}{c} F \\ F^r \end{array}\right\} = 0 \; . \tag{1.4.57}$$

The general solution to (1.4.57) can be written in the form:

$$F(x) = C_1\mathrm{e}^{r_1 x} + C_2\mathrm{e}^{r_2 x} \; , \qquad F^r(x) = C_3\mathrm{e}^{r_1 x} + C_4\mathrm{e}^{r_2 x} \tag{1.4.58}$$

where r_1 and r_2 are the two roots of the characteristic equation. Based on the proper boundary conditions and the matching conditions (from substitution of (1.4.56) into (1.4.44) or (1.4.45)), the unknown constants in (1.4.58) can be determined. In the following, for clarity, the results for the cases of resonant transmitted and reflected waves are described separately.

Case A

For the case where the resonance generated wave is transmitted over the rippled bottom, the discriminant of the characteristic equation of (1.4.57) is always negative, and r_1 and r_2 are:

$$r_{1,2} = \mathrm{i}\mathcal{B}\left[\Omega \pm (\Omega_0^2 + \Omega^2)^{\frac{1}{2}}\right] \tag{1.4.59}$$

where

$$\mathcal{B} \equiv \frac{1}{2}\left(\frac{1}{C_g^r} - \frac{1}{C_g}\right) \; , \quad \text{and} \quad \Omega_0 \equiv 2\frac{|\mathcal{M}\mathcal{N}C_g C_g^r|^{\frac{1}{2}}}{|C_g - C_g^r|} \; .$$

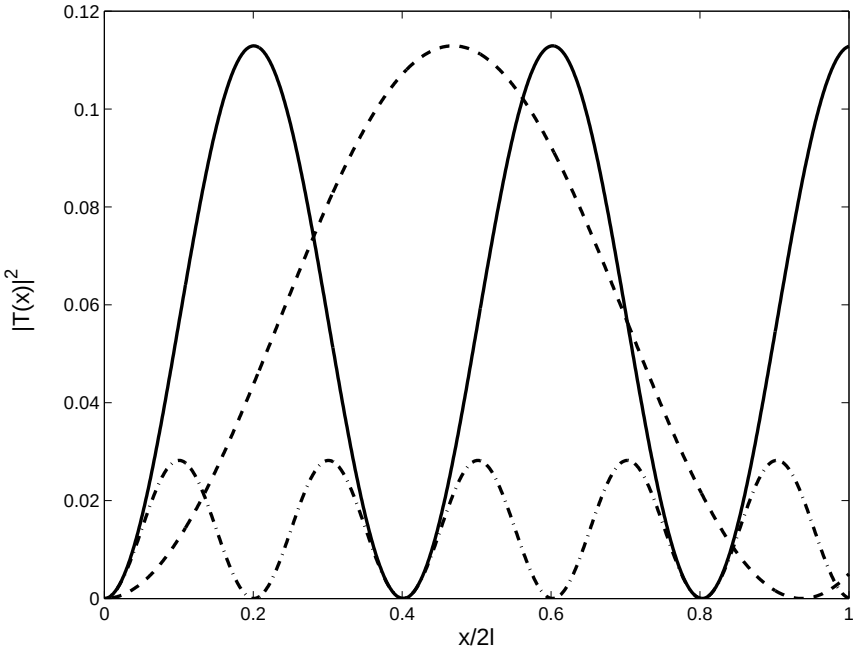

Figure 1-9: Transmission coefficient of the resonance generated internal wave over the rippled bottom. $\Omega/\Omega_0 = 0.5$, $2\kappa L = 7$ (——) ; $\Omega/\Omega_0 = 0.5$, $2\kappa L = 3$ (- - -); $\Omega/\Omega_0 = 2$, $2\kappa L = 7$ (– · –). $\mathcal{R} = 0.5$, $h_\ell/h_u = 1$, $kh_u = 0.57$, $\Omega^2 h_u/g = 0.43$, and $kd = 0.04$.

In the incident side ($x < 0$), $A(x)$=$a \exp[\mathrm{i}(Kx - \Omega t)]$ and $A^T(x)$=0, which lead to the boundary conditions: $F(x)$=1 and $F^T(x)$=0 at x=0. From these boundary conditions it obtaines:

$$F(x) = \mathrm{e}^{\mathrm{i}\mathcal{B}\Omega x}\left[-\mathrm{i}\frac{\Omega}{2\kappa}\left(\frac{1}{C_g^r}+\frac{1}{C_g}\right)\sin(\kappa x)+\cos(\kappa x)\right]\ , \tag{1.4.60a}$$

$$F^T(x) = -\mathrm{e}^{\mathrm{i}\mathcal{B}\Omega x}\frac{\mathcal{N}}{\kappa C_g^r}\sin(\kappa x) \tag{1.4.60b}$$

where κ=$\mathcal{B}(\Omega_0^2+\Omega^2)^{1/2}$. On the transmission side ($x > 2L$)

$$A(x) = aA^c\mathrm{e}^{\mathrm{i}(Kx-\Omega t)}, \qquad A^T(x) = aT\mathrm{e}^{\mathrm{i}(K^r x-\Omega t)} \tag{1.4.61}$$

where A^c and T are the transmission coefficients of the incident and resonance-generated waves and are given by

$$A^c = \mathrm{e}^{2\mathrm{i}\mathcal{B}\Omega L}\left[-\mathrm{i}\frac{\Omega}{2\kappa}\left(\frac{1}{C_g^r}+\frac{1}{C_g}\right)\sin(2\kappa L)+\cos(2\kappa L)\right]\ , \qquad T = -\mathrm{e}^{2\mathrm{i}\mathcal{B}\Omega l}\frac{\mathcal{N}}{\kappa C_g^r}\sin(2\kappa L)\ . \tag{1.4.62}$$

For a surface mode incident wave, as an example, figure 1-9 shows the variation of the

resonant transmitted internal wave over the rippled bottom. Because the characteristic equation has no critical value, for all frequencies only modulation occurs. The amplitude of modulation is independent of the length of the rippled patch but increases as the frequency detuning decreases. Frequency of modulation varies with the frequency detuning because the length has been normalized with $\kappa_0 = \kappa|_{\Omega=0} = \mathcal{B}\Omega_0$.

Case B

For the case where the resonance-generated wave is reflected:

$$r_{1,2} = \left[\mathrm{i}\Omega \pm (\Omega_0^2 - \Omega^2)^{\frac{1}{2}}\right]. \tag{1.4.63}$$

Clearly, Ω_0 is the cutoff frequency. For $|\Omega| < \Omega_0$, $F(x)$ ($F^R(x)$) has both sinusoidally varying and exponentially decaying (growing) parts in x. For $|\Omega| > \Omega_0$, $F(x)$ and $F^R(x)$ are purely sinusoidal in x. For critical detuning Ω=Ω_0, $F(x)$ ($F^r(x)$) has a sinusoidal variation in x with the amplitude linearly decaying (growing) with x.

In this case, the boundary conditions are $F(x)$=1 at x=0 and $F^R(x)$=0 at $x = 2L$. Based on these boundary conditions, $F(x)$ and $F^R(x)$ are obtained. Specifically, for $|\Omega| < \Omega_0$,

$$F(x) = \frac{\mathrm{e}^{\mathrm{i}\mathcal{B}\Omega x}}{\gamma^\dagger - \lambda^\dagger \mathrm{e}^{4\kappa L}}\left[\gamma^\dagger \mathrm{e}^{\kappa x} - \lambda^\dagger \mathrm{e}^{\kappa(4L-x)}\right], \qquad F^R(x) = \frac{\mathrm{e}^{\mathrm{i}\mathcal{B}\Omega x}}{\gamma^\dagger - \lambda^\dagger \mathrm{e}^{4\kappa L}}\left[\mathrm{e}^{\kappa x} - \mathrm{e}^{\kappa(4L-x)}\right] \tag{1.4.64a}$$

where κ=$\mathcal{B}(\Omega_0^2 - \Omega^2)^{1/2}$, $\gamma^\dagger$=$(\mathrm{i}\Omega - r_1 C_g^r)/\mathcal{N}$, and $\lambda^\dagger$=$(\mathrm{i}\Omega - r_2 C_g^r)/\mathcal{N}$. Thus on the incident side ($x < 0$),

$$A(x) = a\mathrm{e}^{\mathrm{i}(Kx-\Omega t)}, \qquad A^R(x) = aR\mathrm{e}^{\mathrm{i}(K^R x-\Omega t)} \tag{1.4.65}$$

and on the transmission side ($x > 2L$),

$$A(x) = aA^c\mathrm{e}^{\mathrm{i}(Kx-\Omega t)}, \qquad A^R(x) = 0 \tag{1.4.66}$$

where the reflection coefficient of the resonance-generated wave, R, and the transmission coefficient of the incident wave, A^c are:

$$R = \frac{1}{\gamma^\dagger - \lambda^\dagger \mathrm{e}^{4\kappa L}}\left[1 - \mathrm{e}^{4\kappa L}\right], \qquad A^c = \frac{\mathrm{e}^{2\mathrm{i}\mathcal{B}\Omega L}}{\gamma^\dagger - \lambda^\dagger \mathrm{e}^{4\kappa L}}(\gamma^\dagger - \lambda^\dagger)\mathrm{e}^{2\kappa L}. \tag{1.4.67}$$

If $|\Omega| > \Omega_0$, the solution is obtained from the above (for $|\Omega| < \Omega_0$) by replacing κ by $i\kappa$.

At the critical frequency $|\Omega|=\Omega_0$, $r_1 = r_2$. The general solution in (1.4.58) must be changed to the form: $F(x)=(C_1 + C_2 x)\exp(r_1 x)$ and $F^R(x)=(C_3 + C_4 x)\exp(r_2 x)$. Using the same boundary condition: $F(x)=1$ at $x=0$ and $F^R(x)=0$ at $x=2L$,

$$F(x) = \left[1 + \frac{i\Omega(C_g^r\mathcal{B} - 1)}{\mathcal{B}^*}x\right] \mathrm{e}^{\mathrm{i}\mathcal{B}\Omega x} \ , \quad F^R(x) = \frac{\mathcal{N}(2L - x)}{\mathcal{B}^*}\mathrm{e}^{\mathrm{i}\mathcal{B}\Omega x} \tag{1.4.68a}$$

where $\mathcal{B}^* = C_g^r + i\Omega(L - \mathcal{B}C_g^r)$. In this case, R and A^c are:

$$R = \frac{2\mathcal{N}L}{C_g^r + i\Omega L(1 - C_g^r\mathcal{B})}, \qquad A^c = \left[1 + \frac{2\mathrm{i}\Omega L(C_g^r\mathcal{B} - 1)}{C_g^r + \mathrm{i}\Omega L(1 - C_g^r\mathcal{B})}\right] \mathrm{e}^{2\mathrm{i}\mathcal{B}\Omega L} \ . \tag{1.4.69}$$

For a surface incident wave, for example, figure 1-10 plots the variation of the reflection coefficient of the resonance generated internal wave over the rippled bottom with various degrees of detuning. For sub-critical detuning ($|\Omega| < \Omega_0$), the exponential behavior is observed. Note that the curve for $2\kappa L$=7 lies below the curve for $2\kappa L$=3; while at the critical frequency the situation is reversed. For super-critical detuning, only modulation occurs. Figure 1-11 compares the results of the resonant reflection or transmission coefficient in the neighborhood of the class I Bragg resonance obtained using the regular perturbation analysis and the multiple-scale approach. Similar result is also obtained by using McKee (1996) approach which is based of the modified mild slope theory of Kirby (1986). These are also shown in figure 1-11. All six class I resonance cases are considered. Two bottom ripple amplitudes d/h_u=0.1 and d/h_u=0.03 are used. Other parameters used are: $\mathcal{R}$=0.5, h_ℓ/h_u=1, $\omega^2 h_u/g$=0.14, and M_b=20. For small bottom ripples amplitude, all three solutions agree each other. For large bottom ripples amplitude, as expected, the multiple-scale solution agrees well with the solution based on the modified mild slop equation, while the regular perturbation solution overestimates the reflection and transmission coefficients of the resonant wave.

Another comparison is made in figure figure 1-12 for ocean stratification of $\mathcal{R} = 0.96$. Again two bottom ripple amplitudes d/h_u=0.1 and d/h_u=0.03 are used. Other parameters used are: $\mathcal{R}$=0.96, h_ℓ/h_u=0.25, $\omega^2 h_u/g$=0.14, and M_b=20. Similar behaviors as in figure 1-11 is observed.

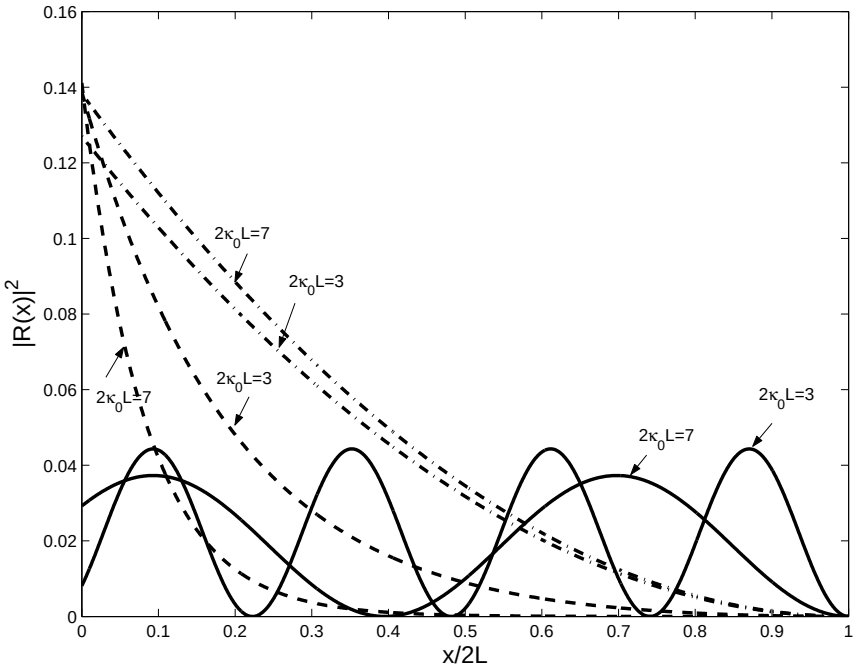

Figure 1-10: Reflection coefficient of the resonance generated internal wave over the rippled bottom. $\Omega/\Omega_0 = 2$ (——); $\Omega/\Omega_0 = 0.5$ (- - -); $\Omega/\Omega_0 = 1$ (– · –). $\mathcal{R} = 0.5$, $h_\ell/h_u = 1$, $\Omega^2 h_u/g = 0.43$, $kd = 0.04$ and $kh_u = 0.57$.

1.5 Regular perturbation analysis for class II and III Bragg resonances

Class II and III Bragg resonances occur at the third order and involve four wave/bottom components. Specifically, two (three) propagating surface/internal waves and two (one) bottom waves are involved in class II (III) resonance. The regular perturbation analysis of these two classes of Bragg resonance are obtained here. Multiple-scale analyses similar to that in §1.4 can be formulated for these cases and, in principle, obtained. The resulting algebra is however extremely involved and is not pursued here.

1.5.1 Class II Bragg resonance

Consider the general problem of an incident wave, wavenumber k and frequency ω, propagating over a rippled bottom consisting of two wave components with wavenumbers k_{b1} and k_{b2}. Without loss of generality, the free-surface elevation of the incident wave and

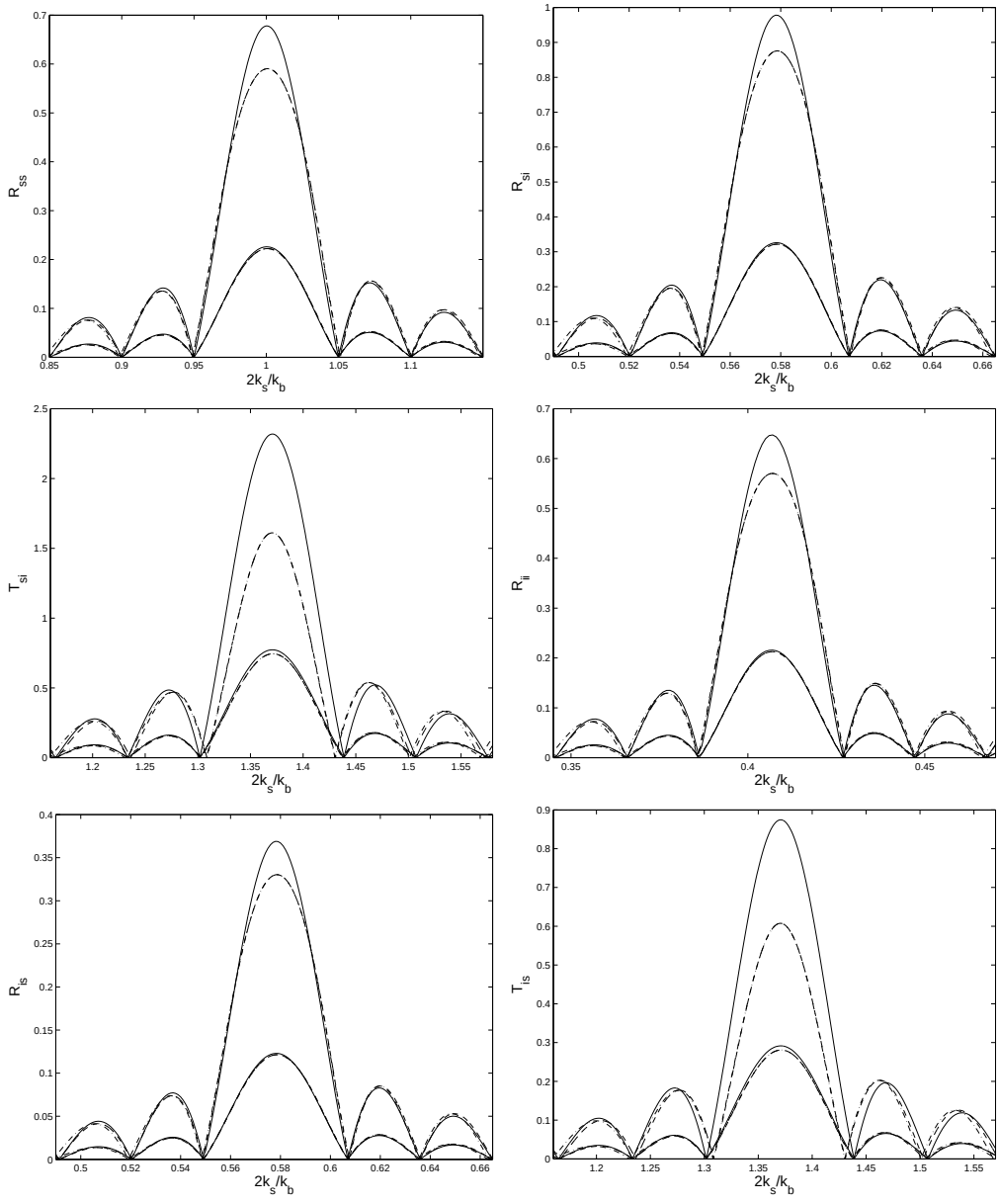

Figure 1-11: Reflection and transmission coefficients of the resonance generated wave due to class I Bragg resonance obtained from: regular perturbation theory (—); the modified mild slope equation (- - -); and the multiple-scale method (- · -) (the latter two are distinguishable only far away from exact resonance). Two bottom rippled amplitudes are considered: d/h_u=0.1 and d/h_u=0.03. The other parameters are: $\mathcal{R}$=0.5, h_ℓ/h_u=1, $\omega^2 h_u/g$=0.14 and M_b=20.

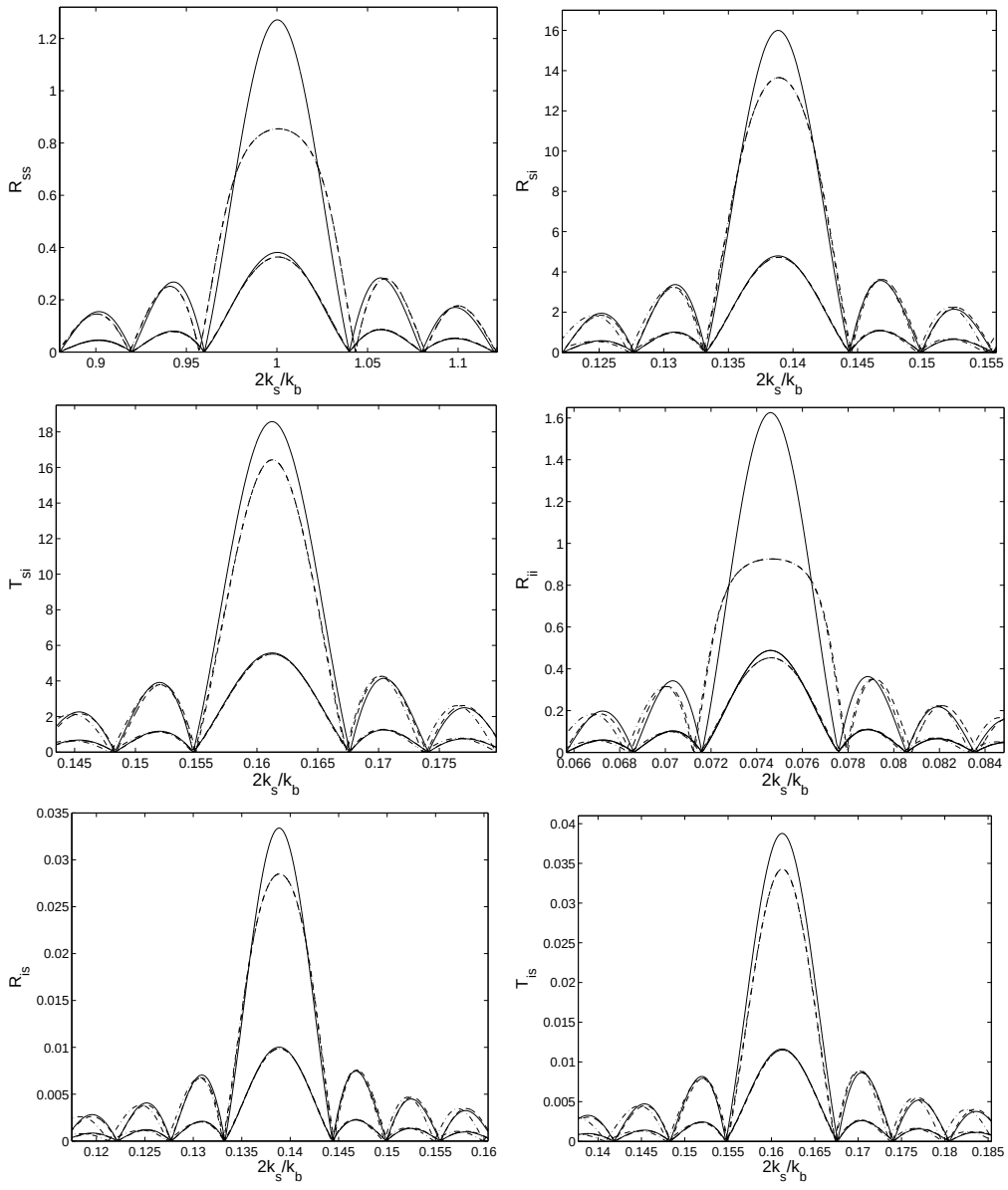

Figure 1-12: Reflection and transmission coefficients of the resonance generated wave due to class I Bragg resonance obtained from: regular perturbation theory (——); the modified mild slope equation (- - -); and the multiple-scale method (– · –) (the latter two are distinguishable only far away from exact resonance). Two bottom rippled amplitudes are considered: d/h_u=0.1 and d/h_u=0.03. The other parameters are: $\mathcal{R}$=0.96, h_ℓ/h_u=0.25, $\omega^2 h_u/g$=0.14 and M_b=25.

bottom elevation are assumed to be:

$$\eta_s^{(1)}(x,t) = a\sin(kx-\omega t)\ , \quad \eta_b(x) = d_1\sin(k_{b1}x) + d_2\sin(k_{b2}x) \tag{1.5.70}$$

where d_1 and d_2 represent the amplitudes of the two bottom ripple components. The objective here is to derive the solution of the third-order boundary-value problem (1.2.3) with m=3, associated with class II resonance.

The second-order solution of the lower-layer potential in the region of rippled bottom is:

$$\phi_\ell^{(2)} = a\sum_{j=1}^{4}\left\{q_j\sinh\left[\bar{k}_j(z+h_u+h_\ell)\right] + D_j\cosh\left[\bar{k}_j(z+h_u+h_\ell)\right]\right\}\sin\left(\bar{k}_j x-\omega t\right) + NT \tag{1.5.71}$$

where

$$D_j = -q_j\left[\omega^4(\mathcal{R}\coth\bar{k}_j h_\ell + \coth\bar{k}_j h_u) - g\bar{k}_j\omega^2(1+\coth\bar{k}_j h_u\coth\bar{k}_j h_\ell)\right.$$
$$\left. +g^2\bar{k}_j^2\coth\bar{k}_j h_\ell(1-\mathcal{R})\right]/\mathcal{D}(\bar{k}_j,\omega)\ , \tag{1.5.72}$$

$$q_j = \frac{\omega\bar{d}_j\lambda(k)}{2\sinh(kh_\ell)}\ , \qquad \lambda(\xi) = \cosh(\xi h_u) - \frac{gk}{\omega^2}\sinh(\xi h_u) \tag{1.5.73}$$

for j=1, ..., 4, and $\bar{k}_{1,2}$=$k\pm k_{b1}$, $\bar{k}_{3,4}$=$k\pm k_{b2}$, $\bar{d}_{1,2}$=$\pm d_1$, and $\bar{d}_{3,4}$=$\pm d_2$. In (1.5.71), the symbol "NT" represents "non-resonant terms" irrelevant to class II resonance. Upon substitution, the inhomogeneous term in the third-order bottom boundary condition in (1.2.3) is:

$$f_6^{(3)} \equiv \eta_{b,x}\phi_{\ell,x}^{(2)} - \eta_b\phi_{\ell,zz}^{(2)} = a\sum_{j=1}^{8}U_j\cos(\hat{k}_j x-\omega t) + NT \tag{1.5.74}$$

where $\hat{k}_{8,1}$=$k\pm 2k_{b1}$, $\hat{k}_{2,3}$=$k-k_{b1}\pm k_{b2}$, $\hat{k}_{4,5}$=$k\pm 2k_{b2}$, and $\hat{k}_{6,7}$=$k+k_{b1}\pm k_{b2}$. The coefficients

U_j, j=1, . . . , 8 are:

$$
\begin{aligned}
U_1 &= -1/2\, d_1 D_2 k^2 - d_1 D_2 {k_{b1}}^2 + 3/2\, d_1 D_2 k k_{b1} \ , \\
U_2 &= (1/2\, d_2 D_2 - 1/2\, d_1 D_3)\, k^2 + (1/2\, d_2 k_{b2} D_2 - d_2 D_2 k_{b1} + 1/2\, d_1 k_{b1} D_3 - d_1 D_3 k_{b2})\, k \\
&\quad +1/2\ (k_{b1} - k_{b2})\, (d_2 D_2 k_{b1} + d_1 D_3 k_{b2}) \ , \\
U_3 &= (-1/2\, d_2 D_2 - 1/2\, d_1 D_4)\, k^2 + (d_2 D_2 k_{b1} + d_1 D_4 k_{b2} + 1/2\, d_1 k_{b1} D_4 + 1/2\, d_2 k_{b2} D_2)\, k \\
&\quad -1/2\ (k_{b2} + k_{b1})\, (d_2 D_2 k_{b1} + d_1 D_4 k_{b2}) \ , \\
U_4 &= 1/2\, d_2 D_3 k^2 + d_2 D_3 {k_{b2}}^2 + 3/2\, d_2 D_3 k k_{b2} \ , \\
U_5 &= -d_2 {k_{b2}}^2 D_4 - 1/2\, d_2 D_4 k^2 + 3/2\, d_2 k_{b2} D_4 k \ , \\
U_6 &= (1/2\, d_2 D_1 + 1/2\, d_1 D_3)\, k^2 + (d_1 D_3 k_{b2} + d_2 D_1 k_{b1} + 1/2\, d_1 k_{b1} D_3 + 1/2\, d_2 k_{b2} D_1)\, k \\
&\quad +1/2\ (k_{b2} + k_{b1})\, (d_2 D_1 k_{b1} + d_1 D_3 k_{b2}) \ , \\
U_7 &= (-1/2\, d_2 D_1 + 1/2\, d_1 D_4)\, k^2 + (-d_2 D_1 k_{b1} - d_1 D_4 k_{b2} + 1/2\, d_1 k_{b1} D_4 + 1/2\, d_2 k_{b2} D_1)\, k \\
&\quad -1/2\ (k_{b1} - k_{b2})\, (d_2 D_1 k_{b1} + d_1 D_4 k_{b2}) \ , \\
U_8 &= d_1 {k_{b1}}^2 D_1 + 3/2\, d_1 k_{b1} D_1 k + 1/2\, d_1 D_1 k^2 \ .
\end{aligned}
$$

Class II resonance is governed by the third-order boundary-value problem, (1.2.3), with $f_j^{(3)}$=0, j=1, . . . , 5, and $f_6^{(3)}$ given by (1.5.74). This boundary-value problem can be solved using the same procedure in §1.3 for the class I resonance. For a patch of bottom ripples located in $|x| \le L$, the displacements of surface and internal waves at far upstream and downstream are obtained:

$$
\eta_u^{(3\mp)}(x,t) = \omega^3 \alpha(k_s) \beta_s^{\mp}(k_s) \cos(k_s x \pm \omega t) + \omega^3 \alpha(k_i) \beta_s^{\mp}(k_i) \cos(k_i x \pm \omega t) \ , \quad (1.5.75)
$$

$$
\eta_\ell^{(3\mp)}(x,t) = \omega^3 \alpha(k_s) \beta_i^{\mp}(k_s) \cos(k_s x \pm \omega t) + \omega^3 \alpha(k_i) \beta_i^{\mp}(k_i) \cos(k_i x \pm \omega t) \ , \quad (1.5.76)
$$

for $x \to \mp\infty$, where

$$
\beta_s^{\mp}(\xi) = 2a \sum_{j=1}^{8} U_j \frac{\sin[(\hat{k}_j \pm \xi) L]}{\hat{k}_j \pm \xi} \ , \qquad \beta_i^{\mp}(\xi) = \lambda(\xi) \beta_s^{\mp}(\xi) \ . \quad (1.5.77)
$$

For illustration, consider a relatively simple case with a monochromatic bottom variation, and let d_1=d_2=$d/2$ and k_{b1}=k_{b2}=k_b. Let the incident wave to be a surface mode with wavenumber k=k_s and frequency ω. Under the condition k_b=$(k_s + k_i)/2$, class II reso-

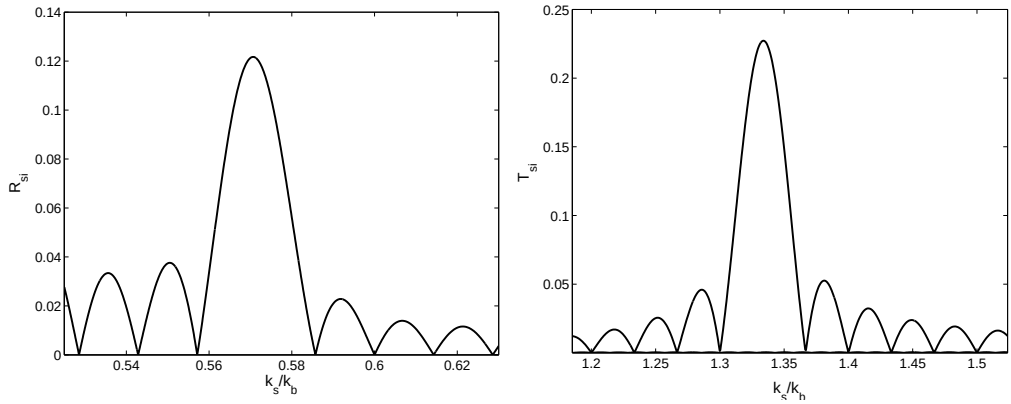

Figure 1-13: Reflection (left) and transmission (right) coefficients of the resonant internal wave in the neighborhood of class II Bragg resonance. Parameters are h_ℓ/h_u=1, $\mathcal{R}$ = 0.5, kh_u=$k_s h_u$=0.4 ($\omega^2 h_u/g$=0.24), kd=0.06, and M_b=40.

nance occurs and the resonance-generated wave is the reflected wave of internal mode. The reflection coefficient of the resonant wave is:

$$R_{si} = \frac{\left|\eta_\ell^{(3-)}\right|}{\left|\eta_u^{(1)}\right|} = \quad 2d^2 L\omega\alpha(k_i)(k_s^2 + 2k_b^2 - 3k_s k_b)\lambda(k_s)\lambda(k_i)\left[\sinh(k_s h_\ell)\mathcal{D}(\bar{k}_4,\omega)\right]^{-1} \times$$
$$\left\{\omega^4(\mathcal{R}\coth\bar{k}_4 h_\ell + \coth\bar{k}_4 h_u) - g\bar{k}_4\omega^2(1 + \coth\bar{k}_4 h_u \coth\bar{k}_4 h_\ell) + \right.$$
$$\left. g^2\bar{k}_4^2 \coth\bar{k}_4 h_\ell(1-\mathcal{R})\right\} . \qquad (1.5.78)$$

As expected, in class II resonance, R_{si} is independent of the incident wave amplitude, and has a quadratic dependence on the ripple amplitude and a linear dependence on the patch length. Figure 1-13 plots the reflection and transmission coefficients of the generated internal wave in the neighborhood of class II Bragg resonance. For this example, M_b=20, the depth ratio is h_ℓ/h_u=1, the density ratio is $\mathcal{R}$=0.5, ripple amplitude is kd=0.06 and the incident wave is a surface mode with kh_u=$k_s h_u$=0.4 ($\omega^2 h_u/g$=0.24). With these parameters, class II Bragg resonances obtain at k/k_b=0.57 and k/k_b=1.34. For the formal(latter), the resonance generated wave is a reflected(transmitted) internal wave. Similarly to class I resonance, the reflection and transmission coefficient of the resonant wave decreases in an oscillatory manner as detuning from the exact resonance condition increases.

1.5.2 Class III Bragg resonance

The regular perturbation analysis for class III Bragg resonance is much more involved than those for class I and class II resonances since all inhomogeneous terms in the third-order boundary-value problem (1.2.3), $f_j^{(3)}$, j=1, ..., 6, must be taken into account. Consider the general case of two incident wave components with the free-surface elevation given by:

$$\eta_u^{(1)} = a_1 \sin(k_1 x - \omega_1 t) + a_2 \sin(k_2 x - \omega_2 t) \tag{1.5.79}$$

where a_1, a_2, k_1, k_2, and ω_1, ω_2 are respectively the amplitude, wavenumber, and frequency of incident wave component 1,2. The rippled bottom is given by: $\eta_b(x)$=$d \sin(k_b x)$. At second order (m=2), resonance is assumed not to occur as the interest here is in the third-order resonance; and the second-order solution of (1.2.3) can be readily obtained. In general, the second order solutions for both potentials and elevations contain terms with wavenumbers $2k_1$, $2k_2$, $k_1 \pm k_2$, $k_1 \pm k_b$, and $k_2 \pm k_b$. Based on the first- and second-order solutions, the forcing terms in the third-order boundary-value problem, $f_j^{(3)}$, j=1, ..., 6, can be determined.

The resulting system of equations at third order can be solved using Fourier transform as in §1.3. The final solutions for the potentials are:

$$\begin{aligned}\phi_u^{(3)}(x,z,t) = \frac{1}{2\pi}\int_{-\infty}^{\infty} \{&[A_{u1}\cosh(\xi z) + B_{u1}\sinh(\xi z)]\cos(\omega_+ t) \\ &+[A_{u2}\cosh(\xi z) + B_{u2}\sinh(\xi z)]\sin(\omega_+ t)\}\, \mathrm{e}^{-\mathrm{i}\xi x}\mathrm{d}\xi \ , \end{aligned} \tag{1.5.80}$$

$$\begin{aligned}\phi_\ell^{(3)}(x,z,t) = \frac{1}{2\pi}\int_{-\infty}^{\infty} \{&[A_{\ell 1}\cosh(\xi z) + B_{\ell 1}\sinh(\xi z)]\cos(\omega_+ t) \\ &+[A_{\ell 2}\cosh(\xi z) + B_{\ell 2}\sinh(\xi z)]\sin(\omega_+ t)\}\, \mathrm{e}^{-\mathrm{i}\xi x}\mathrm{d}\xi \ , \end{aligned} \tag{1.5.81}$$

where ω_+=$\omega_1 + \omega_2$, and

$$A_{uj}\tilde{D} = (\Lambda_{4j} g - su\, sl\, \mathcal{R}\Lambda_{1j} + cl\, g\Lambda_{3j} - cl\, cu\, \Lambda_{1j})\,\omega_+^2 - \xi\, sl\, g\,(\Lambda_{3j} g + \mathcal{R} cu\, \Lambda_{1j} - \Lambda_{2j} - cu\, \Lambda_{1j}) \ ,$$

$$B_{uj}\tilde{D} = \frac{(\Lambda_{4j} + cl\,\Lambda_{3j})\,\omega_+^4}{\xi} + (sl\,\Lambda_{2j} - sl\,\mathcal{R} cu\,\Lambda_{1j} - gsl\,\Lambda_{3j} - \Lambda_{1j}\, cl\, su)\,\omega_+^2 - \Lambda_{1j}\, su\, g\xi\, sl\ (\mathcal{R} - 1) \ ,$$

$$
\begin{aligned}
A_{\ell j}\tilde{D}\xi = &-su\ (su\ sl\,\Lambda_{3j}\mathcal{R} + cl\ cu\,\Lambda_{3j}\mathcal{R} - \Lambda_{4j}\,cu + cu\,\Lambda_{4j}\mathcal{R})\,\omega_+^4 \\
&-\xi\ \big(-su\ sl\ cu\,\Lambda_{2j} - cl\ cu\ su^2\mathcal{R}\Lambda_{1j} - sl\,\mathcal{R}\Lambda_{1j}\,su^3 + su^2\Lambda_{4j}g + \\
&cl\ cu^3\mathcal{R}\Lambda_{1j} - cl\ cu^2\Lambda_{2j} - \Lambda_{4j}\,cu^2 g + su\ cu^2 sl\,\mathcal{R}\Lambda_{1j}\big)\,\omega_+^2 \\
&-gsu\,\xi^2\,(-cl\ cu\,g\Lambda_{3j}\mathcal{R} + cl\ cu\,\Lambda_{2j} + su\ sl\,\Lambda_{2j} - su\ sl\,g\Lambda_{3j}\mathcal{R} - cu\,\Lambda_{4j}g\mathcal{R} + cu\,\Lambda_{4j}g)\ ,
\end{aligned}
$$

$$
\begin{aligned}
B_{\ell j}\tilde{D}\xi = &\big(-su^2 cl\,\Lambda_{3j}\mathcal{R} - su^2\Lambda_{4j}\mathcal{R} - cu\ sl\,\Lambda_{3j}\,su\,\mathcal{R} + cu^2\Lambda_{4j}\big)\,\omega_+^4 \\
&-\xi\ \big(cu^2\mathcal{R}\Lambda_{1j} - su^2\Lambda_{1j}\mathcal{R} - cu\,\Lambda_{2j}\big)\,(cu\ sl + su\ cl)\,\omega_+^2 \\
&-gsu\,\xi^2\,(-cu\ sl\,g\Lambda_{3j}\mathcal{R} - su\ cl\,g\Lambda_{3j}\mathcal{R} + su\,g\Lambda_{4j} - su\,\Lambda_{4j}g\mathcal{R} + su\ cl\,\Lambda_{2j} + cu\ sl\,\Lambda_{2j})
\end{aligned}
$$

for j=1, 2. In the above, the symbols cu, cl, su and sl stand for $\cosh(\xi h_u)$, $\cosh(\xi h_\ell)$, $\sinh(\xi h_u)$ and $\sinh(\xi h_\ell)$ respectively, and

$$
\Lambda_j \equiv \Lambda_{j1}\cos(\omega_+ t) + \Lambda_{j2}\sin(\omega_+ t) = \int_{L_1}^{L_2} V_j(x,t)\mathrm{e}^{\mathrm{i}\xi x}\mathrm{d}x \tag{1.5.82}
$$

for j=1, ..., 4 with V_1=$f_1^{(3)}$, V_2=$f_3^{(3)}$, V_3=$f_5^{(3)}$, and V_4=$f_6^{(3)}$. The free-surface and interfacial wave elevations are then obtained from (1.2.3d) and (1.2.3g) with m=3.

As an illustration of this solution, consider a relatively simple case for which there is only one (right-going) incident wave component, i.e. $\eta_u^{(1)}$=$a\sin(kx-\omega t)$. In the third-order interaction, this incident wave is counted twice, i.e. k_1=k_2=k and ω_1=ω_2=ω. Under the class III resonance condition, the resonant free wave component with wavenumber k_r=$2k\pm k_b$ and frequency ω_r=2ω is generated. Depending on the values of k and k_b, four different situations exist: the generated wave is a transmitted (or reflected) wave of surface-mode if k_r=k_{rs} (or -k_{rs}); and it is a transmitted (or reflected) wave of internal mode if k_r=k_{ri} (or -k_{ri}). Here k_{rs} and k_{ri} are the wavenumbers of surface and internal modes associated with the frequency ω_r.

For this case, V_1, V_2 and V_3 are related to the second-order solution with wavenumber $k_p \equiv k - k_b$ while V_4 is related to the second-order solution with wavenumber $2k$. The

second-order solution with wavenumber k_p is:

$$\eta_u^{(2)} = a_p \cos(k_p x - \omega t) \ , \tag{1.5.83}$$

$$\eta_\ell^{(2)} = b_p \cos(k_p x - \omega t) \ , \tag{1.5.84}$$

$$\phi_u^{(2)} = [A_p \cosh(k_p z) + B_p \sinh(k_p z)] \sin(k_p x - \omega t) \ , \tag{1.5.85}$$

$$\phi_\ell^{(2)} = \{D_p \cosh[k_p(z + h_u + h_\ell)] + E_p \sinh[k_p(z + h_u + h_\ell)]\} \sin(k_p x - \omega t) \tag{1.5.86}$$

where

$$A_p = -\frac{\omega^3 g da k_p}{2\tilde{D}(k_p,\omega)}\tilde{\alpha} \ , \quad B_p = -\frac{\omega^5 da}{2\tilde{D}(k_p,\omega)}\tilde{\alpha} \ , \quad D_p = \frac{\omega da}{2\tilde{D}(k_p,\omega)}\tilde{\alpha} F_p \ , \quad E_p = -\frac{\omega da}{2}\tilde{\alpha} \ ,$$
$$\tilde{\alpha} = \frac{\cosh(kh_u)}{\sinh(kh_\ell)} - \frac{gk}{\omega^2}\frac{\sinh(kh_u)}{\sinh(kh_\ell)} \ , \quad a_p = \frac{\omega A_p}{g} \ , \quad b_p = a_p[\cosh(kh_u) - \frac{gk}{\omega^2}\sinh(kh_u)]$$
$$F_p = (cu\ sl + cl\,\mathcal{R}su)\,\omega^4 - (cl\ cu + su\ sl)\,\omega^2 g k_p + g^2 {k_p}^2 (cl\ su + cl\,\mathcal{R}su) \ .$$

where cu, cl, su and sl stand for $\cosh(k_p h_u)$, $\cosh(k_p h_\ell)$, $\sinh(k_p h_u)$ and $\sinh(k_p h_\ell)$, respectively. V_1, V_2 and V_3 are obtained in the form:

$$V_j = A_j \cos(k_r x - \omega_r t) \tag{1.5.87}$$

for j=1, 2, and 3, where k_r=$2k - k_b$ and the coefficients A_1, A_2, and A_3 are:

$$A_1 = a_p\,\omega^2 Bk - 1/2\ a_p\ Ak^2 g + 1/2\,aA_p\ {k_p}^2 g + BkB_p\ k_p\,\omega - 2\,AkA_p\ k_p\,\omega - aB_p\ k_p\,\omega^2 \ ,$$

$$
\begin{aligned}
A_2 &= 1/2\, g\mathcal{R}bkk_p\, A_p\, \cosh(k_p\, h_u) + 1/2\, g\mathcal{R}b_p\, B \sinh(kh_u)k^2 + 1/2\, g\mathcal{R}bA_p\, \cosh(k_p\, h_u){k_p}^2 \\
&+1/2\, gb_p\ \ C\ \cosh(kh_u)k^2 - 1/2\, gbkk_p\, D_p\, \cosh(k_p\, h_u) - 1/2\, gbD_p\, \cosh(k_p\, h_u){k_p}^2 \\
&-1/2\, g\mathcal{R}bkk_p\, B_p\, \sinh(k_p\, h_u) - 1/2\, gbk_0k_p\, E_p\, \sinh(k_p\, h_u) - 1/2\, g\mathcal{R}bB_p\, \sinh(k_p\, h_u){k_p}^2 \\
&-1/2\, g\mathcal{R}b_p\, A\cosh(kh_u)k^2 + 1/2\, gC\cosh(kh_u)kb_p\, k_p - 1/2\, g\mathcal{R}kb_p\, k_p\, A\cosh(kh_u) \\
&-\mathcal{R}\omega\, AkB_p\, k_p\, \sinh(h_u\,(k-k_p)) + \mathcal{R}k\omega\, k_p\, BB_p\, \cosh(h_u\,(k-k_p)) - 1/2\, \mathcal{R}b_p\, \omega^2 A\sinh(kh_u)k \\
&+1/2\, \mathcal{R}b_p\, \omega^2 B\cosh(kh_u)k + 1/2\, b\omega^2 E_p\, \cosh(k_p\, h_u)k_p - \mathcal{R}k\omega\, k_p\, AA_p\, \cosh(h_u\,(k-k_p)) \\
&+\mathcal{R}\omega\, BkA_p\, k_p\, \sinh(h_u\,(k-k_p)) + 1/2\, \mathcal{R}b\omega^2 A_p\, \sinh(k_p\, h_u)k_p - Ck\omega\, E_p\, k_p\, \sinh(h_u\,(k_0-k_p)) \\
&+Ck_0\omega_0\, k_p\, D_p\, \cosh(h_u\,(k-k_p)) - 1/2\, gbE_p\, \sinh(k_p\, h_u){k_p}^2 + 1/2\, g\mathcal{R}kb_p\, k_p\, B\sinh(kh_u) \\
&-1/2\, \mathcal{R}b\omega^2 B_p\, \cosh(k_p\, h_u)k_p - 1/2\, b_p\ \ C\ \sinh(kh_u)k\omega^2 + 1/2\, b\omega^2 D_p\, \sinh(k_p\, h_u)k_p\ ,
\end{aligned}
$$

$$
\begin{aligned}
A_3 &= 1/2\,(k+k_p)(-k_p\, \sinh(k_p\, h_u)B_p\, b - k_p\, \cosh(k_p\, h_u)D_p\, b + k_p\, \cosh(k_p\, h_u)A_p\, b \\
&-k_p\, \sinh(k_p\, h_u)E_p\, b + C\cosh(kh_u)kb_p + kb_p\, B\sinh(kh_u) - kb_p\, A\cosh(kh_u))\ .
\end{aligned}
$$

Where A, B, C and b are given as functions of a by equations 1.2.5 and 1.2.6. To find V_4, the second-order potential $\phi_\ell^{(2)}$ containing terms with wavenumber $2k$ is needed. It is given by

$$
\phi_\ell^{(2)} = D_d \cosh[k(z + h_u + h_l)] \sin(k_d x - \omega_d t) \tag{1.5.88}
$$

where k_d=$2k$, ω_d=2ω, and

$$
D_d = -\frac{g^2 B_3\, {k_d}^2 \mathcal{R}su - gsu\, {k_d}^2 B_2 - B_3\, \mathcal{R}{\omega_d}^4 su + su^2 k_d \mathcal{R}{\omega_d}^2 B_1 + {\omega_d}^2 cu\, k_d B_2 - {\omega_d}^2 cu^2 \mathcal{R}k_d B_1}{cl\, k_d \left(g^2 {k_d}^2 \mathcal{R}su - \mathcal{R}{\omega_d}^4 su + {\omega_d}^2 gsu\, k_d - {\omega_d}^4 cu - g^2 {k_d}^2 su + gk_d{\omega_d}^2 cu\right)}
$$

where cu ,cl, su and sl stand for $\cosh(k_d h_u)$, $\cosh(k_d h_\ell)$, $\sinh(k_d h_u)$ and $\sinh(k_d h_\ell)$ respectively. In the above, the coefficients B_1, B_2 and B_3 are:

$$
\begin{aligned}
B_1 &= \frac{1}{2}(2\, a\omega^2 Bk + 2\, A^2 k^2 \omega - B^2 k^2 \omega - aAk^2 g)\ , \\
B_2 &= 1/2\, k\, \left(2\, k\mathcal{R}gbB\sinh(kh_u) - kB^2\omega\, \mathcal{R} - 2\, k\mathcal{R}gbA\cosh(kh_u) - kD^2\omega\right. \\
&\left.+2\, kgbD\cosh(kh_\ell) + kA^2\omega\, \mathcal{R} - \mathcal{R}b\omega^2 A\sinh(kh_u) + \mathcal{R}b\omega^2 B\cosh(kh_u) - bD\omega^2\sinh(kh_\ell)\right)\ , \\
B_3 &= -bk^2\left[A\cosh(kh_u) - B\sinh(kh_u) - D\cosh(kh_\ell)\right]\ .
\end{aligned}
$$

As a result, V_4 is obtained to be:

$$V_4 = A_4 \cos[k_r x - \omega_r t] \quad \text{with} \quad A_4 = -dD_d k k_r \ . \tag{1.5.89}$$

Substitution of V_j, j=1, . . . , 4 into (1.5.82) gives

$$\Lambda_{j1} = 2A_j \frac{\xi \cos(k_r L)\sin(\xi L) - k_r \sin(k_r L)\cos(\xi L)}{\xi^2 - k_r^2} \ , \tag{1.5.90}$$

$$\Lambda_{j2} = -2iA_j \frac{\xi \sin(k_r L)\cos(\xi L) - k_r \cos(k_r L)\sin(\xi L)}{\xi^2 - k_r^2} \ . \tag{1.5.91}$$

Finally, the solution for the potentials associated with class III Bragg resonance is

$$\phi_u^{(3)}(x,z,t) = \sum_{\xi=k_s,-k_s,k_i,-k_i} \mathrm{Res}(\xi)\tilde{D}(\xi)\left\{[A_{u1}\cosh(\xi z) + B_{u1}\sinh(\xi z)]\cos(\omega_r t) \right. \\ \left. + [A_{u2}\cosh(\xi z) + B_{u2}\sinh(\xi z)]\sin(\omega_r t)\right\} \mathrm{e}^{-\mathrm{i}\xi x} \ , \tag{1.5.92}$$

$$\phi_\ell^{(3)}(x,z,t) = \sum_{\xi=k_s,-k_s,k_i,-k_i} \mathrm{Res}(\xi)\tilde{D}(\xi)\left\{[A_{\ell 1}\cosh(\xi z) + B_{\ell 1}\sinh(\xi z)]\cos(\omega_r t) \right. \\ \left. + [A_{\ell 2}\cosh(\xi z) + B_{\ell 2}\sinh(\xi z)]\sin(\omega_r t)\right\} \mathrm{e}^{-\mathrm{i}\xi x} \ . \tag{1.5.93}$$

It then can be shown that

$$[(iA_{u2} - A_{u1})\tilde{D}]\big|_{\xi=-k_x} = [(-iA_{u2} - A_{u1})\tilde{D}]\big|_{\xi=k_x} \equiv \beta(k_x) \text{ for } \ x = i, s \ . \tag{1.5.94}$$

Thus, at far upstream ($x \to -\infty$),

$$\phi_u^{(-3)}(x,0,t) = \beta_i \alpha(k_i)\sin(k_i x + \omega_r t) + \beta_s \alpha(k_s)\sin(k_s x + \omega_r t) \ , \tag{1.5.95}$$

$$\eta_u^{(3-)}(x,t) = \frac{\omega_r}{g}\left[\beta_i \alpha(k_i)\cos(k_i x + \omega_r t) + \beta_s \alpha(k_s)\cos(k_s x + \omega_r t)\right] \ , \tag{1.5.96}$$

$$\eta_\ell^{(3-)}(x,t) = \frac{\omega_r}{g}\left[\beta_i \lambda(k_i)\alpha(k_i)\cos(k_i x + \omega_r t) + \beta_s \lambda(k_s)\alpha(k_s)\cos(k_s x + \omega_r t)\right] \ . \tag{1.5.97}$$

and

$$R_{ss} = \frac{|\eta_u^{(3-)}|}{|\eta_u^{(1)}|} \ , \qquad R_{si} = \frac{|\eta_\ell^{(3-)}|}{|\eta_u^{(1)}|} \ . \tag{1.5.98}$$

As an illustration, consider a problem with the following parameters: h_ℓ/h_u=1, $\mathcal{R}$=0.5, kh_u=0.3 ($\omega^2 h_u/g$=0.14), ka=0.06, kd=0.007 and M_b=30. For a surface incident wave,

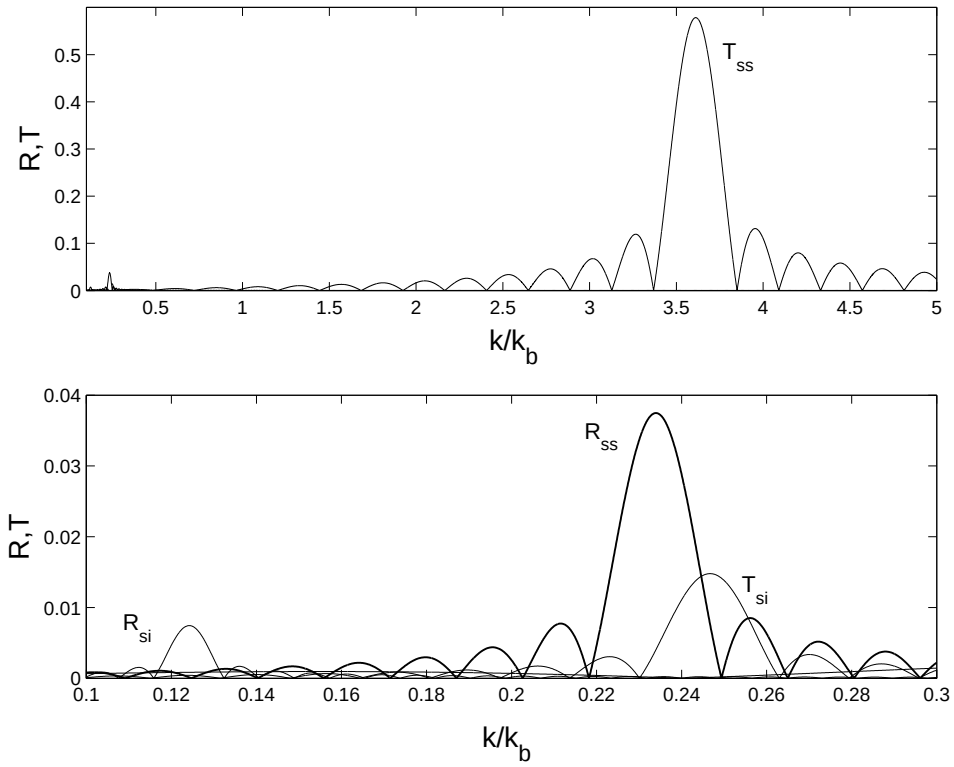

Figure 1-14: Reflection and transmission coefficients of resonant surface and internal waves in the neighborhood of class III Bragg resonance for a single surface incident wave over a rippled bottom. The parameters are h_ℓ/h_u=1, $\mathcal{R}$=0.5, kh_u=0.3 ($\omega^2 h_u/g$=0.14), ka=0.06, kd=0.007, and M_b=30. The lower graph is a close-up of the upper graph for small k/k_b.

class III resonances occur at: (i) k/k_b=3.61 with a resonant transmitted surface wave; (ii) k/k_b=0.124 with a resonant reflected internal wave; (iii) k/k_b=0.234 with a resonant reflected surface wave; and (iv) k/k_b=0.247 with a resonant transmitted internal wave. Figure 1-14 shows the reflection and transmission coefficients of the resonant waves for all four cases of class III resonance when the incident wave has only one component. For a real ocean stratification ($\mathcal{R}$ = 0.96), figure 1-15 shows a similar plot. Parameters in this figure are h_ℓ/h_u=1, $\mathcal{R}$=0.96, kh_u=0.3 ($\omega^2 h_u/g$=0.02), ka=0.06, kd=0.001 and M_b=5. For an internal incident wave, class III resonances occur at: (i) k/k_b=7.9 with a resonant transmitted internal wave; (ii) k/k_b=0.24 with a resonant reflected internal wave; (iii) k/k_b=0.44 with a resonant reflected surface wave; and (iv) k/k_b=0.54 with a resonant transmitted surface wave.

Figures 1-16 and 1-17 show the dependence of the resonated wave amplitude (for the above four cases) on the density ratio $\mathcal{R}$ and the depth ratio h_ℓ/h_u, at the exact class III

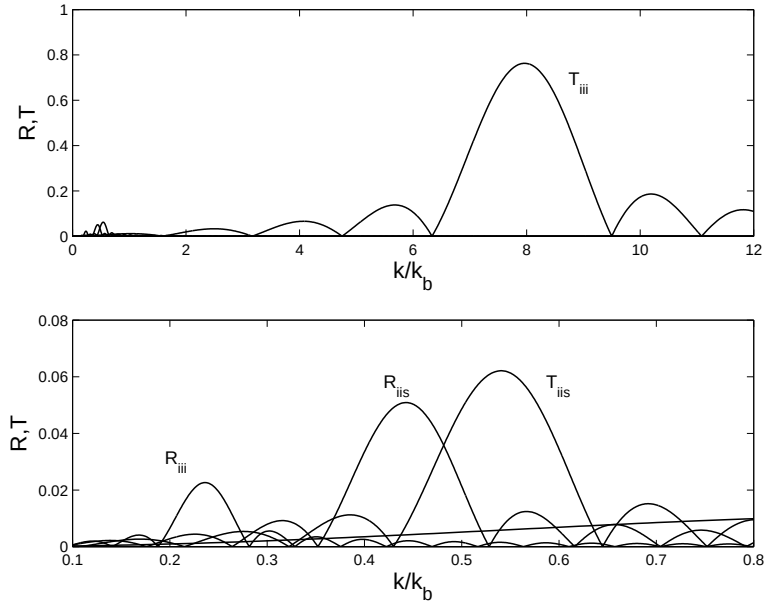

Figure 1-15: Reflection and transmission coefficients of resonant surface and internal waves in the neighborhood of class III Bragg resonance for a single surface incident wave over a rippled bottom. The parameters are h_ℓ/h_u=1, $\mathcal{R}$=0.96, kh_u=0.3 ($\omega^2 h_u/g$=0.02), ka=0.06, kd=0.001, and M_b=5. The lower graph is a close-up of the upper graph for small k/k_b.

Bragg condition. As $\mathcal{R} \to 1$, the amplitude of the resonant internal wave vanishes while that of the resonant surface wave approaches a small finite value. Except for the case of resonant transmitted internal wave, there is a maxima in the amplitude of resonant waves obtained at small $\mathcal{R}$ for the other three cases. In general, the amplitude of resonant transmitted wave is much higher than that of resonant reflected wave. The effect of the depth ratio is somewhat different. The amplitude of resonant internal wave vanishes while that of resonant surface wave approaches to a finite value as $h_\ell/h_u \to 0$. As h_ℓ/h_u increases, resonant surface wave decreases monotonically to zero while resonant internal wave increases to a maxima and then decreases to zero.

Figure 1-18 shows the dependence of the reflection and transmission coefficients of the resonant surface and internal waves on the incident wave frequency due to class III Bragg resonance. As expected, the amplitudes of the resonant surface and internal waves become smaller for larger incident wave frequency as the effect of the bottom on the surface/internal wave motion weakens.

It is to be noted that the case for two different incident waves can be worked out in a similar way. The algebra is much more tedious and the formulas quite lengthy, and are not

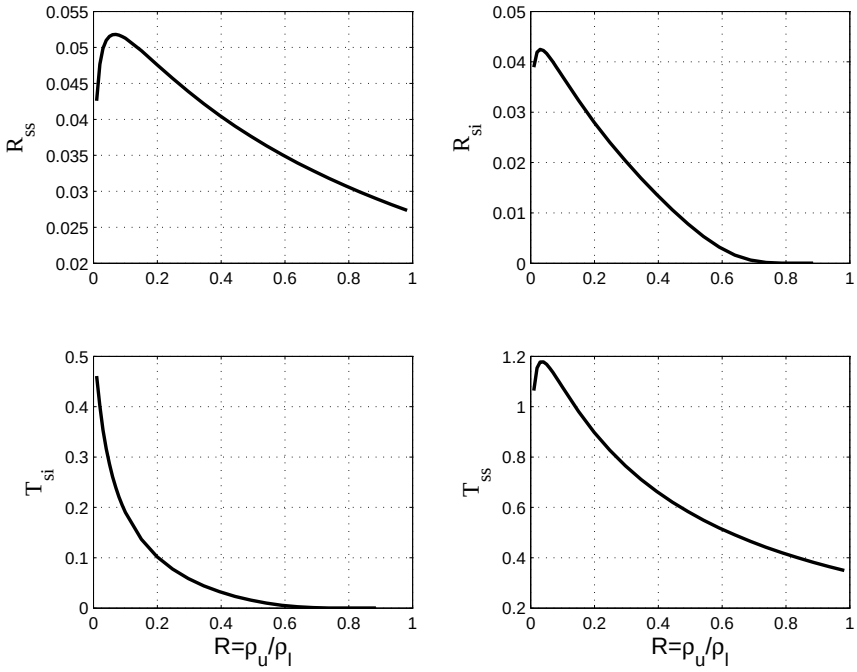

Figure 1-16: Variations of the reflection and transmission coefficients of resonant surface and internal waves at exact class III Bragg resonance as a function of density ratio for a single surface incident wave over a rippled horizontal bottom. (a) $S_{c1} + S_{c2} \rightarrow S_R$, (b) $S_{c1} + S_{c2} \rightarrow I_R$, (c) $S_{c1} + S_{c2} \rightarrow I_T$, (d) $S_{c1} + S_{c2} \rightarrow S_T$. Other parameters are the same as in figure 1-14.

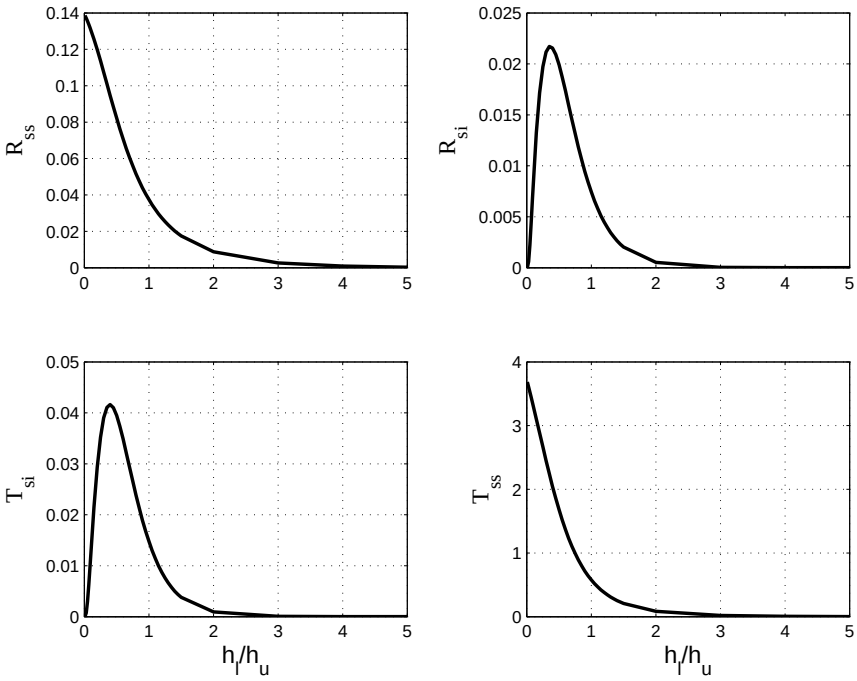

Figure 1-17: Same as figure 1-16 but now variations as a function of the depth ratio h_ℓ/h_u.

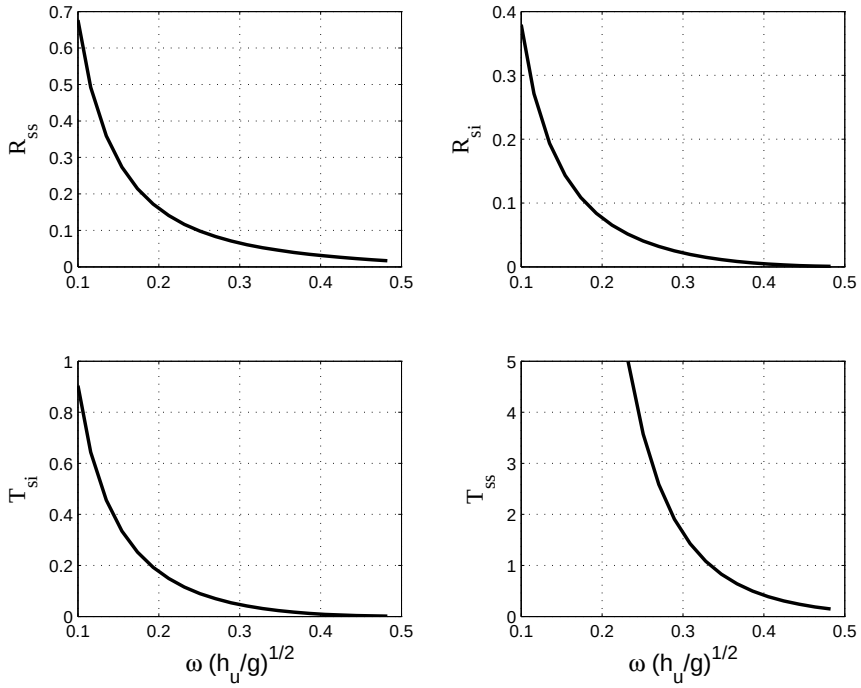

Figure 1-18: Variations of reflection and transmission coefficients of resonant surface and internal waves at exact class III Bragg resonance as a function of incident wave frequency for a single surface incident wave over a rippled horizontal bottom. Other parameters are the same as in figure 1-14.

presented here.

1.6 Illustrative case studies

The Bragg resonance mechanisms involving two-layer density stratification and a rippled bottom discussed in the previous sections have important effects on the evolution of ocean waves under the appropriate conditions. We discuss four specific examples of these: the effect of stratification on classical second-order homogeneous fluid Bragg resonance; strong reflection of internal gravity waves by bottom ripples; generation of high frequency internal waves by long surface waves over bottom topography; and new quartet resonances involving class III Bragg interactions among three free waves and a bottom undulation in the presence of density stratification.

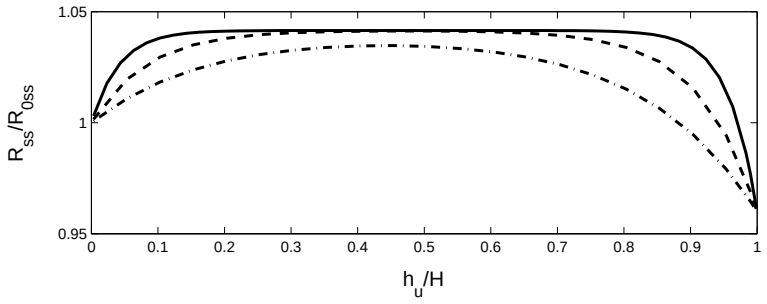

Figure 1-19: Effect of stratification on the reflection coefficient of homogeneous fluid class I Bragg resonance. Parameters are $\mathcal{R} = 0.96$, $d/a = 1$, and, $\omega^2 H/g = 3$ ($- \cdot -$), $\omega^2 H/g = 6$ (- - -), and $\omega^2 H/g = 12$ (——) (in physical domain correspond to a $T = 8$ *sec* wave traveling over a sea of respectively $H = 50\ m, 100\ m, 200\ m$ depth).

1.6.1 Modification of homogeneous fluid Class I Bragg resonance in the presence of stratification

Bragg resonance in a homogeneous fluid is well understood theoretically and experimentally (Mei, 1985; Belzons *et al.*, 1988; Liu & Yue, 1998; Ardhuin & Herbers, 2002; Ardhuin & Magne, 2007). Here we show that ocean stratification can significantly affect the expected homogeneous fluid reflection coefficient. Figure 1-19 shows the change in the class I Bragg reflection coefficient with or without density stratification. Results are shown for $\mathcal{R} = 0.96$ for different total depths $\omega^2 H/g$ with varying thermocline depths h_u/H. Denoting the homogenous fluid reflection coefficient as R_{0ss}, we note that R_{ss}/R_{0ss} approaches 1 as $h_u/H \to 0$, is greater than 1 for intermediate values of h_u/H, and decreases below 1 for h_u/H near 1. The effect is somewhat diminished for longer incident waves (relative to total depth). The change due to the presence of stratification depends in general on $\mathcal{R}$, $\omega^2 H/g$, h_u/H and d/a. For the parameters chosen in Figure 1-19, the overall effect is relatively weak (of the order of $\pm 5\%$).

1.6.2 Bragg reflection of internal waves

Similar to the reflection of surface waves on a homogeneous fluid, bottom ripples can strongly reflect incident internal waves. Figure 1-20 shows the reflection coefficient R_{ii} due to class I Bragg resonance ($I_c \xrightarrow{k_b} I_R$) for $\mathcal{R}$=0.96, h_ℓ/h_u=0.2, $\omega^2 h_u/g$=0.12, d/h_u=0.1, and M_b=20. For stratified layer depths of $h_u = 200\ m$ and $h_\ell = 40\ m$, say, the chosen parameters correspond to relatively short incident internal-mode waves of wavelength $\lambda_i = 200\ m$ and

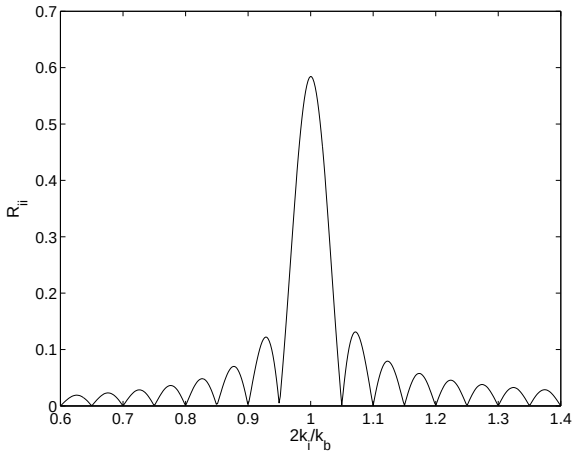

Figure 1-20: Reflection coefficients (R_{ii}) of an internal mode resonance generated wave in the neighborhood of class I Bargg resonance as a function of relative wavenumber $2k_i/k_b$. $\mathcal{R}$=0.96, h_ℓ/h_u=0.2, $\omega^2 h_u/g$=0.12, d/h_u=0.1, and M_b=4.

not atypical bottom ripple wavelength of $\lambda_b = 100\ m$ (Mei *et al.*, 2005; Guazzelli *et al.*, 1991). Figure 1-20 shows that over a distance of about 2 Km (M_b=20), a reflected internal wave of 60% of the incident amplitude can be expected. Systematic study varying the physical parameters (Alam, 2008) shows that $\mathcal{R}_{ii}$ is generally greater for longer interfacial waves, shallower lower layer depth and stronger stratification.

1.6.3 Generation of high frequency internal waves by long surface waves

High-frequency internal waves are frequently observed in lakes and coastal waters (Garrett & Munk, 1975). Although many different generation mechanisms have been proposed (e.g. Thorpe *et al.*, 1996), the precise origin of these waves is still a matter of current investigation (e.g. Boegman *et al.*, 2003). The elucidation of internal wave Bragg resonance here offer another possible explanation. We show here that resonance short internal waves can be generated by the interaction of very long surface wave (such as seishes in lakes) with bottom topography.

Figure 1-21 shows an example of generation of high frequency internal waves due to Bragg resonance of long incident surface waves ($S_c \xrightarrow{k_{b1}} I_R$ and $S_c \xrightarrow{k_{b2}} I_T$). Parameters chosen are $\mathcal{R}$=0.96, h_ℓ/h_u=0.5, $\omega^2 h_u/g$=0.04, d/h_ℓ=0.5, and M_b=20. These may correspond to, for example, total and thermocline depths of $H = 75\ m$ and $h_u = 50\ m$, surface wave of wavelength $\lambda_{in} = 2\ km$, and short resonant internal waves of period $T = 70\ sec$. In this example the resonance is relatively selective, however, it is strong. The strength ,as before,

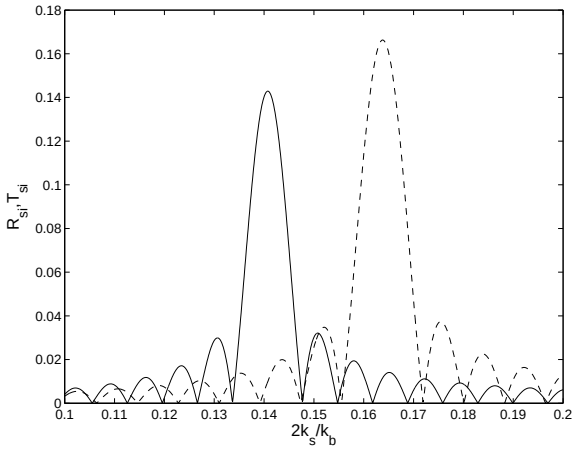

Figure 1-21: Reflection (——) and transmission (- - -) coefficients (R_{si}, T_{si}) for an incident surface mode wave (wavenumber k_s) that resonant an internal mode wave in the neighborhood of class I Bargg resonance, as a function of relative wavenumber $2k_s/k_b$. $\mathcal{R}$=0.96, h_ℓ/h_u=0.5, $\omega^2 h_u/g$=0.04, d/h_ℓ=0.5, and M_b=20.

increases as the length of the bottom patch increases.

1.6.4 Class III Bragg resonance among surface and internal waves

In the absence of bottom topography, Ball (1964) and Wen (1995*b*); Hill & Foda (1996); Jamali (1998) studied the triad resonance involving two surface and one internal waves, and one surface and two internal waves, respectively. For realistically weak ocean stratification with $1 - R \ll 1$, such triad resonances are highly selective. In the former, the only case involves two oppositely traveling surface waves of very close wavelengths resonant with an internal wave of half the wavelength. In the latter, the two internal waves have to be oppositely traveling and of almost the same wavelength, now resonant with a surface wave of half the period.

Unlike the above, if bottom ripples are present, resonance involving three surface/internal waves obtains for a broad range of conditions under Class III Bragg resonance. In particular, these conditions include co-propagating waves (as well as counter-propagating waves), and cover realistic cases of long wavelength and period internal waves relative to surface waves. Figure 1-22 shows the different possibilities of surface, internal, and bottom wavenumbers for Class III Bragg resonance involving two incident surface-mode waves (k_{s1}, k_{s2}), an internal mode wave (k_i), and a bottom topography with component (k_b), for $\mathcal{R}$=0.96 and h_ℓ/h_u=2.3 (i.e. $S_{c1} \pm S_{c2} \xrightarrow{k_{b1}} I_R$ and $S_{c1} \pm S_{c2} \xrightarrow{k_{b2}} I_T$). The cases involving (a) co-

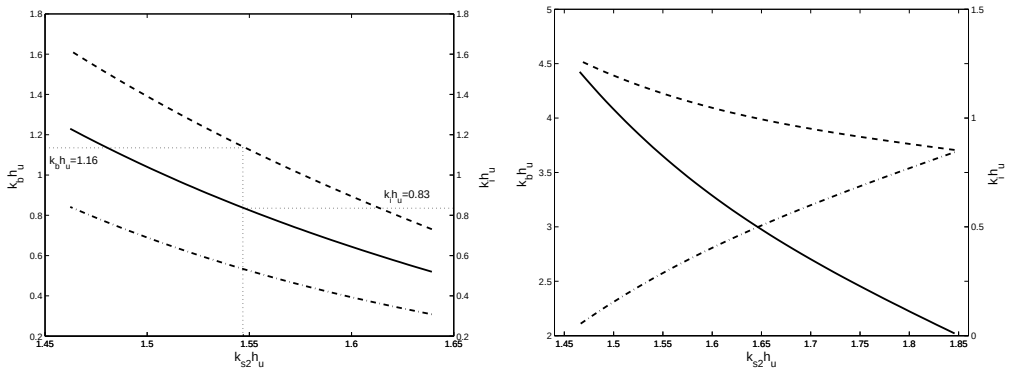

Figure 1-22: Class III Bragg resonance involving two (a) co-propagating, and (b) counter-propagating, surface-modes waves (wavenumbers k_{s1}, k_{s2}); an internal mode wave (wavenumber k_i), and a bottom ripple component (wavenumber k_b). The physical parameters are $\mathcal{R}$=0.96, h_ℓ/h_u=2.3, and, for specificness, $k_{s1}h_u = 1.85$. Given k_{s2} (bottom axis), say, the resonance curves corresponding to co-propagating (– · –) or counter-propagating (- - -) internal mode waves (relative to k_{s1}) allow one to obtain the two resonant values of k_b (left axis); while the resonant curve represented by —— obtains the (unique) resonant value of k_i (right axis).

propagating, and (b) counter-propagating surface waves are shown separately; and in the former case, the resonant internal wave can be co- or counter-propagating. If two incident waves are co-propagating, both of k_bs and k_i decrease as $|k_{s1} - k_{s2}|$ increases, while if two incident waves are counter-propagating, as $|k_{s1} - k_{s2}|$ increases, k_i decreases, but one of k_bs (associated with resonant internal wave that co-propagates with k_{s1} increases. Since the stratification is weak, the depth of thermocline has a small effect on the resonance condition. For example results for thermoclines of $h_\ell/h_u = 2.3$ and $h_\ell/h_u = 0.4$ are barely distinguishable.

For illustration, for the fixed value $k_{s1}h_u = 1.85$ ($\omega_{s1}^2 h_u/g$=1.9), Figure 1-22(a) shows that for a chosen value of co-propagating $k_{s2}h_u = 1.55$, bottom components of wavenumber $k_b h_u = 1.16$ respectively resonates a co-propagating, counter-propagating internal wave of $k_i h_u = 0.83$. In dimensional values, for a total depth of $H = 100m$ ($h_u = 30m$), say, these correspond to two co-propagating incident surface waves of wavelengths λ_{s1} ≈102m and λ_{s2} ≈122m (corresponding periods of T_1 ≈8s, T_2 ≈8.8s), bottom wavelength of λ_b ≈116m, and resonant internal wave of wavelength λ_i ≈226m.

The rate of growth b of the Class III Bragg resonant internal wave with two incident surface waves and one bottom component can be obtained by regular perturbation. The closed-form formula for the growth rate b is similar as before but is more complicated and

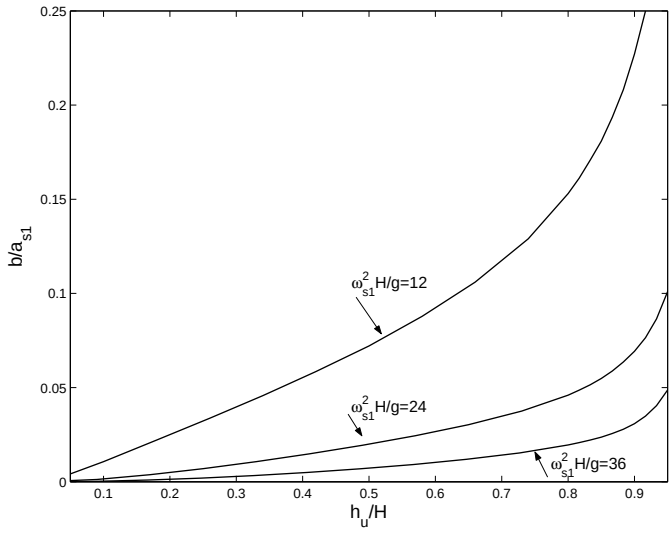

Figure 1-23: Effect of total depth of sea and the depth of themocline on the growth rate b of internal wave generation under Class III Bragg resonance. Parameters are $R = 0.96$ and two co-propagating incident surface waves a_{s2}/a_{s1}=1.2, d/a_{s1}=6.5, ka_{s1}=0.2.

algebraically lengthy, and is not given here. Figure 1-23 shows the value of b for different total and thermocline depths for the $S_{c1} + S_{c2} \rightarrow I_r$ Class III Bragg resonance. This resonance is stronger if the thermocline is closer to the bottom, and if the sea is shallower. From regular perturbation analysis, the growth rate is linearly proportional to the amplitude of incident waves and the bottom topography. For a thermocline close to the free surface, b increases almost linearly with h_u, whereas as $h_u/H \rightarrow 1$, b increases exponentially. For given h_u/H, b also increases rapidly as the incident wave period increases.

1.7 Conclusion

In this chapter the generalized two-dimensional Bragg resonance of waves in a two-layer density stratified fluid over a rippled bottom is studied analytically using perturbation theory.

Bragg resonances obtain involving triad (class I) and quartet (class II and III) interactions at second and third order (in wave/bottom steepness) respectively in which at least one of the participant is a component of the rippled bottom. The results are a generalization of the unstratified (single layer) fluid case of Liu & Yue (1998), but, because of the possibility of internal mode waves, now admit many (new) resonance cases and combinations. These are enumerated and represented schematically in Feynman-like diagrams. In class I

and II Bragg resonances only one frequency exists, while in the class III Bragg resonance, the frequency of resonant wave can be the sum or the difference of frequency of incident waves resulting in the possibility for the generation of very long or short waves. For all three classes of resonances, regular perturbation solutions are obtained which predict the resonances and the growth of the resonant transmission or reflection waves for a finite bottom patch. For very long bottom patches, regular perturbation results are not valid, and analyses involving slow-variables and multiple scales are needed. This is obtained here for the case of class I resonance.

Extension of the current analysis to three dimensions is algebraically more involved but straightforward. An analysis of the case of oblique incidence for class I is given in Appendix F. The differences are not significant. It is shown that the growth rate of the resonant wave in fact decreases as the angle of incident increases, similar to the case of homogeneous fluid Bragg resonance (see for example Liu & Yue, 1998) or triad resonance between surface/internal waves over a flat bottom (see for example Jamali *et al.*, 2003).

This chapter provides the analytic basis and guidance for understanding the complex resonant interactions involving surface/internal mode waves travelling over a rippled bottom. In practice, the general problem consists of surface/internal mode waves and bottom topography containing multiple (indeed a spectrum of) components, plus resonant generated wave components, obtaining multiple resonances and resonant combinations among these components. For this general problem, a direct numerical simulation of the nonlinear evolution is needed. This is the subject of the second chapter of this thesis.

Chapter 2

Bragg resonance of waves in a two-layer fluid propagating over bottom ripples: Perturbation analysis

2.1 Introduction

The main objective of this chapter is the general high-order and multiple Bragg resonance interactions of surface/internal waves in a two-layer stratified fluid propagating over a patch of wavy bottom. In the first chapter, perturbation analyses for three different classes of Bragg resonances are developed that obtain when interactions up to third order in wave/bottom steepness are considered. At second order, class I Bragg resonance involves two surface/internal waves and one bottom ripple component. At third order, class II and III Bragg resonance involve quartets of components: two surface/internal and two bottom ripple components, and three surface/internal waves and one bottom ripple component, respectively. Chapter one enumerates the multiple possible combinations and cases under these resonance classes, elucidates the different mechanisms, and obtains predictions of the (initial) growth/evolution of the resonant wave. While perturbation analyses provide the essential framework and understand specific predictions, the general problem of interest involving multiple (resonantly) interacting surface/internal/bottom components up to high

(possibly more than third) order becomes quickly intractable analytically, and numerical solutions must be sought. This is the subject of this chapter.

In this chapter a powerful high-order spectral method (HOS), originally developed for nonlinear wave-wave and wave-bottom interactions in a one-layer fluid (Dommermuth & Yue, 1987; Liu & Yue, 1998), is extended to the case of a two-layer density stratified fluid. HOS is the extension of Zakharov (1968) mode coupling idea in a direct computational approach. This method computationally accounts for nonlinear wave-wave and wave-bottom interactions up to an arbitrary high order M in the wave (or bottom) steepness, and follows the (time) evolution of a large number of wave modes, say $N{=}O(10^3)$ per horizontal dimension. By using the fast transform techniques, the computational effort is (approximately) linearly proportional to M and N. For moderately steep waves and bottom ripples, the method achieves an exponential convergence of the solution with respect to M and N. The extension of HOS to a two-layer fluid over non-uniform bottom preserves these computational properties and is extremely efficient and effective (in some sense ideal) for the problem at hand.

The mathematical formulation of the HOS method for a two-layer fluid in the presence of variable bottom topography is described in §2.2. In §2.3, the implementation issues are discusses and a validation of the method by testing the convergence with different numerical parameters (including N and M) using the fully-nonlinear Stokes wave solution in a two-layer fluid as the benchmark is described. In §2.4, direct numerical simulations are used to investigate nonlinear resonant interactions of surface/internal waves and bottom undulations. In order to relate the present time-domain simulation to the theoretical results in the frequency domain, a robust algorithm for the decomposition of Fourier wave components of a nonlinear wavefield from the time history of the wavefield evolution is developed in §2.4.1. The classical second-order triad resonance of surface and internal waves with a flat bottom is considered first (§2.4.2). Quantitative comparisons between the numerical prediction and perturbation solution are obtained and the higher-order effects (not accounted for in the theory) are characterized. The three classes of Bragg resonance of surface/internal waves over bottom ripples are studied in §2.4.3, §2.4.4 and §2.4.5, respectively. In each case, the present HOS predictions are validated and compared against the theoretical predictions of chapter one. The effects of greater steepness and higher-order interactions on the resonances are then quantified and characterized. Finally, in §2.4.6, a somewhat more

complicated problem involving multiple Bragg resonances with a bottom containing three different (sinusoidal) ripple components is considered. The long-time evolution is studied over such a bottom of a single incident surface wave chosen to (initially) satisfy a class I Bragg resonance condition. Because of the presence of the additional (resonant) bottom wavenumbers, multiple higher-order resonances ensue as predicted by theory and confirmed numerically. As time increases, these resonant interactions spread the energy in the initial incident waves over a broad range of frequencies, and the wave motion is shown to become chaotic.

2.2 Mathematical formulation

In this section, the mathematical formulation of a numerical method for the computation of nonlinear interactions of gravity surface and interfacial waves with varying bottom topography is described. This method is a direct extension of the high-order spectral (HOS) method for the simulation of nonlinear wave-wave and wave-bottom interactions in a single layer fluid (Dommermuth & Yue, 1987; Liu & Yue, 1998). The extended method is capable of accounting for nonlinear interactions of broadband wave components on the surface, interface, and the bottom up to an arbitrary high order in the wave/bottom steepness.

2.2.1 Initial boundary-value problem

Consider the motion of a two-layer fluid over a variable bottom topography. A Cartesian coordinate system is defined with the x-axis on the mean free surface and the z-axis positive upward, as shown in figure 2-1. The upper and lower layers of fluid have respectively depths and densities of h_u, ρ_u and h_ℓ, ρ_ℓ (hereafter subscripts u and ℓ are used to respectively denote upper and lower layer quantities); and the bottom elevation is given by η_b=$\eta_b(x)$. In each layer, assume that the fluid is homogeneous, incompressible, immiscible and inviscid; and the motion irrotational and described by the velocity potential $\phi_u(x,z,t)$ or $\phi_\ell(x,z,t)$. The equations governing the motion of a two-layer fluid are (ignoring surface tension):

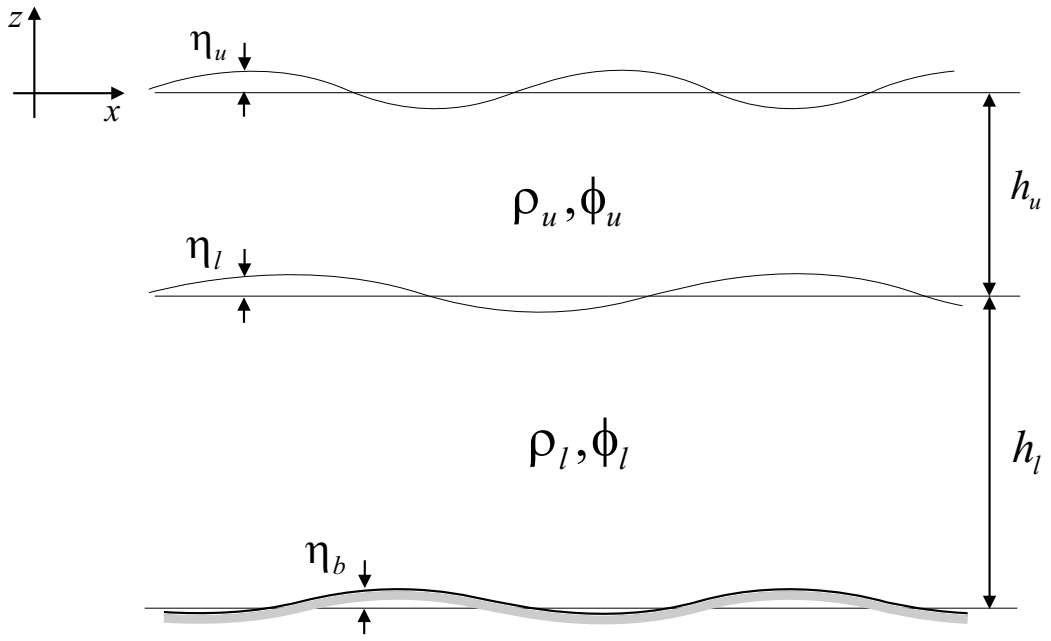

Figure 2-1: Definition sketch.

$$\nabla^2\phi_u = 0 \qquad -h_u + \eta_\ell < z < \eta_u \tag{2.2.1a}$$

$$\nabla^2\phi_\ell = 0 \qquad -h_u - h_\ell + \eta_b < z < -h_u + \eta_\ell \tag{2.2.1b}$$

$$\eta_{u,t} + \eta_{u,x}\phi_{u,x} - \phi_{u,z} = 0 \qquad z = \eta_u \tag{2.2.1c}$$

$$\phi_{u,t} + \tfrac{1}{2}(\phi_{u,x}^2 + \phi_{u,z}^2) + g\eta_u = 0 \qquad z = \eta_u \tag{2.2.1d}$$

$$\eta_{\ell,t} + \eta_{\ell,x}\phi_{u,x} - \phi_{u,z} = 0 \qquad z = -h_u + \eta_\ell \tag{2.2.1e}$$

$$\eta_{\ell,t} + \eta_{\ell,x}\phi_{\ell,x} - \phi_{\ell,z} = 0 \qquad z = -h_u + \eta_\ell \tag{2.2.1f}$$

$$\rho_u[\phi_{u,t} + \tfrac{1}{2}(\phi_{u,x}^2 + \phi_{u,z}^2) + g\eta_\ell] -$$
$$\rho_\ell[\phi_{\ell,t} + \tfrac{1}{2}(\phi_{\ell,x}^2 + \phi_{\ell,z}^2) + g\eta_\ell] = 0 \qquad z = -h_u + \eta_\ell \tag{2.2.1g}$$

$$\eta_{b,x}\phi_{\ell,x} - \phi_{\ell,z} = 0 \qquad z = -h_u - h_\ell + \eta_b. \tag{2.2.1h}$$

where η_u=$\eta_u(x,t)$, η_ℓ=$\eta_\ell(x,t)$, are respectively the free surface and interface wave elevations, and g the gravitational acceleration. For an initial-value problem, the conditions are prescribed at initial time (t=0) for the surface and interface elevations ($\eta_u(x,0)$, $\eta_\ell(x,0)$) and velocity potentials ($\phi_u(x,\eta_u(x,0),0)$, $\phi_u(x,-h_u+\eta_\ell(x,0),0)$, $\phi_\ell(x,-h_u+\eta_\ell(x,0),0)$) are specified. For computation, periodic boundary condition in the horizontal direction is

assumed.

2.2.2 Evolution equations

Let's define the surface potential ϕ_u^S for the upper layer, and the interface potentials for the upper and lower layers ϕ_u^I and ϕ_ℓ^I as follows:

$$\phi_u^S(x,t) \equiv \phi_u(x,\eta_u(x,t),t) \ , \quad \text{and} \quad \phi_{u/\ell}^I(x,t) \equiv \phi_{u/\ell}(x,-h_u+\eta_\ell(x,t),t) \ . \tag{2.2.2}$$

In the neighborhood of the interface, for convenience, let's define a new potential $\psi(x,z,t) \equiv \phi_\ell(x,z,t) - \mathcal{R}\phi_u(x,z,t)$ where $\mathcal{R} \equiv \rho_u/\rho_\ell$. Let's further define ψ^I to be the value of ψ evaluated on the interface:

$$\psi^I(x,t) \equiv \phi_\ell^I(x,t) - \mathcal{R}\phi_u^I(x,t) \ . \tag{2.2.3}$$

In terms of these quantities, the kinematic and dynamic boundary conditions on the surface ((2.2.1c) and (2.2.1d)) and interface ((2.2.1e) and (2.2.1g)) can be rewritten in the forms:

$$\eta_{u,t} = -\eta_{u,x}\phi_{u,x}^S + (1+\eta_{u,x}^2)\ \phi_{u,z} \ , \qquad z=\eta_u \ , \tag{2.2.4}$$

$$\phi_{u,t}^S = -g\eta_u - \frac{1}{2}(\phi_{u,x}^S)^2 + \frac{1}{2}(1+\eta_{u,x}^2)\phi_{u,z}^2 \ , \qquad z=\eta_u \ , \tag{2.2.5}$$

$$\eta_{\ell,t} = -\eta_{\ell,x}\phi_{u,x}^I + (1+\eta_{\ell,x}^2)\ \phi_{u,z} \ , \qquad z=-h_u+\eta_\ell \ , \tag{2.2.6}$$

$$\begin{aligned}\psi_{,t}^I &= \frac{1}{2}[\mathcal{R}(\phi_{u,x}^I)^2 - (\phi_{\ell,x}^I)^2] \\ &\quad + \frac{1}{2}(1+\eta_{\ell,x}^2)(\phi_{\ell,z}^2 - \mathcal{R}\phi_{u,z}^2) - g\eta_\ell(1-\mathcal{R}) \ , \qquad z=-h_u+\eta_\ell \ .\end{aligned} \tag{2.2.7}$$

In the HOS approach, (2.2.4)-(2.2.7) are the evolution equations for η_u, ϕ_u^S, η_ℓ and ψ^I. These depend on the vertical surface velocity, $\phi_{u,z}(x,\eta_u,t)$, and the vertical interface velocities, $\phi_{u,z}(x,-h_u+\eta_\ell,t)$ and $\phi_{\ell,z}(x,-h_u+\eta_\ell,t)$, which are obtained from the boundary-value problem solution.

2.2.3 Perturbation expansions

To solve the boundary-value problem, assume that $\phi_u, \phi_\ell, \eta_u, \eta_\ell$ and all their derivatives are $O(\epsilon)$, where ϵ is a small quantity that measures the steepness of the free surface, interface, and bottom. By expanding ϕ_u and ϕ_ℓ in perturbation series up to an arbitrary order M in

ϵ:

$$\phi_u(x,z,t) = \sum_{m=1}^{M} \phi_u^{(m)}(x,z,t) \ , \qquad \phi_\ell(x,z,t) = \sum_{m=1}^{M} \phi_\ell^{(m)}(x,z,t) \tag{2.2.8}$$

where the superscript "(m)" represents a quantity of $O(\epsilon^m)$.

On the free surface, as in a one-layer fluid, the surface potential $\phi_u^S(x,t)$ can be expanded in a Taylor series with respect to the mean free surface z=0:

$$\phi_u^S(x,t) = \sum_{m=1}^{M} \phi_u^{(m)}(x,\eta_u,t) = \sum_{m=1}^{M} \sum_{k=0}^{M-m} \frac{\eta_u^k}{k!} \frac{\partial^k}{\partial z^k} \phi_u^{(m)}(x,z,t)\big|_{z=0} \ . \tag{2.2.9}$$

At each time t, η_u and ϕ_u^S are considered to be known from time integration of (2.2.4)-(2.2.5). From (2.2.9), now it obtains a sequence of Dirichlet boundary conditions on z=0 for $\phi_u^{(m)}$:

$$\phi_u^{(m)}(x,0,t) = f_u^{(m)} \tag{2.2.10}$$

with

$$f_u^{(1)} = \phi_u^S \ , \tag{2.2.11}$$

$$f_u^{(m)} = -\sum_{k=1}^{m-1} \frac{\eta_u^k}{k!} \frac{\partial^k}{\partial z^k} \phi_u^{(m-k)}(x,z,t)\big|_{z=0} \ , \quad m = 2,3,\ldots,M \ . \tag{2.2.12}$$

Similarly, on the interface, ψ^I is expanded in a Taylor series with respect to the mean position of the interface z=$-h_u$:

$$\psi^I(x,t) = \sum_{m=1}^{M} \psi^{(m)}(x,-h_u+\eta_\ell,t) = \sum_{m=1}^{M} \sum_{k=0}^{M-m} \frac{\eta_\ell^k}{k!} \frac{\partial^k}{\partial z^k} \psi^{(m)}(x,z,t)\big|_{z=-h_u} \ . \tag{2.2.13}$$

As on the free surface, at any time t, η_ℓ and ψ^I are given from integrating (2.2.6)-(2.2.7). From (2.2.13), it again obtains a sequence of Dirichlet boundary conditions on z=$-h_u$ for $\phi^{(m)}$:

$$\psi^{(m)}(x,-h_u,t) = f_{\ell 1}^{(m)} \tag{2.2.14}$$

with

$$f_{\ell 1}^{(1)} = \psi^I \,, \tag{2.2.15}$$

$$f_{\ell 1}^{(m)} = -\sum_{k=1}^{m-1} \frac{\eta_\ell^k}{k!} \frac{\partial^k}{\partial z^k} \psi^{(m-k)}(x,z,t)\big|_{z=-h_u} \,, \quad m=2,3,\ldots,M \,. \tag{2.2.16}$$

On the interface, there are two kinematic boundary conditions, (2.2.1e) and (2.2.1f). In addition to (2.2.6) used as the evolution equation for η_ℓ, the other one can be rewritten as:

$$\Phi_{,z}(x,z,t) = \eta_{\ell,x}\Phi_{,x} \,, \qquad z=-h_u+\eta_\ell \tag{2.2.17}$$

where $\Phi \equiv \phi_u(x,z,t) - \phi_\ell(x,z,t)$. Note that (2.2.17) is the difference of (2.2.1e) and (2.2.1f). Upon expanding $\Phi(x,z,t)$ on the interface $z{=}-h_u+\eta_\ell$ in a Taylor series with respect to $z{=}-h_u$,

$$\begin{aligned} \Phi(x,-h_u+\eta_\ell,t) &= \sum_{m=1}^{M} \Phi^{(m)}(x,-h_u+\eta_\ell,t) \\ &= \sum_{m=1}^{M} \sum_{k=0}^{M-m} \frac{\eta_\ell^k}{k!} \frac{\partial^k}{\partial z^k} \Phi^{(m)}(x,z,t)\big|_{z=-h_u} \,. \end{aligned} \tag{2.2.18}$$

Substituting (2.2.18) into (2.2.17) and collecting terms at each order, a sequence of Neumann boundary conditions is obtained at $z{=}-h_u$ for $\Phi^{(m)}$:

$$\Phi_{,z}^{(m)}(x,-h_u,t) = f_{\ell 2}^{(m)} \tag{2.2.19}$$

with

$$f_{\ell 2}^{(1)} = 0 \,, \tag{2.2.20}$$

$$f_{\ell 2}^{(m)} = \sum_{k=1}^{m-1} \frac{\partial}{\partial x} \left[\frac{\eta_\ell^k}{k!} \frac{\partial^{(k-1)}}{\partial z^{(k-1)}} \Phi_{,x}^{(m-k)}(x,z,t)\big|_{z=-h_u} \right] \,, \tag{2.2.21}$$

for $m{=}2,3,\ldots,M$.

On the bottom $z{=}-h_u-h_\ell+\eta_b$, ϕ_ℓ is expanded in a Taylor series with respect to the mean bottom position $z{=}-h_u-h_\ell$. Upon substituting the expansion into the bottom boundary condition (2.2.1h), a sequence of Neumann boundary conditions is obtained at

z=$-h_u - h_\ell$ for $\phi_\ell^{(m)}$:

$$\phi_{\ell,z}^{(m)}(x, -h_u - h_\ell, t) = f_b^{(m)} \tag{2.2.22}$$

with

$$f_b^{(1)} = 0\,, \tag{2.2.23}$$

$$f_b^{(m)} = \sum_{k=1}^{m-1} \frac{\partial}{\partial x}\left[\frac{\eta_b^k}{k!}\frac{\partial^{(k-1)}}{\partial z^{(k-1)}}\phi_{\ell,x}^{(m-k)}(x,z,t)\big|_{z=-h_u-h_\ell}\right]\,, \quad m = 2, 3, \ldots, M. \tag{2.2.24}$$

With these expansions, a sequence of linearized boundary-value problems is obtained for the perturbed potentials $\phi_u^{(m)}$ and $\phi_\ell^{(m)}$, m=$1, 2, \ldots, M$. Specifically, at each order m, $\phi_u^{(m)}$ and $\phi_\ell^{(m)}$ satisfy Laplace's equation respectively in the region $0 \geq z \geq -h_u$ and $-h_u \geq z \geq -h_u - h_\ell$ with the boundary conditions: (i) $\phi_u^{(m)}(x, 0, t)$=$f_u^{(m)}$; (ii) $\psi^{(m)}(x, -h_u, t)$=$f_{\ell 1}^{(m)}$; (iii) $\Phi_{,z}^{(m)}(x, -h_u, t)$=$f_{\ell 2}^{(m)}$; (iv) $\phi_{\ell,z}^{(m)}(x, -h_u - h_\ell, t)$=$f_b^{(m)}$; and (v) $\phi_u^{(m)}$ and $\phi_\ell^{(m)}$ are periodic in x. These boundary-value problems can be solved sequentially up to an arbitrary order M starting from m=1.

2.2.4 Spectral solution for $\phi_u^{(m)}$ and $\phi_\ell^{(m)}$

The spectral method is now applied to solve the boundary-value problems for $\phi_u^{(m)}$ and $\phi_\ell^{(m)}$, m=$1, 2, \ldots, M$. At each order m, the solutions of $\phi_u^{(m)}$ and $\phi_\ell^{(m)}$ is constructed in terms of Fourier basis functions:

$$\phi_u^{(m)}(x,z,t) = \sum_{n=-N}^{N-1}\left\{A_n^{(m)}(t)\frac{\cosh[k_n(z+h_u)]}{\cosh(k_n h_u)} + B_n^{(m)}(t)\frac{\sinh(k_n z)}{\cosh(k_n h_u)}\right\}e^{ik_n x} \tag{2.2.25}$$

$$\phi_\ell^{(m)}(x,z,t) = \sum_{n=-N}^{N-1}\left\{C_n^{(m)}(t)\frac{\cosh[k_n(z+h_u+h_\ell)]}{\cosh(k_n h_\ell)} + D_n^{(m)}(t)\frac{\sinh[k_n(z+h_u+h_\ell)]}{\cosh(k_n h_\ell)}\right\}e^{ik_n x} \tag{2.2.26}$$

where k_n=$2\pi n/L_x$ with L_x being the length of the computational domain, and $A_n^{(m)}$, $B_n^{(m)}$, $C_n^{(m)}$, and $D_n^{(m)}$ are the complex modal amplitudes. One notes that for sufficiently smooth $\phi_u^{(m)}$ and $\phi_\ell^{(m)}$, $A_n^{(m)}$, $B_n^{(m)}$, $C_n^{(m)}$, and $D_n^{(m)}$ decay exponentially in magnitude with $|n|$. Clearly, $\phi_u^{(m)}$ and $\phi_\ell^{(m)}$ in (2.2.25) and (2.2.26) are harmonic and satisfy the boundary condition (v). The unknown amplitudes $A_n^{(m)}$, $B_n^{(m)}$, $C_n^{(m)}$, and $D_n^{(m)}$ are determined by the imposition of the other four boundary conditions (i), (ii), (iii) and (iv) to $\phi_u^{(m)}$ and $\phi_\ell^{(m)}$ in

(2.2.25) and (2.2.26).

Specifically, $A_n^{(m)}$ is determined from the boundary condition (i), $D_n^{(m)}$ from the boundary condition (iv), and $B_n^{(m)}$ and $C_n^{(m)}$ from the boundary conditions (ii) and (iii). Upon substitution,

$$
\begin{aligned}
A_n^{(m)} &= \tilde{f}_{un}^{(m)} \,, && \text{(2.2.27a)}\\
B_n^{(m)} &= \Big[k_n \tilde{f}_{un}^{(m)} \mathcal{R} \sinh k_n h_\ell + \tilde{f}_{bn}^{(m)} \cosh k_n h_u + k_n \tilde{f}_{\ell 1n}^{(m)} \sinh k_n h_\ell \cosh k_n h_u \\
&\quad + \tilde{f}_{\ell 2n}^{(m)} \cosh k_n h_u \cosh k_n h_\ell \Big] / \Delta_n \,, && \text{(2.2.27b)}\\
C_n^{(m)} &= -\cosh k_n h_\ell \, \Big[-k_n \tilde{f}_{un}^{(m)} \mathcal{R} + \tilde{f}_{bn}^{(m)} (\mathcal{R} \sinh k_n h_u \cosh k_n h\ell + \sinh k_n h_\ell \cosh k_n h_u) \\
&\quad - k_n \tilde{f}_{\ell 1n}^{(m)} \cosh k_n h_u + \tilde{f}_{\ell 2n}^{(m)} \mathcal{R} \sinh k_n h_u \Big] / \Delta_n \,, && \text{(2.2.27c)}\\
D_n^{(m)} &= \frac{\cosh(k_n h_\ell)}{k_n} \tilde{f}_{bn}^{(m)} \,, && \text{(2.2.27d)}
\end{aligned}
$$

for $n{=}0, \pm 1, \ldots, \pm N$. In (2.2.27), $\Delta_n \equiv k_n(\cosh k_n h_u \cosh k_n h_\ell + \mathcal{R} \sinh k_n h_u \sinh k_n h_\ell)$, and $\tilde{f}_{un}^{(m)}$, $\tilde{f}_{\ell 1n}^{(m)}$, $\tilde{f}_{\ell 2n}^{(m)}$, and $\tilde{f}_{bn}^{(m)}$ are respectively the $n-$th Fourier modal amplitudes of $f_u^{(m)}$, $f_{\ell 1}^{(m)}$, $f_{\ell 2}^{(m)}$, and $f_b^{(m)}$.

2.2.5 Evaluation of the interface potentials and surface/interface vertical velocities

Once the boundary-value solution at order m is obtained, the vertical velocities of the fluid on the mean free surface and interface at that order are obtained from (2.2.25) and (2.2.26):

$$
\begin{aligned}
\phi_{u,z}^{(m)}(x,0,t) &= \sum_{n=-N}^{N} k_n \Big[A_n^{(m)}(t) \tanh(k_n h_u) + B_n^{(m)}(t)\Big] e^{ik_n x} \,, && \text{(2.2.28a)}\\
\phi_{u,z}^{(m)}(x,-h_u,t) &= \sum_{n=-N}^{N} k_n B_n^{(m)}(t) e^{ik_n x} \,, && \text{(2.2.28b)}\\
\phi_{\ell,z}^{(m)}(x,-h_u,t) &= \sum_{n=-N}^{N} k_n \Big[C_n^{(m)}(t) \tanh(k_n h_u) + D_n^{(m)}(t)\Big] e^{ik_n x} \,, && \text{(2.2.28c)}
\end{aligned}
$$

for $m{=}1, 2, \ldots, M$.

After the boundary-value solution is obtained up to the specified order M, the interface

potentials and the surface/interface vertical velocities are evaluated by:

$$\phi_u^I(x,t) = \sum_{m=1}^{M}\sum_{k=0}^{M-m}\frac{\eta_u^k}{k!}\frac{\partial^k}{\partial z^k}\phi_u^{(m)}(x,-h_u,t)\ , \tag{2.2.29a}$$

$$\phi_\ell^I(x,t) = \sum_{m=1}^{M}\sum_{k=0}^{M-m}\frac{\eta_u^k}{k!}\frac{\partial^k}{\partial z^k}\phi_\ell^{(m)}(x,-h_u,t)\ , \tag{2.2.29b}$$

$$\phi_{u,z}(x,\eta_u,t) = \sum_{m=1}^{M}\sum_{k=0}^{M-m}\frac{\eta_u^k}{k!}\frac{\partial^{(k+1)}}{\partial z^{(k+1)}}\phi_u^{(m)}(x,0,t)\ , \tag{2.2.29c}$$

$$\phi_{u,z}(x,-h_u+\eta_\ell,t) = \sum_{m=1}^{M}\sum_{k=0}^{M-m}\frac{\eta_\ell^k}{k!}\frac{\partial^{(k+1)}}{\partial z^{(k+1)}}\phi_u^{(m)}(x,-h_u,t)\ , \tag{2.2.29d}$$

$$\phi_{\ell,z}(x,-h_u+\eta_\ell,t) = \sum_{m=1}^{M}\sum_{k=0}^{M-m}\frac{\eta_\ell^k}{k!}\frac{\partial^{(k+1)}}{\partial z^{(k+1)}}\phi_\ell^{(m)}(x,-h_u,t)\ , \tag{2.2.29e}$$

in which the higher $z-$derivatives of $\phi_{u/\ell}^{(m)}$ are evaluated by converting into $x-$derivatives using Laplace's equation, e.g. , $\phi_{u/\ell,zz}^{(m)}=-\phi_{u/\ell,xx}^{(m)}$, $\phi_{u/\ell,zzz}^{(m)}=-\phi_{u/\ell,zxx}^{(m)}$, etc. The $x-$derivatives are evaluated easily in the Fourier space.

2.3 Implementation and validation

2.3.1 Implementation

The time simulation of nonlinear interactions of surface and interfacial waves with variable bottom topography up to a specified order M consists of two main steps: (a) at each time t, given the surface and interface elevations (η_u, η_ℓ), surface potential (ϕ^S), and a weighted potential combination at the interface ($\psi^I=\phi_\ell^I-\mathcal{R}\phi_u^I$), solve the boundary-value problems for ϕ_u and ϕ_ℓ up to the specified order M and evaluate the surface velocity, $\phi_{u,z}(x,\eta_u,t)$, and interface velocities, $\phi_{u,z}(x,-h_u+\eta_\ell,t)$ and $\phi_{\ell,z}(x,-h_u+\eta_\ell,t)$; and (b) integrate the evolution equations, (2.2.4)-(2.2.7), in time to obtain the new values of η_u, η_ℓ, ϕ^S and ψ^I at time $t+\Delta t$, where Δt is the time step. The two steps (a)-(b) are repeated starting from initial values.

In the present method, the boundary-value problems for ϕ_u and ϕ_ℓ are solved up to the specified order M by a pseudo-spectral approach. Specifically, all spatial derivatives (of quantities such as $\phi_u^{(m)}$, $\psi^{(m)}$ and $\Phi^{(m)}$) are evaluated in wave number space while nonlinear terms and products are calculated in physical space at a discrete set of points

x_j, j=1, 2, ..., $2N$ on the mean surface and interface. For Fourier basis functions used, the collocation points x_j, j=1, 2, ..., $2N$, are equally spaced, and fast Fourier transform (FFT) is used to project between the wavenumber and physical domain. For time integration, the fourth-order Runge-Kutta scheme is employed. Overall, the operation count for the solution of the complete problem up to order M is $O(MN \ln N)$ per time step.

For specific simulations, the bottom ripples are typically placed in a patch centered in the computational domain. The disturbance generated by interactions among surface waves, interfacial waves and bottom ripples propagates toward the side boundaries of the computational domain in time. For a fixed length of the computational domain, the simulation is stopped before these disturbances reach the side boundaries (this is checked by repeating the simulation in a large computational domain). The simulation time for a given domain can be extended by employing a tapering technique of Dommermuth & Yue (1988) where the solutions are multiplied by a function that tapers smoothly to zero at the two boundaries.

2.3.2 Convergence tests using a two-layer fluid Stokes wave solution

The HOS method for a one-layer fluid on a rippled bottom has been validated extensively (Liu & Yue, 1998). To check the correctness and accuracy of the extension to a two-layer fluid, a fully-nonlinear solution of a Stokes wave in a two-layer fluid (on a uniform bottom) is used as a benchmark. The benchmark solution is obtained using Newton's iterative method (see Appendix A). As an example, figure 2-2 shows the profiles of surface/interface elevations and velocity potentials for a two-layer fluid Stokes wave of the internal mode. The decrease in the error with respect to the number of Newton iterations is also shown. For moderate wave steepness, the error is generally smaller than 10^{-14} after 50 iterations. The benchmark solution used below for the validation of the HOS computations is accurate to 14 decimal place and is hereafter considered to be the "exact" solution.

It is first shown the convergence of the boundary-value problem solution with respect to the perturbation order M and the number of spectral modes per wave length N. The boundary conditions are specified on the surface and the interface from the (exact) nonlinear solution of a Stokes wave, and solved for the surface and interface vertical velocities using the HOS approach. The steepness of the nonlinear solution, ϵ, is defined as the product of the wavenumber and half the crest-trough height. A typical result is given in table 2.1 for

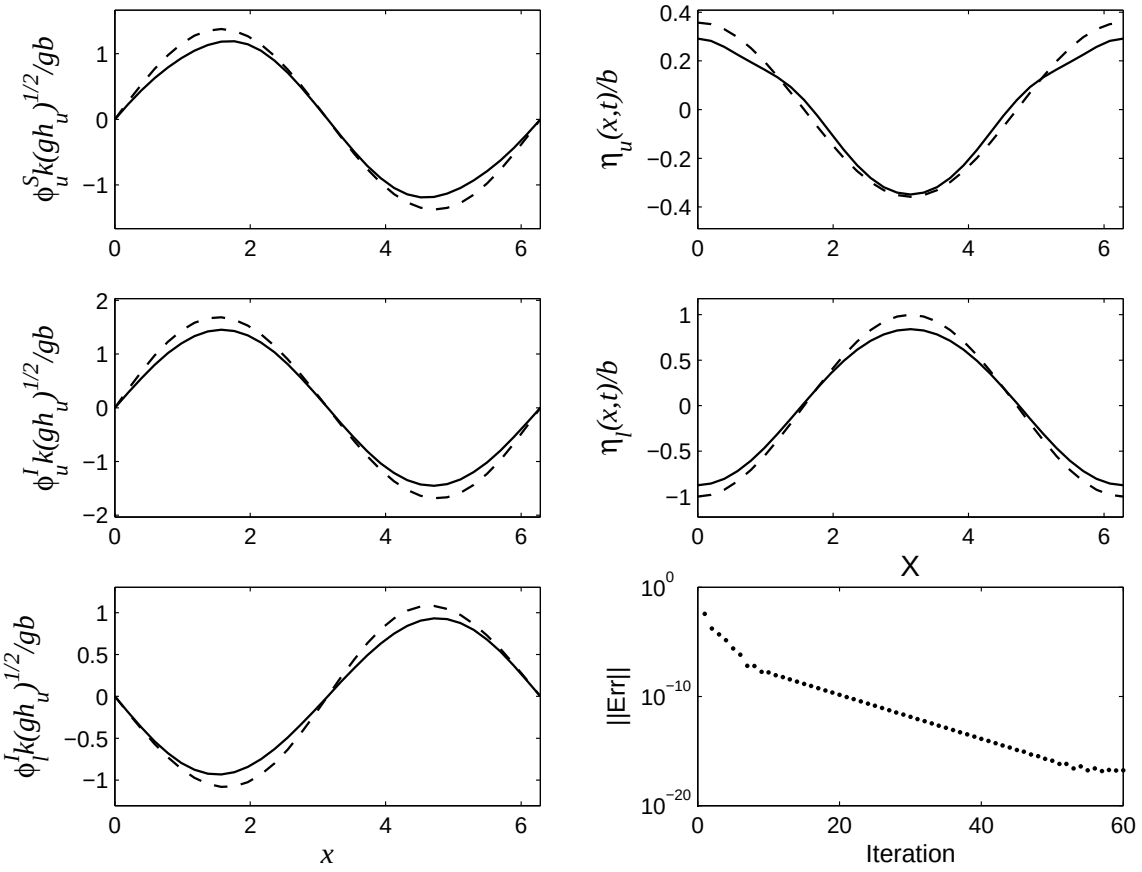

Figure 2-2: Profiles of a steady internal mode Stokes wave in a two-layer density stratified fluid for the normalized free surface and interface elevations: $\eta_u(x,t)$ and $\eta_\ell(x,t)$; the normalized velocity potentials on the free surface and interface: ϕ_u^S, and ϕ_u^I, ϕ_ℓ^I. The plotted curves are the initial guess (- - -), the solution after 50 iterations (——), and the averaged error as a function of the number of iterations ($\cdot\ \cdot\ \cdot$). The physical parameters are: kb=0.07, where b is the initial amplitude measured on the interface, h_u/h_ℓ=1/2, kh_u=1, and $\mathcal{R}$=0.5.

N	$M=1$	$M=2$	$M=3$	$M=4$	$M=6$	$M=8$
4	0.55×10^{-2}	0.13×10^{-2}	0.70×10^{-3}	0.69×10^{-3}	0.69×10^{-3}	0.69×10^{-3}
8	0.90×10^{-3}	0.12×10^{-3}	0.86×10^{-5}	0.21×10^{-5}	0.17×10^{-5}	0.17×10^{-5}
16	0.64×10^{-3}	0.85×10^{-4}	0.60×10^{-5}	0.78×10^{-6}	0.83×10^{-8}	0.67×10^{-9}
32	0.45×10^{-3}	0.60×10^{-4}	0.42×10^{-5}	0.55×10^{-6}	0.55×10^{-8}	0.56×10^{-10}

Table 2.1: Maximum error of the normalized vertical velocity of upper layer fluid at the interface, $\phi_{u,z}(x,-h_u+\eta_\ell,0)(gh_u)^{1/2}/ga$, for a Stokes wave in a two-layer fluid with ϵ=0.1, h_ℓ/h_u=1, and $\mathcal{R}$=0.5.

	$T/\Delta t$				
t/T	30	40	50	100	200
1	0.18×10^{-2}	0.72×10^{-3}	0.36×10^{-3}	0.43×10^{-4}	0.53×10^{-5}
10	0.38×10^{-2}	0.14×10^{-2}	0.62×10^{-3}	0.59×10^{-4}	0.65×10^{-5}

Table 2.2: Maximum error of the normalized vertical velocity of the upper layer fluid at the interface, $\phi_{u,z}(x,-h_u+\eta_\ell,t)(gh_u)^{1/2}/ga$, for a Stokes wave in a two-layer fluid with ϵ=0.1, h_ℓ/h_u=1, and $\mathcal{R}$=0.5 after time integration of t/T=1, 10 with different time steps. The HOS parameters are N=32, M=3

the maximum error in the interface vertical velocity with increasing M and N for ϵ=0.1, depth ratio h_ℓ/h_u=1 and density ratio $\mathcal{R}$=0.5. For sufficiently large M, the error decays exponentially fast with increasing N. For sufficiently large N, exponential convergence with M also obtains.

To test the accuracy of the time integration, The HOS is used to simulate the nonlinear evolution of the two-layer fluid Stokes wave train using the exact solution as initial conditions. Table 2.2 shows the maximum absolute error in the interface vertical velocity after an evolution of t/T=1 and 10 with different time steps. Here T is the fundamental period of the Stokes wave. For these computations, N=32 (per wavelength) and M=3 are used to ensure that the error in solving the boundary-value problem itself is negligible (see table 1). For the fourth-order Runge-Kutta scheme, the global error decreases as $O((\Delta t/T)^4)$ after a time integration t/T=O(1).

2.4 Numerical results

The extended HOS method of previous section is used here to perform direct numerical simulations of the nonlinear interactions of surface/interfacial waves with bottom undulations. The numerical results are compared with theoretical predictions first for the second-

order two-layer fluid resonant interaction problem with a flat bottom (e.g. Ball, 1964; Wen, 1995*b*); and then for Bragg scattering in a two-layer density stratified fluid, specifically the three classes of resonances for which perturbation results are obtained in chapter one. In addition to further validation of the numerical method, of special interest is to evaluate the effect of higher order nonlinearities not accounted for in the perturbation theory. Finally, to illustrate the use of the numerical method, HOS simulation is applied to the long-time interaction of an initially monochromatic incident wave with a (select) three-component rippled bottom. The wavenumber components of the problem (initially) satisfy class I resonance; while the generation of the resultant resonant wave(s) leads to multiple resonances involving multiple combinations of the components. As time increases, it is shown that the wave motion eventually turns from regular to chaotic.

2.4.1 Determination of reflection and transmission coefficients

The numerical simulation is performed in the time domain starting from initial conditions and typically carried out until steady state (limit cycle) is reached in the (inner) spatial domain for the quantities of interest.

One objective is to obtain the numerical predictions of quantities such as the spatially-varying reflection and transmission coefficients and compare these to existing theoretical results. The HOS simulation captures the nonlinear interactions among all the surface/interfacial wave and bottom ripple components (up to the specified order M) as they evolve in time. The HOS wavefield (in space and time) thus contains wave components that include surface and internal mode free and locked waves associated with the incident and the resonance generated waves, including those that have the same frequencies but different wavenumbers, etc. It should also be pointed out that because of nonlinearity in the simulations, these components in general do not satisfy (exactly) linear dispersion relationships. Here a robust scheme to extract the quantities of interest from such wavefields is described.

Our approach is an extension/improvement of the method of Goda & Suzuki (1976), which is found to be not sufficiently robust for the present application. Without loss of generality, assume a wavefield containing two surface wave components with the same frequency ω but different wavenumbers k_1 and k_2 given by

$$\eta(x,t) = a_1(x)\cos(k_1 x - \omega t + \psi_1) + a_2(x)\cos(k_2 x - \omega t + \psi_2)\ , \tag{2.4.30}$$

where a_1, a_2 and ψ_1, ψ_2 are respectively the (slowly-varying) amplitudes and phases of the two waves. Given $\eta(x,t)$ in the computational domain over a certain period of time, the objective is to determine $a_1(x)$ and $a_2(x)$ for (2.4.30). To capture the slowly varying $a_1(x)$ and $a_2(x)$, they are first represented by Chebshev polynomials:

$$a_1(x) = \sum_{n=1}^{N_T} \alpha_{1n} T_{n-1}(x) \ , \qquad a_2(x) = \sum_{n=1}^{N_T} \alpha_{2n} T_{n-1}(x) \tag{2.4.31}$$

where T_n is the $n-$th order Chebyshev polynomial of the first kind, α_{1n} and α_{2n} the unknown modal amplitudes, and N_T the number of Chebyshev modes retained in the expansion. The unknown coefficients α_{1n} and α_{2n} can be obtained from known values of $a_1(x_j)$ and $a_2(x_j)$ at collocations points x_j for the Chebyshev polynomial.

To find $a_1(x_j)$ and $a_2(x_j)$ at some collocation point x_j, a small window W_j centered at $x{=}x_j$ is chosen with a length of $\Delta\ell$ generally much smaller than the length of the entire wavefield. Inside this window, we again represent $a_1(x)$ and $a_2(x)$ in expansions of the form of (2.4.31) using N_{Tj} terms where N_{Tj} can be somewhat smaller than N_T. For the present work, it is found that typical values of $N_T{=}6$ or 7, and $N_{T_j}{=}2$ or 3 adequate to obtain accurate (smooth) predictions of the transmission/reflection coefficients. Now $q = 1, \ldots, L_j$ are defined as uniformly spaced points in W_j and write:

$$\eta(x_q,t) = \eta_j^c(x_q)\cos(\omega t) + \eta_j^s(x_q)\sin(\omega t) \ , \quad q = 1, \ldots, L_j \ , \quad x_q \in W_j \ . \tag{2.4.32}$$

At each x_q within W_j, the amplitudes $\eta^c(x_q)$ and $\eta^s(x_q)$ are obtained using Fourier transform in time of the wavefield time histories at that point. Note that $\eta_j^c(x)$ and $\eta_j^s(x)$ contain fast dependence on x. Substituting the expansions for the amplitudes in W_j into (2.4.30) and equating the result with (2.4.32), it obtains for each x_q two equations for the unknown modal amplitudes at that point. For the window W_j, together a system of $2L_j$ linear equations for $2N_{Tj}$ unknown Chevbyshev coefficients and two phases for that window. This system is typically over-determined with $L_j \gg N_{Tj}$, and the unknown amplitudes (and phases) are obtained using least-squares. With these modal amplitudes determined, it obtains $a_1(x_j)$ and $a_2(x_j)$ at the center of W_j.

By repeating this process for a large number of collocation points (relative to N_T) for $a_1(x_j)$ and $a_2(x_j)$ from which the expansion coefficients α_{1n} and α_{2n} in (2.4.31) can be

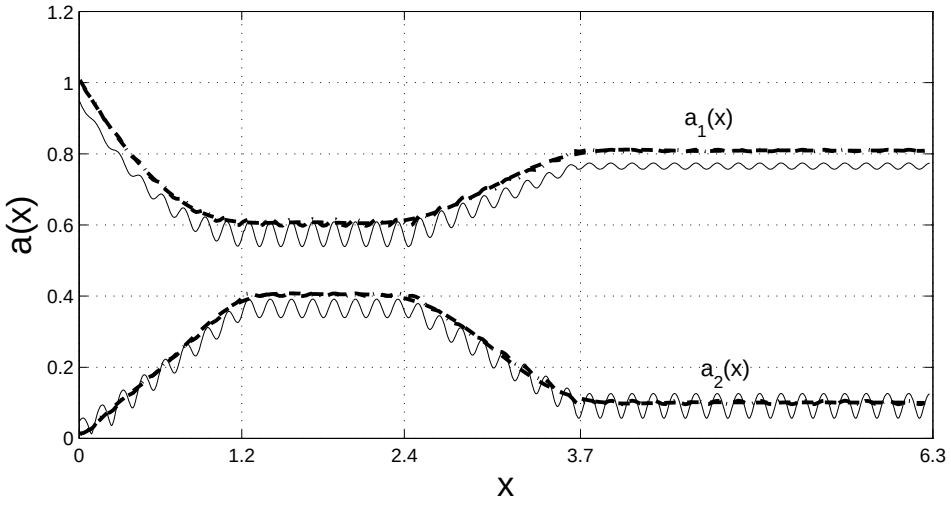

Figure 2-3: Spatial variations of the slowly-varying amplitudes of a two component wave train obtained using the present scheme (– · –) and the method of Goda & Suzuki (1976) (——), compared with the exact solution (· · ·). Note that the solution using the present scheme is graphically indistinguishable from the exact solution.

obtained, say, by using the orthogonality of Chevbyshev polynomials. It is to be noted that the scheme of Goda & Suzuki (1976) corresponds to the local (W_j) step only (without (2.4.31)) of the present scheme with the simplest choice of N_{Tj}=1 and L_j=2.

As an illustration, consider a sample synthetic wavefield given by the superposition of two wave components with wavenumbers k_1, k_2=32, 72; and slowly varying amplitudes $a_1(x)$ and $a_2(x)$ given by the "exact" curves in figure 2-3. Since in practice the wavenumbers are not exactly known/given, to show the robustness of the scheme, instead of the exact, approximate values of the wavenumbers $\tilde{k}_1$, $\tilde{k}_2$=30, 76 are used in the assumed decomposition (2.4.30). Figure 2-3 shows the predicted amplitudes $a_1(x)$, $a_2(x)$ obtained using the present algorithm and those using the method of Goda & Suzuki (1976) method as compared to the exact functions. In this case, the Goda & Suzuki (1976) predictions show highly oscillatory behavior with mean values deviating somewhat from the exact curve. In contrast, the predictions using the present scheme are graphically indistinguishable from the exact result.

2.4.2 Resonance of waves in a two-layer fluid on uniform depth

For a two-layer fluid over a flat horizontal bottom, Ball (1964) showed that a resonant triad can be formed with two surface mode and one internal mode wave components. Later Wen (1995*b*), Hill & Foda (1996), Hill & Foda (1998) and Jamali (1998), showed that a similar triad can also be formed by one surface mode and two internal mode wave components (see Appendix C for a new case from this category). For illustration and as a further validation of the numerical simulation, HOS is applied to this problem and compare and elucidate the numerical predictions against perturbation solutions.

First consider the case in which resonant interaction of two free surface waves generates a free internal mode wave. Let (a_1, k_1, ω_1) and (a_2, k_2, ω_2) represent the wave amplitudes, wavenumbers and frequencies of the two incident surface waves. The wavenumber and frequency of each wave satisfies the dispersion relation (1.2.7).

If the two incident waves satisfy the resonance condition, i.e. $\mathcal{D}(k_r, \omega_r)$=0 with k_r=k_1+k_2 and ω_r=$\omega_1 + \omega_2$, a free internal mode wave with wavenumber k_r and frequency ω_r will be resonated. The amplitude of the resonant wave initially grows linearly with time. This initial growth can be predicted using regular perturbation analysis to the second order and is given by:

$$|\eta_\ell^{(2)}| = \gamma t + \text{non-growing terms} \,, \tag{2.4.33}$$

where η_ℓ represents the interfacial wave elevation and the growth rate γ is:

$$\begin{aligned} \gamma \;\; = \;\; & \big[cu\,\omega^4\alpha - cu\,(-M_1\,cu + M_3)\omega^3 - su\,k_r\,(g\alpha + M_2\,cu)\omega^2 \\ & + gsu\,k_r\,(-M_1\,cu + M_3)\omega + gsu^2{k_r}^2 M_2\big]\,/(2g\omega\;su\;k_r) \end{aligned} \tag{2.4.34}$$

with the coefficients

$$\begin{aligned} \alpha = \big[& M_2\,su\,(\mathcal{R}su\,sl + cu\,cl)\omega^3 + g(-sl\,cu^2 M_1 + \mathcal{R}sl\,su^2 M_1 + M_4\,cl\,su + sl\,M_3\,cu)\omega^2 \\ & -gk_r\,su\,(cl\,M_2\,su + cu\,\mathcal{R}sl\,M_2 - sl\,M_5)\omega + k_r\,g^2 su\,sl\,(-1+\mathcal{R})(-M_1\,cu + M_3)\big] \\ & /\,\big[g\,(cu\,sl + cl\,su)\,\omega^3 + 2\,g^2 k_r\;(-1+\mathcal{R})\,su\,sl\,\omega\big] \end{aligned}$$

$$
\begin{aligned}
M_1 &= 1/2\,(k_1+k_2)(k_2 a_1 A_2 + A_1 a_2 k_1)\\
M_2 &= 1/2\,B_1 k_1 B_2 k_2 - 1/2\,A_1 k_1 A_2 k_2 - 1/2\,a_1 B_2 k_2 \omega_2 - 1/2\,a_2 B_1 k_1 \omega_1\\
M_3 &= -1/2\,(k_1+k_2)(k_1 b_2 B_1 su_1 - k_1 b_2 A_1 cu_1 + b_1 B_2 k_2 su_2 - k_2 A_2 cu_2\, b_1)\\
M_4 &= 1/2\,(k_1+k_2)(b_2 D_1 cl_1\, k_1 + D_2 b_1 k_2 cl_2)\\
M_5 &= -1/2\,b_1 D_2 sl_2\, k_2\omega_2 + 1/2\,\mathcal{R} A_1 su_1\, k_1 B_2 cu_2\, k_2 - 1/2\,\mathcal{R} k_1 B_1 su_1\, k_2 A_2 cu_2\\
&\quad +1/2\,\mathcal{R} k_1 B_1 su_1\, k_2 B_2 su_2 - 1/2\,b_2 D_1 sl_1\, k_1\omega_1 - 1/2\,\mathcal{R} b_1\omega_2 A_2 su_2\, k_2\\
&\quad +1/2\,\mathcal{R} k_1 A_1 cu_1\, k_2 A_2 cu_2 + 1/2\,D_1 sl_1\, k_1 D_2 sl_2\, k_2 + 1/2\,\mathcal{R} b_1\omega_2 B_2 cu_2\, k_2\\
&\quad -1/2\,D_1 cl_1\, k_1 D_2 cl_2\, k_2 + 1/2\,\mathcal{R} b_2\omega_1 B_1 cu_1\, k_1 - 1/2\,\mathcal{R} k_1 A_1 cu_1\, k_2 B_2 su_2\\
&\quad -1/2\,\mathcal{R} A_1 su_1\, k_1 A_2 su_2\, k_2 + 1/2\,\mathcal{R} B_1 cu_1\, k_1 A_2 su_2\, k_2 - 1/2\,\mathcal{R} B_1 cu_1\, k_1 B_2 cu_2\, k_2\\
&\quad -1/2\,\mathcal{R} b_2\omega_1 A_1 su_1\, k_1
\end{aligned}
$$

$$
cu = \cosh(k_r h_u), \quad su = \sinh(k_r h_u), \quad cl = \cosh(k_r h_\ell), \quad sl = \sinh(k_r h_\ell)
$$

$$
cu_i = \cosh(k_i h_u), \quad su_i = \sinh(k_i h_u), \quad cl_i = \cosh(k_i h_\ell), \quad sl_i = \sinh(k_i h_\ell)
$$

$$
b_i = a_i\left(\cosh k_i h_u - \frac{g k_i}{\omega_i^2}\sinh k_i h_u\right), \quad A_i = -\frac{g a_i}{\omega_i}, \quad B_i = -\frac{a_i\omega_i}{k_i}, \quad D_i = -\frac{b_i\omega_i}{k_i \sinh k_i h_\ell}
$$

for i=1, 2.

For numerical simulation, consider an example with $\mathcal{R}$=0.5[1]; h_ℓ/h_u=0.5; and two surface mode waves travelling in the opposite directions with $k_1 h_u$=0.060 ($\omega_1^2 h_u/g = 0.005$), a_1/h_u=0.005, a_2/a_1=2, k_2/k_1=2.2 ($\omega_2^2 h_u/g = 0.025$). With these parameters, the resonated internal mode wave has k_r/k_1=3.2. The regular perturbation solution gives a growth rate of $\gamma/(a_1/T_1) = 1.3\times10^{-3}$ for the generated wave where T_1 is the period of the k_1 wavenumber wave. In the HOS simulation, a computational domain with length $L_x = 2\pi$ is chosen. The initial conditions of the surface/interface elevations and potentials are given by superposition of the (linearized) solutions of the two incident surface waves. The other numerical parameters used are: N=512, M=4, and $T_1/\Delta t$=128.

Figure 2-4 shows the variation of the amplitudes of the two (incident) surface mode waves and the generated internal mode wave as a function of dimensionless time t/T_1. The HOS simulation result is compared to prediction from regular perturbation theory, valid for the initial growth stage. In the resonant interaction, the generated internal mode wave

[1]While real ocean stratification is generally weak, typically a somewhat larger values of $1-\mathcal{R}$ is chosen to accentuate and elucidate the qualitative features and comparisons to perturbation theory. The HOS method itself is completely general and robust for any $\mathcal{R}$.

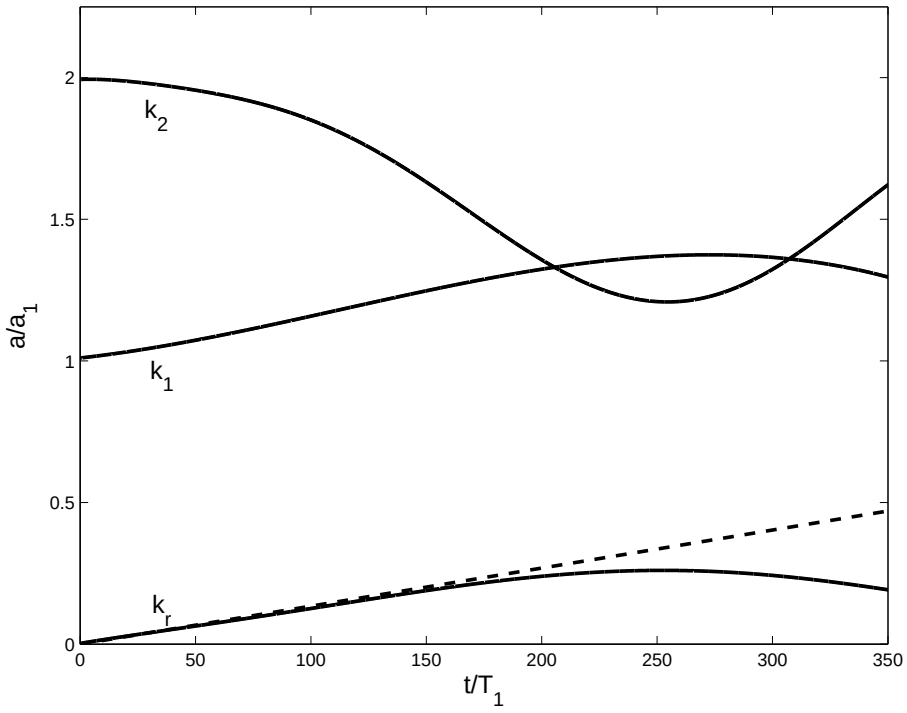

Figure 2-4: Time evolution of the amplitudes of two incident surface mode waves (wavenumber k_1, k_2) and the resonance generated internal mode wave (wavenumber k_r) undergoing resonant triad interaction obtained using the present numerical method (——). Plotted for comparison is the regular perturbation prediction for the initial growth of the resonant wave amplitude (equation 2.4.33, - - -). Chosen parameters are $\mathcal{R}$=0.5, h_ℓ/h_u=0.5, $k_1 h_u$=0.060 ($\omega_1^2 h_u/g = 0.005$), a_1/h_u=0.005, a_2/a_1=2, k_2/k_1=2.2 ($\omega_2^2 h_u/g = 0.025$) and simulation parameters are $L_x = 2\pi$, N=512, M=4, and $T_1/\Delta t$=128.

increases in amplitude with time, extracting energy from the two incident surface mode waves. The computational result compares well with the regular perturbation solution for the initial growth rate of the resonant wave. At larger time, the two predictions deviate, as expected, with the numerical solution growing to a maximum value and then decreasing as the interaction continues. Unlike the perturbation theory, the numerical simulation conserves total energy and accounts for long time evolution and even higher-order interaction effects not present in the regular perturbation theory.

The results for the second case in which the resonant triad is composed of one surface mode wave and two internal mode waves is presented here. For illustration consider that a free surface wave is generated by the resonant interaction of two free internal mode waves. As a numerical example, consider two incident internal mode waves travel in opposite directions, and the physical parameters: $\mathcal{R}$=0.5, h_ℓ/h_u=0.5, $k_1 h_u$=0.13 ($\omega_1^2 h_u/g = 7 \times 10^{-4}$), a_1/h_u=0.005, a_2/a_1=2, and k_2/k_1=0.45 ($\omega_2^2 h_u/g = 3 \times 10^{-3}$), where k_1, k_2; ω_1, ω_2, and a_1, a_2 are respectively the wavenumber, frequency and amplitude of the first and second incident internal mode waves. The generated surface wave has a wavenumber of k_r/k_1=0.55 and propagates in the direction of k_1 wave. For the numerical simulation, the computational parameters used are: $L_x = 2\pi$, N=512, M=4, and $T_1/\Delta t$=512. In figure 2-5, the variation of the amplitudes of the incident internal mode waves and the generated surface mode wave is plotted as a function of time. Similarly to the first case, the regular perturbation solution can also be derived. For this example the growth rate of the generated surface mode wave predicted by regular perturbation analysis is $\gamma/(a_1/T_1) = 2.8 \times 10^{-3}$, which is shown in the figure for comparison. As expected, the present numerical computation and the regular perturbation analysis match well at the initial stage of the interaction, but again deviate at large time as the regular perturbation solution fails.

Comparing the two cases, it is seen that when the resonance between two incident internal mode waves generates a surface mode wave, the amplitudes of both incident waves decrease for the growth of the generated wave. In contrast, when the interaction between two surface mode waves generates an internal mode wave, the amplitudes of the internal wave and one of the incident surface waves (the one with the longer wavelength) increase at the cost of the other incident wave whose amplitude decreases.

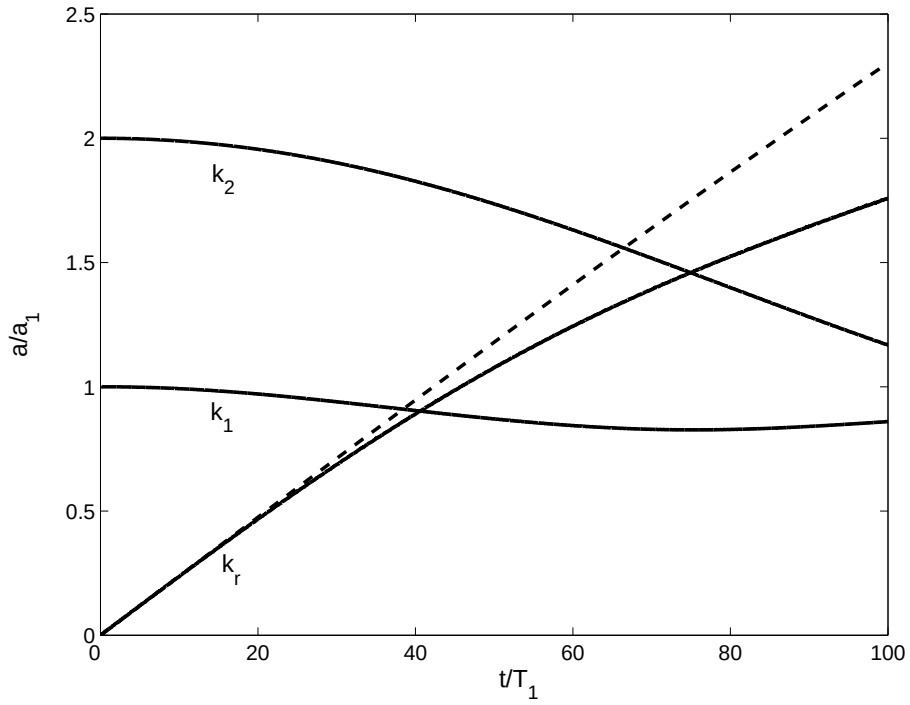

Figure 2-5: Time evolution of the amplitudes of two incident internal mode waves (wavenumber k_1, k_2) and the resonance generated surface mode wave (wavenumber k_r) undergoing resonant triad interaction obtained using the present numerical method (——). Plotted for comparison is the regular perturbation prediction for the initial growth of the resonant wave amplitude (derived similarly to equation 2.4.33,- - -). Chosen parameters are $\mathcal{R}$=0.5, h_ℓ/h_u=0.5, $k_1 h_u$=0.13 ($\omega_1^2 h_u/g = 7\times10^{-4}$), a_1/h_u=0.005, a_2/a_1=2, k_2/k_1=0.45 ($\omega_2^2 h_u/g = 3\times10^{-3}$) and for numerical simulation $L_x = 2\pi$, N=512, M=4, and $T_1/\Delta t$=512.

2.4.3 Class I Bragg Resonance

Here HOS time simulation is applied to class I Bragg resonant interactions of surface and interfacial waves with a patch of bottom ripples. In addition to cross-validation with the perturbation analysis of chapter one for the leading-order effect, the focus is also on the effects of higher order interactions associated with the wave/ripple steepness and the length of the rippled bottom.

Transmission of an inter-mode resonant wave

When an inter-mode resonance occurs, a new wave-mode is generated. For example, a surface mode wave may appear on an otherwise flat free surface due to resonant interaction of an internal mode wave with bottom ripples; and an internal mode wave can be generated when a surface mode wave interacts resonantly with bottom ripples.

In the resonance of inter-modes in transmission, the resonant wave travels in the same direction as the incident wave. According to chapter one, this type of class I Bragg resonance occurs if the bottom wavenumber k_b satisfies the condition, k_b=$k_i - k_s$, where k_i and k_s are the wavenumbers of internal and surface mode waves for any specified frequency ω. Both k_i and k_s are related to ω by the dispersion relation, $\mathcal{D}(k_i,\omega)$=$\mathcal{D}(k_s,\omega)$=0. There are two cases for this type of resonance: one is with the surface mode wave as the incident wave and the internal mode wave as the resonance generated wave ($S_c \xrightarrow{k_b} I_T$); and the other with the internal mode wave as the incident wave and the surface mode wave as the generated wave ($I_c \xrightarrow{k_b} S_T$);

For $S_c \xrightarrow{k_b} I_T$, figure 2-6 shows a sample computational result for the variation of the amplitudes of the incident surface mode wave and the generated internal mode wave over a patch of bottom ripples after the steady state of the wave-bottom interaction is reached. In this simulation, the physical parameters used are: incident wave steepness $\epsilon_s \equiv k_s a$=0.004, depth ratio h_ℓ/h_u=1, density ratio $\mathcal{R}$=0.5, $k_s h_u$=0.35 ($\omega^2 h_u/g$ = 0.19), bottom wavenumber k_b/k_s=1.47, bottom steepness $\epsilon_b \equiv k_b d$=0.04, and length of the rippled bottom $M_b = 2L/\lambda_b$=40; and computational parameters: length of the computational domain $L_x = 2\pi$, total number of spectral modes N=2048, order of nonlinearity M=2 and 3, time step $T/\Delta t$=60, and simulation time T_S/T=80, where T=$2\pi/\omega$ is the period of the incident surface mode wave (which is equal to the period of the resonance generated wave

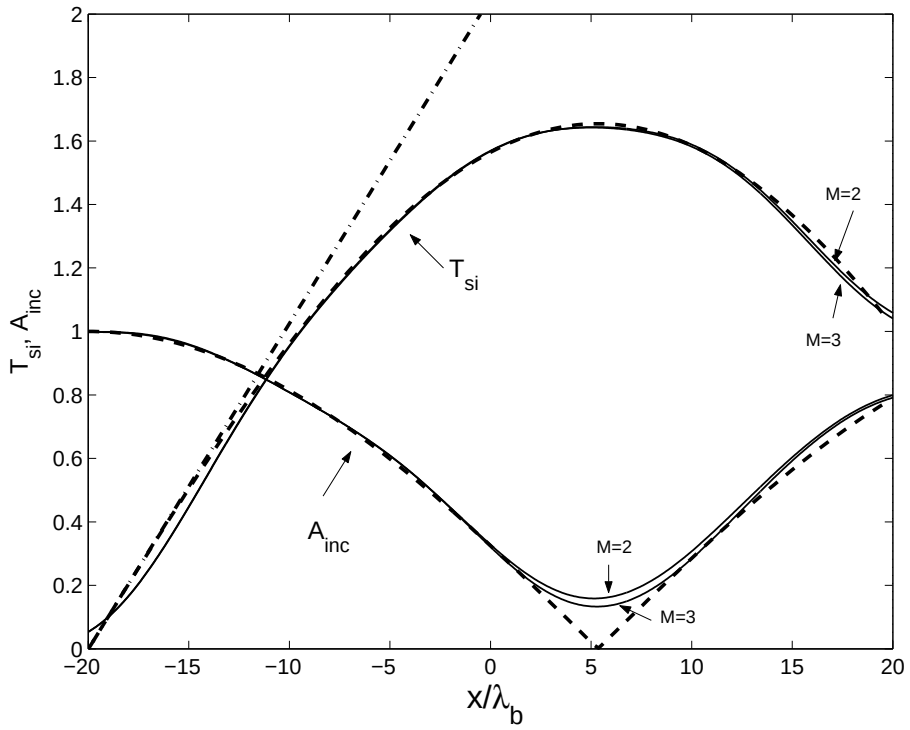

Figure 2-6: Spatial variation of the transmission coefficient of the incident surface mode wave (A_{inc}) and the resonance generated internal mode wave (T_{si}) over a patch of bottom ripples under class I Bragg resonance condition. Physical parameters: h_ℓ/h_u=1, $\mathcal{R}$=0.5, $k_s h_u$=0.35 ($\omega^2 h_u/g$ = 0.19), k_b/k_s=1.47, ϵ_b=0.04, M_b=40, ϵ_s=0.004, and computational parameters: N=2048, M=2,3 , $T/\Delta t$=60, and T_S/T=80. Results plotted are: numerical simulation (——), and predictions from regular perturbation (– · –) and multiple-scale analyses (- - -).

in class I Bragg resonance). The HOS results are compared to the theoretical predictions of chapter one which are second-order regular perturbation theory and multiple-scale analysis.

The direct computational result, which is convergent with M, compares well with the regular perturbation solution for approximately first ten bottom ripples. Beyond this region, the regular perturbation solution substantially overestimates the growth of the resonant wave. On the other hand, the computational result agrees perfectly with the solution of the multiple-scale analysis for both incident and resonant waves over the entire patch of bottom ripples. In this case, the amplitude of the resonant (internal mode) wave increases from zero to about 1.6 times the amplitude of the incident (surface mode) wave, taking almost all of the incident wave energy, after a distance of interaction of about 25 bottom ripples, and then decreases while giving energy back to the incident wave.

One objective of the numerical simulation is to assess the possible role and importance,

in this type of Bragg resonance, of (even) higher order (in wave and/or bottom steepness) interactions not accounted for in the theory. Figure 2-7 shows a similar case as above but with a much greater (surface) incident wave steepness ϵ_s=0.04. All other physical parameters are identical to those in figure 2-6. For numerical simulations, HOS results for orders M=2, 3 and 4 are given. The numerical results using M=3 has evidently converged and is graphically indistinguishable from that using M=4.

The difference between the M=2 and the M=3,4 results represents the higher-order effects in the wave-bottom interaction, and the latter deviates from the leading-order perturbation theories after relatively short interaction lengths. The overall apparent effect of including higher order interactions is the reduction in the variations and the maximum/minimum amplitudes of both the incident and the resonant (transmitted) waves; and a noticeable lowering of the (spatial) modulation wavelengths of these interacting wave amplitudes. In particular, the vanishing of the incident wave amplitude after some interaction distance (as the resonated wave reaches maximum) predicted by the multiple-scale theory analysis does not obtain.

To elucidate the higher order effects of bottom ripple steepness, figure 2-8 shows the spatial variation of the amplitude of the surface mode incident wave and the transmission coefficient of resonant internal mode with different bottom steepnesses (all other physical parameters are the same as those in figure 2-7). The (converged) numerical solutions with M=4 are again compared with the theoretical predictions of the regular perturbation and multiple-scale analyses. For mild bottom ripples, the resonance is dominated by the leading-order (i.e. second-order) wave-bottom interaction and the numerical solution and predictions of the regular and multiple-scale perturbation analyses agree well over the entire patch of the bottom ripples considered. As the bottom ripples become steeper, the higher-order simulation results deviate significantly from theoretical predictions. The monotonic growth of the resonant internal mode wave amplitude with distance predicted by regular perturbation does not obtain; while the multiple-scale prediction appreciably overestimates both the maximum and the wavelength of the (spatial) modulation of the resonant wave amplitude.

Direct simulation and comparison to theory are also obtained for the case of $I_c \xrightarrow{k_b} S_T$. The features and observations are very similar to the above, and are omitted.

It is of some interest to address the case of wave evolution over a very long bottom patch

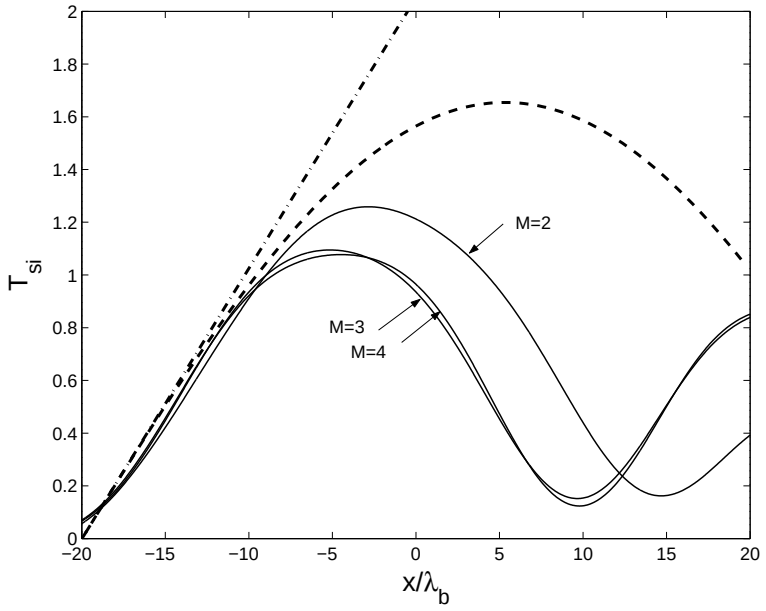

(a)

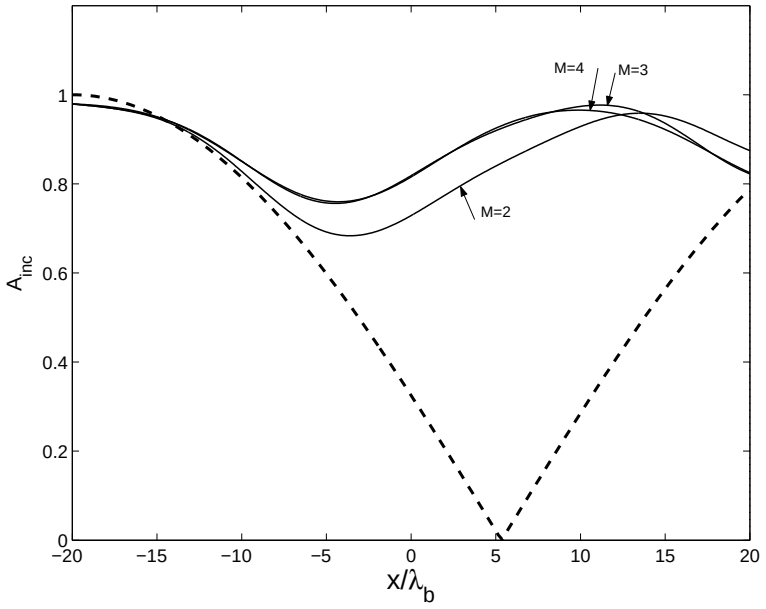

(b)

Figure 2-7: Spatial variation of (a) the transmission coefficient of the resonance generated internal mode wave (T_{si}), and (b) the amplitude of the incident surface mode wave (A_{inc}), over a patch of bottom ripples under class I Bragg resonance condition. Physical parameters are h_ℓ/h_u=1, $\mathcal{R}$=0.5, $k_s h_u$=0.35 ($\omega^2 h_u/g$ = 0.19), k_b/k_s=1.47, M_b=40, ϵ_b=0.04, ϵ_s=0.04, and computational parameters: N=2048, M=2,3 and 4, $T/\Delta t$=60, and T_S/T=80. Results plotted are: numerical simulation (——), and predictions from regular perturbation (– · –) and multiple-scale analyses (- - -).

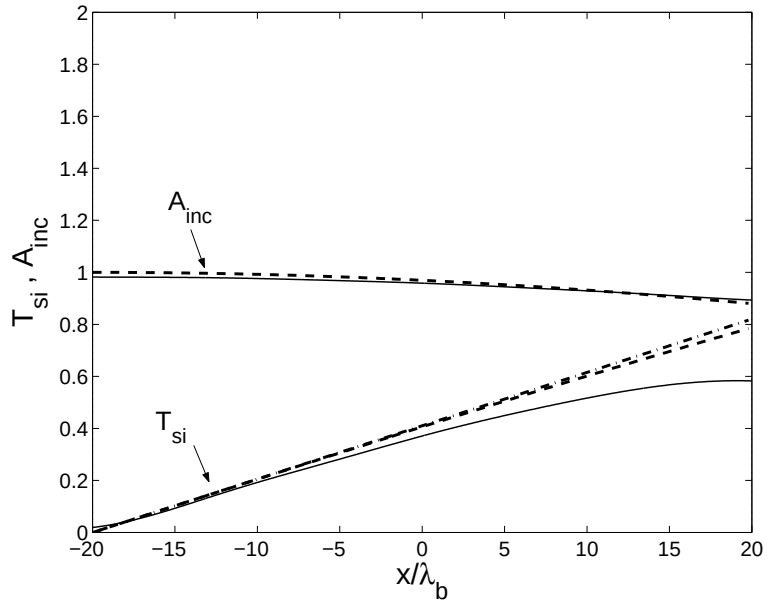

(a)

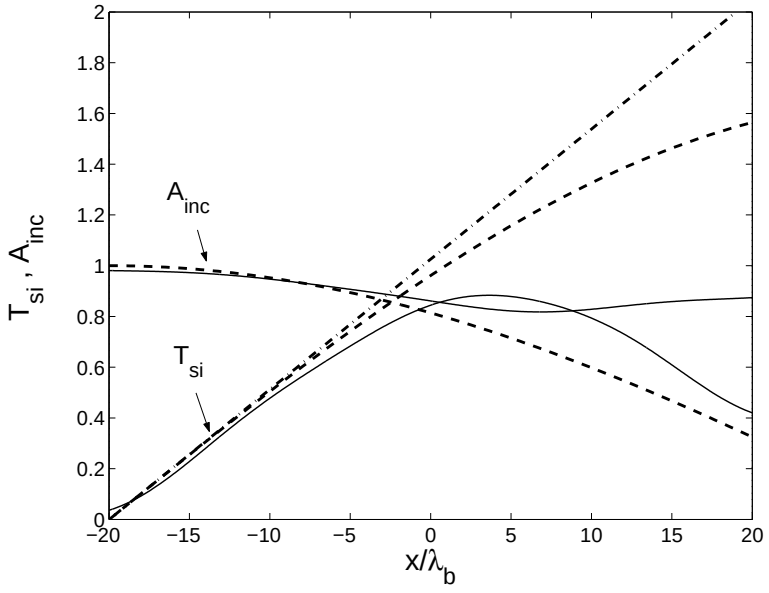

(b)

Figure 2-8: Spatial variation of the transmission coefficient of the resonance generated internal mode wave (T_{si}), and the amplitude of the incident surface mode wave (A_{inc}), over a patch of bottom ripples with (a) $\epsilon_b = 0.008$ and (b) $\epsilon_b = 0.02$ under class I Bragg resonance condition. Other physical parameters: $\mathcal{R}$=0.5, h_ℓ/h_u=1, $k_s h_u$=0.35 ($\omega^2 h_u/g = 0.19$), k_b/k_s=1.47, M_b=40, ϵ_s=0.04, and computational parameters: N=2048, M=4, $T/\Delta t$=60, and T_S/T=80. Results plotted are: numerical simulation(——), and predictions from regular perturbation (– · –) and multiple-scale analyses(- - -).

of (periodic) ripples. As computation effort increases (linearly) with M_b, the direct numerical solution of this problem using HOS eventually becomes impractical. If the interactions near the (two) edges of the bottom patch are not of primary concern, the problem can be recast in terms of the time evolution of waves travelling over a periodic domain.

Figure 2-9 shows such a case for an incident surface mode wave, where the time variations of amplitudes of the incident and resonance generated (internal mode) waves obtained by numerical simulations are compared to those from perturbation analyses. The physical parameters are: h_ℓ/h_u=1, $\mathcal{R}$=0.5, $k_s h_u$=0.35 ($\omega^2 h_u/g = 0.19$), k_b/k_s=1.47, ϵ_b=0.04 and for two incident wave steepnesses ϵ_s=0.004 and 0.04. The computational parameters for a domain satisfying periodic boundary conditions are: $L_x = 2\pi$, N=2048, M=4, $T/\Delta t$=60.

Another example for real ocean stratification of $\mathcal{R} = 0.96$ is plotted in figure 2-10. The physical parameters are: h_ℓ/h_u=0.5, $\mathcal{R}$=0.96, $k_s h_u$=0.16 ($\omega^2 h_u/g = 0.04$), ϵ_b=0.1 and for two incident wave steepnesses ϵ_s=0.0005 and 0.005. Note that although the initial surface steepness is small, since the transmission coefficient is greater than unity, the steepness of resonant internal reaches high values ($\epsilon_i > 0.2$) where the effect of nonlinearity becomes important.

The results in figure 2-9 and 2-10 display similar features to those for the spatial variations of the amplitudes over a finite patch of bottom ripples. The regular perturbation solution, which predicts a linear growth with time for the resonant wave and a constant amplitude for the incident wave, compares well with the multiple-scale analysis and the nonlinear HOS computation in the initial evolution for $t/T < 10$. Beyond the initial development, the regular perturbation solution of the resonant wave amplitude diverges as t increases while the multiple-scale analysis and HOS computation show periodic oscillatory time variations for the amplitudes of both incident and resonant waves. For relatively mild incident waves, the prediction of the multiple-scale analysis matches perfectly to the HOS computation. As the incident wave steepness increases, the HOS result deviates from the (leading-order) multiple-scale analysis prediction with decreases in both the amplitude and period of the time modulations. This effect of higher-order nonlinear interactions on the evolution appears consistent with all the other cases considered.

As in a one-layer fluid, the nonlinear interactions among the surface and interfacial waves and bottom ripples also change the dispersion relation, and, the nonlinear Bragg resonance condition for the interacting wavenumbers is shifted from that given by the linearized dis-

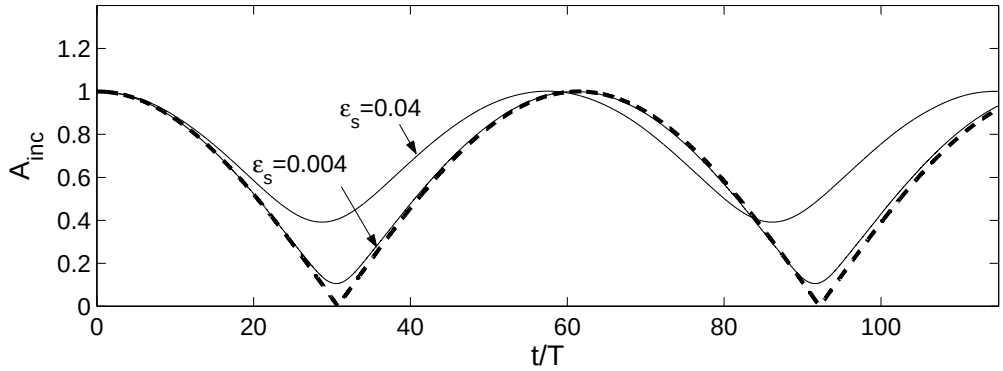

(a)

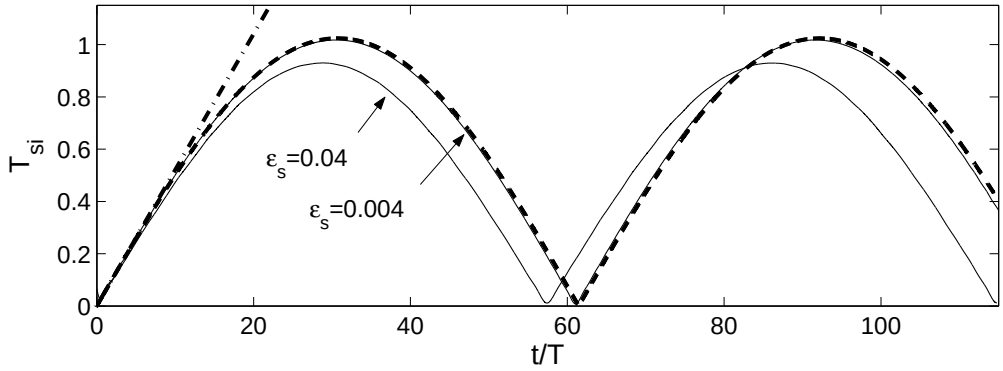

(b)

Figure 2-9: Temporal variation of (a) the amplitude of the incident surface mode wave (A_{inc}) and (b) the transmission coefficient of resonance generated internal mode wave (T_{si}) over an infinitely long patch of bottom ripples under class I Bragg resonance condition. Physical parameters are h_ℓ/h_u=1, $\mathcal{R}$=0.5, $k_s h_u$=0.35 ($\omega^2 h_u/g$ = 0.19), k_b/k_s=1.47, ϵ_b=0.04, and computational parameters: N=2048, M=4, $T/\Delta t$=60. Results plotted are: numerical simulation (——) for ϵ_s=0.004 & 0.04, and predictions from regular perturbation (– · –) and multiple-scale analyses(- - -).

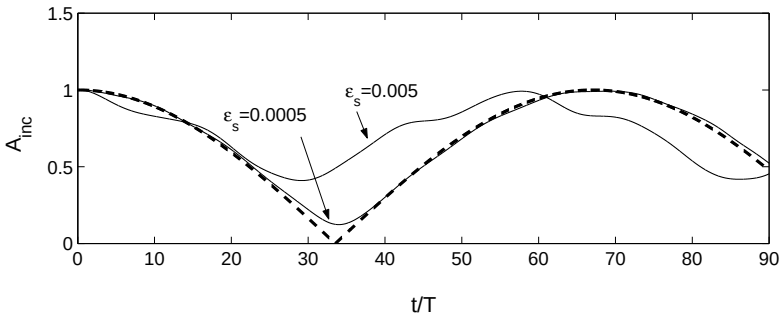

(a)

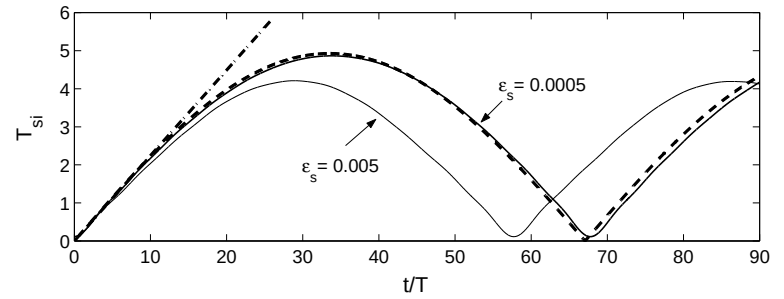

(b)

Figure 2-10: Temporal variation of (a) the amplitude of the incident surface mode wave (A_{inc}) and (b) the transmission coefficient of resonance generated internal mode wave (T_{si}) over a periodic patch of bottom ripples under class I Bragg resonance condition. Physical parameters are h_ℓ/h_u=0.5, $\mathcal{R}$=0.96, $k_s h_u$=0.16 ($\omega^2 h_u/g = 0.04$), ϵ_b=0.1, and computational parameters: N=2048, M=4, $T/\Delta t$=64. Results plotted are: numerical simulation (——) for ϵ_s=0.0005 & 0.005, and predictions from regular perturbation (derived from ALY equation 3.16, – · –) and multiple-scale analyses(ALY equation B.14, - - -).

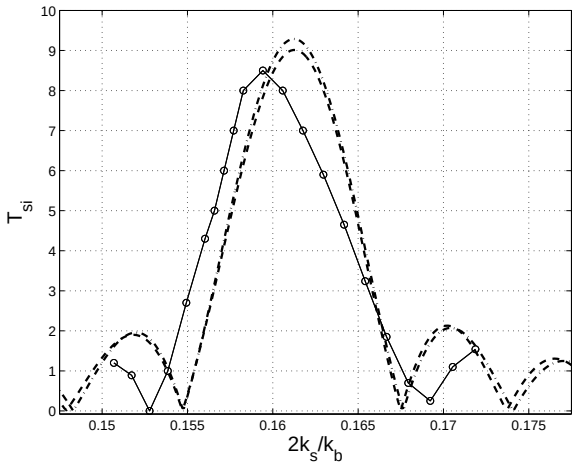

Figure 2-11: Trasnmission coefficient of the resonant internal mode wave (T_{si}) due to class I Bragg resonance as a function of wavenumber detuning $2k_s/k_b$. Physical parameters are h_ℓ/h_u=0.5, $\mathcal{R}$=0.96, $k_s h_u$=0.16 ($\omega^2 h_u/g$ = 0.04), ϵ_s=0.005, d/h_ℓ=0.1, M_b=20, and computational parameters: N=2048, M=4, $T/\Delta t$=64, and T_S/T=80. Results plotted are: numerical simulation (——) and predictions from regular perturbation (ALY equation 3.11, – · –) and multiple-scale analyses.(ALY equations 4.7 & B.26, - - -)

persion relation. To illustrate this, figure 2-11 plots the the reflection coefficient of the generated wave in the neighborhood of the class I resonance condition. Both the numerical simulation result (with M=4) and the theoretical prediction of the regular perturbation and multiple-scale analyses are shown. These results are obtained for h_ℓ/h_u=0.5, $\mathcal{R}$=0.96, $k_s h_u$=0.16 ($\omega^2 h_u/g$ = 0.04), ϵ_s=0.005, d/h_ℓ=0.1, M_b=20, and computational parameters: N=2048, M=4, $T/\Delta t$=64, and T_S/T=80. The numerical result shows the distinct down shift of the peak amplitude wavenumber $2k_s/k_b$ compared to regular and multiple-scale perturbation predictions, with a magnitude that is found to increase with the bottom steepness. As for the value of the maximum amplitude itself, the HOS result is seen to be somewhat lower than that predicted from regular perturbation and multiple-scale theory. One notes that features of the results for $I_c \xrightarrow{k_b} S_R$ including comparisons of HOS computations and perturbation analyses and higher-order interaction effects are qualitatively similar to the above for $S_c \xrightarrow{k_b} I_R$, and are not repeated.

Reflection of an inter-mode resonant wave

Consider the case of inter-mode class I Bragg resonance where the incident and resonant wave propagate in opposite directions. Again, there are two possible cases corresponding to the incident (resonant reflected) wave being (i) a surface (internal) mode ($S_c \xrightarrow{k_b} I_R$);

and (ii) an internal (surface) mode wave ($I_c \xrightarrow{k_b} S_R$).

Figure 2-12 is for the case of $S_c \xrightarrow{k_b} I_R$. The numerical result (converged with M=4) is compared with regular and multiple-scale perturbation analyses predictions of the variations of the incident and resonant reflected wave amplitudes over the rippled bottom patch. The physical parameters are: h_ℓ/h_u=1, $\mathcal{R}$=0.5, $k_s h_u$=0.45 ($\omega^2 h_u/g = 0.29$), ϵ_s=0.05, k_b/k_s=3.52, M_b=40; with computational parameters: N=2048, M=4, $T/\Delta t$=64, and T_S/T=80.

To illustrate the effect of higher-order nonlinear interactions, two bottom steepness are considered: ϵ_b=0.07 and 0.14, shown respectively in figures 2-12a and 2-12b. In this case, the resonant reflected wave amplitude increases (from zero) with distance from the down-wave edge of the bottom patch while the incident wave amplitude decreases with distance from the up-wave edge. For the smaller bottom ripple steepness case with $k_b d$=0.07, the numerical result compares well with the multiple-scale analysis prediction over the entire patch of bottom ripples. In contrast, regular perturbation analysis up to second order does not predict a decrease in the amplitude of the incident wave, and obtains a constant growth rate for the resonant wave (with a value equal to the initial growth of the multiple-scale solution). For the case with somewhat greater bottom ripple steepness, the effect of higher-order interactions in the HOS results is apparent with the multiple-scale solution appreciably overestimating the growth of the resonant wave amplitude and the decrease of the incident wave amplitude.

To illustrate the effect of nonlinearity on the dispersion relation, figure 2-13 plots the the reflection coefficient of the generated wave in the neighborhood of the class I resonance condition. Both the numerical simulation result (with M=4) and the theoretical prediction of the regular perturbation and multiple-scale analyses are shown. These results are obtained for h_ℓ/h_u=1, $\mathcal{R}$=0.5, $k_s h_u$=0.30 ($\omega^2 h_u/g = 0.14$), ϵ_s=0.03, d/h_u=0.09, M_b=40, and computational parameters: N=2048, M=4, $T/\Delta t$=64, and T_S/T=80.

similar features are observes as in figure 2-11.

Reflection of a same-mode resonant wave

Class I Bragg resonance also obtains for counter-propagating incident and resonance-generated waves of the same mode. The incident (and reflected) wave can be surface or internal mode, i.e., $S_c \xrightarrow{k_b} S_R$ or $I_c \xrightarrow{k_b} I_R$. The case of $S_c \xrightarrow{k_b} S_R$ is the direct extension

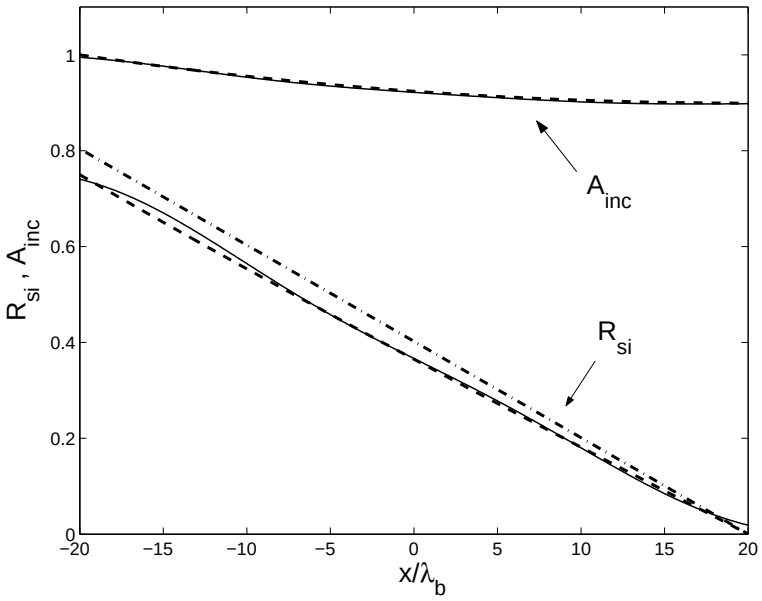

(a)

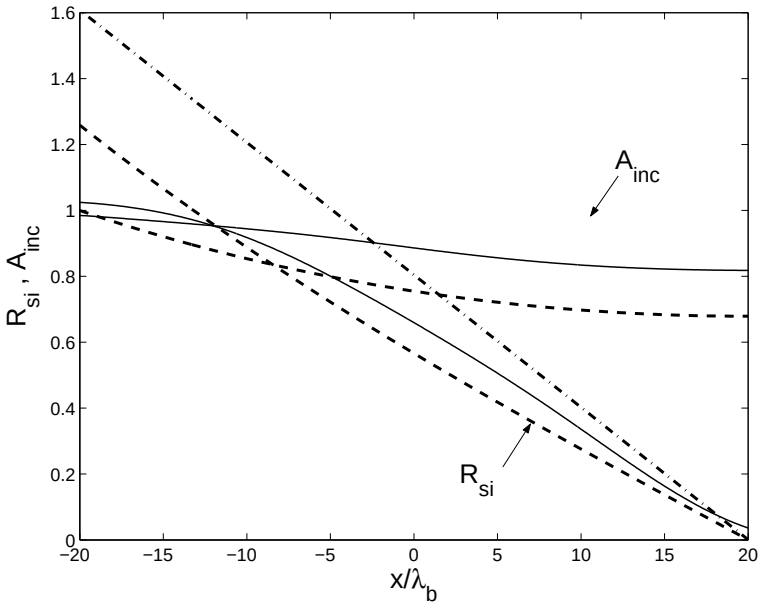

(b)

Figure 2-12: Spatial variation of the reflection coefficient of the resonant internal mode wave (R_{si}) and the amplitude of incident surface mode wave (A_{inc}) over a patch of bottom ripples under class I Bragg resonance. Physical parameters are h_ℓ/h_u=1, $\mathcal{R}$=0.5, $k_s h_u$=0.45 ($\omega^2 h_u/g$ = 0.29), ϵ_s=0.05, k_b/k_s=3.52, M_b=40, and computational parameters: N=2048, M=4, $T/\Delta t$=64, and T_S/T=80. Results plotted are: numerical simulation (——) and predictions from regular perturbation (– · –) and multiple-scale analysis (- - -) for ϵ_b = (a) 0.07, and (b) 0.14.

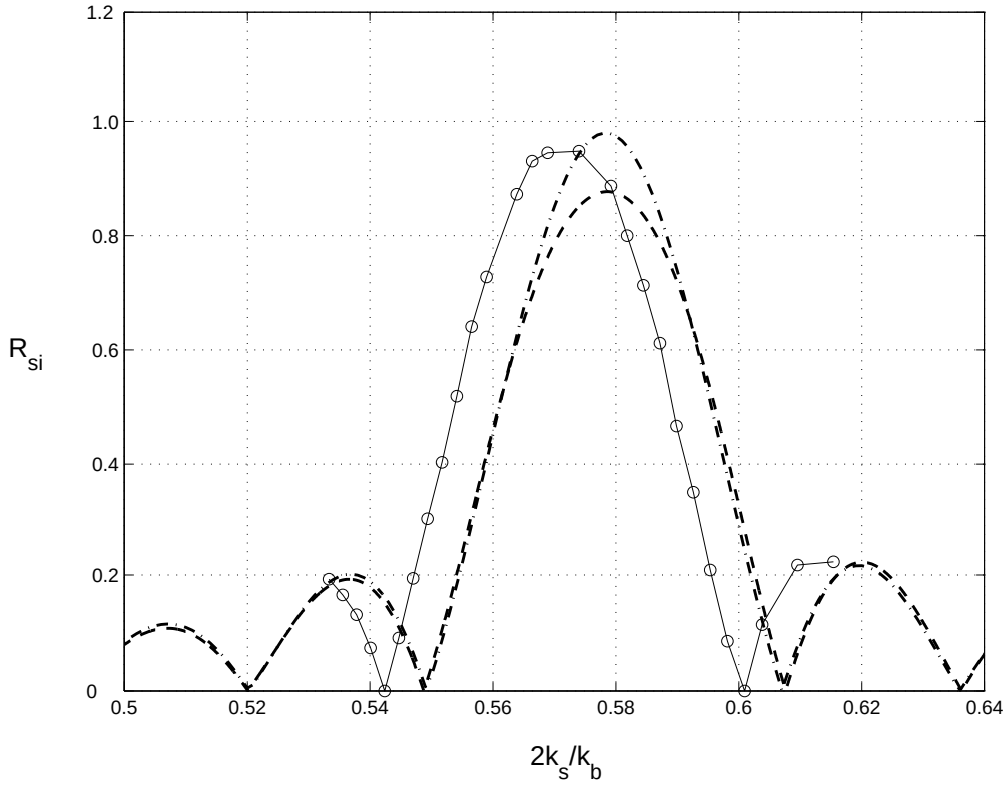

Figure 2-13: Reflection coefficient of the resonant internal mode wave (R_{si}) due to class I Bragg resonance as a function of wavenumber detuning $2k_s/k_b$. Physical parameters are h_ℓ/h_u=1, $\mathcal{R}$=0.5, $k_s h_u$=0.30 ($\omega^2 h_u/g = 0.14$), ϵ_s=0.03, d/h_u=0.09, M_b=40, and computational parameters: N=2048, M=4, $T/\Delta t$=64, and T_S/T=80. Results plotted are: numerical simulation (——) and predictions from regular perturbation (– · –) and multiple-scale analyses.(- - -)

of the class I Bragg resonance in a one-layer fluid to a two-layer fluid (e.g. Liu & Yue, 1998). As $R \to 1$ in the limit, it is confirmed that the present numerical (and chapter one theoretical) results converge to the known one-layer fluid solution.

Figure 2-14 shows the results for the case of $I_c \xrightarrow{k_b} I_R$. The variation of the amplitudes of the incident and reflected internal mode waves over a patch of bottom ripples, obtained using the HOS computation and the perturbation analyses are plotted. Physical parameters are h_ℓ/h_u=1, $\mathcal{R}$=0.5, $k_i h_u$=1.45 ($\omega^2 h_u/g = 0.42$), M_b=80, $d/h_u = 0.05$, $\epsilon_i = 0.15$; and computational parameters are N=2048, M=4, $T/\Delta t$=64, and T_S/T=80. The theoretical predictions of the regular perturbation and multiple-scale analyses at the exact Bragg condition, $2k_i/k_b$=1.0, are shown. To illustrate the detuning effect, the HOS results are obtained with four bottom wavenumbers in the neighborhood of the exact resonance condition $2k_i/k_b$=0.970, 0.987, 0.997, and 1.0. As in all other resonance cases, the regular perturbation prediction is valid for only the initial growth of the resonant wave. The multiple-scale prediction (with $2k_i/k_b$=1) compares well with the HOS result with $2k_i/k_b$=0.987. This quantifies the significant nonlinear effect in the downward shift of the position of peak resonant reflection (cf.figure 2-13).

2.4.4 Class II Bragg Resonance

Chapter one discussed the condition for class II Bragg resonance involving third-order interactions among one surface (or internal) mode wave and two bottom ripple components given by $\mathcal{D}(k_r, \omega)$=0 with $k_r = k \pm (k_{b1} + k_{b2})$, where k, k_r, k_{b1} and k_{b2} are respectively the wavenumbers of the incident wave (of frequency ω), the resonance generated wave, and the bottom ripple components. This is a direct extension of class I resonance to third order, and, as in that case, may similarly involve a resonance generated wave that is transmitted or reflected, and is in the same or different mode as the incident wave.

Figure 2-15 shows the numerical simulation result for the variation of the transmission coefficients of an incident surface mode wave and resonance generated internal mode wave over a patch of bottom ripples under the exact class II Bragg condition. The physical parameters are: h_ℓ/h_u=1, $\mathcal{R}$=0.5, M_b=26, $k_s h_u$=0.40 ($\omega^2 h_u/g = 0.24$), k_b/k_s=0.75, $\epsilon_s = 0.03$ and $\epsilon_b = 0.08$ where the bottom ripple component is counted twice in the class II Bragg resonance interaction. Computational parameters are N=2048, M=4, $T/\Delta t$=64, and T_S/T=80. For comparison, the regular perturbation prediction of chapter one is also

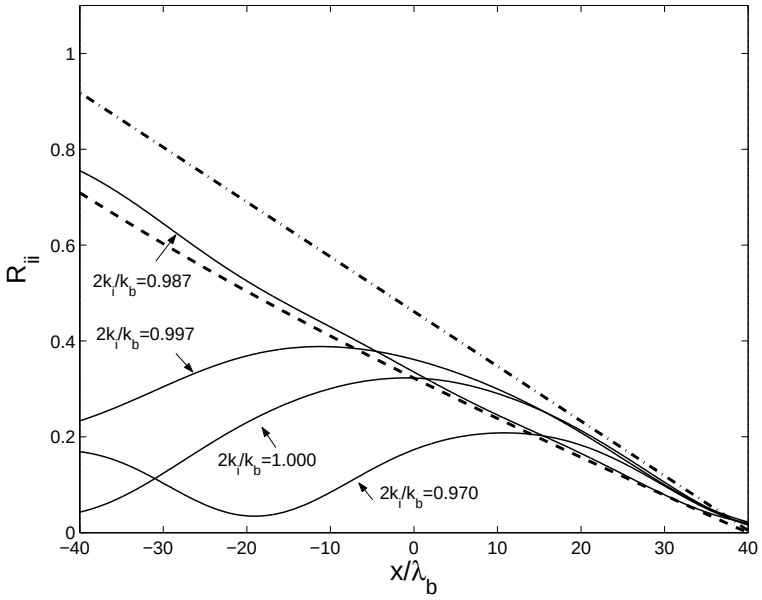

(a)

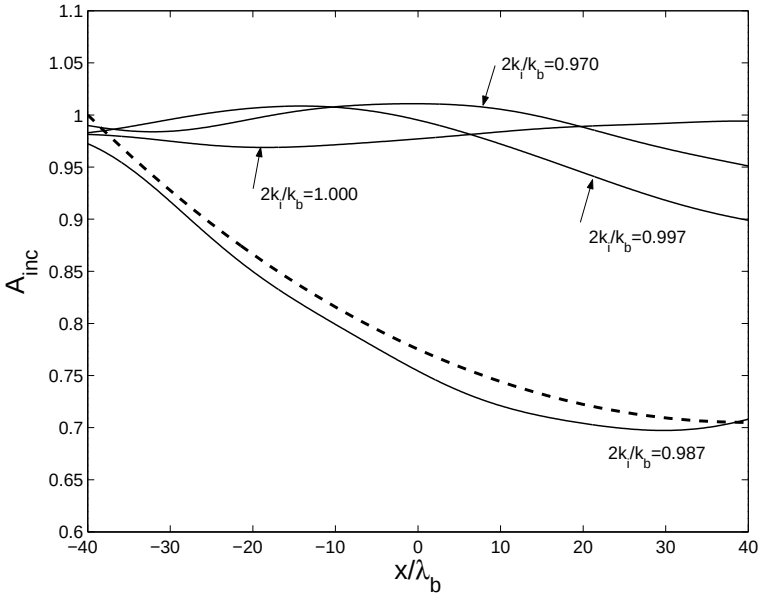

(b)

Figure 2-14: Variation of (a) the reflection coefficient of the resonant internal mode wave (R_{ii}) and (b) the amplitude of the incident internal mode wave (A_{inc}) over a patch of bottom ripples under class I Bragg resonance. Physical parameters are h_ℓ/h_u=1, $\mathcal{R}$=0.5, $k_i h_u$=1.45 ($\omega^2 h_u/g$ = 0.42), d/h_u = 0.05, ϵ_i=0.158 and bottom wavenumbers indicated in the figure, and computational parameters: N=2048, M=4, $T/\Delta t$=64, and T_S/T=80. Results plotted are numerical simulation (——) and predictions with $2k_i/k_b$ = 1.0 from regular perturbation (– · –) and multiple-scale analysis (- - -).

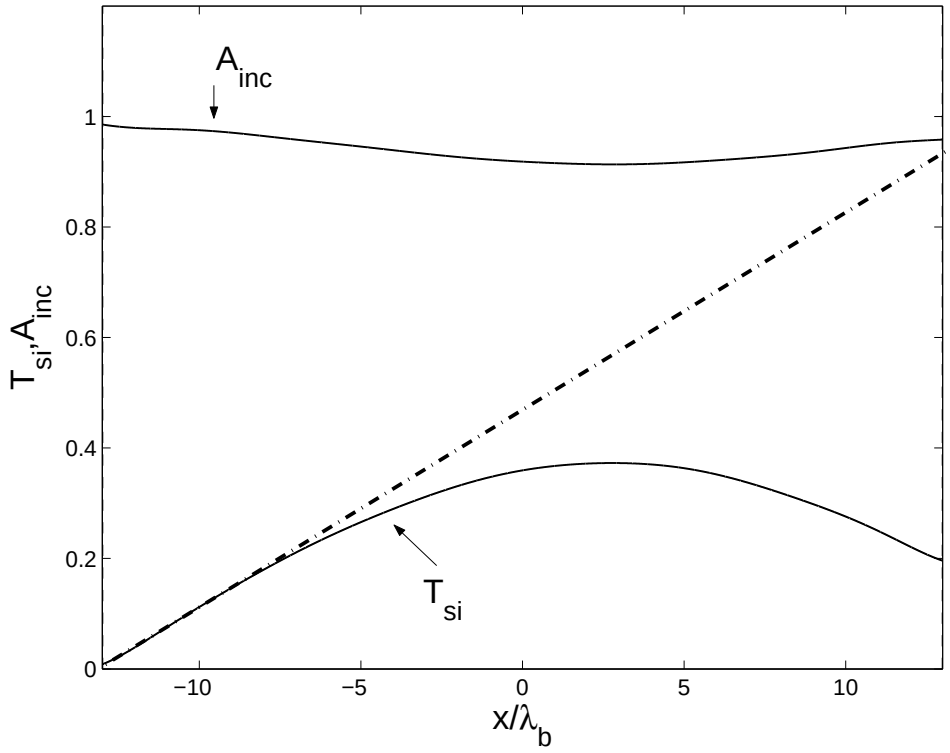

Figure 2-15: Spatial variation of the incident wave amplitude (A_{inc}) and transmission coefficient of the resonant wave (T_{si}) under the exact class II Bragg resonance condition over a bottom patch of sinusoidal ripples. Physical parameters are h_ℓ/h_u=1, $\mathcal{R}$=0.5 ($\omega^2 h_u/g$ = 0.24), M_b=26, $k_s h_u$=0.40, k_b/k_s=0.75, ϵ_s = 0.03 and ϵ_b = 0.08, and computational parameters: N=2048, M=4, $T/\Delta t$=64, and T_S/T=80. Results plotted are the prediction from regular perturbation analysis (– · –) and direct computation (——).

plotted. As expected, the numerical and perturbation results agree during the initial growth of the resonance generated wave. As the interaction distance increases, the numerical solution deviates from the straight line growth predicted by theory, and eventually decreases after reaching a maximum.

Figure 2-16 shows a similar plot but for ocean stratification of $\mathcal{R}$ = 0.96. The physical parameters are: h_ℓ/h_u=0.5, M_b=200, $k_s h_u$=0.16 ($\omega^2 h_u/g$ = 0.04), ϵ_s = 0.005 and ϵ_b = 0.05 where the bottom ripple component is counted twice in the class II Bragg resonance interaction. Computational parameters are N=2048, M=4, $T/\Delta t$=64, and T_S/T=120. Similar features are observed.

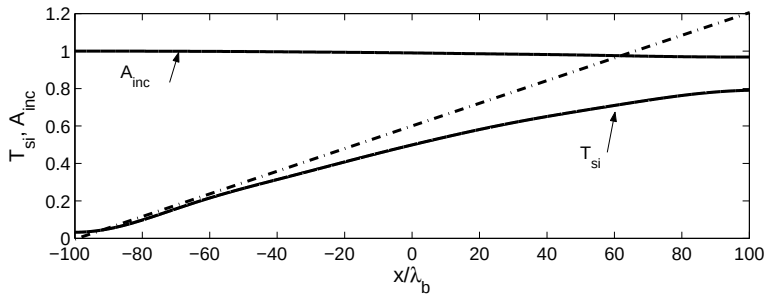

Figure 2-16: Spatial variation of the incident wave amplitude (A_{inc}) and transmission coefficient of the resonant wave (T_{si}) under the exact class II Bragg resonance condition over a bottom patch of sinusoidal ripples. Physical parameters are h_ℓ/h_u=0.5, $\mathcal{R}$=0.96 ($\omega^2 h_u/g = 0.04$), M_b=200, $k_s h_u$=0.16, $\epsilon_s = 0.005$ and $\epsilon_b = 0.05$, and computational parameters: N=2048, M=4, $T/\Delta t$=64, and T_S/T=120. Results plotted are the prediction from regular perturbation analysis (ALY equation 3.22, – · –) and direct computation (——).

2.4.5 Class III Bragg Resonance

Class III Bragg resonance occurs when two incident wave components interact with one bottom ripple component to generate a third wave. The major importance of class III Bragg resonance is that, unlike class I and II, the resonance generated wave has a frequency in general different from those of the incident waves.

Figures 2-17 shows the numerical result (with M=4) near class III Bragg resonance for the variation of amplitude of the resonance generated wave over the patch of bottom ripples. The HOS result is compared with the prediction of the third-order regular perturbation theory for two incident wave steepness: ϵ_s=0.036 and 0.064. The other physical parameters are h_ℓ/h_u=1, $\mathcal{R}$=0.5, M_b=36, $k_s h_u$=0.30 ($\omega^2 h_u/g = 0.14$), k_b/k_s=4.31, $\epsilon_b = 0.12$ and computational parameters N=2048, M=4, $T/\Delta t$=64, and T_S/T=80. In this example the single surface-mode incident wave is counted twice in the resonance quartet. Due to third order class III Bragg resonance, a reflected surface-mode wave is generated. As expected, the high-order numerical and theoretical results compare better for smaller incident wave steepness and shorter interactions (in this case of the Bragg resonance, reflected wave propagating from the down wave end of the bottom patch). Figure 2-18 shows the variation of the amplitude of the resonant reflected wave in the neighborhood of the class III Bragg resonance. The regular perturbation prediction is also shown for comparison. For comparison, two cases with different incident wave steepness ϵ_s=0.036 and 0.064 are presented. Consistent with the result in figure 2-17 and similar to the class I result in figure 2-13, the regular

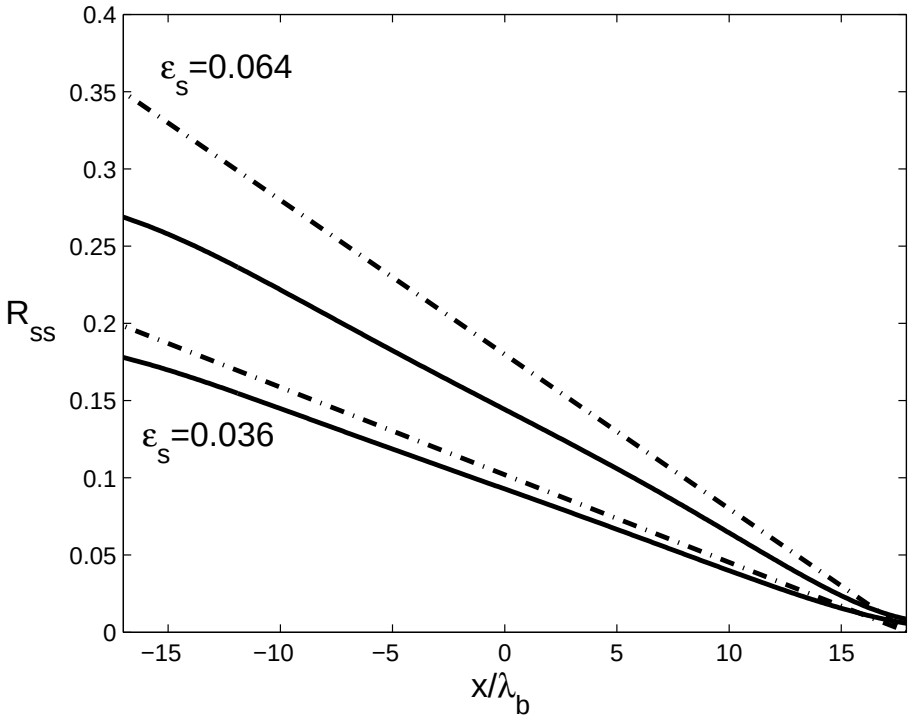

Figure 2-17: Spatial variation of the reflection coefficient of resonance generated wave (R_{ss}) under class III Bragg resonance over a patch of bottom ripples. Physical parameters are h_ℓ/h_u=1, $\mathcal{R}$=0.5, M_b=36, $k_s h_u$=0.30 ($\omega^2 h_u/g$ = 0.14), k_b/k_s=4.31, ϵ_b = 0.12 and computational parameters are N=2048, M=4, $T/\Delta t$=64, and T_S/T=80. Results plotted are the prediction from regular perturbation analysis (– · –), and direct computation (——) for $\epsilon_s = 0.036$ and $\epsilon_s = 0.064$.

perturbation theory over predicts the maximum amplitude of the reflected wave amplitude. This overprediction increases with incident wave steepness. Also similar to figure 2-13, high-order numerical results show the distinct downshift in the k_s/k_b location, relative to the exact condition predicted by leading-order theory, at which the maximum amplitude (and exact resonance) occurs. This wavenumber downshift, as expected, increases with the steepness of the incident wave. Depending on the physical parameters, a class III resonance generated wave can also be a transmitted wave. For illustration, consider a surface mode wave and an internal mode wave of the same frequency co-propagating over a patch of bottom ripples. In reality, a mixture of same-frequency co-propagating surface and internal mode waves are unavoidable when a wave maker excites a two-layer density stratified fluid at a given frequency. Now if the bottom ripples contain a wavenumber component that satisfies the class III Bragg condition, a wave at twice the frequency of the incident wave(s) will be resonated. As an example, consider the case where the resonant transmitted wave is an internal mode wave. For the numerical simulation h_ℓ/h_u=1, $\mathcal{R}$=0.5, $k_s h_u$=0.40 ($\omega^2 h_u/g = 0.25$), k_i/k_s=2.50, $k_s a$=0.03, $M_b = 10$, k_b/k_i=1.50, $\epsilon_b = 0.42$ and b/a=1.70 where a is the surface amplitude of the surface mode incident wave and b is the interfacial amplitude of the internal mode wave. Computational parameters are N=2048, M=4, $T/\Delta t$=64, $T_s/T = 120$.

Figure 2-19 shows the spatial variations of the amplitudes of incident surface-mode and internal mode waves and the resonant internal mode transmitted wave over the bottom ripple patch. The amplitude of the resonance generated wave increases with the interaction distance in the cost of decreases in the amplitude of the two incident waves. To conclude this subsection, consider the class III Bragg resonance over a very long patch of bottom ripples. Similar to figure 2-9, problem is cast in terms of the (long) time evolution of the waves over a periodic rippled bottom domain. As an illustration, consider two internal mode incident waves with $\omega_1^2 h_u/g = 0.19$, $\omega_2/\omega_1 = 0.62$ ($k_{i1}h_u$=0.86, k_{i2}/k_{i1}=0.59), $k_{i1}b_1$=0.02, and b_2/b_1=1.70. The two-layer fluid has h_ℓ/h_u=1 and $\mathcal{R}$=0.5. For the bottom ripple, $\epsilon_b = 0.02$ is used, and the wavenumber is chosen to be k_b/k_{i1}=0.27 such that resonant interaction between two right-going internal mode waves generates a right-going surface mode wave with wavenumber $k_r = k_s = k_{i1} - k_{i2} - k_b = 0.13/h_u$ and frequency $\omega_r^2 h_u/g = 0.03$. Note that the wavelength of the generated surface wave is much shorter than those of two incident internal waves. Computational parameters are N=2048, M=4, $T/\Delta t$=64. Figure 2-20

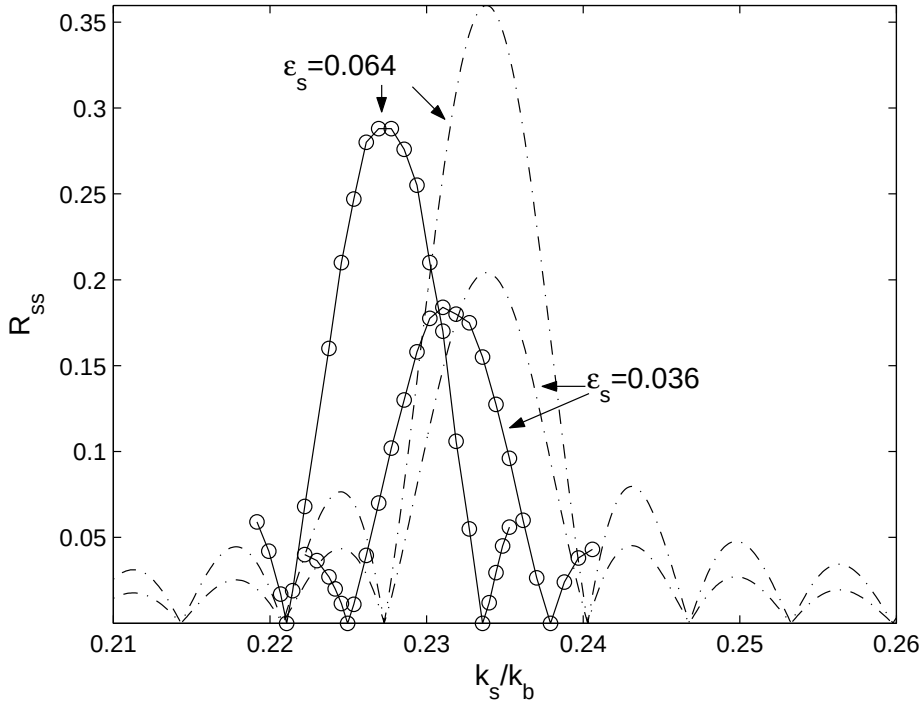

Figure 2-18: Class III sub-harmonic Bragg reflection coefficient (R_{ss}) in the neighborhood of the linearized Bragg resonance condition ($k_s/k_b = 0.234$). Physical parameters are h_ℓ/h_u=1, $\mathcal{R}$=0.5, M_b=36, $k_s h_u$=0.30 ($\omega^2 h_u/g = 0.14$), d/h_u=0.09, and computational parameters: N=2048, M=4, $T/\Delta t$=64, and T_S/T=80. Results plotted are numerical simulation (——) and prediction from regular perturbation analysis (– · –) for two incident steepnesses $\epsilon_s = 0.036$ and $\epsilon_s = 0.064$.

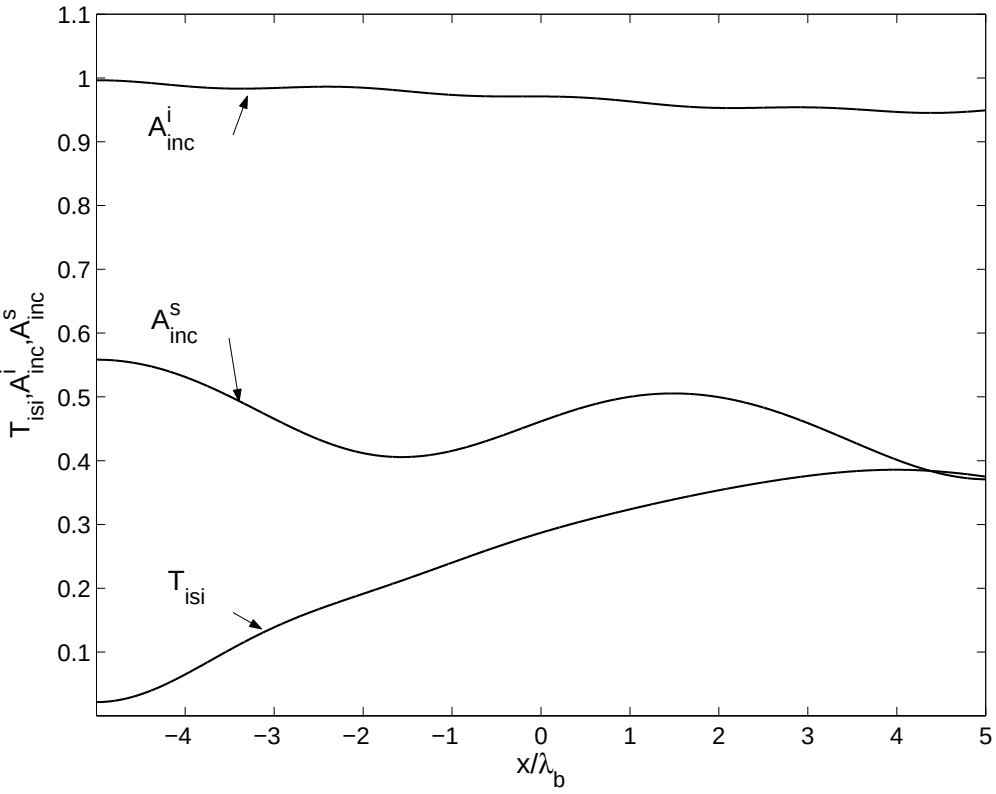

Figure 2-19: Spatial variation of the amplitudes of incident surface mode and internal mode waves (A^s_{inc}, A^i_{inc}) and transmission coefficient of the resonant internal mode wave (T_{isi}) under class III Bragg resonance over a patch of bottom ripples. Physical parameters are h_ℓ/h_u=1, $\mathcal{R}$=0.5, $k_s h_u$=0.40 ($\omega^2 h_u/g$ = 0.25), k_i/k_s=2.50, $k_s a$=0.03, b/a=1.70, , k_b/k_i=1.50, ϵ_b = 0.42; and computational parameters: N=2048, M=4, $T/\Delta t$=64 and T_s/T=120. Amplitudes are normalized by the interface amplitude of the incident internal mode wave b.

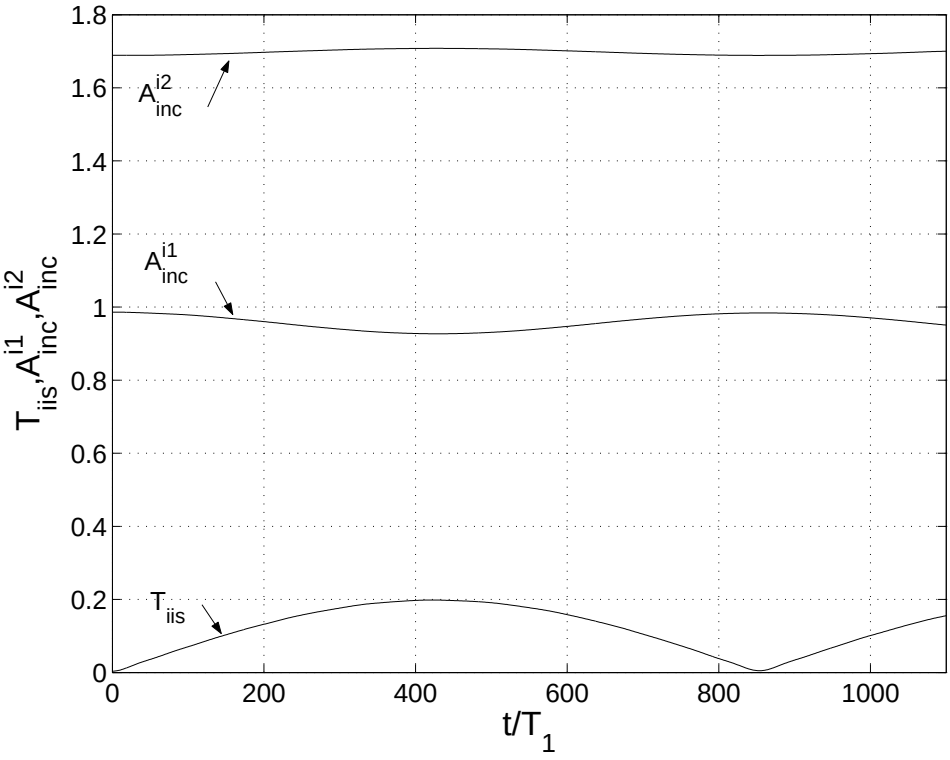

Figure 2-20: Time variation of the amplitudes of the incident internal mode waves ($A^{i1}_{inc}, A^{i2}_{inc}$) and the resonant surface mode wave (T_{iis}) under class III Bragg resonance over an infinitely long patch of bottom ripples. Physical parameters are h_ℓ/h_u=1, $\mathcal{R}$=0.5, $\omega_2/\omega_1 = 0.62$, ($k_{i1}h_u$=0.86, k_{i2}/k_{i1}=0.59), $k_{i1}b_1$=0.02, b_2/b_1=1.70, k_b/k_{i1}=0.27, $\epsilon_b = 0.02$; and computational parameters: N=2048, M=4, $T_1/\Delta t$=64. Amplitudes are normalized by the incident internal wave amplitude b_1.

shows the simulation result for the time variation of the amplitudes of the incident and resonant waves. It is seen that a transmitted surface wave of appreciable amplitude can be developed over a long evolution.

As the last example we numerically consider the last case of previous chapter (illustrative case studies) where two incident surface mode waves upon interacting with bottom undulations resonate an internal mode wave ($S_{c1}+S_{c2} \xrightarrow{k_b} I_R$). Numerical simulation is performed in time domain (over a long patch) and with the physical parameters: h_ℓ/h_u=0.42, $\mathcal{R}$=0.96, $k_{s1}h_u$=4.3 ($\omega^2 h_u/g = 4.3$) , $k_{s1}a_{s1}$=0.2 , k_{s2}/k_{s1}=0.84 , $k_{s2}a_{s2}$=0.2 , and ϵ_b=0.2, and computational parameters: N=2048, M=4,5, and $T/\Delta t$=64. Figure 2-21 shows the growth of the amplitude of resonance generated internal mode wave due to Class III Bragg resonance.

In a realistic ocean situation, the above result can be interpreted as follows. In a total

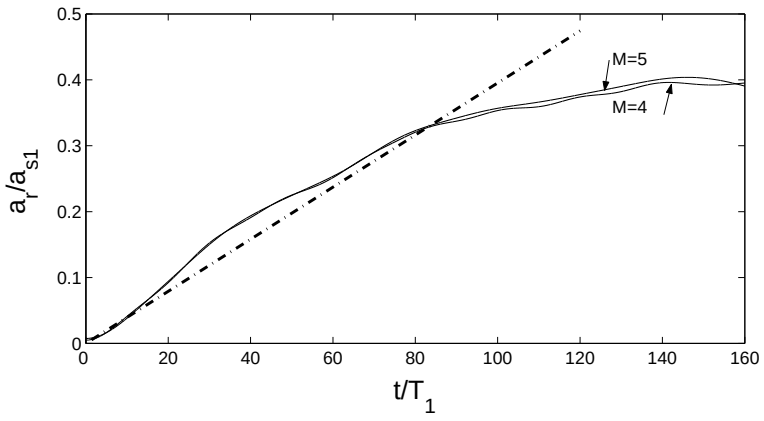

Figure 2-21: Comparison of the regular perturbation result and numerical simulation performed by HOS for resonant internal wave generation under Class III Bragg resonance ($S_{c1} + S_{c2} \xrightarrow{k_b} I_R$). Physical parameters are h_ℓ/h_u=0.42, $\mathcal{R}$=0.96, $k_{s1}h_u$=4.3 , $k_{s1}a_{s1}$=0.2 , k_{s2}/k_{s1}=0.84 , $k_{s2}a_{s2}$=0.2 , ϵ_b=0.2, and computational parameters: N=2048, M=4,5, $T/\Delta t$=64.

water depth of $H = 100m$ with the themocline at $h_u = 70m$, two typical ocean surface waves with periods $T_{s1}, T_{s2} = 8.00, 8.75$ *sec* and amplitudes $a_{s1} \sim a_{s2} \sim 3m$ in the presence of bottom ripples of $\lambda_b \sim 160m$ and amplitude $d \sim 5m$, can resonate a train of relatively high-frequency internal waves ($T \sim 2$ *min*) with amplitude up to $a_r \sim 1.5$ *m*. The generated interfacial wave moves in the opposite direction of incident waves and hence scatters back the forward traveling energy of the incident waves.

Features of higher nonlinearity effects are qualitatively similar to those of Class I.

2.4.6 Multiple Resonance

In practical applications, the incident wavefield and/or the bottom topography contain multiple components and combinations that may satisfy the resonance conditions. As these resonant waves are generated, they themselves may satisfy and engage in multiple resonances with the incident/bottom components. While theoretical considerations such as those in previous chapter provide valuable guidance and fundamental understanding (and results for comparisons for specific cases such as those considered above), extensions beyond these becomes very complex and the general problem is intractable. This is one of the main objectives for the development here of the direct numerical simulation capability.

As illustration, we consider a generalized but still relatively simple problem where an incident wave composed of two linearly superimposed wave-trains interacts with a rippled

bottom containing two wavenumber components. Our interest is the features associated with the development of multiple resonances and long-time evolutions. For specificity, we choose a configuration with h_ℓ/h_u=2.3, $\mathcal{R}$=0.96, and two surface-mode incident waves with $k_{s1}h_u$=0.26 ($\omega_{s1}^2 h_u/g = 0.19$), $\epsilon_{s1} = 0.03$, and, $k_{s2}h_u$=0.24 ($\omega_{s1}^2 h_u/g = 0.15$), $\epsilon_{s1} =$ 0.01. We consider a bottom ripple patch containing two wavenumber components with dimensionless wavenumbers $k_{b1}h_u$=0.25 and $k_{b2}h_u$=0.20 and $k_{b3}h_u$=0.77 and with the same bottom component amplitudes d/h_ℓ=0.2.

For these conditions, it is seen that $k_{s1} - k_{s2} + k_{b1}$=k_{it} and $k_{s1} - k_{s2} - k_{b2}$=k_{ir} (both with the frequency ω_i=$\omega_{s1} - \omega_{s2}$) satisfy class III Bragg resonance condition with the resonance generated internal-mode wave with wavenumber $k_{it}h_u$=$k_{ir}h_u$=0.22. With these new internal-mode wave and the same bottom components, at the forth order, two new resonances occur:

$$k_{s5} = k_{s1} + k_{ir} + k_{b1} = 0.30/h_u \ , \qquad \omega_{s5} = 2\omega_{s1} - \omega_{s2} \tag{2.4.35}$$

and

$$k_{s6} = k_{s2} - k_{it} + k_{b2} = 0.21/h_u \ , \qquad \omega_{s6} = 2\omega_{s2} - \omega_{s1} \tag{2.4.36}$$

Note that resonant energy exchange may also occur near the exact resonance points (cf. figures 2-13). In this case, for instance, the combination of the incident wave k_{s1} and k_{b1} at the third order gives $k_{s1} - 2k_{b1} = -0.24/h_u$ with associated frequency ω_{s1} that does not satisfy the dispersion relation, but is very close to the pair $(-k_{s1}, \omega_{s1})$ which is a resonance point and therefore permits resonant energy exchanges. Figure 2-22 shows the location of the component of this example on Ball's diagram for the dispersion relationship. In a direct numerical simulation, we use, as initial conditions, the exact solution for the incident surface wave, and computational parameters $N = 1024$, $M = 6$ and dimensionless domain length $L_x = 2\pi$. Figure 2-23 shows the growth of the amplitudes of the resonance generated waves of k_i, k_{s5} and k_{s6} during the initial stage of the evolution ($t < 100T$). Modulation in time can be observed in the incident and resonance generated waves. A rough correlation can be seen between the minimum of the amplitude of the incident wave and maximum of the amplitude of the resonance generated waves.

Figure 2-24 plots the spectrum of the nonlinear wavefield at $t = 100T$, in which all wave

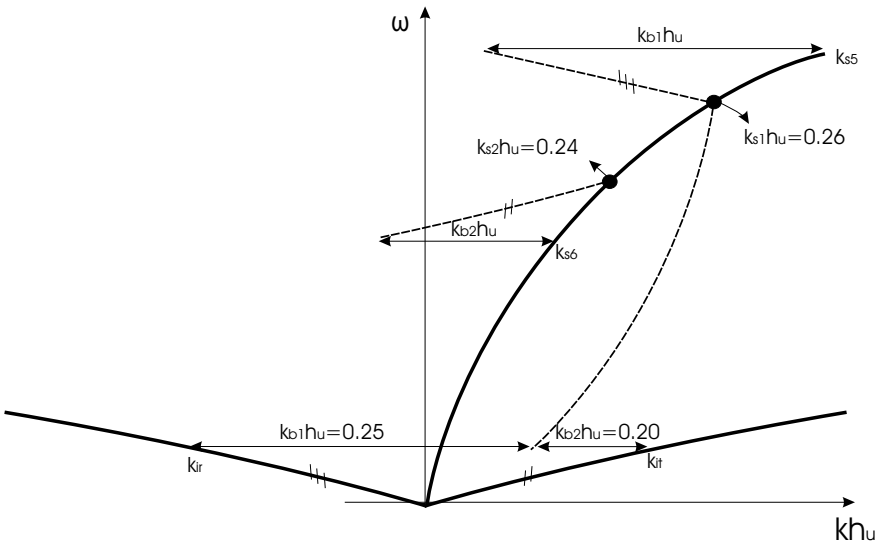

Figure 2-22: Location of multiple resonance points on Ball's diagram.

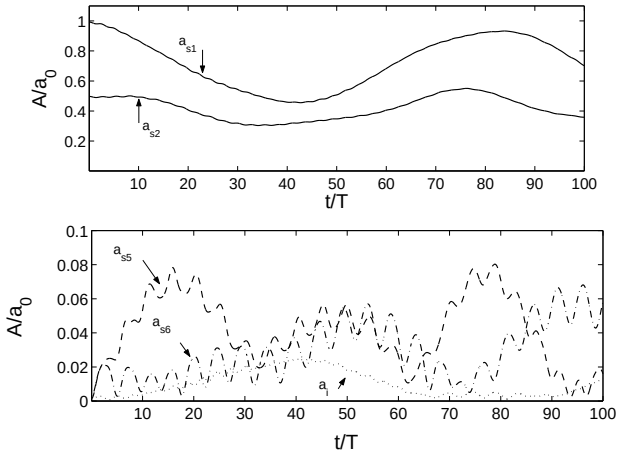

Figure 2-23: Time variation of the amplitudes of the incident waves (——) and resonance generated waves with wavenumbers k_r=k_{ir}=$k_{s1}-k_{s2}-k_{b1}$ and k_r=k_{it}=$k_{s1}-k_{s2}+k_{b2}$ ($\cdot\ \cdot\ \cdot$); k_r=k_{s5}=$k_{s1}+k_{ir}+k_{b1}$ (- - -); and k_r=k_{s6}=$k_{s2}-k_{it}+k_{b2}$ ($-\cdot-$).

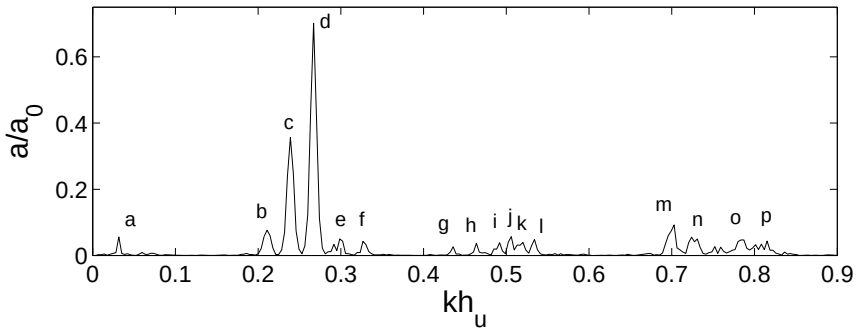

Figure 2-24: Amplitude spectrum of the waves at $t/T = 100$. The letters a-p in the figure indicate wave components with wavenumbers: a, $k_{s1} - k_{s2}$; b, k_{s6}; c, k_{s2}; d, k_{s1}; e, k_{s5}; f, $3k_{s1} - 2k_{s2}$; g, $k_{s2} + k_{b2}$; h, $k_{s1} + k_{b1}$; i, $k_{s2} + k_{b1}$; j, $k_{s1} + k_{s2}$; k, $k_{s1} + k_{b1}$; l, $2k_{s1}$; m, $3k_{s2}$; n, $2k_{s2} + k_{b1}$; o, $3k_{s1}$; and p, $4k_{s1} - k_{s2}$. All wave amplitudes are measured on the free surface.

components including both free and locked waves are identified. Note that some of the locked waves are close to the resonant points, and can then be significantly developed in the evolution. Because of this, the wavefield becomes increasingly complex as the nonlinear interactions continue. Figure 2-25a shows the time evolution of the amplitude of the first incident surface mode wave (a_{s1}) and the resonant internal mode wave (a_i, associated with the class III Bragg resonance). After some regular oscillations during which energy is exchanged between waves (as expected from the perturbation analysis), the variation of the amplitudes of these waves starts to behave irregularly at $t/T \sim 1500$. The loss of order can also be seen in the frequency amplitude spectrum of the free-surface elevation, figure 2-26, for the free-surface elevation at a fixed point x=0 in the time period $2500 < t/T < 3500$. The energy of the wavefield, initially confined to two incident free waves (and their higher-order locked-wave harmonics), is now distributed, by multiple resonance and near-resonance interactions with the bottom ripples and amongst waves, to cover a broad-band spectrum. For comparison, and as an independent check, the spectrum of the wavefield evolved over the same time with the same initial condition but a flat bottom is obtained also by direct HOS simulation and shown. Figure 2-27 is the evolution of the amplitude of the incident surface mode wave (counterpart of figure 2-25a) when there is no stratification (i.e. $\mathcal{R}$=1). As can be seen, in the same time frame no (qualitative) loss of order is observed. To quantify the chaotic behavior of the wave motion, we compute the Lyapunov exponent of this system. We obtain the maximum Lyapunov exponent from the motion history of points on the free surface following classical methods (e.g., Argyris *et al.*, 1994). Figure 2-28 shows the

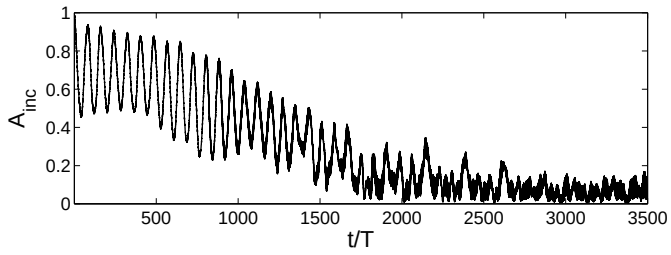

(a)

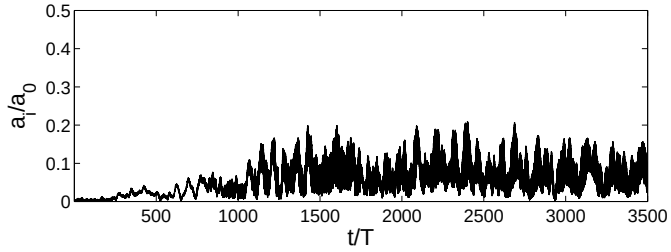

(b)

Figure 2-25: Time variation of the amplitudes of (a) the incident wave (a_{s1}/a_0) and (b) the resonant internal mode wave (a_i/a_0) with wavenumber $k_i h_u = 0.22$.

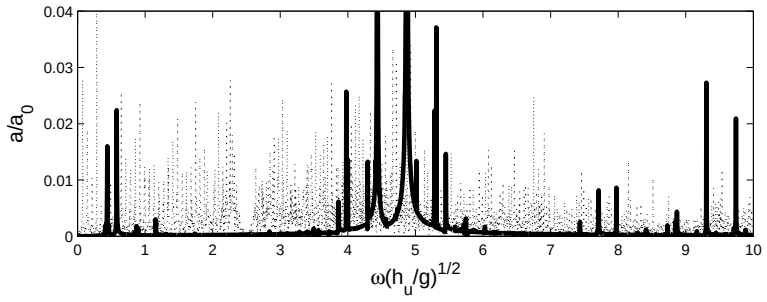

Figure 2-26: Frequency amplitude spectrum of the free-surface wave elevation at a fixed location in the wave domain with a flat bottom (——) and a rippled bottom ($\cdot\ \cdot\ \cdot$).

time evolution of this maximum Lyapunov exponent. The exponent becomes positive after a short initial phase of evolution and approaches an asymptotic (constant) value of $\lambda_{max} \simeq 0.9$ as the evolution continues. In contrast, in the case of uniform depth or no stratification ($\mathcal{R}$=1), this Lyapunov exponent is non-positive and reaches zero asymptotically.

The observed features of multiple resonances among surface/internal/bottom wave components leading to chaotic wave motion are found to obtain for broad ranges of physical parameters. In particular, as the stratification strengthens, the time to chaotic motion decreases and the strength of the chaotic behavior increases. Figure 2-28b shows the maximum Lyapunov exponent for a case with $\mathcal{R}$=0.5 involving initially a single surface-mode

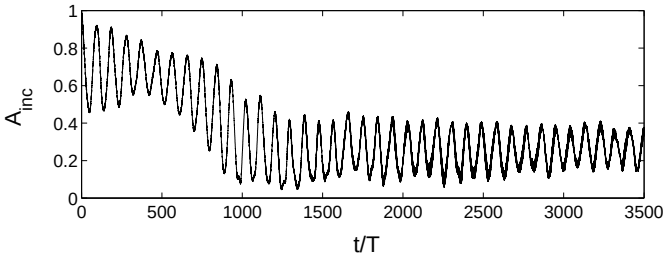

Figure 2-27: Time variation of the amplitudes of the incident wave (A_{inc}=a_{s1}/a_0) for the same setup as in figure 2-25a but with $\mathcal{R} = 1$

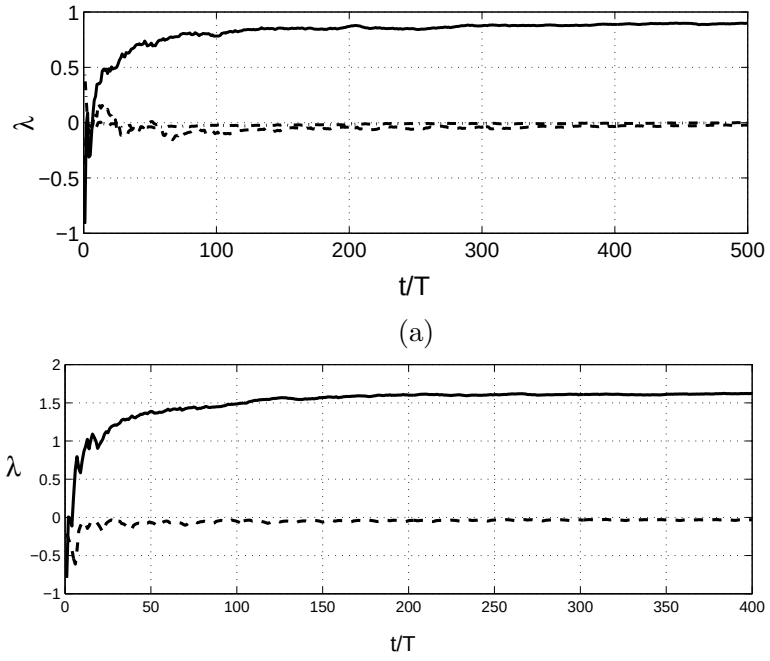

Figure 2-28: Maximum lyapunov exponent as a function of time for a flat bottom (- - -) and a rippled bottom (——) for (a). $\mathcal{R}$=0.96 example, compared also with no stratification ($\mathcal{R} = 1$, – · –) case and (b). $\mathcal{R}$=0.5 example

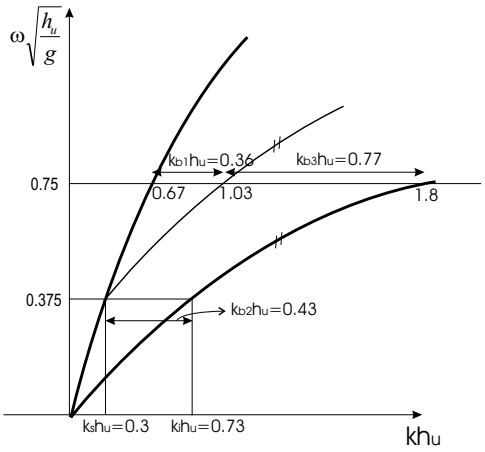

Figure 2-29: Location of multiple resonance points on Ball's diagram.

incident wave (with h_ℓ/h_u=1, k_sh_u=0.30, $\epsilon_s = 0.03$) traveling over a bottom ripple patch containing multiple wavenumber components. The conjugate of this incident wave is an internal-mode wave with wavenumber k_ih_u=0.73. Multiple resonances involving different Bragg mechanisms occur for select sets of bottom component wavenumbers. Figure 2-28b corresponds to a case of a bottom with three wavenumbers given by $k_{b1}h_u$=0.36, $k_{b2}h_u$=0.43 and $k_{b3}h_u$=0.77 and with the same dimensionless amplitude d/h_u=0.094.

For these conditions, it is seen that $k_s + k_{b2}$=k_i satisfies a class I Bragg resonance condition with the resonance generated internal-mode wave with wavenumber k_ih_u=0.73 (see figure 2-29). With this new internal-mode wave and the other two bottom components, two class III Bragg resonances occur k_{s3}=$k_s + k_i - k_{b1}$=$0.67/h_u$ (ω_{s3}=2ω) and k_{i3}=$k_s + k_i + k_{b3}$=$1.8/h_u$ (ω_{i3}=2ω) where subscripts $s3, i3$ refer to third-order resonant surface-mode and internal-mode waves. At the fourth order, the interaction among the incident wave k_s, the generated internal wave k_i and two ripple components (k_{b1} and k_{b2}) is nearly resonant and generates an internal-mode wave component with wavenumber k_{i4}=$k_s + k_i + k_{b1} + k_{b2}$=$1.82/h_u$ (ω_{i4}=2ω).

Figure 2-30 shows the time evolution of the amplitude of the incident surface mode wave and the transmitted resonant internal mode wave in this example. Here the variation of the amplitudes of these waves starts to behave irregularly at a much shorter time of $t/T \sim 200$ (c.f. figure 2-25a). Figure 2-28b shows that the steady state value of the maximum Lyapunov exponent is higher than that for $\mathcal{R} = 0.96$ case which is an indication of higher strength chaotic behavior.

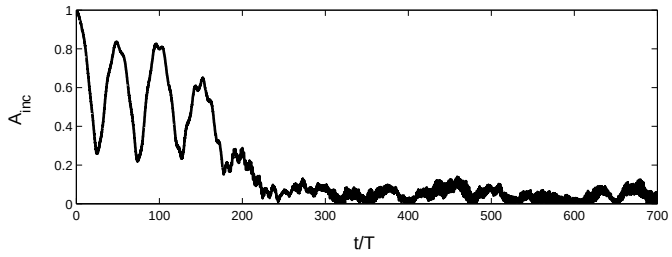

(a)

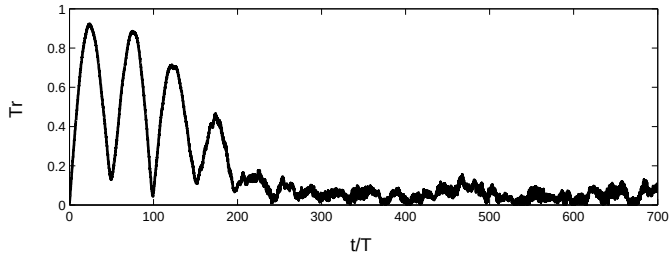

(b)

Figure 2-30: Time variation of the amplitudes of (a) the incident wave (A_{inc}) and (b) the transmitted class I resonant internal mode wave (T_r) with wavenumber $k_i h_u = 0.73$ and frequency $\omega^2 h_u/g = 0.14$.

2.5 Conclusion

To complement the perturbation analyses of chapter one, an efficient and accurate computational method is developed for the study of general nonlinear interactions of surface/interfacial waves with variable bottom topography in a two-layer density stratified fluid. The method is based on the extension, to include interfacial waves, of a powerful high-order spectral (HOS) method originally developed for the study of nonlinear gravity wave-wave and wave-bottom interactions in a homogenous fluid. The method developed here accounts for nonlinear interactions of surface/interfacial waves with bottom ripples up to an arbitrary high order M and, as with the original HOS, achieves an exponential convergence with respect to the number of spectral modes modes N used (for the surface, interfacial and bottom), and an almost linear computational effort with respect to N and M. Systematic validation and convergence tests are performed including the directed comparison to the exact solution of a fully-nonlinear two-layer Stokes wave.

The numerical method is used to study a number of canonical problems corresponding to different classes of Bragg resonances and the results are compared to the perturbation results of chapter one for these cases. The comparisons are excellent within the region

of validity of the perturbation results, deviating typically for longer interaction distance and greater wave/bottom steepness, highlighting the importance of (even) higher-order nonlinear interactions not accounted for in the theory.

As a final example, a more general but still relatively simple case is considered involving a single (two-layer) incident wave propagating over a rippled bottom containing three wavenumber components. By selecting these wavenumbers, conditions for multiple resonances obtain with the resulting evolution leading to the creation of many new Bragg transmitted/reflected waves and eventually chaotic motion after some time.

Chapter 3

Waves due to an oscillating and translating disturbance in a two-layer density stratified fluid

3.1 Introduction

The linear problem of wave generation and propagation by a submerged disturbance, when it translates with a constant speed while its strength is sinusoidally oscillating in time, is considered analytically and numerically in a two-layer density stratified fluid. Understanding of waves due to the motion of a submerged body has practical applications ranging from non-acoustic detection of underwater vehicles Wei *et al.* (2005), to seakeeping and wave load calculations on moored/floating offshore structures. In stratified waters, and particularly in littoral zones, it can help understanding of generation of internal gravity waves. Inversely, density stratification hence ocean-body composition can be found from the wake pattern behind a moving object Avital & Miloh (1999, 1994).

In a homogeneous fluid, the linear two-dimensional problem of far-field waves created by an oscillating and translating disturbance was studied by Haskind (1954)(see also Wehausen & Laitone (1960)), followed by others who included effects of nonlinearity and considered the asymptotic behaviors near the critical frequency (see for example Akylas (1984*a*),Akylas (1984*b*),Liu & Yue (1993),Palm & Grue (1999)).

For a two-layer density stratified fluid, the steady flow past a submerged obstacle is well

studied (see e.g. the monograph by Baines (1997) where the rigid-lid assumption is used). In the presence of a free surface and deep lower layer, Voitsenya (1958) derived the three-dimensional potential for a pulsating source and a vortex. For the same setup, Hudimac (1961) showed that a moving ship generates an internal-wave system similar to the surface Kelvin waves. For speeds less than a critical speed, the internal ship wave consists of both transverse and divergent waves, while above that critical speed, only divergent wave persists Crapper (1967); Sharman & Wurtele (1983).

For finite stratified layer depths, Yeung & Nguyen (1999) obtained the Green function for a constant strength source moving with steady speed in the upper layer. These results are extended, theoretically and experimentally, by Wei *et al.* (2005) to a dipole located in the lower layer. For a two semi-infinite fluids, Lu & Chwang (2005) derived analytical expressions for the three dimensional interfacial waves due to a fundamental singularity (see Appendix D).

The present chapter is motivated by the possibility of observing surface and internal disturbance associated with ships and submarines in strong stratified waters such as in warm littoral zones. Here the general two- and three-dimensional problem of wave generation by an oscillatory source translating with steady forward speed in a two-layer density stratified fluid is considered. Depending on the Froude number and dimensionless frequency of the motion, and the ratios of depths and densities of the two layers, up to eight distinct far-field free waves obtain, and, for sufficiently small forward speed, two of these can advance ahead of the source.

The formulation of the problem is given in §3.2, followed by a kinematic analysis based on the dispersion relation which obtains the wavenumber and frequency of the far-field waves. To obtain the amplitudes of these waves and information in the near field, the boundary-value problem for the Green function is solved in two and three dimensions. The Green functions differ depending on whether the source is located in the upper or lower fluid , and their dependencies on the physical parameters are discussed. In the limit of deep fluid layers, the Green function simplifies substantially and each of the wave components can be worked out explicitly. In the last section, an efficient numerical scheme for the general problem of possibly multiple disturbances with time-varying speeds and motion frequencies is developed. The algorithm is the extension of a high-order spectral method originally developed to simulate nonlinear gravity wave-wave interactions Dommermuth &

Yue (1987), which obtains exponential convergence with the number of spectral modes. The numerical method of course provides independent validation of the earlier analysis. This is performed in §4.2 for the near- and far-field waves.

3.2 Problem Formulation

Consider a two-layer density stratified fluid where the upper and lower fluid layers have respectively mean depths h_u and h_ℓ, and fluid densities ρ_u and ρ_ℓ (density ratio $\mathcal{R} \equiv \rho_u/\rho_\ell$). Hereafter, subscript u/ℓ denotes quantities associated with the upper/lower fluid layers. In a Cartesian coordinate system with x, y-axis on the mean free surface and z-axis positive upward, the two-layer fluid rests on a flat horizontal bottom $z = -h_u - h_\ell$ and have surface and interface elevations $\eta_u(x, y, t)$ and $\eta_\ell(x, y, t)$ respectively.

Consider a point source with pulsating strength $m = m_0 \cos \omega_0 t$, moving with forward speed $\mathbf{u} = U\hat{i}$, located at a fixed (mean) depth $z = z_0$. Assume that the fluids in both layers are homogeneous, incompressible, immiscible and inviscid so that the fluid motion is irrotational. The effect of surface tension is neglected. The flow in each layer is described by a velocity potential, $\phi_u(x, y, z, t)$ and $\phi_\ell(x, y, z, t)$. In a frame of reference fixed with still water at infinity, the linearized governing equations are:

$$\nabla^2 \phi_u = m_0 \; \delta(x_0 + Ut, 0, -z_0) \cos \omega_0 t \quad -h_u < z < 0 \tag{3.2.1a}$$

$$\nabla^2 \phi_\ell = 0 \quad -h_u - h_\ell < z < -h_u \tag{3.2.1b}$$

$$\eta_{u,t} = \phi_{u,z} \quad z = 0 \tag{3.2.1c}$$

$$\phi_{u,t} + g\eta_u = 0 \quad z = 0 \tag{3.2.1d}$$

$$\eta_{\ell,t} = \phi_{u,z} \quad z = -h_u \tag{3.2.1e}$$

$$\eta_{\ell,t} = \phi_{\ell,z} \quad z = -h_u \tag{3.2.1f}$$

$$\mathcal{R}(\phi_{u,t} + g\eta_\ell) = (\phi_{\ell,t} + g\eta_\ell) \quad z = -h_u \tag{3.2.1g}$$

$$\phi_{u,z} = 0 \quad z = -h_u + h_\ell \tag{3.2.1h}$$

where δ is the Dirac delta function, g gravity, and $x = x_0 + Ut$ the position of the moving source assumed to be in the upper fluid layer ($z_0 > -h_u$). If the source is located in the lower layer, the right-hand sides of (3.2.1a) and (3.2.1b) are exchanged, but the remaining discussion in this section is unaffected.

Before deriving the solution to (3.2.1), some insight can be obtained from the dispersion relation. The solution for a free plane propagating wave in a two-layer fluid can be written as (see Lamb (1932))

$$\eta_u = a\ \mathrm{e}^{\mathrm{i}(\mathbf{k}\cdot\mathbf{x}-\omega t)} \tag{3.2.2a}$$

$$\eta_\ell = b\ \mathrm{e}^{\mathrm{i}(\mathbf{k}\cdot\mathbf{x}-\omega t)} \tag{3.2.2b}$$

$$\phi_u = -\mathrm{i}(A\cosh kz + B\sinh kz)\ \mathrm{e}^{\mathrm{i}(\mathbf{k}\cdot\mathbf{x}-\omega t)} \tag{3.2.2c}$$

$$\phi_\ell = -\mathrm{i}C\cosh k(z+h_u+h_\ell)\ \mathrm{e}^{\mathrm{i}(\mathbf{k}\cdot\mathbf{x}-\omega t)} \tag{3.2.2d}$$

where ω and $\mathbf{k}$ represent the frequency and wavenumber of a wave respectively, and $k = |\mathbf{k}|$. Coefficients a and b are amplitudes of surface and interfacial elevations, and are related by

$$\frac{b}{a} = \cosh kh_u - \frac{gk}{\omega^2}\sinh kh_u\ . \tag{3.2.3}$$

In terms of a and b, the coefficients A, B and C are given by

$$A = \frac{ga}{\omega},\quad B = \frac{\omega a}{k},\quad C = \frac{\omega b}{k\sinh kh_\ell}\ . \tag{3.2.4}$$

In (3.2.2), ω and k satisfy the dispersion relation:

$$\mathcal{D}(\omega,k) \equiv \omega^4(\mathcal{R}+\coth kh_u\coth kh_\ell) - \omega^2 gk(\coth kh_u+\coth kh_\ell) + g^2k^2(1-\mathcal{R}) = 0. \tag{3.2.5}$$

It is easy to see that for a given wavenumber $k > 0$, (3.2.5) has four solution: $\pm\omega_s(k), \pm\omega_i(k)$, with $\omega_s > \omega_i > 0$ Ball (1964), where $\pm\omega_s(k)$ and $\pm\omega_i(k)$ are denoted as the surface-mode and internal-mode waves respectively.

In a frame of reference moving with the source, the far-field waves are solutions to the dispersion relation (3.2.5) with the frequency replaced by encounter frequency (see for example Faltinsen (1993)):

$$\mathcal{D}(\pm\omega_0 + Uk_j, k_j) = 0. \tag{3.2.6}$$

Roots of (3.2.6) are at the intersections of the surface and internal mode branches of station-

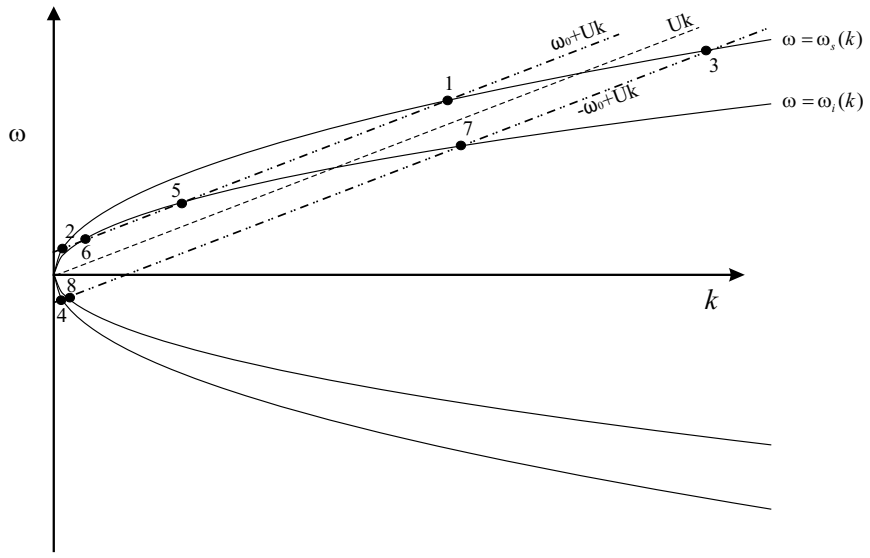

Figure 3-1: Schematic of the dispersion relationship for far-field waves generated by a moving and oscillating disturbance in a two-layer density stratified fluid. The figure also shows the numbering convention for these waves. Encounter frequency lines $\omega = \pm\omega_0 + Uk$: $- \cdot -$, can have up to N_w=8 intersections with the dispersion relation curves —— (equation (3.2.5)).

ary frame dispersion relation (3.2.5) with the encounter frequency lines, i.e., $\pm\omega_{s,i}(k_j) = \pm\omega_0 + Uk_j$, as illustrated in figure 3-1, where the numbering convention for the roots are also defined. Equation (3.2.6) can have up to N_W=8 real solutions for a given ω_0. The number of solutions N_W is a function of the four dimensionless quantities of the problem: density ratio $\mathcal{R} \equiv \rho_u/\rho_\ell$; dimensionless frequency $\tau \equiv U\omega_0/g$; depth ratio $h \equiv h_u/H$, where H=$h_u + h_\ell$ is the total depth; and Froude number $\mathcal{F} \equiv U^2/(gH)$.

When the encounter frequency line becomes tangent to one of the dispersion relation branches, two of the roots coalesce, and the critical frequencies at which this occur are labeled $\tau_{cr,s}$ or $\tau_{cr,i}$ according to whether it is the $\omega_s(k)$ or $\omega_i(k)$ branch of the dispersion relation. Generally, for $\tau > \tau_{cr,s}$, N_W=4; for $\tau_{cr,i} < \tau < \tau_{cr,s}$, N_W=6; and for $\tau < \tau_{cr,i}$, N_W=8 far-field waves associated with the oscillating and translating disturbance.

In general, waves associated with k_p, p=3, 4, 7, 8, (the "p waves") are always present regardless of the physical parameters; while those associated with k_q, q=1, 2, 5, 6, (the "q" waves) may not exist depending on τ_{cr}. Qualitatively, p/q waves have smaller/greater phase speed compared to U.

The dimensionless critical frequencies $\tau_{cr,s}, \tau_{cr,i}$ are functions of $\mathcal{R}$, $\mathcal{F}$ and h and can be

found numerically. Figure 3-2 shows the dependence of $\tau_{cr,s}, \tau_{cr,i}$ on $\mathcal{F}$ and h for $\mathcal{R}$=0.2 and 0.95. It is seen that $\tau_{cr,s}$ has a weak dependence on h and $\mathcal{R}$ while $\tau_{cr,i}$ has a relatively stronger dependence. It is to be noted that no real surface/interface τ_{cr} can be found if

$$\mathcal{F} > \frac{1}{2}\left(1 \pm \sqrt{1 - 4h(1-h)(1-\mathcal{R})}\right) \equiv \mathcal{F}_{cr} \tag{3.2.7}$$

where $+/-$ refers to the surface/internal mode. Figure 3-3 shows the variation of $\mathcal{F}_{cr}$ with $\mathcal{R}$ and h. For $\mathcal{R}$ close to unity, the critical Froude number associated with the surface mode, $\mathcal{F}_{cr,s} \approx 1$, and that associated with the internal mode, $\mathcal{F}_{cr,s} \approx 0$. Thus in a realistic ocean where $1 - \mathcal{R}$ is small, no internal wave propagate ahead of the disturbance unless $\mathcal{F}$ is comparably small. For given $\mathcal{R}$, the maximum range of $\mathcal{F}$ for upstream waves occurs at $h = 0.5$ (h_u=h_ℓ) where $\mathcal{F}_{cr}$ are extremal. In the limiting case of deep layers, kh_u $kh_l \gg 1$, the far-field wavenumbers in two dimensions can be obtained in closed form. In this limit, (3.2.5) reduces to:

$$\omega_s^2 = gk, \quad \omega_i^2 = gk\left(\frac{1-\mathcal{R}}{1+\mathcal{R}}\right) \tag{3.2.8}$$

The resultant waves at infinity are solutions of following four equations

$$\pm\omega_0 + Uk = \pm\sqrt{gk}\ , \qquad \pm\omega_0 + Uk = \pm\sqrt{gk\left(\frac{1-\mathcal{R}}{1+\mathcal{R}}\right)}\ . \tag{3.2.9}$$

Depending on the values of τ and $\mathcal{R}$, and the sign before ω_0, each of these equations can have either two or zero real roots. The first equation of (3.2.9) is for surface-mode waves and is the same as that for homogeneous fluid. The second equation of (3.2.9) is for internal-mode waves where g is effectively replaced by the reduced gravity $g(1-\mathcal{R})/(1+\mathcal{R})$. The roots to (3.2.9) are:

$$k_{1,2} = \frac{\nu}{2\tau^2}[1 - 2\tau \pm (1-4\tau)^{\frac{1}{2}}], \tag{3.2.10}$$

$$k_{3,4} = \frac{\nu}{2\tau^2}[1 + 2\tau \pm (1+4\tau)^{\frac{1}{2}}], \tag{3.2.11}$$

$$k_{5,6} = \frac{\nu_\ell}{2\tau_\ell^2}[1 - 2\tau_\ell \pm (1-4\tau_\ell)^{\frac{1}{2}}], \tag{3.2.12}$$

$$k_{7,8} = \frac{\nu_\ell}{2\tau_\ell^2}[1 + 2\tau_\ell \pm (1+4\tau_\ell)^{\frac{1}{2}}], \tag{3.2.13}$$

where $\nu = \omega_0^2/g$, and $\nu_\ell = \nu(1+\mathcal{R})/(1-\mathcal{R})$, $\tau_\ell = \tau(1+\mathcal{R})/(1-\mathcal{R})$. It is clear that: N_w=4 for

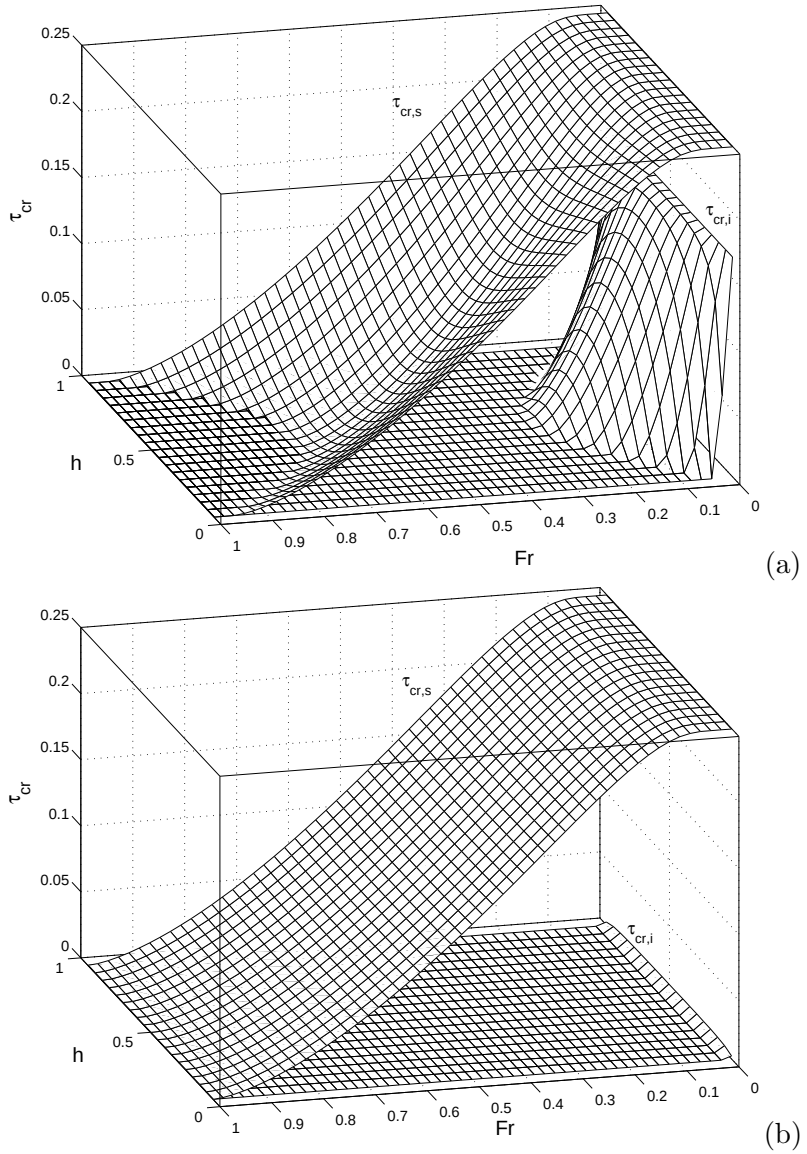

Figure 3-2: Critical dimensionless frequencies $\tau_{cr,s}$, $\tau_{cr,i}$ as a functions of Froude number $\mathcal{F}$, and depth ratio h for (a) $\mathcal{R} = 0.2$ and (b) $\mathcal{R} = 0.95$.

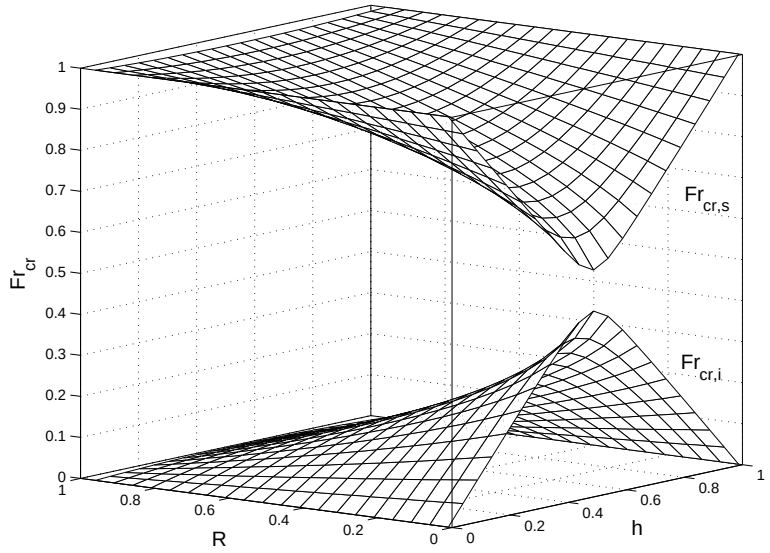

Figure 3-3: Critical Froude numbers $\mathcal{F}_{cr,s}$, $\mathcal{F}_{cr,i}$ as functions of $\mathcal{R}$ and h.

$\tau > 1/4$; N_W=6 for $0.25(1-\mathcal{R})/(1+\mathcal{R}) < \tau < 1/4$; and N_W=8 for $\tau < 0.25(1-\mathcal{R})/(1+\mathcal{R})$.

In a stationary frame, the surface/internal wave associated with k_4/k_8 propagate backward (negative phase and group speed $C_p, C_g < 0$); the other waves propagate forward ($C_p, C_g > 0$) with the k_2/k_6 waves, if they exist, moving ahead of the disturbance ($C_g > U$), and the k_1/k_5 and k_3/k_7 waves trailing behind the disturbance ($C_g < U$). The difference between the two latter pairs of waves is that $C_p > U$ for k_1/k_5, if they exist, and $C_p < U$ for k_3, k_7.

3.3 Green function

The kinematic analysis of the preceding section gives wavenumbers of the waves that appear at the far field of an oscillating translating disturbance in a two-layer density stratified fluid. To determine amplitude of these waves and also surface and interface elevation in the near field of the disturbance, the boundary value problem needs to be solved analytically. In this section, the Green function for the velocity potential associated with a steadily translating point source of sinusoidally oscillating strength in a two-layer density stratified fluid is obtained. For the source located in the upper layer the general form of the two-dimensional Green function is presented, and study the limiting case of deep layers where the expressions are simplified considerably. The corresponding Green function for the source in the lower layer is given in section 3.3.3. Finally the Green function for the

three-dimensional case for a source located in either the upper or lower layer is obtained (section 3.3.5).

3.3.1 Two-dimensional source in the upper layer

Here a source having an oscillatory strength $m = m_0 \cos\omega_0 t$ and moving with a uniform speed $\mathbf{u} = U\hat{i}$ is considered in the upper layer of a two-dimensional two-layer density stratified fluid. The following dimensionless variables are used:

$$t = \omega_0 t^*, \quad x, z, z_0, h = \frac{x^*, z^*, z_0^*, h_u}{H}, \quad \tau = \frac{U\omega_0}{g},$$
$$\mathcal{F} = \frac{U^2}{gH}, \quad m = \frac{m_0 H^2}{\phi_0}, \quad k = \frac{gk^*}{\omega_0^2} \tag{3.3.14}$$

where $(\ )^*$ indicates dimensional variables and ϕ_0 scales the velocity potential. In a frame of reference moving with the source, the dimensionless governing equations are:

$$\nabla\varphi_u = m\delta(x - x_0)\cos\omega_0 t \qquad -h < z < 0 \tag{3.3.15}$$
$$\nabla\varphi_\ell = 0 \qquad -1 < z < -h \tag{3.3.16}$$
$$\tau^2\varphi_{u,tt} + 2\tau\mathcal{F}\varphi_{u,xt} + \mathcal{F}^2\varphi_{u,xx} + \mathcal{F}\varphi_{u,z} = 0 \qquad z = 0 \tag{3.3.17}$$
$$\varphi_{u,z} = \varphi_{\ell,z} \qquad z = -h \tag{3.3.18}$$
$$\mathcal{R}(\tau^2\varphi_{u,tt} + 2\tau\mathcal{F}\varphi_{u,xt} + \mathcal{F}^2\varphi_{u,xx} + \mathcal{F}\varphi_{u,z}) =$$
$$\tau^2\varphi_{\ell,tt} + 2\tau\mathcal{F}\varphi_{\ell,xt} + \mathcal{F}^2\varphi_{\ell,xx} + \mathcal{F}\varphi_{\ell,z} \qquad z = -h \tag{3.3.19}$$
$$\varphi_{\ell,z} = 0 \qquad z = -1. \tag{3.3.20}$$

where x_0=0, $z_0 > -h$ is the position of the source in the upper layer. A steady solution in this frame of reference (fixed with the source) is sought and it is assumed:

$$\varphi_u(x,z,t) = \Re\{m\ \phi_u(x,z)\ \mathrm{e}^{\mathrm{i}t}\},\ \varphi_\ell(x,z,t) = \Re\{m\ \phi_\ell(x,z)\ \mathrm{e}^{\mathrm{i}t}\}\ , \tag{3.3.21}$$

and consider a solution of the following form:

$$\phi_u = \frac{\ln r}{2\pi} + \frac{\ln r_2}{2\pi} + \mathcal{H}_u(x,z)$$
$$\phi_\ell = \mathcal{H}_\ell(x,z) \tag{3.3.22}$$

where

$$r^2 = x^2 + (z - z_0)^2, \quad r_2^2 = x^2 + (z + z_0 + 2h)^2. \tag{3.3.23}$$

with r_2 being the location of the image of the point source with respect to the interface. To solve for $\mathcal{H}_u, \mathcal{H}_\ell$, Fourier transform in x is invoked (see Wehausen & Laitone (1960)). The function $\ln(r)$ in two dimension does not have a Fourier transform (see McCauley (1979) for a variant definition using Laplace equation), however it can be written it in an integral form :

$$\ln \sqrt{x^2 + a^2} = -\int_0^\infty \frac{\mathrm{e}^{-ka} \cos kx - \cos k}{k} \mathrm{d}k \; . \tag{3.3.24}$$

The second term in the numerator is not a function of x, z. However it enters the boundary-value problem through $\phi_{u/\ell,tt}$ (equations (3.3.17), (3.3.19)). Thorne (1953) subtracts the potential of the virtual singularity from the real singularity (i.e. $\ln r - \ln r_2$) to avoid the new term under the integral. Debnath (1971) used a similar expression as ours without the constant term (see the definition of M_1 after equation 34 in his paper and compare with his equation 22) which strictly does not allow an inverse Fourier transform.

The solution to the boundary-value problem can be written in the form:

$$\begin{aligned}
\phi_u = & \frac{\ln r}{2\pi} + \frac{\ln r_2}{2\pi} \\
& + \int_0^\infty \left[(A^+ \cosh \alpha k z + B^+ \sinh \alpha k z) \; \frac{\mathrm{e}^{\mathrm{i}\alpha k x}}{2} \right. \\
& \qquad \left. + (A^- \cosh \alpha k z + B^- \sinh \alpha k z) \; \frac{\mathrm{e}^{-\mathrm{i}\alpha k x}}{2} - \frac{\cos \alpha k}{\pi k} \right] \mathrm{d}k
\end{aligned} \tag{3.3.25}$$

$$\phi_\ell = \int_0^\infty \left[C^+ \cosh \alpha k (z+1) \; \frac{\mathrm{e}^{\mathrm{i}\alpha k x}}{2} + C^- \cosh \alpha k (z+1) \; \frac{\mathrm{e}^{-\mathrm{i}\alpha k x}}{2} \right] \mathrm{d}k \; , \tag{3.3.26}$$

where $\alpha \equiv \tau^2/\mathcal{F}$. Upon substitution in the boundary conditions, the coefficients $A^\pm, B^\pm$ and $C^\pm$ can be found:

$$X^\pm = \frac{\hat{X}^\pm}{\lambda^{\pm 4} - (\omega_s^2 + \omega_i^2)\lambda^{\pm 2} + \omega_s^2 \omega_i^2} \tag{3.3.27}$$

where X can be either of A, B or C and

$$\hat{A}^{\pm} = \beta\,\lambda^{\pm^4} + \frac{k\,(-\mathcal{R}sl\,\gamma + cl\;cu\,\beta + \mathcal{R}sl\;su\,\beta - sl\,\beta\,cu + sl\,\mathcal{R}\beta\,cu)\,\lambda^{\pm^2}}{sl\;su\,\mathcal{R} + cu\;cl} + \frac{k^2 sl\;cu\,\beta\;(-1+\mathcal{R})}{sl\;su\,\mathcal{R} + cu\;cl} \tag{3.3.28}$$

$$\hat{B}^{\pm} = \frac{(sl\;cu\,\mathcal{R}\beta + \beta\;cl\;su - \mathcal{R}sl\,\gamma)\,\lambda^{\pm^4}}{sl\;su\,\mathcal{R} + cu\;cl} + \frac{k\beta\;(sl\;cu\,\mathcal{R} + cl\;su - sl\;su + sl\;su\,\mathcal{R})\,\lambda^{\pm^2}}{sl\;su\,\mathcal{R} + cu\;cl} + \frac{k^2\beta\;sl\;su\;(-1+\mathcal{R})}{sl\;su\,\mathcal{R} + cu\;cl} \tag{3.3.29}$$

$$\hat{C}^{\pm} = \frac{\mathcal{R}\left(cu^2\beta - cu\,\gamma - su^2\beta\right)\lambda^{\pm^4}}{cu\;cl + sl\;su\,\mathcal{R}} + \frac{\mathcal{R}k\left(-su^2\beta + cu^2\beta + su\,\gamma\right)\lambda^{\pm^2}}{cu\;cl + sl\;su\,\mathcal{R}} \tag{3.3.30}$$

where

$$\begin{aligned} &\lambda^{\pm} = 1 \pm \tau k, \quad \beta = \frac{\cosh\alpha k(z_0+h)}{\pi\;k\;\exp(\alpha k h)}, \quad \gamma = \frac{\mathrm{e}^{-\alpha k(z_0+h)}}{\pi k} \\ &su \equiv \sinh(\alpha k h), \quad cu \equiv \cosh(\alpha k h), \\ &sl \equiv \sinh[\alpha k(1-h)], \quad cl \equiv \cosh[\alpha k(1-h)]\;, \end{aligned} \tag{3.3.31}$$

and the frequencies $\omega_{s,i}$ are surface-mode and internal-mode solutions to the dimensionless dispersion relation

$$\omega^4[\mathcal{R} + \coth\alpha k h\;\coth\alpha k(1-h)] - \omega^2 k[\coth\alpha k h + \coth\alpha k(1-h)] + k^2(1-\mathcal{R}) = 0. \tag{3.3.32}$$

From (3.2.1c) and (3.2.1e), the surface and interface elevations are now given by

$$\eta_u = -\frac{g\eta_u^*}{\omega_0\phi_0} = -\frac{g\eta_u^*}{\omega_0 m_0 H^2} = \varphi_{u,t} + \frac{\mathcal{F}}{\tau}\varphi_{u,x}\;, \quad z = 0, \tag{3.3.33}$$

$$\eta_\ell = \frac{g\eta_\ell^*}{\omega_0\phi_0} = \frac{g\eta_\ell^*}{\omega_0 m_0 H^2} = \frac{\mathcal{R}(\varphi_{u,t} - \mathcal{F}/\tau\;\varphi_{u,x}) - (\varphi_{\ell,t} - \mathcal{F}/\tau\;\varphi_{\ell,x})}{(1-\mathcal{R})}\;, \quad z = -h \tag{3.3.34}$$

For numerical evaluation of (3.3.25) and (3.3.26), the integrals can be transformed into Cauchy principal-value integrals, where the singular values are roots of the denominator of

(3.3.27). To do this, (3.3.25) and (3.3.26) are rewritten in the expanded form:

$$\begin{aligned}\phi_u = &\frac{\ln r}{2\pi} + \frac{\ln r_2}{2\pi} \\ &+ \int_0^\infty \left[\frac{(\hat{A}^+ \cosh \alpha k z + \hat{B}^+ \sinh \alpha k z)}{2\ \mathcal{G}^+} \ \mathrm{e}^{\mathrm{i}\alpha k x} \right. \\ &\left. + \frac{(\hat{A}^- \cosh \alpha k z + \hat{B}^- \sinh \alpha k z)}{2\ \mathcal{G}^-} \ \mathrm{e}^{-\mathrm{i}\alpha k x} - \frac{\cos \alpha k}{\pi k} \right] \mathrm{d}k \end{aligned} \tag{3.3.35}$$

$$\phi_\ell = \int_0^\infty \left[\frac{\hat{C}^+}{2\ \mathcal{G}^+} \cosh \alpha k (z+1) \ \mathrm{e}^{\mathrm{i}\alpha k x} + \frac{\hat{C}^-}{2\ \mathcal{G}^-} \cosh \alpha k (z+1) \ \mathrm{e}^{-\mathrm{i}\alpha k x} \right] \mathrm{d}k \tag{3.3.36}$$

where

$$\mathcal{G}^\pm = \lambda^{\pm 4} - (\omega_s^2 + \omega_i^2)\lambda^{\pm 2} + \omega_s^2 \omega_i^2 \ . \tag{3.3.37}$$

$\mathcal{G}^+$ can have maximum number of four real roots and $\mathcal{G}^-$ has always four real roots. Assuming all eight real roots exist, (3.3.25) and (3.3.26) can finally be expressed as:

$$\begin{aligned}\phi_u = &\frac{\ln r}{2\pi} + \frac{\ln r_2}{2\pi} \\ &+ \sum_{k=k_1,k_2,k_5,k_6} (-1)^w \mathrm{i}\pi \frac{(\hat{A}^+ \cosh \alpha k z + \hat{B}^+ \sinh \alpha k z)}{2\ \mathcal{F}^+} \ \mathrm{e}^{\mathrm{i}\alpha k x} \\ &+ \sum_{k=k_3,k_4,k_7,k_8} (-1)^w \mathrm{i}\pi \frac{(\hat{A}^- \cosh \alpha k z + \hat{B}^- \sinh \alpha k z)}{2\ \mathcal{F}^-} \ \mathrm{e}^{-\mathrm{i}\alpha k x} \\ &+ \mathrm{PV} \int_0^\infty \left[\frac{(\hat{A}^+ \cosh \alpha k z + \hat{B}^+ \sinh \alpha k z)}{2\ \mathcal{G}^+} \ \mathrm{e}^{\mathrm{i}\alpha k x} \right. \\ &\left. + \frac{(\hat{A}^- \cosh \alpha k z + \hat{B}^- \sinh \alpha k z)}{2\ \mathcal{G}^-} \ \mathrm{e}^{-\mathrm{i}\alpha k x} - \frac{\cos \alpha k}{\pi k} \right] \mathrm{d}k \end{aligned} \tag{3.3.38}$$

$$\begin{aligned}\phi_\ell = &\sum_{k=k_1,k_2,k_5,k_6} (-1)^w \mathrm{i}\pi \frac{\hat{C}^+}{2\ \mathcal{F}^+} \cosh \alpha k (z+1) \ \mathrm{e}^{\mathrm{i}\alpha k x} \\ &+ \sum_{k=k_3,k_4,k_7,k_8} (-1)^w \mathrm{i}\pi \frac{\hat{C}^-}{2\ \mathcal{F}^-} \cosh \alpha k (z+1) \ \mathrm{e}^{-\mathrm{i}\alpha k x} \\ &+ \mathrm{PV} \int_0^\infty \left[\frac{\hat{C}^+}{2\ \mathcal{G}^+} \cosh \alpha k (z+1) \ \mathrm{e}^{\mathrm{i}\alpha k x} + \frac{\hat{C}^-}{2\ \mathcal{G}^-} \cosh \alpha k (z+1) \ \mathrm{e}^{-\mathrm{i}\alpha k x} \right] \mathrm{d}k, \end{aligned} \tag{3.3.39}$$

where

$$\mathcal{F}^{\pm} = \frac{d}{dk}\ \left\{\lambda^{\pm 4} - (\omega_s^2 + \omega_i^2)\lambda^{\pm 2} + \omega_s^2\omega_i^2\right\} \tag{3.3.40}$$

and, for $k = k_2, k_6$, $w = 1$, otherwise $w = 2$. If any of k_1, k_2, k_5, k_6 is non-real (they disappear as "pairs"), the corresponding term in the sum is skipped.

The far-field amplitudes can be found by contour integration of (3.3.25) and (3.3.26). To satisfy radiation condition of outgoing waves at infinity, the contour integration along the real k axis must be indented below the poles for k_2,k_6 (if they exist) and above those associated with all the other wavenumbers. After some algebra, the final expressions for the far-field amplitudes are:

$$\phi_u^{\infty} = \pi\frac{\hat{A}^+\cosh\alpha kz + \hat{B}^+\sinh\alpha kz}{2\mathcal{F}^+}, \quad \phi_\ell^{\infty} = \pi\frac{\hat{C}^+\cosh\alpha k(z+1)}{2\mathcal{F}^+}\ , \tag{3.3.41}$$

for $k = k_1, k_2, k_5, k_6$, and,

$$\phi_u^{\infty} = \pi\frac{\hat{A}^-\cosh\alpha kz + \hat{B}^-\sinh\alpha kz}{2\mathcal{F}^-}, \quad \phi_\ell^{\infty} = \pi\frac{\hat{C}^+\cosh\alpha k(z+1)}{2\mathcal{F}^+}\ , \tag{3.3.42}$$

for $k = k_3, k_4, k_7, k_8$.

3.3.2 Deep-layers limiting case

When both layers are deep, the Green function can be reduced to independent integrals in Fourier space. These reduced expressions are two-layer counterparts of the well known deep-water homogeneous-fluid Green function (see Liu & Yue (1993) for example).

The Green function expressions depend on the value of τ relative to $\tau_{cr,i}$, $\tau_{cr,s}$. For $\tau < \tau_{cr,i}$, N_W=8 distinct waves exist. After some algebra, the final form of the solution can

be expressed as:

$$\begin{aligned}
\phi_u &= \frac{1}{2\pi}\ln\, r + \frac{1}{2\pi}\ln\, r_2 \\
&\quad + \int_0^\infty \left[\frac{\hat{A}^+ \cosh \alpha k z + \hat{B}^+ \sinh \alpha k z}{2\ \tau^4} \sum_{q=1,2,5,6} \frac{a_q}{k-k_q}\ \mathrm{e}^{\mathrm{i}\alpha k x} \right. \\
&\quad \left. + \frac{\hat{A}^- \cosh \alpha k z + \hat{B}^- \sinh \alpha k z}{2\ \tau^4} \sum_{q=3,4,7,8} \frac{a_q}{k-k_q}\ \mathrm{e}^{-\mathrm{i}\alpha k x} - \frac{\cos \alpha k}{\pi k} \right] \mathrm{d}k \qquad (3.3.43) \\
\phi_\ell &= \int_0^\infty \left[\frac{\hat{C}^+\ \mathrm{e}^{\mathrm{i}\alpha k x}}{2\tau^4} \sum_{q=1,2,5,6} \frac{a_q}{k-k_q} \right. \\
&\quad \left. + \frac{\hat{C}^-\ \mathrm{e}^{-\mathrm{i}\alpha k x}}{2\tau^4} \sum_{q=3,4,7,8} \frac{a_q}{k-k_q} \right] \cosh \alpha k(z+1)\ \mathrm{d}k \qquad (3.3.44)
\end{aligned}$$

where

$$a_q = \prod_{j=\{1,2,5,6\}-q} \frac{1}{k_q - k_j} \quad \text{for} \quad q = 1,2,5,6; \qquad (3.3.45)$$

$$a_q = \prod_{j=\{3,4,7,8\}-q} \frac{1}{k_q - k_j} \quad \text{for} \quad q = 3,4,7,8. \qquad (3.3.46)$$

The integrals contain simple poles at $k = k_1, \cdots, k_8$. To satisfy radiation condition, the contour integration must be indented below k_2, k_6 and above the other wavenumbers.

For $\tau_{cr,i} < \tau < \tau_{cr,s}$, N_W=6, and

$$\begin{aligned}
\phi_u &= \frac{1}{2\pi}\ln\, r + \frac{1}{2\pi}\ln\, r_2 + \int_0^\infty \left[\frac{\hat{A}^+ \cosh \alpha k z + \hat{B}^+ \sinh \alpha k z}{2\ \tau^4} \sum_{q=1,2} \frac{a_q}{k-k_q}\ \mathrm{e}^{\mathrm{i}\alpha k x} \right. \\
&\quad \left. + \frac{\hat{A}^- \cosh \alpha k z + \hat{B}^- \sinh \alpha k z}{2\ \tau^4} \sum_{q=3,4,7,8} \frac{a_q}{k-k_q}\ \mathrm{e}^{-\mathrm{i}\alpha k x} - \frac{\cos \alpha k}{\pi k} \right] \mathrm{d}k \qquad (3.3.47) \\
\phi_\ell &= \int_0^\infty \left[\frac{\hat{C}^+\ \mathrm{e}^{\mathrm{i}\alpha k x}}{2\tau^4} \sum_{q=1,2} \frac{a_q}{k-k_q} \right. \\
&\quad \left. + \frac{\hat{C}^-\ \mathrm{e}^{-\mathrm{i}\alpha k x}}{2\tau^4} \sum_{q=3,4,7,8} \frac{a_q}{k-k_q} \right] \cosh \alpha k(z+1)\ \mathrm{d}k \qquad (3.3.48)
\end{aligned}$$

where now

$$a_1 = \frac{\tau^2}{\lambda^2(k_1) - \omega_i^2(k_1)} \cdot \frac{1}{k_1 - k_2}; \tag{3.3.49}$$

$$a_2 = \frac{\tau^2}{\lambda^2(k_2) - \omega_i^2(k_2)} \cdot \frac{1}{k_2 - k_1}; \text{and} \tag{3.3.50}$$

$$a_q = \prod_{j=\{3,4,7,8\}-q} \frac{1}{k_q - k_j} \quad \text{for} \quad q = 3, 4, 7, 8; \tag{3.3.51}$$

and the contour integrations for (3.3.47) and (3.3.48) (and below) must be treated similarly to satisfy radiation condition.

Finally, for $\tau > \tau_{cr,s}$, N_W=4, and

$$\begin{aligned} \phi_u &= \frac{1}{2\pi}\ln r + \frac{1}{2\pi}\ln r_2 + \int_0^\infty \left\{ \frac{\hat{A}^- \cosh \alpha k z + \hat{B}^- \sinh \alpha k z}{2\ \tau^4} \right. \\ &\quad \left. \times \sum_{q=3,4,7,8} \frac{a_q}{k - k_q}\ \mathrm{e}^{-\mathrm{i}\alpha k x} - \frac{\cos \alpha k}{\pi k} \right\}\ \mathrm{d}k \end{aligned} \tag{3.3.52}$$

$$\phi_\ell = \int_0^\infty \frac{\hat{C}^-\ \mathrm{e}^{-\mathrm{i}\alpha k x}}{2\tau^4} \sum_{q=3,4,7,8} \frac{a_q}{k - k_q} \cosh \alpha k(z+1)\ \mathrm{d}k \tag{3.3.53}$$

where

$$a_q = \prod_{j=\{3,4,7,8\}-q} \frac{1}{k_q - k_j} \quad \text{for} \quad q = 3, 4, 7, 8. \tag{3.3.54}$$

3.3.3 Source in the lower layer

For the source point in the lower layer, the derivation is quite similar and the details are omitted. Here the final expressions for the Green functions is provided:

$$\begin{aligned} \phi_u &= \int_0^\infty \left[(A^+ \cosh \alpha k z + B^+ \sinh \alpha k z)\ \frac{e^{\mathrm{i}\alpha k x}}{2} \right. \\ &\quad \left. + (A^- \cosh \alpha k z + B^- \sinh \alpha k z)\ \frac{e^{-\mathrm{i}\alpha k x}}{2} \right] \mathrm{d}k \end{aligned} \tag{3.3.55}$$

$$\begin{aligned} \phi_\ell &= \frac{\ln r}{2\pi} + \frac{\ln r_3}{2\pi} + \int_0^\infty \left[C^+ \cosh \alpha k(z+1)\ \frac{e^{\mathrm{i}\alpha k x}}{2} \right. \\ &\quad \left. + C^- \cosh \alpha k(z+1)\ \frac{e^{-\mathrm{i}\alpha k x}}{2} - \frac{\cos \alpha k}{\pi k} \right] \mathrm{d}k \end{aligned} \tag{3.3.56}$$

where $r_3^2 \equiv x^2 + (2 + z + z_0)^2$ is the locating of the image of the point source about the bottom. Applying the boundary conditions, the coefficients $A^{\pm}, B^{\pm}$ and $C^{\pm}$ are:

$$X^{\pm} = \frac{\hat{X}^{\pm}}{\lambda^{\pm 4} - (\omega_s^2 + \omega_i^2)\lambda^{\pm 2} + \omega_s^2 \omega_i^2} \tag{3.3.57}$$

where X is either of A, B or C and

$$\hat{A}^{\pm} = \frac{k\lambda^{\pm 2}\beta\ (sl + cl)}{sl\,\mathcal{R}su + cl\ cu}; \qquad \hat{B}^{\pm} = \frac{\lambda^{\pm 4}\beta\ (sl + cl)}{sl\ su\,\mathcal{R} + cl\ cu} \tag{3.3.58}$$

$$\hat{C}^{\pm} = -\frac{\beta\ (su\,\mathcal{R} - cu)\,\lambda^{\pm 4}}{sl\ su\,\mathcal{R} + cl\ cu} + \frac{\beta\,k\,(-su + cu)\,\lambda^{\pm 2}}{sl\ su\,\mathcal{R} + cl\ cu} + \frac{\beta\,k^2 su\ (\mathcal{R} - 1)}{sl\ su\,\mathcal{R} + cl\ cu} \tag{3.3.59}$$

where now

$$\beta = \frac{\cosh \alpha k(z_0 + 1)}{\pi\ k\ \mathrm{e}^{\alpha k(1-h)}}\ . \tag{3.3.60}$$

3.3.4 Discussion

The Green functions obtained provide the solution everywhere. Of special interest of course is the wave amplitudes in the far field. These wave amplitudes, in general $a_{u,n}$, $a_{\ell,n}$, $n = 1, \ldots, 8$, on the upper (surface), lower (interfacial) layers, depend on the characteristics of the moving oscillating source, τ, $\mathcal{F}$ and z_0, as well as those of the ocean environment, h, $\mathcal{R}$.

Figures 3-4a, b plot $a_{u,n}$, n=1,2,3,4, and $a_{\ell,n}$, n=5,6,7,8 respectively for the surface and internal mode waves as a function of the density ratio $\mathcal{R}$. The other parameters used are $\mathcal{F}$ =0.032, τ=0.1 h=0.5, and z_0=-0.02. With the source in the upper layer in this case, the dependence on $\mathcal{R}$ of $a_{u,n}$ is relatively weak, while $a_{\ell,n}$generally increase with $\mathcal{R}$ (with a rate that depends on the specific mode n). This is expected because, relative to the density of the lower fluid, the momentum introduced by the source in the upper layer increases as $\mathcal{R}$ increases. For other parameters fixed, $\tau_{cr,i}$ decreases as $\mathcal{R}$ increases. Beyond a certain value of $\mathcal{R}$ ($\mathcal{R}$=0.4 in this case), $\tau_{cr,i} < \tau$, N_W decreases from 8 to 6, and the amplitudes associated with the two modes that are eliminated blow up (corresponding to their group velocity approaching U). Based on Figure 3-4, hereafter, focus will be on two values of density ratio, $\mathcal{R}$=0.2 and 0.95, only the latter value of course corresponds to conditions in

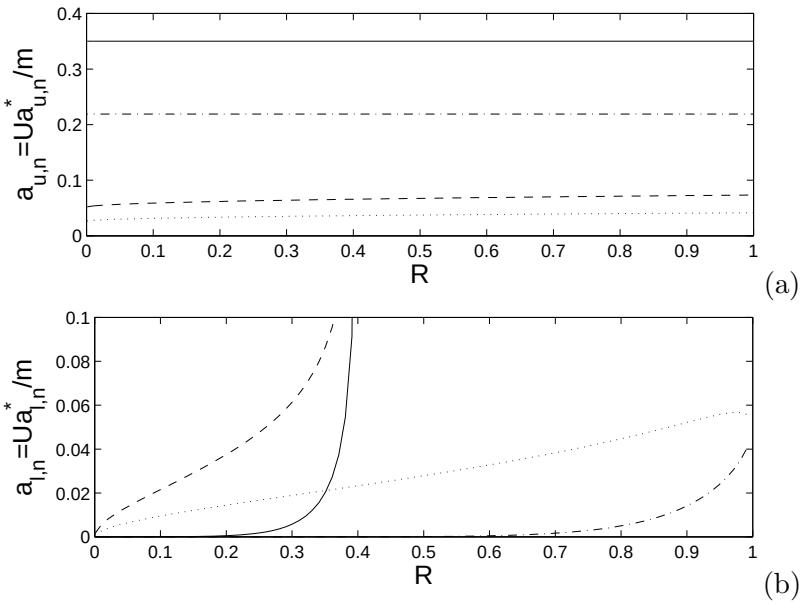

Figure 3-4: Far-field wave amplitudes $a_{u,n}$, $a_{\ell,n}$, as functions of $\mathcal{R}$ for $\mathcal{F}$=0.03, τ=0.1, z_0=-0.02, h=0.5. In figure (a) for $a_{u,n}$: $a_{u,1}$ —— ; $a_{u,2}$ - - - ; $a_{u,3}$ – · – ; and $a_{u,4}$ · · · . In figure (b) for $a_{\ell,n}$: $a_{\ell,5}$ —— ; $a_{\ell,6}$ - - - ; $a_{\ell,7}$ – · – ; and $a_{\ell,8}$ · · · .

the physical ocean.

Figures 3-5a-d show the dependence of a_n on τ for $\mathcal{R}$=0.2,0.95. The other physical parameters are $\mathcal{F}$=0.03, h=0.5, and z_0=-0.02. As τ increases, the amplitudes of the p/q waves decrease/increase. As τ approaches $\tau_{cr,s}$, $\tau_{cr,i}$, the respective q wave amplitudes become unbounded and they disappear. In the limit $\tau \to 0$, i.e., a steady translating source, the wavenumbers associated with respectively $a_{u,1}$, $a_{u,3}$ and $a_{\ell,5}$, $a_{\ell,7}$ coincide and the amplitudes have the same value. In this limit, the wavenumbers associated with $a_{u,2}$, $a_{u,4}$ and $a_{\ell,6}$, $a_{\ell,8}$ go to zero but the amplitudes remain finite. The magnitudes of $a_{u,n}$ and $a_{\ell,n}$are comparable here because the source is placed close to the free surface. As z_0 decreases towards the interface, $a_{\ell,n}$ does not change appreciably, while $a_{u,n}$ decreases significantly. The main difference between $\mathcal{R}$=0.2 and $\mathcal{R}$=0.95 is that, for the latter, $\tau_{cr,i}$=0 and the $a_{\ell,5}$ and $a_{\ell,6}$ waves do not exist (N_W=6). In fact, for $\mathcal{F}$ <0.5 (a similar expression obtains for $\mathcal{F}$ >0.5), it can be shown from (3.2.7) that the maximum $\mathcal{R}$ for $a_{\ell,5}$ and $a_{\ell,6}$ waves to exist is given by:

$$\mathcal{R}_{\max} = 1 - \frac{\mathcal{F}}{h(1-h)}(1-\mathcal{F}). \tag{3.3.61}$$

For the present case with $\mathcal{F}$=0.03 and h=0.5,$\mathcal{R}_{\max}$=0.88. Comparing Figures 3-5a,b and

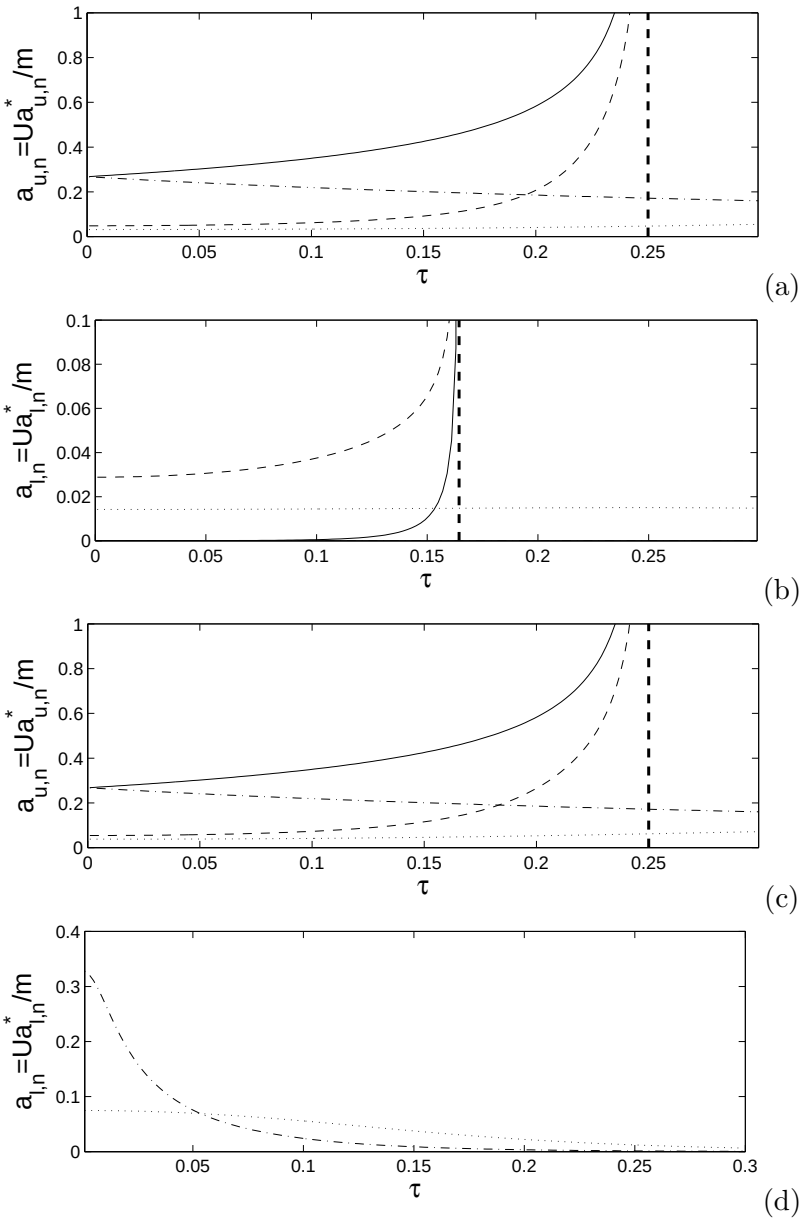

Figure 3-5: Far-field wave amplitudes $a_{u,n}$, $a_{\ell,n}$, as functions of τ for $\mathcal{F}$=0.03, z_0=-0.02, h=0.5, and, (a,b) $\mathcal{R}$=0.2; (c,d) $\mathcal{R}$=0.95. In figures (a,c) for $a_{u,n}$: $a_{u,1}$ —— ; $a_{u,2}$ - - - ; $a_{u,3}$ – · – ; and $a_{u,4}$ · · · . In figures (b,d) for $a_{\ell,n}$: $a_{\ell,5}$ —— ; $a_{\ell,6}$ - - - ; $a_{\ell,7}$ – · – ; and $a_{\ell,8}$ · · · .

c,d, the behaviors for $a_{u,n}$ are similar, while for $a_{\ell,n}$ the amplitudes for $\mathcal{R}$ $\sim$1 are much greater as expected, particularly in this case for $a_{\ell,7}$ which grows rapidly as τ becomes small.

Figure 3-6 shows the effect of $\mathcal{F}$ on a_n (with $\mathcal{F}$ varying, a_n are now non-dimensionalized by $g/(m\omega_0)$); for chosen parameters τ=0.1, h=0.5, and z_0=-0.02. Generally, as $\mathcal{F}$ increases, there are values $\mathcal{F}$=$\mathcal{F}_{\max}$, at which $a_{u,3}$ and $a_{\ell,7}$ obtain maximum and then decay. If the range of $\mathcal{F}$ in Figure 3-6 is extended, it is found that this is in fact the case for all p waves. Similar to previous figures, there are critical values $\mathcal{F}_{cr}$, given the other parameters, beyond which respective q waves disappear; with the general feature that the corresponding amplitudes grow unbounded as $\mathcal{F}$ approached these $\mathcal{F}_{cr}$ values. The magnitude of $\mathcal{R}$ affects the values of $\mathcal{F}_{\max}$ and $\mathcal{F}_{cr}$, with these values greater/smaller for the surface/intenal mode wave amplitudes for larger $\mathcal{R}$.

Dependence of a_n on the depth ratio h (with $\mathcal{F}$=0.03, τ=0.1 and z_0=-0.02) is shown in figure 3-7. In the ocean, h (for given total depth H) can vary significantly due to the passage of long interfacial waves. In littoral zones, the amplitude of these waves can be an appreciable fraction of H (e.g. Shen & He (2005)). Figure 3-7 shows that most of the variations in the far-field wave amplitudes occur for smaller h. As h increases, $a_{u,n}/a_{\ell,n}$ generally increases/diminishes. These dependencies are more prominent for $a_{\ell,n}$. In particular, for $\mathcal{R}$=0.2, there is a critical depth ratio near which $a_{\ell,5}$ and $a_{\ell,6}$ go unbounded and below which they disappear. Comparing the $\mathcal{R}$=0.95 case to the $\mathcal{R}$=0.2 case, the qualitative features obtain but are much weaker. Concentrating on this more physically relevant case of $\mathcal{R}$=0.95, figure 3-7c,d shows that the resistance on the disturbance due to wave generation generally decreases as h increases from small values.

Finally the effect of z_0 is considered in figure 3-8. As expected, there is a sharp variation in wave amplitudes around $z_0 \sim -h$ especially for smaller $\mathcal{R}$. As the location of the disturbance approaches the interface from below, a_n (especially $a_{\ell,n}$) increase markedly. As z_0 crosses $-h$, a_n drop abruptly proportionate to the abrupt drop in the density. As the disturbance approaches the free surface, $a_{\ell,n}$ decreases from its maximum value at $z_0 = -h$, while $a_{u,n}$ increases (eventually becoming unbounded as $z_0 \rightarrow$0). The wave resistance on the disturbance as it crosses the interface consequently follows a similar qualitative trend.

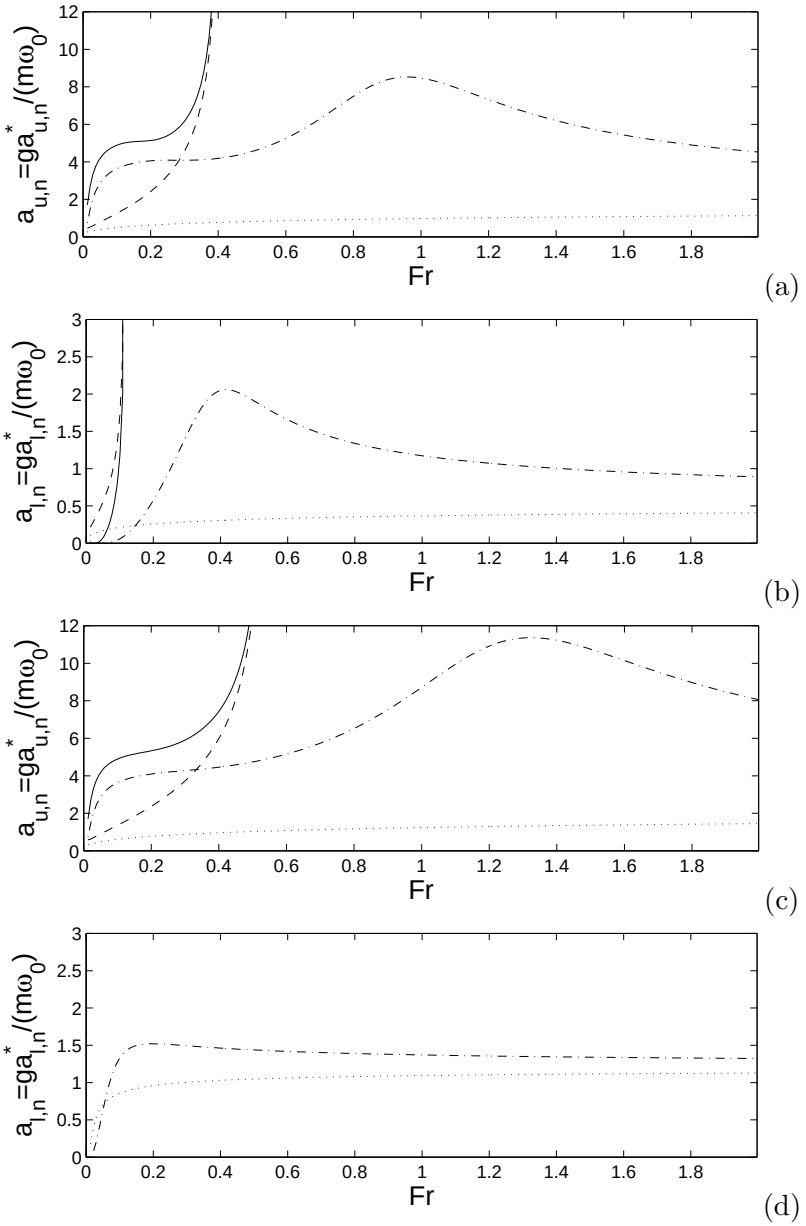

Figure 3-6: Far-field wave amplitudes $a_{u,n}$, $a_{\ell,n}$, as functions of $\mathcal{F}$ for τ=0.1, z_0=-0.02, h=0.5, and, (a,b) $\mathcal{R}$=0.2; (c,d) $\mathcal{R}$=0.95. In figures (a,c) for $a_{u,n}$: $a_{u,1}$ —— ; $a_{u,2}$ - - - ; $a_{u,3}$ – · – ; and $a_{u,4}$ · · · . In figures (b,d) for $a_{\ell,n}$: $a_{\ell,5}$ —— ; $a_{\ell,6}$ - - - ; $a_{\ell,7}$ – · – ; and $a_{\ell,8}$ · · · .

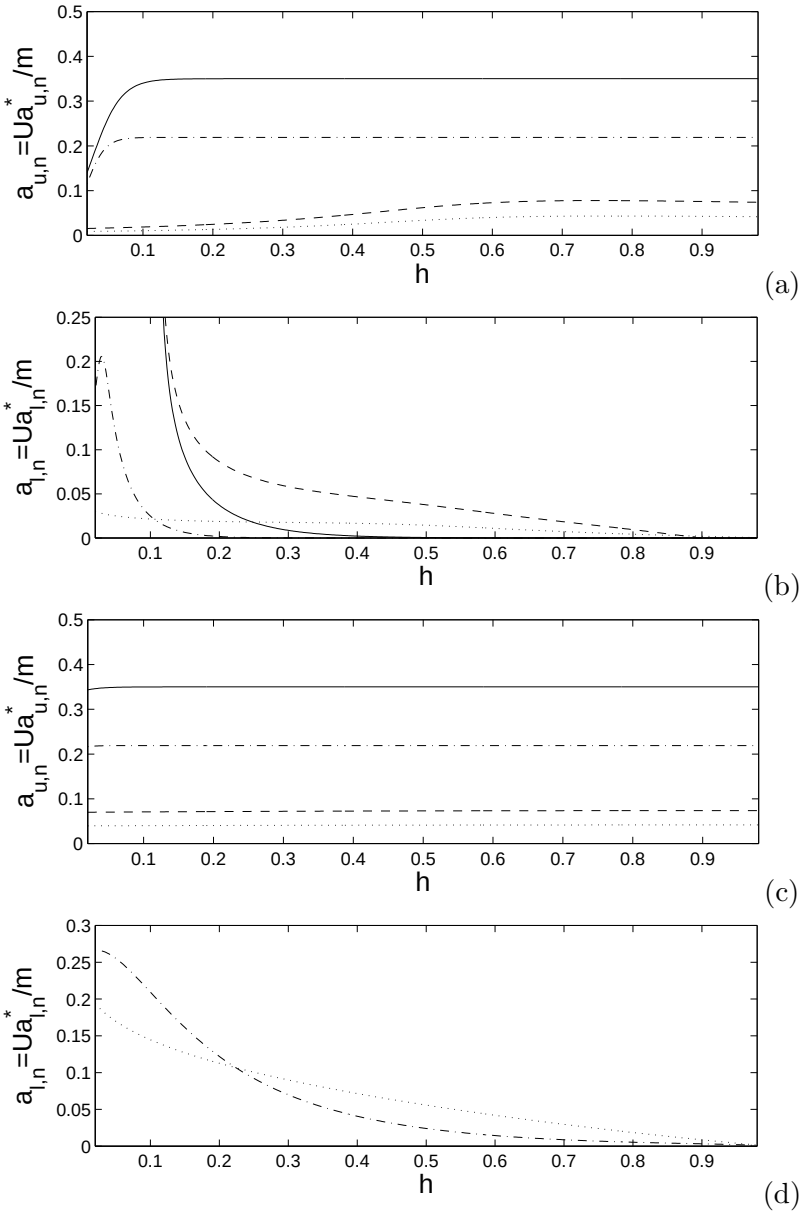

Figure 3-7: Far-field wave amplitudes $a_{u,n}$, $a_{\ell,n}$, as functions of h for $\mathcal{F}$=0.03, z_0=-0.02, τ=0.1, and, (a,b) $\mathcal{R}$=0.2; (c,d) $\mathcal{R}$=0.95. In figures (a,c) for $a_{u,n}$: $a_{u,1}$ —— ; $a_{u,2}$ - - - ; $a_{u,3}$ – · – ; and $a_{u,4}$ · · · . In figures (b,d) for $a_{\ell,n}$: $a_{\ell,5}$ —— ; $a_{\ell,6}$ - - - ; $a_{\ell,7}$ – · – ; and $a_{\ell,8}$ · · · .

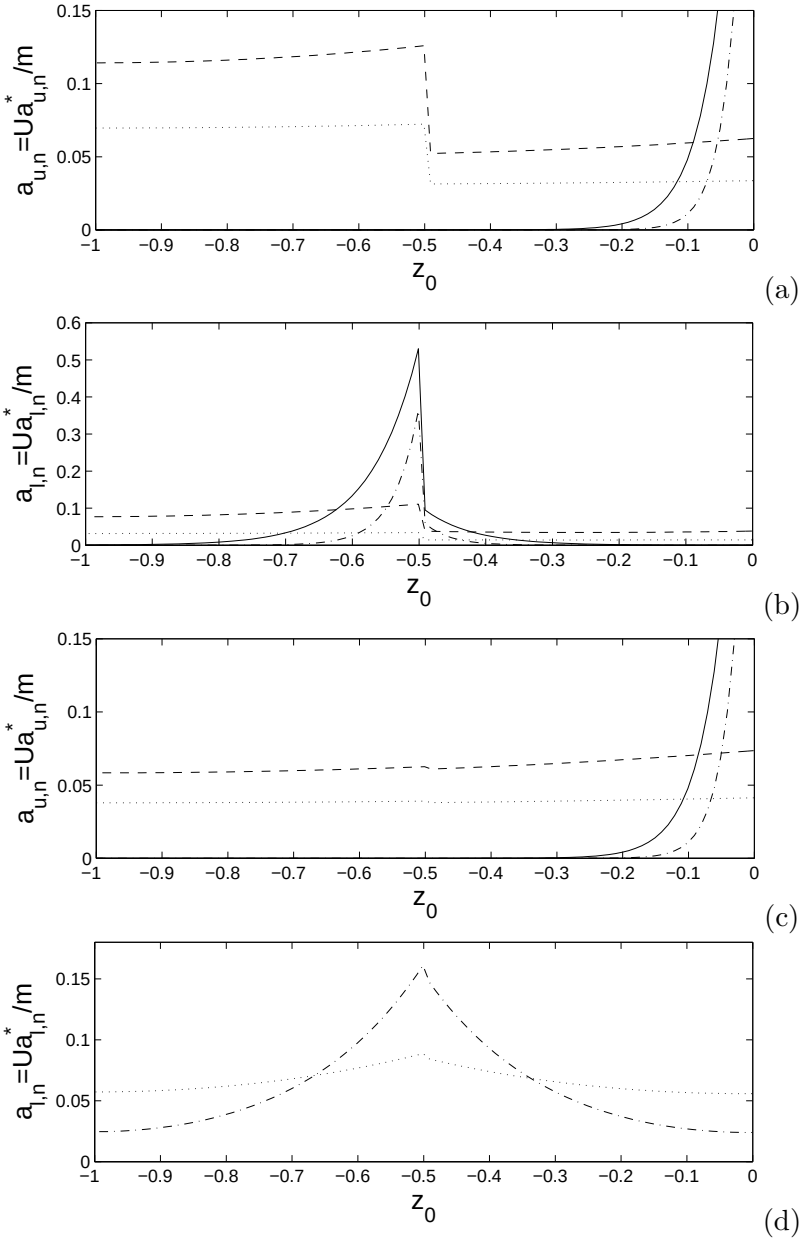

Figure 3-8: Far-field wave amplitudes $a_{u,n}$, $a_{\ell,n}$, as functions of z_0 for $\mathcal{F}$=0.03, τ=0.1, h=0.5, and, (a,b) $\mathcal{R}$=0.2; (c,d) $\mathcal{R}$=0.95. In figures (a,c) for $a_{u,n}$: $a_{u,1}$ —— ; $a_{u,2}$ - - - ; $a_{u,3}$ – · – ; and $a_{u,4}$ · · · . In figures (b,d) for $a_{\ell,n}$: $a_{\ell,5}$ —— ; $a_{\ell,6}$ - - - ; $a_{\ell,7}$ – · – ; and $a_{\ell,8}$ · · · .

3.3.5 Three-dimensional Green function

In three dimensions, the Green function can be similarly obtained. The analysis is in fact somewhat simpler because the fundamental singularity is no longer logarithmic (see Apendix B). The derivation is quite similar, and here the final expressions for the three-dimensional Green function is given. For the source in the upper layer,

$$\begin{aligned}\phi_u &= \frac{1}{r_4}+\frac{1}{r_5}+ \\ &\quad \int_{-\pi}^{\pi}\int_0^{\infty} (A\cosh\alpha kz + B\sinh kz)\; e^{i\alpha k(x\cos\theta+y\sin\theta)}\; dk\; d\theta\;, \qquad (3.3.62)\\ \phi_\ell &= \int_{-\pi}^{\pi}\int_0^{\infty} C\cosh\alpha k(z+1)\; e^{i\alpha k(x\cos\theta+y\sin\theta)}\; dk\; d\theta\;. \qquad (3.3.63)\end{aligned}$$

where $r_4^2 \equiv x^2+y^2+(z-z_0)^2$, $r_5^2 \equiv x^2+y^2+(z+2h+z_0)^2$. The coefficients A, B and C are obtained as

$$X = \frac{\hat{X}}{\lambda^4-(\omega_s^2+\omega_i^2)\lambda^2+\omega_s^2\omega_i^2} \qquad (3.3.64)$$

where X is either of A, B or C with

$$\begin{aligned}\hat{A} &= -\beta\,\lambda^4 - \frac{k\,(-\mathcal{R}sl\,\gamma + cl\,cu\,\beta + \mathcal{R}sl\,su\,\beta - sl\,\beta\,cu + sl\,\mathcal{R}\beta\,cu)\,\lambda^2}{sl\,su\,\mathcal{R}+cu\,cl} \\ &\quad -\frac{k^2 sl\,cu\,\beta\;(-1+\mathcal{R})}{sl\,su\,\mathcal{R}+cu\,cl} \qquad (3.3.65)\\ \hat{B} &= \frac{(sl\,cu\,\mathcal{R}\beta+\beta\,cl\,su-\mathcal{R}sl\,\gamma)\,\lambda^4}{sl\,su\,\mathcal{R}+cu\,cl} + \frac{k\beta\;(sl\,cu\,\mathcal{R}+cl\,su-sl\,su+sl\,su\,\mathcal{R})\,\lambda^2}{sl\,su\,\mathcal{R}+cu\,cl} \\ &\quad +\frac{k^2\beta\,sl\,su\;(-1+\mathcal{R})}{sl\,su\,\mathcal{R}+cu\,cl} \qquad (3.3.66)\\ \hat{C} &= -\frac{\mathcal{R}\left(cu^2\beta-cu\,\gamma-su^2\beta\right)\lambda^4}{cu\,cl+sl\,su\,\mathcal{R}} - \frac{\mathcal{R}k\left(-su^2\beta+cu^2\beta+su\,\gamma\right)\lambda^2}{cu\,cl+sl\,su\,\mathcal{R}} \qquad (3.3.67)\end{aligned}$$

where

$$\lambda = 1+\tau k\cos\theta, \quad \beta = \frac{\cosh\alpha k(z_0+h)}{\pi\;\exp(\alpha kh)}, \quad \gamma = \frac{\mathrm{e}^{-\alpha k(z_0+h)}}{\pi}\;.$$

For the source in the lower layer,

$$\phi_u = \int_{-\pi}^{\pi}\int_0^{\infty} \left(A\cosh\alpha kz + B\sinh\alpha kz\right)\, e^{i\alpha k(x\cos\theta + y\sin\theta)}\, dk\; d\theta\;, \tag{3.3.68}$$

$$\phi_\ell = \frac{1}{r_4} + \frac{1}{r_6} + \int_{-\pi}^{\pi}\int_0^{\infty} C\cosh\alpha k(z+1)\, e^{i\alpha k(x\cos\theta + y\sin\theta)}\, dk\; d\theta\;, \tag{3.3.69}$$

where $r_6^2 \equiv x^2 + y^2 + (2+z+z_0)^2$, and

$$\hat{A} = -\frac{k\lambda^2\beta\ (sl+cl)}{sl\ su\,\mathcal{R} + cl\ cu}, \qquad \hat{B} = -\frac{\lambda^4\beta\ (sl+cl)}{sl\,\mathcal{R}su + cl\ cu}, \tag{3.3.70}$$

$$\hat{C} = \frac{\beta\ (su\,\mathcal{R} - cu)\,\lambda^4}{sl\ su\,\mathcal{R} + cl\ cu} - \frac{\beta\,k\,(cu - su)\,\lambda^2}{sl\ su\,\mathcal{R} + cl\ cu} - \frac{\beta\,k^2 su\ (\mathcal{R}-1)}{sl\ su\,\mathcal{R} + cl\ cu}, \tag{3.3.71}$$

where

$$\lambda = 1 + \tau k\cos\theta, \quad \beta = \frac{\cosh\alpha k(z_0+1)}{\pi\ \mathrm{e}^{\alpha k(1-h)}}. \tag{3.3.72}$$

The limiting case of deep layers is instructive. For brevity, only the case with N_W=8 ($\tau < \tau_{cr,i}$) is considered. For the source in the upper layer:

$$\begin{aligned}
\phi_u &= \frac{1}{r_4} + \frac{1}{r_5} + \frac{2}{\pi}\int_0^{\frac{\pi}{2}}\int_0^{\infty} \frac{1}{\tau^4\cos^4\theta}(A\cosh\alpha kz + B\sinh\alpha kz) \\
&\quad \times \sum_{q=1,2,5,6} \frac{a_q}{k-k_q}\ \mathrm{e}^{\mathrm{i}\alpha k(x\cos\theta + y\sin\theta)}\ \mathrm{d}k\ \mathrm{d}\theta \qquad (3.3.73) \\
&\quad + \frac{2}{\pi}\int_{\frac{\pi}{2}}^{\pi}\int_0^{\infty} \frac{1}{\tau^4\cos^4\theta}(A\cosh\alpha kz + B\sinh\alpha kz) \\
&\quad \sum_{q=3,4,7,8} \frac{a_q}{k-k_q}\ \mathrm{e}^{\mathrm{i}\alpha k(x\cos\theta + y\sin\theta)}\ \mathrm{d}k\ \mathrm{d}\theta \qquad (3.3.74) \\
\phi_\ell &= \frac{2}{\pi}\int_0^{\frac{\pi}{2}}\int_0^{\infty} \frac{1}{\tau^4\cos^4\theta}\ C\cosh\alpha k(z+1) \\
&\quad \times \sum_{q=1,2,5,6} \frac{a_q}{k-k_q}\ \mathrm{e}^{\mathrm{i}\alpha k(x\cos\theta + y\sin\theta)}\ \mathrm{d}k\ \mathrm{d}\theta \qquad (3.3.75) \\
&\quad + \frac{2}{\pi}\int_{\frac{\pi}{2}}^{\pi}\int_0^{\infty} \frac{1}{\tau^4\cos^4\theta}\ C\cosh\alpha k(z+1) \\
&\quad \times \sum_{q=3,4,7,8} \frac{a_q}{k-k_q}\ \mathrm{e}^{\mathrm{i}\alpha k(x\cos\theta + y\sin\theta)}\ \mathrm{d}k\ \mathrm{d}\theta \qquad (3.3.76)
\end{aligned}$$

where

$$a_q = \prod_{j=\{1,2,5,6\}-q} \frac{1}{k_q - k_j} \quad \text{for} \quad q = 1,2,5,6; \tag{3.3.77}$$

$$a_q = \prod_{j=\{3,4,7,8\}-q} \frac{1}{k_q - k_j} \quad \text{for} \quad q = 3,4,7,8. \tag{3.3.78}$$

For the source in the lower layer, the expressions for the deep layers Green function are:

$$\begin{aligned}
\phi_u &= \frac{2}{\pi}\int_0^{\frac{\pi}{2}}\int_0^{\infty} \frac{1}{\tau^4\cos^4\theta}(A\cosh\alpha kz + B\sinh\alpha kz) \\
&\quad \times \sum_{q=1,2,5,6} \frac{a_q}{k-k_q}\, \mathrm{e}^{\mathrm{i}\alpha k(x\cos\theta + y\sin\theta)}\, \mathrm{d}k\, \mathrm{d}\theta \qquad (3.3.79) \\
&\quad + \frac{2}{\pi}\int_{\frac{\pi}{2}}^{\pi}\int_0^{\infty} \frac{1}{\tau^4\cos^4\theta}(A\cosh\alpha kz + B\sinh\alpha kz) \\
&\quad \times \sum_{q=3,4,7,8} \frac{a_q}{k-k_q}\, \mathrm{e}^{\mathrm{i}\alpha k(x\cos\theta + y\sin\theta)}\, \mathrm{d}k\, \mathrm{d}\theta \qquad (3.3.80) \\
\phi_\ell &= \frac{1}{r_4} + \frac{1}{r_6} + \frac{2}{\pi}\int_0^{\frac{\pi}{2}}\int_0^{\infty} \frac{1}{\tau^4\cos^4\theta}\, C\cosh\alpha k(z+1) \\
&\quad \times \sum_{q=1,2,5,6} \frac{a_q}{k-k_q}\, \mathrm{e}^{\mathrm{i}\alpha k(x\cos\theta + y\sin\theta)}\, \mathrm{d}k\, \mathrm{d}\theta\,, \qquad (3.3.81) \\
&\quad + \frac{2}{\pi}\int_{\frac{\pi}{2}}^{\pi}\int_0^{\infty} \frac{1}{\tau^4\cos^4\theta}\, C\cosh\alpha k(z+1) \\
&\quad \times \sum_{q=3,4,7,8} \frac{a_q}{k-k_q}\, \mathrm{e}^{\mathrm{i}\alpha k(x\cos\theta + y\sin\theta)}\, \mathrm{d}k\, \mathrm{d}\theta\,. \qquad (3.3.82)
\end{aligned}$$

3.4 Direct numerical simulation

For the general problem involving possibly multiple bodies and arbitrary time-dependence in the motions, the solution can be more generally and efficiently obtained by a direct numerical method. Here a highly efficient numerical scheme based on spectral expansion of potentials is presented (§3.4.1). The numerical method is general for two and three dimensional problems and can be extended to account for nonlinear effects Tsai & Yue (1996). Here the focus will be on the linearized two-dimensional problem.

3.4.1 Formulation of the spectral method

Consider the linearized governing equations (3.2.1) with a point source located in either the upper or lower layer. For later convenience, let's define $\varphi_u = \phi_u + \bar{\phi}_u$, $\varphi_\ell = \phi_\ell + \bar{\phi}_\ell$;

where $\bar{\phi}_u, \bar{\phi}_\ell$ represent the potential of the point source in an unbounded homogeneous fluid, and, in the neighborhood of the interface, let's define a new potential $\psi(x,z,t) \equiv \phi_\ell(x,z,t) - \mathcal{R}\phi_u(x,z,t)$. In terms of these quantities, and in the frame of reference moving with the disturbance, the kinematic and dynamic boundary conditions on the surface and interface can be written in the forms:

$$\eta_{u,t} = -U\eta_{u,x} + \phi_{u,z} + \bar{\phi}_{u,z} \ , \quad z = 0 \ , \tag{3.4.83a}$$

$$\phi_{u,t} = -U\phi_{u,x} - g\eta_u - \bar{\phi}_{u,t} \ , \quad z = 0 \ , \tag{3.4.83b}$$

$$\eta_{\ell,t} = -U\eta_{\ell,x} + \phi_{u,z} + \bar{\phi}_{u,z} \ , \quad z = -h_u \tag{3.4.83c}$$

$$\psi_{,t} = -U\psi_{,x} - g\eta_\ell(1-\mathcal{R}) - (\bar{\phi}_{\ell,t} - \mathcal{R}\bar{\phi}_{u,t}) \ , \ z = -h_u \ . \tag{3.4.83d}$$

In the numerical simulation, (3.4.83) are used as evolution equations for $\eta_u(x,t)$, $\phi_u(x,0,t)$, $\eta_\ell(x,t)$ and $\psi(x,-h_u,t)$, given the vertical surface velocity, $\phi_{u,z}(x,0,t)$, and the vertical interface velocities, $\phi_{u,z}(x,-h_u,t)$ and $\phi_{\ell,z}(x,-h_u,t)$, which are obtained from the solution of the boundary-value problem.

To find these velocities, the solutions for ϕ_u and ϕ_ℓ are constructed in terms of Fourier basis functions:

$$\phi_u(x,z,t) = \sum_{n=-N}^{N-1} \left\{ A_n(t)\frac{\cosh[k_n(z+h_u)]}{\cosh(k_n h_u)} + B_n(t)\frac{\sinh(k_n z)}{\cosh(k_n h_u)} \right\} \mathrm{e}^{\mathrm{i}k_n x} \tag{3.4.84}$$

$$\phi_\ell(x,z,t) = \sum_{n=-N}^{N-1} C_n(t)\frac{\cosh[k_n(z+h_u+h_\ell)]}{\cosh(k_n h_\ell)} \ \mathrm{e}^{\mathrm{i}k_n x} \tag{3.4.85}$$

where k_n=$2\pi n/L$ with L being the length of the computational domain, and A_n, B_n, and C_n are the complex modal amplitudes. Clearly, ϕ_u and ϕ_ℓ in (3.4.84) and (3.4.85) are harmonic and satisfy the bottom boundary condition (3.2.1h). It is to be noted that, for sufficiently smooth ϕ_u and ϕ_ℓ, (3.4.84) and (3.4.85) converge exponentially with increasing N. If initial conditions are given at time t_0:

$$\phi_u(x,0,t_0) = f_1(x), \qquad \psi(x,-h_u,t_0) = f_2(x), \tag{3.4.86}$$

then, by satisfying the remaining boundary conditions, the unknown amplitudes A_n, B_n,

and C_n are obtained as

$$A_n = \tilde{f}_{1n} \,, \tag{3.4.87a}$$

$$B_n = \frac{\tilde{f}_{2n} + \mathcal{R}\tilde{f}_{1n}/\cosh(k_n h_u)}{\text{cotanh } k_n h_\ell + \mathcal{R}\tanh k_n h_u} \,, \tag{3.4.87b}$$

$$C_n = \frac{B_n}{\tanh k_n h_\ell} \,. \tag{3.4.87c}$$

for n=0, $\pm 1, \ldots, \pm N$. In (3.4.87), $\tilde{f}_{1n}$ and $\tilde{f}_{2n}$ are respectively the $n-$th Fourier modal amplitudes of $f_1(x)$ and $f_2(x)$. Once the boundary-value solution is obtained, the vertical velocities of the fluid on the free surface and interface are obtained from (3.4.84) and (3.4.85):

$$\phi_{u,z}(x,0,t) = \sum_{n=-N}^{N} k_n \left[A_n(t)\tanh(k_n h_u) + B_n(t)\right] e^{ik_n x}, \tag{3.4.88a}$$

$$\phi_{u,z}(x,-h_u,t) = \sum_{n=-N}^{N} k_n B_n(t) e^{ik_n x} \,, \tag{3.4.88b}$$

$$\phi_{\ell,z}(x,-h_u,t) = \sum_{n=-N}^{N} k_n C_n(t)\tanh(k_n h_u) e^{ik_n x} \,. \tag{3.4.88c}$$

To complete the evolution equations (3.4.83), if the source is located in the lower layer

$$\bar{\phi}_u = 0 \,, \tag{3.4.89}$$

$$\bar{\phi}_\ell = \frac{m_0}{2\pi}\sin\omega_0 t(\ln r_1 + \ln r_2) \,, \tag{3.4.90}$$

where

$$r_1^2 = \sin^2\left(\frac{x-x_0}{2L/\pi}\right) + \sinh^2\left(\frac{z-z_0}{2L/\pi}\right), \tag{3.4.91}$$

$$r_2^2 = \sin^2\left(\frac{x-x_0}{2L/\pi}\right) + \sinh^2\left(\frac{z+2h_u+2h_\ell+z_0}{2L/\pi}\right) \,, \tag{3.4.92}$$

and if the source is located in the upper layer:

$$\bar{\phi}_u = \frac{m_0}{2\pi}\sin\omega_0 t(\ln r_1 + \ln r_2) \,, \tag{3.4.93}$$

$$\bar{\phi}_\ell = 0 \,, \tag{3.4.94}$$

	$N=8$	$N=16$	$N=32$
Err	0.28×10^{-2}	0.65×10^{-5}	0.54×10^{-12}

Table 3.1: Maximum error of the vertical interface velocity of a linearized wave matching the elevation profile of a Stokes wave in a two-layer fluid with $\epsilon = ka$ =0.1, h_ℓ/h_u=1, and $\mathcal{R}$=0.95.

where

$$r_1^2 = \sin^2\left(\frac{x-x_0}{2L/\pi}\right) + \sinh^2\left(\frac{z-z_0}{2L/\pi}\right), \tag{3.4.95}$$

$$r_2^2 = \sin^2\left(\frac{x-x_0}{2L/\pi}\right) + \sinh^2\left(\frac{z+2h_u+z_0}{2L/\pi}\right). \tag{3.4.96}$$

The time simulation of the initial-boundary-value problem consists of two main steps: (a) at each time t, given the surface and interface elevations $\eta_u(x,t)$ and $\eta_\ell(x,t)$, the surface potential and interfacial potentials $\phi_u(x,0,t)$ and $\psi(x,-h_u,t)$=$\phi_\ell(x,-h_u,t)-\mathcal{R}\phi_u(x,-h_u,t)$; solve the boundary-value problems for ϕ_u and ϕ_ℓ and evaluate the surface and interfacial velocities $\phi_{u,z}(x,0,t)$, $\phi_{u,z}(x,-h_u,t)$ and $\phi_{\ell,z}(x,-h_u,t)$; and (b) integrate the evolution equations (3.4.83) in time to obtain the new values of $\eta_u(x,t+\Delta t)$, $\eta_\ell(x,t+\Delta t)$, $\phi_u(x,0,t+\Delta t)$ and $\psi(x,-h_u,t+\Delta t)$, where Δt is the time step. In the present work, a fourth-order Runge-Kutta integration scheme (with global truncation error $O((\Delta t/T)^4)$) is used. The two steps (a)-(b) are repeated starting from initial values.

To check the correctness and accuracy of our numerical scheme, an exact linearized solution for a wave in two fluid layers with a surface and interfacial wave elevations matching a Stokes wave solution is used. Table 3.1 shows the exponential convergence in interface vertical velocity (compared to exact values) of the numerical spectral method with number of modes N.

3.4.2 Comparison with Theory

The numerical scheme of course provides an independent check of our analytic results in §3. For the numerical solution, the problem of §3 in a frame of reference moving with the disturbance (at x=0) and starting from quiescent initial conditions is considered. The simulation is performed until steady state is reached in a finite portion $|x| < \bar{L}/2$ of the (periodic) computational domain whose length L is chosen to be sufficient large so that the

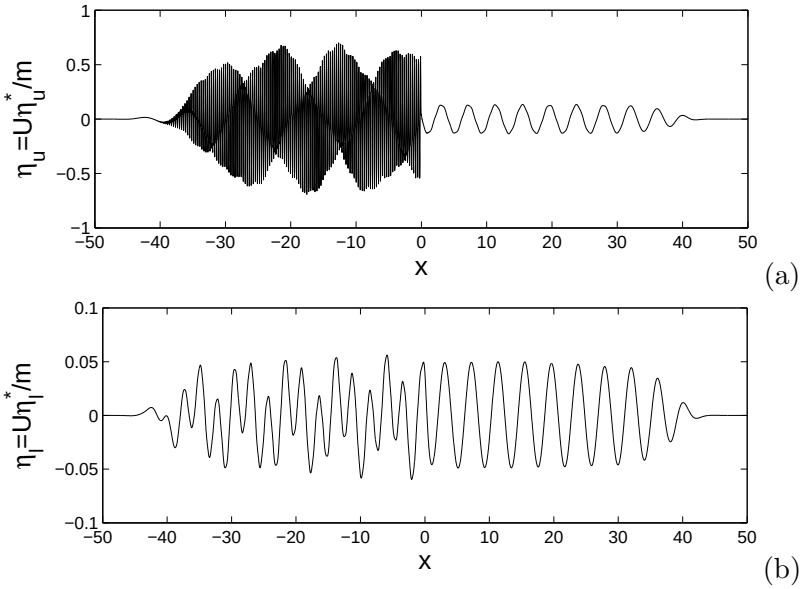

Figure 3-9: Direct simulation results for (a) free surface, and (b) interfacial, wave elevations for $\mathcal{R}$=0.2, $\mathcal{F}$=0.03, τ=0.16, z_0=-0.02, h=0.5. The numerical parameters are N=4096, δt=0.03, simulation time T_f=1000.

solution within $\bar{L}$ is unaffected. In practice, this can be achieved by applying a tapering filter for $|x| > L_f/2$ where $\bar{L} < L_f < L$. With this treatment, the simulation can proceed for a long time for a fixed $\bar{L}$ without increasing L.

Figures 3-9 show the surface and interfacial elevation for a problem with $\mathcal{R}$=0.2, $\mathcal{F}$=0.032, τ=0.16, z_0=-0.02, and h=0.5 after a simulation time of T_f=1000. The computational parameters are: L=100, L_f=75, N=4096, and δt=0.03. With these parameters, the solution has reached steady state for $\bar{L} \approx 65$. For this set of parameters, $\tau_{cr,\ell} < \tau < \tau_{cr,u}$, N_W=6 (four surface and two internal mode waves) and no internal-mode wave propagate ahead of the disturbance (the interface wave elevation seen in front of the disturbance in figure 3-9b is associated with the k_2 forward traveling surface-mode wave). Note also that the magnitudes of $a_{u,n}$ are greater than those of $a_{\ell,n}$ in figure 3-9 because of the (somewhat arbitrary) choice of z_0=-0.02.

Figure 3-10 compares the surface elevation computed by direct simulation with theoretical results of §3. For the analytical results, the principal value integrals in (3.3.38), (3.3.39) are evaluated using adaptive Lobatto quadrature. The comparison is almost within graphical accuracy, with the numerics capturing both the small k_2 wavenumber wave train ahead of the source and the modulated wave train (containing the small k_4 wavenumber

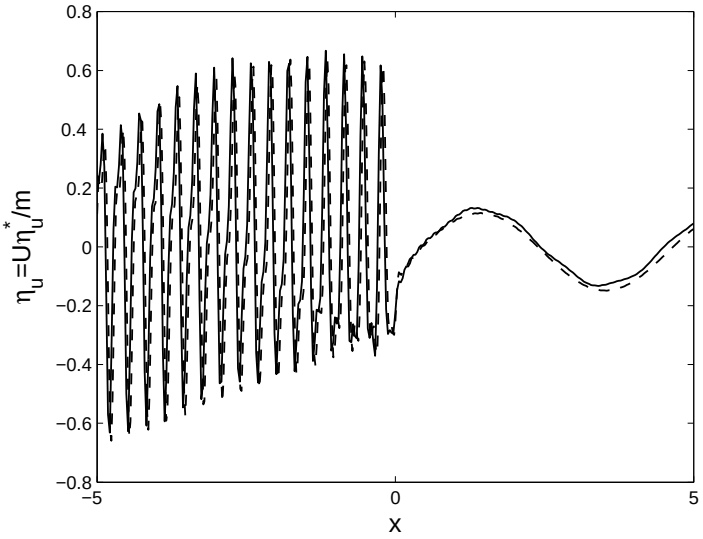

Figure 3-10: Comparison of direct simulation (——) with theoretical prediction (- - -) for the near field of the moving disturbance for $\mathcal{R}$ =0.2, $\mathcal{F}$=0.03, τ=0.16, z_0=-0.02, h=0.5. The numerical parameters are N=4096, δt=0.03, and T_f=750.

and the larger k_1, k_3 wavenumber components) behind. To compare the predictions for the far-field amplitudes, the direct simulation results need to be processed for the constituent wave components. For a wavefield with N_c (expected) wave components, the amplitudes and phases at x are obtained by sampling the numerical result at say $N_p > 2N_c$ uniformly spaced points (δx apart) centered at x, and then solving for the $2N_c$ unknown amplitude and phases by inverting an overdetermined linear algebraic system. The choice of δx and N_p is somewhat important, and it generally required $k_{max}\delta x \ll 1$ and $N_p k_{min}\delta x \gtrsim O(1)$ to capture respectively the shortest and longest waves.

Figures 3-11 and 3-12 show such set of results obtained from the numerics for the conditions: (a) N_W=8: $\mathcal{F}$=0.032, τ=0.16, z_0=-0.02, h=1 and $\mathcal{R}$=0.2; and (b) N_W=4: $\mathcal{F}$=0.128, τ=0.32, z_0=-0.02, h=1 and $\mathcal{R}$=0.95; respectively. The numerical results are compared to the far-field theoretical predictions (tabulated in Table 3.2). The simulation results and theoretical far-field amplitudes compare well for all the wave modes with the comparison somewhat better for the higher wavenumber components, since there are more of these waves sampled in the (finite) computational domain.

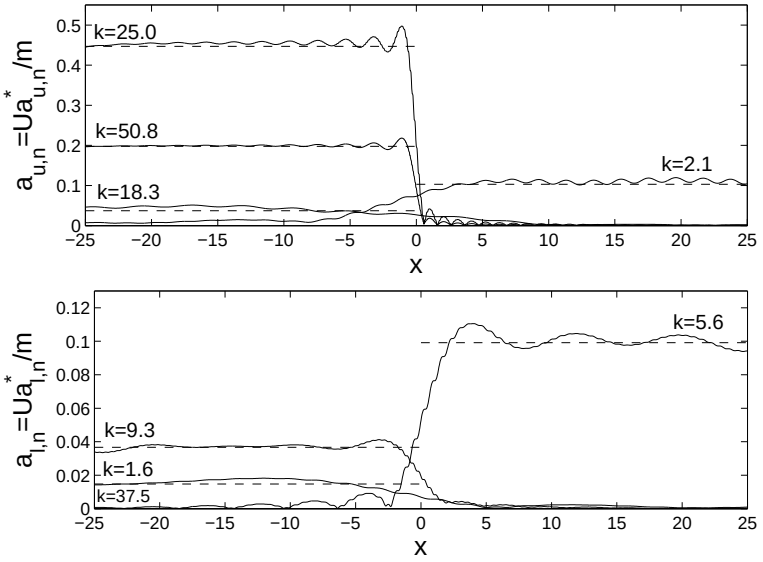

Figure 3-11: Comparison of numerical simulations results (——) for the farfield wave amplitudes compared with asymptotic theoretical values (- - -) for $\mathcal{R}$=0.2, $\mathcal{F}$=0.032, τ=0.16, z_0=-0.02, h=0.5. The numerical parameters are N=4096, δt=0.03, and T_f=1000.

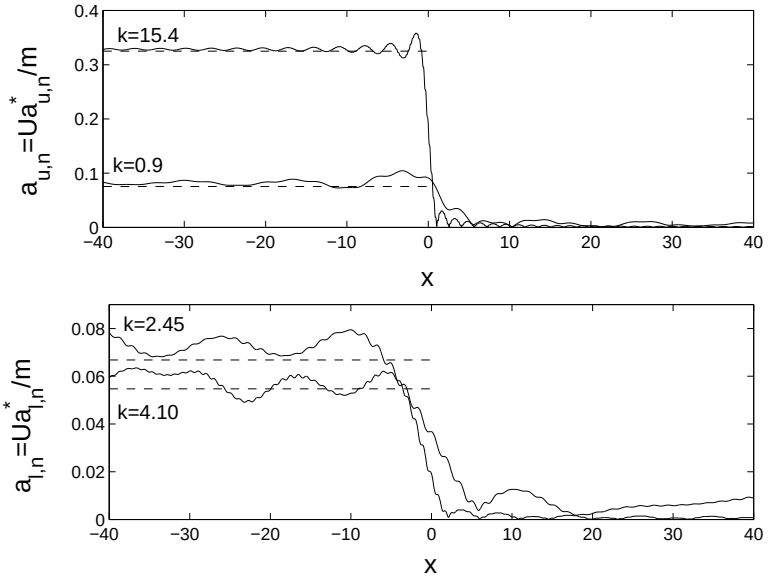

Figure 3-12: Comparison of numerical simulations results (——) for the farfield wave amplitudes compared with asymptotic theoretical values (- - -) for $\mathcal{R}$=0.95, $\mathcal{F}$=0.128, τ=0.32, z_0=-0.02, h=0.5. The numerical parameters are N=4096, δt=0.03, and T_f=1000.

	(a)				(b)			
n	k	ω	a_u	a_ℓ	k	ω	a_u	a_ℓ
1	25.0	5.00	0.447	0.000	–	–	–	–
2	2.1	1.34	0.130	0.027	–	–	–	–
3	50.8	7.13	0.198	0.000	15.38	3.92	0.325	0.001
4	1.1	-0.82	0.037	0.011	0.87	-0.72	0.075	0.035
5	9.3	2.49	0.004	0.037	–	–	–	–
6	5.6	1.89	0.041	0.099	–	–	–	–
7	37.5	5.00	0.000	0.000	4.10	0.31	0.001	0.055
8	1.6	-0.74	0.017	0.015	2.45	-0.22	0.001	0.067

Table 3.2: Theoretical values for the dimensionless wave-number (k), frequency (ω), and surface- and interface-mode wave amplitudes a_u ,a_ℓ for (a) $\mathcal{R}$=0.2, h=0.5, $\mathcal{F}$=0.032, τ=0.16, z_0=-0.02; and (b)$\mathcal{R}$=0.95, $\mathcal{F}$=0.128, h=0.5, τ=0.32, z_0=-0.02.

3.5 Conclusion

The linear problem of wave generation by a translating pulsating point source in a two-layer density stratified fluid is studied analytically and numerically. The problem is motivated by the possibility of observing/characterizing the waves associated with ships and submarines in strong stratified waters that may be present, for example, in warm littoral zones.

From the dispersion relation, it is shown that N_w=4,6 or 8 waves can exist at the farfield of the disturbance depending on the parameters associated with the disturbance ($\mathcal{F}$, τ, z_0) and the ocean body ($\mathcal{R}$, h). The two- and three-dimensional Green functions are obtained analytically by solving the respective boundary-value problem. The Green functions give the entire wavefield and, of special interest, the far-field amplitudes associated with the N_w waves. These amplitudes depend qualitatively on the location of the disturbance (in the upper or lower fluid), the Froude number $\mathcal{F}$ and dimensionless frequency of pulsation τ of the disturbance, and the density ratio $\mathcal{R}$ and depth ratio h of the stratified layers. These dependencies are elucidated and discussed for $\mathcal{R}$=0.2 and 0.95, the latter being typical of real oceans.

For direct simulation, a spectral-based numerical scheme is developed. The numerical scheme is capable of simulating the general problem involving one or more bodies moving/oscillating arbitrarily with time. The numerical method, of course, also provides an independent check of the theoretical results, which is performed. An extension of out numerical scheme to a blunt body is presented in Appendix E.

Chapter 4

Resonance between waves of an oscillating/translating disturbance in two-layer density stratified fluids

4.1 Introduction

In this chapter, the second order (triad) resonance between ship waves in a two-layer density stratified fluid is considered analytically and numerically. A steadily translating and sinusoidally oscillating singularity in a homogeneous fluid is known to generate four unsteady waves and one co-moving wave, as seen in the ship frame of reference. Each pair of these waves, although may satisfy the resonance condition with a third free wave, can not exchange energy and hence no new wave can be formed (D′yachenko & Zakharov, 1994). However, if stratification is taken into account, as is the case in many open seas, oceans and lakes, resonance triads with non-zero amplitudes may form: two surface wave and one internal wave or two internal waves and one surface wave are possible candidates for such a resonance. Here we show that the existence of line of the sudden density change (i.e. the thermocline) along with second order nonlinearity can play a significant role in optical (non-acoustic) detection of underwater/surface vehicles.

In a two-layer density stratified fluid, Ball (1964) showed that two oppositely traveling surface waves can resonate an internal wave. Later on, Wen (1995*a*); Hill & Foda (1996) and Jamali *et al.* (2003) showed that similar triad resonance may occur between two oppositely

traveling internal waves and one surface wave. To close the second order problem in a two-layer setup, the effect of topography (Bragg resonance) was taken into account in chapter one and two of this thesis. The third order analysis, where Bragg resonance is between three free waves and a bottom topography components was further studied.

Motivated by the need for the determination of the trace of ships and submarines in strong stratified waters such as littoral zones of warm seas and oceans, here we consider the second order problem of interaction between waves generated by an oscillatory singularity that steadily translates in a two-layer density stratified fluid. Depending on the ratio of depths and densities of fluid layers, Froude number and the frequency of oscillation of the disturbance, linear theory predicts up to eight distinct free waves at the farfield of the object. Two out of these eight waves, that only exist if the source speed and frequency is small enough, advance ahead of the source and the rest trail the ship (chapter four).

Although exact resonance condition is only satisfied at a finite number of condition, countless near-resonance cases are possible; some with the possibility of generating high amplitude near-resonance waves. To develop an efficient numerical scheme for the general problem of accelerating/variable strength disturbance that takes into account all resonance and near-resonance interactions a spectral-based algorithm is also developed in this chapter. The algorithm is the extension of a high-order spectral method originally developed to simulate nonlinear gravity wave-wave interactions (Dommermuth & Yue, 1987). Cross validation of numerical-analytical results are performed.

4.2 Problem Formulation

The formulation is the nonlinear extension of the formulation considered in chapter four. A Cartesian coordinate system is defined with x, y-axis on the mean free surface and z-axis positive upward. A two-layer density stratified fluid is considered where the upper and lower fluid layers have respectively mean depths h_u and h_ℓ, and fluid densities ρ_u and ρ_ℓ (subscripts u and ℓ hereafter denote quantities associated with the upper and lower fluid layers, respectively). The two-layer fluid rests on a flat horizontal bottom $z = -h_u - h_\ell$. A point source initially located at $x = x_0$ travels in the upper layer with a speed $\mathbf{u} = U\hat{i}$ at a fixed depth $z = -z_0$ while its strength is varying sinusoidally with time according to $m = m_0 \cos \omega_0 t$ where m_0 is the amplitude of the source strength and ω_0 is its frequency of

oscillation.

Assume that the fluids in both layers are homogeneous, incompressible, immiscible and inviscid so that the fluid motion is irrotational. The effect of surface tension is neglected. The flow in each layer is described by a velocity potential, $\phi_u(x,y,z,t)$ and $\phi_\ell(x,y,z,t)$. The nonlinear governing equations are:

$$\nabla^2\phi_u = m_0\ \delta(x_0+Ut,0,-z_0)\cos\omega_0 t \qquad -h_u+\eta_\ell < z < \eta_u \tag{4.2.1a}$$

$$\nabla^2\phi_\ell = 0 \qquad -h_u-h_\ell+\eta_b < z < -h_u+\eta_\ell \tag{4.2.1b}$$

$$\eta_{u,t}+\eta_{u,x}\phi_{u,x}-\phi_{u,z}=0 \qquad z=\eta_u \tag{4.2.1c}$$

$$\phi_{u,t}+\tfrac{1}{2}(\phi_{u,x}^2+\phi_{u,z}^2)+g\eta_u=0 \qquad z=\eta_u \tag{4.2.1d}$$

$$\eta_{\ell,t}+\eta_{\ell,x}\phi_{u,x}-\phi_{u,z}=0 \qquad z=-h_u+\eta_\ell \tag{4.2.1e}$$

$$\eta_{\ell,t}+\eta_{\ell,x}\phi_{\ell,x}-\phi_{\ell,z}=0 \qquad z=-h_u+\eta_\ell \tag{4.2.1f}$$

$$\rho_u[\phi_{u,t}+\tfrac{1}{2}(\phi_{u,x}^2+\phi_{u,z}^2)+g\eta_\ell]-$$
$$\rho_\ell[\phi_{\ell,t}+\tfrac{1}{2}(\phi_{\ell,x}^2+\phi_{\ell,z}^2)+g\eta_\ell]=0 \qquad z=-h_u+\eta_\ell \tag{4.2.1g}$$

$$\eta_{b,x}\phi_{\ell,x}-\phi_{\ell,z}=0 \qquad z=-h_u-h_\ell+\eta_b. \tag{4.2.1h}$$

where $\mathcal{R}\equiv\rho_u/\rho_\ell$ is the density ratio, $\eta_u(x,y,t)$ and $\eta_\ell(x,y,t)$ are the elevations of the free-surface and the interface respectively, g is the gravity acceleration, and δ is the Dirac's delta function. If the source is located in the lower layer, the right-hand sides of equations (4.2.1a) and (4.2.1b) need to be exchanged, but the rest of the discussion in this section remains the same.

4.3 The Resonance

Three waves in a homogeneous fluid are known to be non-resonant (D′yachenko & Zakharov, 1994). In a two-layer density stratified fluid however, Ball (1964) showed that two surface mode waves and a shorter internal mode wave can form a trial resonance if appropriate resonance condition is satisfied. Later, Wen (1995*b*); Hill & Foda (1996) and Jamali (1998) showed that similar possibility exist for a triad resonance between two internal mode waves and a longer surface mode wave.

In this section it is shown that in a two-layer density stratified fluid triad resonances can

happen between two of disturbance waves and a third free wave. In practice the disturbance oscillation is due to the excitation forcing of an incident wave. The disturbance generated N_W waves have the same encounter frequency as the encounter frequency of incident wave ($\pm\omega_0$). Therefore incident wave must be one of the N_W disturbance waves. However, while disturbance waves appear either in front on behind the ship and not both, the incident wave exist on both sides.

For the resonance to happen between two out of N_W disturbance generated waves, namely (k_I, ω_I) and (k_{II}, ω_{II}), we have to have $\mathrm{D}(k_r, \omega_r) = 0$ where $k_r = k_I \pm k_{II}$ and $\omega_r = \omega_I \pm \omega_{II}$. Although in deep-layer limiting case closed form solution for wavenumbers of disturbance wave and hence resonance condition can be found, in a finite depth water the conditions are sought by searching the entire space of parameters.

Before considering a general case of finite depth dispersion relation we notice that an infimum wavenumber of generated waves can be found using shallow water dispersion relation:

$$k_{inf} = \frac{\omega_0}{U + \sqrt{gH}}, \tag{4.3.2}$$

or in dimensionless variables

$$k^*_{inf} = \frac{\sqrt{\mathrm{Fr}}}{\tau(1 + \sqrt{\mathrm{Fr}})} \tag{4.3.3}$$

Having the infimum wavenumber, it can be shown that under the following condition, deep layer assumption can be employed:

$$h = O(1), \quad \frac{\tau}{\sqrt{\mathrm{Fr}}} \gg 1, \quad \mathrm{Fr} < O(1/\epsilon). \tag{4.3.4}$$

In many physical situations this is correspond to a finite frequency of oscillation and very small forward motion. Under the above assumption closed form solutions can be found for the wavenumber of generated waves.

Table 4.1 lists the values of τ for which resonance occurs among the wake waves of an oscillating vessel in a two-layer density stratified fluid under assumptions (4.3.2,4.3.3) with $R = 0.9$. It is to be noted that if a resonant wave has a wavenumber less than the minimum wavenumber of original ship waves, it needs extra care and may even disappear.

τ	*wave* 1	*wave* 2	ω_r/ω_0	I/S
0.0027	6	-8	2.011	S
0.0522	1	-3	2.011	I
0.0699	1	-7	11.9	S
0.0900	2	8	0.5848	I
0.0900	1	7	11.11	S
0.1235	3	-7	8.1	S
0.1235	4	-8	0.4263	I
0.1302	2	-8	1.647	S
0.1516	2	4	0.3471	I
0.1843	2	-7	0.6263	I
0.1873	3	7	6.889	S
0.2493	1	-2	0.2111	I
0.2499	1	-7	1.464	S
0.6556	4	7	0.3626	I
1.233	4	-7	0.8113	S
3.335	4	-8	0.2998	S
4.737	7	-8	0.2111	S
9.000	3	4	0.1111	I

Table 4.1: Resonance τ in deep two-layer density stratified fluid for $R = 0.9$. At each given τ, resonance can occur between *wave* 1 and *wave* 2 (consult figure 4-1) that generates an internal or surface mode resonant wave (last column) with relative frequency ω_r/ω_0 where ω_0 is the ship oscillating frequency.

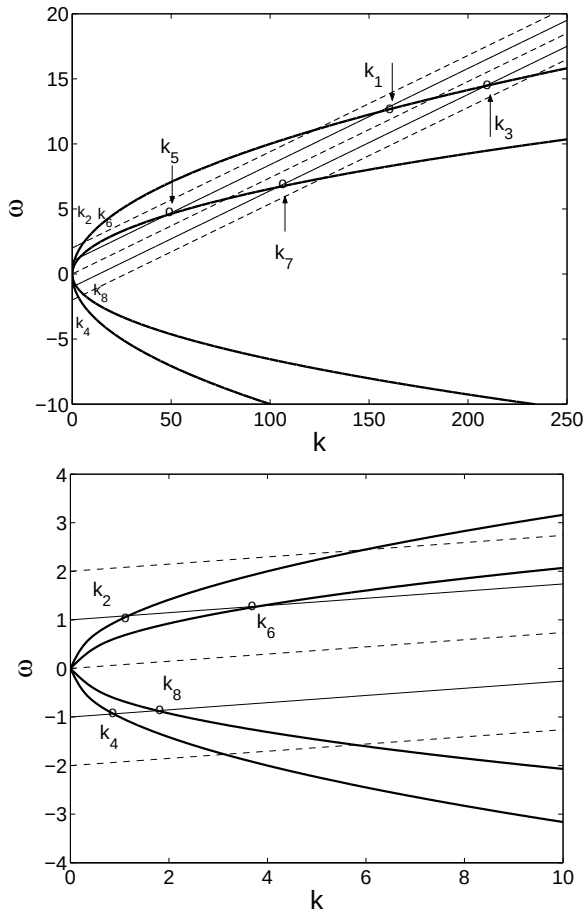

Figure 4-1: Schematic of the dispersion relationship for far-field waves generated by a moving and oscillating disturbance in a two-layer density stratified fluid. The figure also shows the numbering convention for these waves. Encounter frequency lines $\omega = \pm 1 + \tau k$: ——, can have up to N_w=8 intersections with the dispersion relation curves (thick solid curves, equation (1.2.7)). Parameters are $R = 0.4$, Fr $= 0.001$, $\tau = 0.074$ and $h = 1$, and, figure b is the near zero close up of figure a.

	τ	*wave* 1	*wave* 2	ω_r/ω_0	I/S
a_1	0.0522	1	-3	2.0111	I
a_2	0.0699	1	-7	11.902	S
a_3	0.0894	2	8	0.58833	I
a_4	0.0900	1	7	11.1111	S
a_5	0.1235	3	-7	8.0973	S
a_6	0.1236	4	-8	0.42525	I
a_7	0.1302	2	-8	1.6469	S
a_8	0.1516	2	4	0.34708	I
a_9	0.1843	2	-7	0.62626	I
a_{10}	0.1873	3	7	6.889	S
a_{11}	0.2493	1	-2	0.21225	I
a_{12}	0.2499	1	-7	1.4647	S
a_{13}	0.6557	4	7	0.36258	I
a_{14}	1.233	4	-7	0.8113	S
a_{15}	3.337	4	-8	0.29975	S
a_{16}	4.738	7	-8	0.21108	S
a_{17}	9.004	3	4	0.11108	I

	τ	*wave* 1	*wave* 2	ω_r/ω_0	I/S
b_1	0.2747	4	7	0.32059	I
b_2	1.234	4	-7	0.72906	S
b_3	2.821	4	-8	0.3189	S
b_4	3.886	7	-8	0.23132	S
b_5	9.004	3	4	0.11108	I

	τ	*wave* 1	*wave* 2	ω_r/ω_0	I/S
c_1	9.075	3	4	0.11054	I

Table 4.2: Resonance cases in a finite depth two-layer density stratified fluid for R=0.9, h=2, and: $\mathcal{F}$=0.005< $\mathcal{F}_{cr_i}$ (left table); $\mathcal{F}_{cr_i} < \mathcal{F}$=0.60< $\mathcal{F}_{cr_s}$ (right top table); $\mathcal{F}$=2> $\mathcal{F}_{cr_s}$ (right bottom table). At each given τ, resonance can occur between *wave* 1 and *wave* 2 (consult figure 4-1) that generates an internal or surface mode resonant wave (last column) with relative frequency ω_r/ω_0 where ω_0 is the ship oscillating frequency.

Table 4.2 lists the values of τ for which a resonance occurs among the disturbance waves. Chosen parameters are $\mathcal{R}$=0.9, $h = 2$ and for a. $\mathcal{F}$=0.005< $\mathcal{F}_{cr_i}$; b. $Fr_{cr_i} < \mathcal{F}$=0.60< $\mathcal{F}_{cr_s}$; and c. $\mathcal{F}$=2> $\mathcal{F}_{cr_s}$. Clearly as $\mathcal{F}$ increases the number of resonance cases decreases.

Resonance cases can be categorized into three groups:

Group a: Triad resonances that can occur in the absence of the incident wave. If k_r denotes the resonant wave then triad resonances of this group can happen either ahead of the disturbance between (k_2, k_6, k_r) (no such a case is seen in table 4.2) and/or behind the disturbance between (k_n, k_m, k_r), $m, n \in \{1, 3, 4, 5, 7, 8\}$, $m \neq n$ (all cases of table 4.2 except a_3, a_7, a_8, a_9 and a_{11}). We define the relative group speed of the resonant wave (in

the disturbance co-moving frame of reference) $C_{gr}^{(s)} = -U + C_{gr}$ where C_{gr} is the group speed of the resonant wave as seen in a stationary frame of reference. Then in the former case $C_{gr}^{(s)} > 0$ and in the latter case $C_{gr}^{(s)} < 0$ always. Therefore in all cases of group a, resonant waves formed ahead move forward, and resonant waves formed behind move backward, hence all possible resonance generated waves move away from the ship.

Group b: The incident wave (k_i) is needed for this resonance to happen, and the triad resonance is either between (k_i, k_n, k_r), n=2,6 ($k_i = k_p,\ p = 1, 3, 4, 5, 7, 8$, i.e. a head sea), with $C_{gr}^{(s)} > 0$ (no such a case in table 4.2), and/or between (k_i, k_m, k_r), m=1,3,4,5,7,8 ($k_i = k_q,\ p = 2, 6$, i.e. a following sea) with $C_{gr}^{(s)} < 0$ (cases $a_3, a_7, a_8, a_9, a_{11}$ in table 4.2). The behavior of this group is qualitatively similar to group a in the sense that resonant waves move away from the disturbance. Note that when a wave is taken as an incident wave it means that it exists both fore and aft of the disturbance.

Group c: The incident wave (k_i) is needed for this resonance to happen and the triad resonance is between (k_i, k_n, k_r), n=2,6 ($k_i = k_p,\ p = 1, 3, 4, 5, 7, 8$, i.e. a head sea) with $C_{gr}^{(s)} < 0$ (cases $a_3, a_7, a_8, a_9, a_{11}$ in table 4.2), and/or, between (k_i, k_m, k_r), m=1,3,4,5,7,8, ($k_i = k_q,\ p = 2, 6$, i.e. a following sea) with $C_{gr}^{(s)} > 0$ (no such a case in table 4.2). In this case resonant waves form ahead/behind the disturbance move backward/forward (i.e. toward) the disturbance and eventually hit the disturbance making it to oscillate with the encounter frequency of the (new) resonant wave. Due to this new oscillation the disturbance will send out a new group of waves that makes the wake pattern even more complicated.

Envelope of the resonant waves of group a,b reaches a steady state after a long time and can be calculated. Consider two of the disturbance waves (a_I, κ_I, Ω_I) and ($a_{II}, \kappa_{II}, \Omega_{II}$), where $a_i(x,t)$ is the amplitude, κ_i the wave number and Ω_i the frequency. If κ_r=κ_I+κ_{II} and Ω_r=$\Omega_I + \Omega_{II}$ satisfy the dispersion relation, then a new free (resonant) wave of (a_r, κ_r, Ω_r) will be formed on the surface/interface. Away from the near field of the disturbance and in the disturbance co-omoving frame of reference the following system of partial differential equations governs the temporal/spatial evolution of amplitudes (Craik, 1988):

$$\frac{\partial a_I}{\partial t} + C_{gI}^{(s)} \frac{\partial a_I}{\partial x} = \beta_I a_{II} a_r, \tag{4.3.5}$$

$$\frac{\partial a_{II}}{\partial t} + C_{gII}^{(s)} \frac{\partial a_{II}}{\partial x} = \beta_{II} a_I a_r, \tag{4.3.6}$$

$$\frac{\partial a_r}{\partial t} + C_{gr}^{(s)} \frac{\partial a_r}{\partial x} = \beta_r a_I a_{II}, \tag{4.3.7}$$

If we assume that the near field is small, then boundary/initial conditions for Group a,b waves are:

$$a_I(x,0)=0,\ a_I(0,t)=a_{I0},\ a_{II}(x,0)=0,\ a_{II}(0,t)=a_{II0},\ a_r(x,0)=0. \tag{4.3.8}$$

where a_{I0} and a_{II0} are farfield amplitudes of two disturbance waves participating in the resonance for group a waves, and one farfield amplitude and one incident wave amplitude for group b waves. The steady state solution of equation 4.3.5 can be expressed in closed form in terms of Jacobian Elliptic functions (Ball, 1964) with the property of all wave amplitudes modulating along the spatial coordinate. we are particularly interested in the initial rate of growth of the resonant wave, i.e. β_r. This coefficient can be derived by assuming a slow amplitude variation in time (or space) and invoking multiple-scales techniques (The coefficient is algebraically lengthy and is given for example by Jamali, 1998). In the steady state the amplitude of the resonant wave not very far from the disturbance is given by

$$a_r^{(s)}=\begin{cases}\frac{\beta_r}{C_{gr}^{(s)}}x^{(s)}, & \text{if } C_{gr}^{(s)}\cdot x^{(s)}>0,\\ 0, & \text{otherwise.}\end{cases} \tag{4.3.9}$$

Clearly this solution goes unbounded if $C_{gr}^{(s)}\to 0$. This case is similar to the disturbance motion near the critical speed, and higher nonlinearities are needed to be taken into account (see for example Dagan & Miloh, 1982; Liu & Yue, 1993; Akylas, 1984*b*, for the treatment of near critical speeds in homogeneous fluids).

Evolution of the envelop of amplitude of group c resonances is more complicated and the envelop never reaches a steady state. In group c, wave interactions occur both fore and aft of the disturbance, and the passage of resonant waves over the disturbance sets up a new wave-disturbance interaction that introduces even more number of waves to the water. To find the evolution of the amplitude of waves under the triad resonance governing equations (4.2.1) needs to be solved to the second order; The algebra is quite cumbersome and instead we will develop a very general numerical scheme in §4 to be able to address the quantitative features of this type of resonance.

To obtain a qualitative picture, however, an illustrative example is considered here. Consider case a_3 of table 4.2 where the resonance is between $(k_i=k_8,k_2,k_r)$. For this resonance to happen a head sea of $k_i=k_8$ ($C_{g8}^{(s)}<0$) has to oscillate the disturbance, making

it sending out many waves including k_2 ($C_{g2}^{(s)} > 0$). Waves k_2, k_8 now interact ahead of the disturbance to form a (new) resonant wave k_r that is known to have a negative relative group speed ($C_{gr}^{(s)} < 0$). Wave k_r moves toward the disturbance and acts as a new head sea incident wave. Part of the energy of the resonant wave goes into excitation of the disturbance and another part keeps moving along $-x$ axis. The incident wave $k_i = k_8$ already exist at $x^{(s)} < 0$ and now wave k_r upon passing the disturbance joins the incident wave k_8 behind the disturbance. But $k_i = k_8$ and k_r are in resonance with k_2! Therefore wave k_2 (previously only exist at $x^{(s)} > 0$) is formed at $x^{(s)} < 0$ moving toward the disturbance ($C_{g2}^{(s)} > 0$). The multiple interactions keep on going. For the purpose of illustration of different possibilities, here we show three example of resonance cases:

Example one: Fast resonant surface wave generated by slow motion near the Thermocline

Second order (traid) resonant waves can have both positive and negative group/phase velocities (absolute and relative to the ship). Their relative group velocities, nevertheless, never exceeds the maximum relative group velocity of existing waves in the ship wake. This can be seen from figure 4-1. All resonant waves are on the lines $\omega = \pm 2\omega_0 + Uk$ and $\omega = UK$. In deep layers to have a wave in front of the ship $\tau < 1/4$, and it can be shown that to have a resonant wave ahead of the ship, $\tau < 1/8$. But even when this condition is satisfied, wave k_2 is always faster than this resonant wave. Therefore no resonant wave can propagate faster than existing ship waves ahead of the ship. With a similar argument it is seen that no wave can propagate (backward) behind the ship faster that the original ship waves. However, we will show that the relative amplitude of generated waves can turn the resonant wave into an important item in surface/interface tracing of objects.

If an object moves and oscillates near the thermocline of a two-layer density stratified fluid, and if the thermocline is deep enough, amplitude of surface waves are much smaller than those of interfacial waves. Now if two of generated interfacial waves satisfy a resonance condition with a surface mode wave, now energy can go to the surface via resonance. Now if the resonance is strong enough a new wave appears on the surface which is not predicted by the linear theory and if stratification is not taken into account.

As an example, consider a slowly moving submarine of $\mathrm{Fr} = 1e-4$ near thermocline of

a $\mathcal{R} = 0.90$ stratified fluid of $h^* = 2$. A relatively short internal wave hitting from stern side causes the ship to oscillate with dimensionless frequency $\tau = 0.004$. In sea of depth 40 m, submarine speed is less than 0.5 $knot$ (1 Km/hr, and hence can be imposed by a weak ocean stream too), and the period of heaving is $T = 30$ sec. If the submarine is near the thermocline at the depth of about $z = -15$ m, it can generate high amplitude internal waves while its effect on the surface is negligible. But with chosen parameters resonance condition between two of submarine-generated internal waves (i.e. k_6 the incident wave that causes submarine to oscillate and k_8 of resultant waves) is satisfied and a new surface wave is generated. With the chosen dimensional depth, the resonant surface wave is a fast moving wave ($T = 15$ sec) and its amplitude initially grows by the rate of $1.2a_1a_2$ m/min where a_1, a_2 are amplitudes of generated internal waves. In this example the amplitude of ship waves on the surface are an order of magnitude smaller than those on the interface:

$$\frac{a_4}{a_6} = 0.11, \quad \frac{a_2}{a_6} = 0.11. \tag{4.3.10}$$

This newly generated surface wave has a positive group velocity higher than the velocity of the submarine. Therefore it overtakes the submarine and carries information ahead. Note that since k_6 is an incident wave, it does not have any information about the object and its motion for a downstream observer. We also showed that k_2 is relatively small for him to be detectable. Therefore the resonant wave can be a potential major source of detection ahead of the submarine.

To numerically illustrate the effect of nonlinearity in this case, consider an array of oscillating objects in a weak stream. Off-shore oil platforms are being installed closer and closer to each other now a days, and their mutual interaction has already rung the alert of the need for more sophisticated considerations (McIver, 1984). Many wave energy converter farms in the form of arrays are now under development. Their optimum spacing and direction with respect to the incident wave poses another important question (Simon, 1982). Wind farms are now moving offshore (Gaudiosi, 1996) and wind/current/wave induced vibrations make them vulnerable. A fleet of ships/submarines advancing in the ocean and encountering waves is another example of an array of objects experiencing forward motion (or incident current) along with oscillations. For this example, we pick a length scale of $L = 1$ km (i.e. each 1 km in real world will be projected to 2π in HOS), and time scale

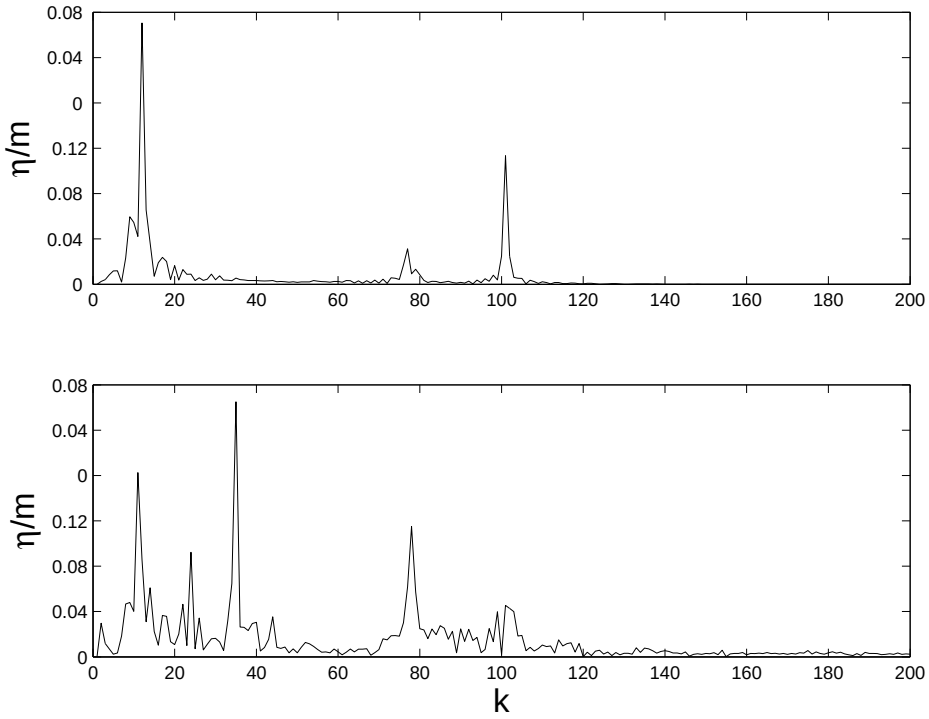

Figure 4-2: An array of oscillating objects in a slow stream. $R = 90$, Fr $= 0.0001$, $h = 2$, $\tau = 0.004$. Resonance occurs between two internal waves of $k_6 = 100$ and $k_8 = 76$ to generate a surface wave of $k_r = 24$.

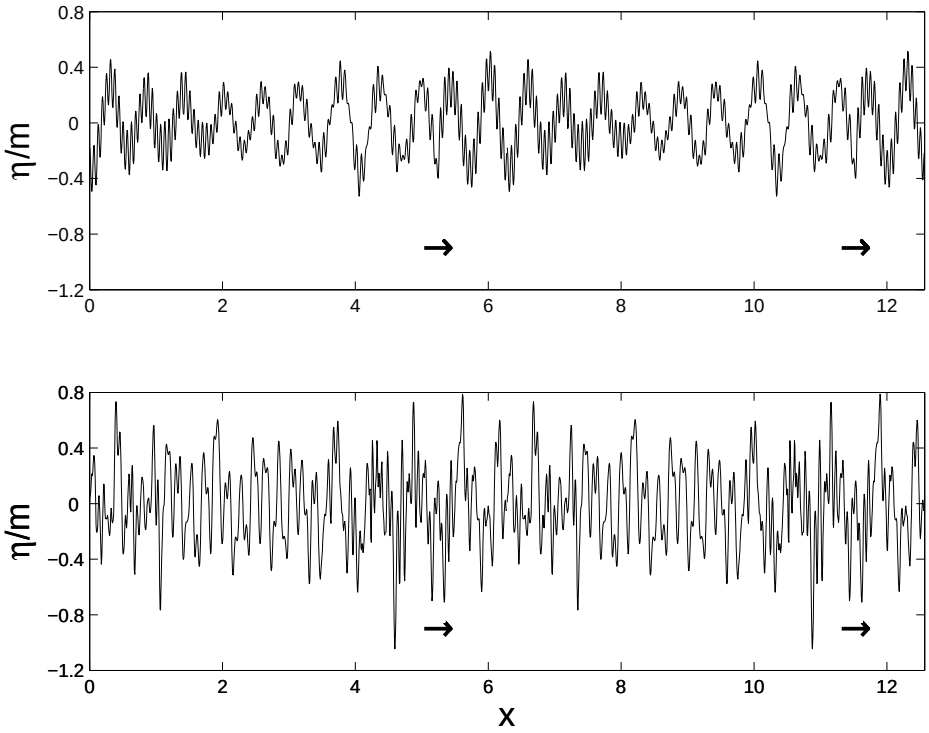

Figure 4-3: An array of oscillating objects in a slow stream. $R = 90$, Fr $= 0.0001$, $h = 2$, $\tau = 0.004$. Resonance occurs between two internal waves of $k_6 = 100$ and $k_8 = 76$ to generate a surface wave of $k_r = 24$.

of $T = 10$ *sec*. We assume objects are each 1 km apart and we look at the evolution of surface elevation and spectrum. The object moves close to the thermocline at the depth of 20 m. Figures 4-2 and 4-3 respectively show the comparison between spectrum and the surface of the sea after two hours of physical time. In both figures the top plot is the linear simulation and the bottom is direct simulation encountering higher order nonlinearities. x-coordinate of the objects locations is shown by arrows. For chosen normalizations in our direct simulation, $k_6 = 100$, $k_8 = 76$ and $k_2 = k_4 = 10$. However we know that the combination $k_r = k_6 - k_8 = 24$ satisfies the resonance condition. As can be seen in figure 4-2-b, a strong peak appears at $k_r = 24$. It is also seen that energy is depleted from the internal mode k_6 and surface mode K_2, k_4 to feed existing internal mode of k_8 and new wave of k_r. The interaction does not stop here and new generated wave of k_r along with k_2, k_4 form another near-resonance case of $k_r 2 = k_2 + k_r = 34$. Note that since k_r is a free wave, the latter resonance occurs even if we only consider second order interactions. Since the amplitude of generated waves vary with x, the linear spectrum is not perfectly spiky.

Figure 4-3 shows that how multiple resonance between a submerged body waves can result in a very complicated surface pattern.

Example two: Resonant wave that hit the ship

Can a ship get hit by a resonant wave of its own waves? The answer is yes. For this to happen stratification is necessary, and since the resonance is between surface and internal waves, the depth of thermocline has to be small enough such that amplitude of generated waves are of almost same orders of magnitudes and hence resonance is strong.

For instance consider a sea of $R = 0.9$ and $h = 4$ and a ship moving with $Fr = 0.02$. There are two internal waves that can force the ship to oscillate with dimensionless frequency $\tau = 0.13$, we consider the one with negative group velocity (as seen from a stationary observer who sees the ship speed positive) hitting the ship from the bow side (k_8). In physical variables if the total depth is 40 m, the ship speed is 5.5 $knots$ and its period of oscillation should be $T = 13.5$ sec that can be imposed by an internal wave of wavelength 67 m.

Other than k_8, five other waves $(k_1, k_2, k_3, k_4, k_7)$ will be generated amongst them k_2 will propagate ahead of the ship. Now k_2 and part of k_8 ahead of the ship can resonate each other to generate a surface mode wave with absolute (and relative) negative group velocity in front of the ship. The resonant wave will eventually hit the ship. Among other effects this new wave causes the ship to oscillate with higher frequency that can send out more waves. For physical parameters chosen above this new surface wave has period of 8.3 sec.

Hit resonance between waves of a self-oscillating ship may occur too, but only for strong stratification. Under deep layer assumptions for example, for $R = 0.5$, at $\tau = 0.122$ waves k_1 and k_7 behind the ship generate (in subtraction) a resonant wave with positive group velocity higher than the ship. This wave will hit the ship eventually.

Example three: Generation of a co-moving resonant surface wave by fast motion near thermocline

Second order analysis predicts that an underwater vehicle moving relatively fast near

the thermocline can generate a surface roughness (wave) that almost moves with the object. If the submerged object keeps its steady motion, the amplitude of surface wave increases both because of resonance and confinement of the resonant wave energy to the nearby ship area (similar to what happens near critical speed of ship).

As an illustration consider a submarine with Froude number Fr = 0.8 near thermocline of a $\mathcal{R} = 0.90$ stratified fluid of $h^* = 2$. A relatively short internal wave hitting from bow side causes the ship to oscillate with dimensionless frequency $\tau = 0.2$. In this example, if submarine oscillate by itself the resonance will occur too. In sea of depth 40 m, submarine speed is about 35 $knots$ (65 Km/hr) and period of forced heaving is $T = 5.6$ sec. If the submarine is near the thermocline at the depth of about $z = -15$ m, it again can generate high amplitude internal waves while its effect on the surface is negligible. But with chosen parameters resonance condition is satisfied to generate a surface wave of period $T = 18$ sec and hence group velocity of 57 Km/hr that will almost stick to the ship.

All resonance discussed here can happen in a weaker stratified fluid too. An an example, consider the motion of a boat in a $\mathcal{R} = 0.97$ stratified fluid of $h^* = 2$. The boat dimensionless frequency and Froude number are respectively $\tau = 1.47$ and Fr = 0.6. In physical domain the configuration is correspond to a ship moving with speed 16 $knots$ (30 Km/hr) while oscillating with period of 3.3 sec in a stratified area of total depth 10 m and a thermocline of depth 3.3 m measured from water surface.

Kinematic analysis of the dispersion relation shows that in this case four waves propagate behind the ship. Waves k_4, k_7 form a triad resonance with another surface wave: wave k_4 is a surface mode wave with real wavelength of $\lambda_4 = 53$ m, and wave k_7 is an internal mode wave with real wavelength of $\lambda_4 = 23$ m. The resonant surface mode wave will have a real wavelength of 42 m.

4.4 Direct Simulation

In this section a higher order spectral method scheme is used to numerically simulated the wave generation by an oscillating translating source. We will show that resonance between ship waves in a two-layer density stratified fluid is indeed possible.

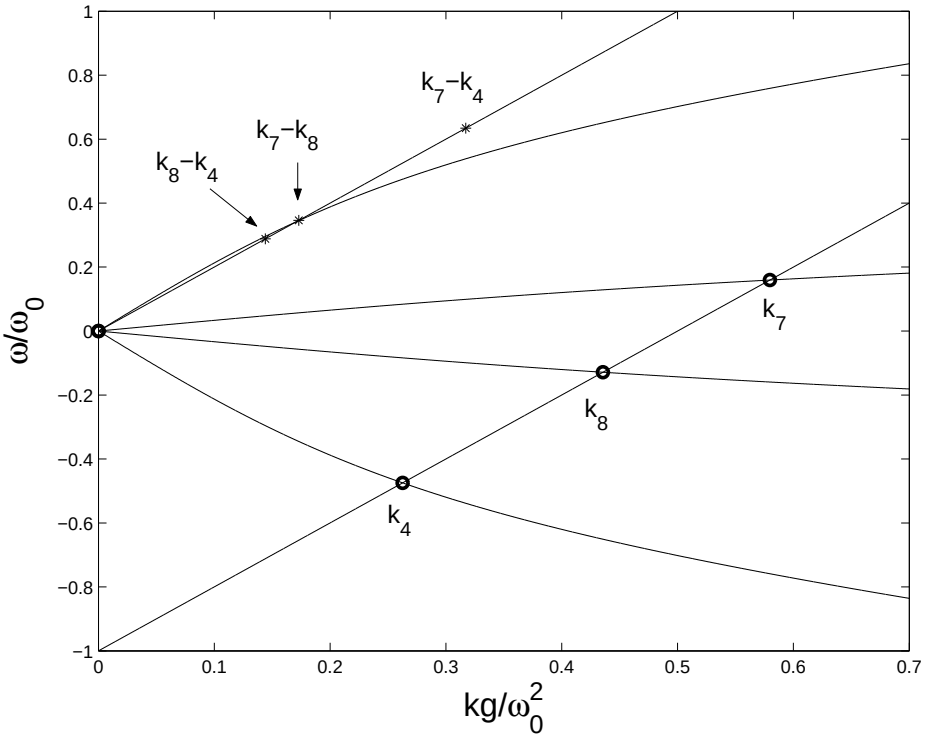

Figure 4-4: Dispersion relation and resonant/near-resonant waves for $R = 0.9,\ h = 2,\ \tau = 2.0$ and $\mathrm{Fr} = 0.8$.

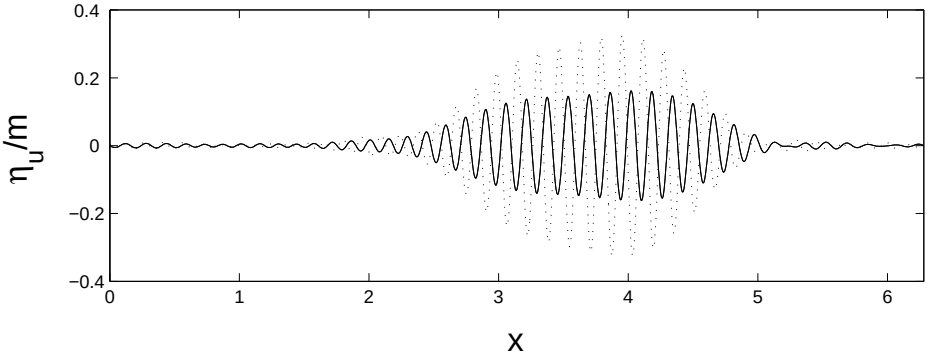

Figure 4-5: Reconstruction of wave $k_r = 40$ for $R = 0.9,\ h = 2,\ \tau = 2.0$ and $\mathrm{Fr} = 0.8$. Plotted data are linear numerical simulation (——) and third order nonlinear numerical simulation (...)

4.4.1 HOS formulation

Assume the total potential $\phi_{u,\ell}$ can be divided into two parts as:

$$\phi_u = \varphi_u + \bar{\phi}_u, \tag{4.4.11}$$

$$\phi_\ell = \varphi_\ell + \bar{\phi}_\ell, \tag{4.4.12}$$

where

$$\nabla^2 \bar{\phi}_u = \delta(x - x0, y - y0), \tag{4.4.13}$$

$$\bar{\phi}_{\ell,z} = 0 \quad @ \quad z = -h_u - h_\ell. \tag{4.4.14}$$

Following Zakharov (1968), we define the surface potential ϕ_u^S for upper layer and the interface potentials $\phi_{u/\ell}^S$ for both upper and lower layers by

$$\varphi_u^S(x,t) \equiv \varphi_u(x, \eta_s(x,t), t) \ , \quad \text{and} \quad \varphi_{u/\ell}^I(x,t) \equiv \varphi_{u/\ell}(x, -h_u + \eta_i(x,t), t) \ . \tag{4.4.15}$$

In the neighborhood of the interface, for convenience, we define a new potential $\psi(x,z,t) \equiv \varphi_\ell(x,z,t) - R\varphi_u(x,z,t)$. We further define ψ^I to be the value of ψ evaluated on the interface:

$$\psi^I(x,t) \equiv \varphi_\ell^I(x,t) - R\varphi_u^I(x,t) \ . \tag{4.4.16}$$

In terms of these quantities, we can rewrite the kinematic and dynamic boundary conditions on the surface ((4.2.1c) and (4.2.1d)) and interface ((2.2.1f) and (4.2.1g)) in the forms:

$$\eta_{s,t} + \eta_{s,x}\varphi_{u,x}^S - (1 + \eta_{s,x}^2)\ \varphi_{u,z} = \bar{\phi}_{u,z} - \eta_{s,x}\bar{\phi}_{u,x} \ , \quad z = \eta_s \ , \tag{4.4.17}$$

$$\begin{aligned} &\varphi_{u,t}^S + g\eta_s + 1/2{\varphi_{u,x}^S}^2 - 1/2(1 + \eta_{s,x}^2)\varphi_{u,z}^2 \\ &\qquad = -\bar{\phi}_{u,x}\varphi_{u,x}^S - 1/2(\bar{\phi}_{u,x}^2 + \bar{\phi}_{u,z}^2) - \bar{\phi}_{u,t} \ , \quad z = \eta_s \ , \end{aligned} \tag{4.4.18}$$

$$\eta_{i,t} + \eta_{i,x}\varphi_{u,x}^I - (1 + \eta_{s,i}^2)\ \varphi_{u,z} = \bar{\phi}_{u,z} - \eta_{i,x}\bar{\phi}_{u,x} \ , \quad z = -h_u + \eta_i \ , \tag{4.4.19}$$

$$\begin{aligned} &\psi_{,t}^I + g\eta_i(1 - R) + 1/2[{\varphi_{\ell,x}^I}^2 - R{\varphi_{u,x}^I}^2] - 1/2(1 + \eta_{i,x}^2)(\varphi_{\ell,z}^2 - R\varphi_{u,z}^2) \\ &\qquad = -(\bar{\phi}_{\ell,x}\varphi_{\ell,x}^I - R\bar{\phi}_{u,x}\varphi_{u,x}^I) - 1/2[(\bar{\phi}_{\ell,x}^2 + \bar{\phi}_{\ell,z}^2) - R(\bar{\phi}_{u,x}^2 + \bar{\phi}_{u,z}^2)] \\ &\qquad\quad -(\bar{\phi}_{\ell,t} - R\bar{\phi}_{u,t}) \ , \quad z = -h_u + \eta_i \ . \end{aligned} \tag{4.4.20}$$

In the time simulation of nonlinear two-layer fluid motion with the HOS approach, these four equations are used as evolution equations for η_s, φ_u^S, η_i and ψ^I provided that the vertical surface velocity, $\varphi_{u,z}(x,\eta_s,t)$, and the vertical interface velocities, $\varphi_{u,z}(x,-h_u+\eta_i,t)$ and $\varphi_{\ell,z}(x,-h_u+\eta_i,t)$, are obtained from the boundary-value solution.

In our problem of motion of an oscillating source located in the lower layer in a two-layer density stratified fluid, we have:

$$\bar{\phi}_u = Ux \tag{4.4.21}$$

$$\bar{\phi}_\ell = Ux + \frac{m_0}{2\pi}\sin\omega_0 t(\ln r_1 + \ln r_2) \tag{4.4.22}$$

where

$$r_1^2 = \sin^2\left(\frac{x-x_0}{2L/\pi}\right) + \sinh^2\left(\frac{z-z_0}{2L/\pi}\right), \tag{4.4.23}$$

$$r_2^2 = \sin^2\left(\frac{x-x_0}{2L/\pi}\right) + \sinh^2\left(\frac{z+2h_u+2h_\ell+z_0}{2L/\pi}\right). \tag{4.4.24}$$

if the source is located in the lower layer, and

$$\bar{\phi}_u = Ux + \frac{m_0}{2\pi}\sin\omega_0 t(\ln r_1 + \ln r_2) \tag{4.4.25}$$

$$\bar{\phi}_\ell = Ux \tag{4.4.26}$$

where

$$r_1^2 = \sin^2\left(\frac{x-x_0}{2L/\pi}\right) + \sinh^2\left(\frac{z-z_0}{2L/\pi}\right), \tag{4.4.27}$$

$$r_2^2 = \sin^2\left(\frac{x-x_0}{2L/\pi}\right) + \sinh^2\left(\frac{z+2h_u+z_0}{2L/\pi}\right). \tag{4.4.28}$$

if the source is located in the upper layer.

4.4.2 Validation

For illustration, consider the motion of a boat in a $\mathcal{R} = 0.90$ stratified fluid of finite upper layer and deep lower layer (in numerical simulation we take $h^* = 200$). The boat dimensionless frequency and Froude number are respectively $\tau = 0.4171$ and $\mathrm{Fr} = 0.004$. In physical domain the configuration is correspond to a ship moving with speed 32 Km/hr

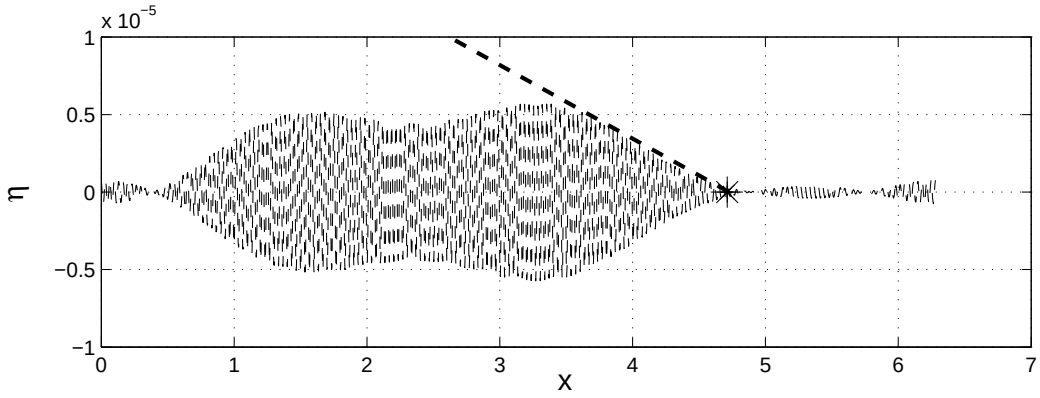

Figure 4-6: $\mathcal{R}$=0.9, $\mathcal{F}$=004, h=200

while oscillating with period of 13.5 *sec* in a stratified area of total depth 2 km and a thermocline of depth 10 m measured from water surface.

Kinematic analysis of the dispersion relation shows that in this case four waves propagate behind the ship. Waves k_4, k_7 form a triad resonance with another internal wave: wave k_4 is a surface mode wave with real wavelength of $\lambda_4 = 500\ m$, and wave 7 is an internal mode wave with real wavelength of $\lambda_4 = 90\ m$. The resonant internal mode wave will have a real wavelength of 75 m. see figure 4-6 The amplitude of generated waves are functions of the strength of the source (boat), but if the amplitude of the generated surface mode wave (k_4) is about 0.5 m, then amplitude of k_7 on the interface is about 1 m and maximum amplitude of the resonant internal mode wave is about $0.25m$.

4.4.3 Multiple Resonance

Real ocean surface is composed of many wave components. Hence, in essence, ships and submarines are subjected to many excitation frequencies. Multiple resonance between generated waves may result in a complicated surface pattern making it impossible to track the ship.

As an illustration consider a sea of $R = 0.9$ and $h = 4$ and an object of speed $\mathrm{Fr} = 0.032$ and the depth of $z_0/H = 0.1$. Assume that the ship is oscillating with three dimensionless frequencies of $\tau^{(1)} = 0.24$, $\tau^{(2)} = 0.49$ and $\tau^{(3)} = 0.58$. If we choose a length scale of $L/H = 16.7$ where L is the horizontal distance projected to the interval $[0, 2\pi]$ in HOS, then table 4.3 lists the dimensionless wavenumber and frequencies in a stationary frame

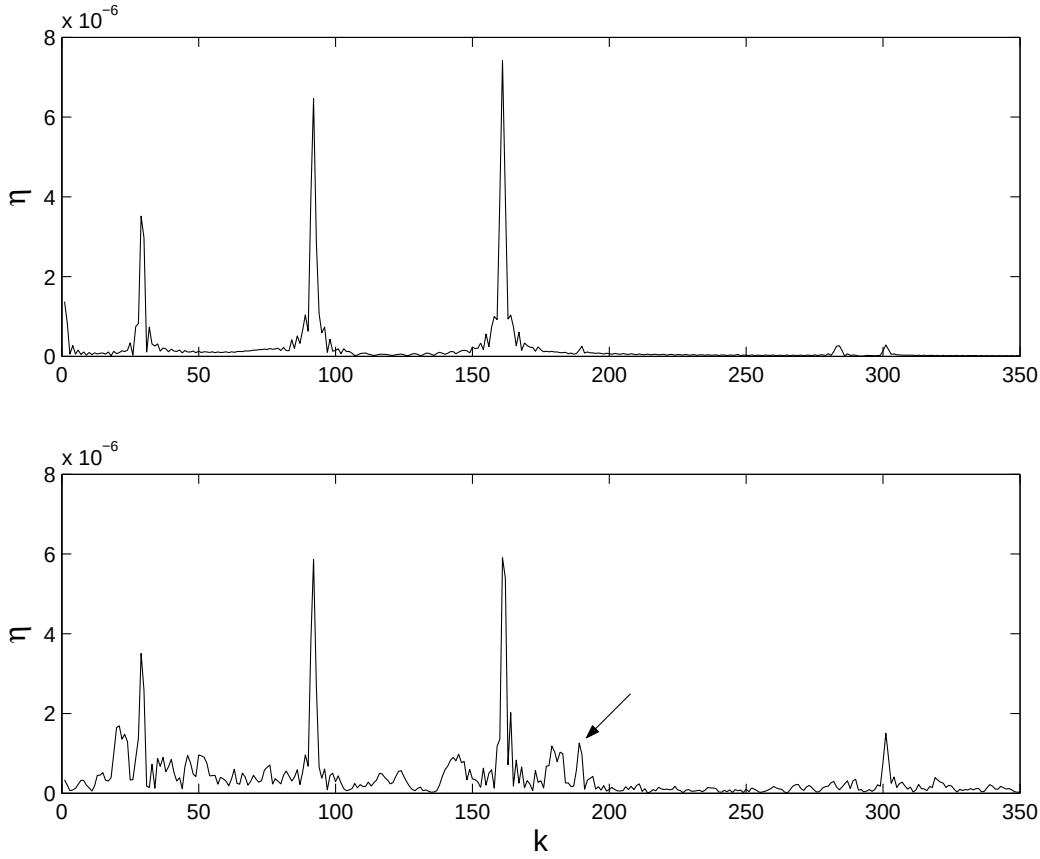

Figure 4-7: $\mathcal{R}90$, $\mathcal{F}$=004, h=200

n	$k^{(1)}$	$\omega^{(1)}$	$k^{(2)}$	$\omega^{(2)}$	$k^{(3)}$	$\omega^{(3)}$
1	187	13.7	0	0	0	0
2	83	9.1	0	0	0	0
3	750	27.4	961	31	1041	32.3
4	23	-4.5	67	-8.2	90	-9.4
5	0	0	0	0	0	0
6	0	0	0	0	0	0
7	198	3.2	352	4.3	411	4.6
8	81	-1.9	183	-3.9	226	-3.4

Table 4.3: Normalized wavenumber and frequencies used for the multiple-resonance example associated respectively with $\tau_1 = 0.24,\ \tau_2 = 0.487$ and $\tau_3 = 0.585$. Fixed parameters are $\mathcal{R} = 0.9, \mathrm{Fr} = 0.032$ and $h = 4$.

of reference. In a sea of depth $H = 100\ m$, the thermocline associated with our example needs to be at the depth of $h_u = 20\ m$ below the water surface and the object needs to be oscillating with periods of $T^{(1)} = 15\ sec$, $T^{(2)} = 7.3\ sec$ and $T^{(3)} = 6\ sec$. The major ship waves are those belong to τ_3 which is near the linear surface critical frequency of the ship. The second and third frequencies are chosen such that via resonance they alter the major wave frequency behind the ship. Specifically

$$k_{r1} = k_7^{(1)} - k_4^{(2)} = 131, \quad k_{r2} = k_8^{(2)} - k_8^{(3)} = -43, \tag{4.4.29}$$

are two surface-mode resonant wave with encounter frequencies of $\omega_{r1}^{en} = 5.71$ and $\omega_{r1}^{en} = -4.64$ which are close to the major ship wave encounter frequency $\omega_1^{(1),en} = 5.48$. Figure 4-8 shows the surface elevation and surface spectrum for linear simulation. The major two peaks on the surface spectrum (in x) are for wavenumbers $k_1^{(1)} = 187$ that trails the ship and and $k_2^{(1)} = 83$ that moves ahead of the ship. To measure how the spectrum changes as waves depart from the ship, we put two surface elevation sensors on the water: one placed at the distance $x_1 = \pi/10$ $(500m)$ behind the ship and the other at $x_2 = \pi/2$ $(2500m)$ behind the ship. The spectrum gained from these two sensors are shown in figure 4-9. As expected, for linear simulation spectrum does not change with the distance. Figure 4-10 and 4-11 is the result of the same setup when nonlinearity is taken into account ($M = 3$ in HOS). The wave in front does not change much and the x-spectrum as can be seen from figure 4-10 is regular near $k_2^{(1)} = 83$. However, the spectrum behind the ship changes considerably and initial confined energy near $k_1^{(1)} = 187$ spreads over a range of frequencies. However, this energy

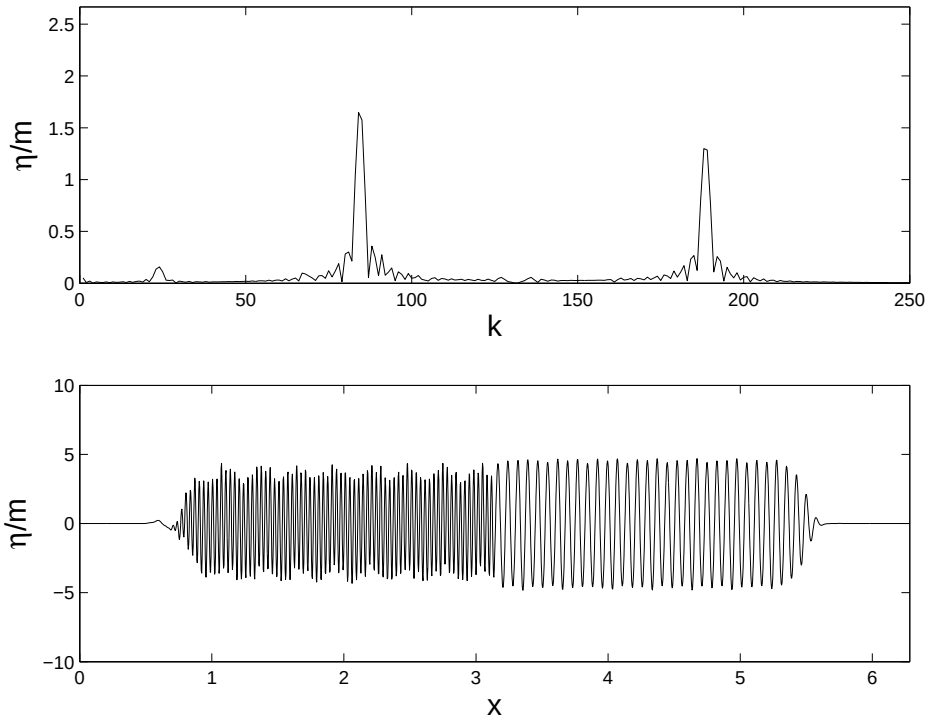

Figure 4-8: Surface spectrum and real elevation of an oscillating and translating source from linear direct simulation. Parameters are $\mathcal{R} = 0.9$, Fr $= 0.032$, $h = 4$ and source oscillate with superposition of three frequencies: $\tau^{(1)} = 0.24$, $\tau^{(2)} = 0.49$, and $\tau^{(3)} = 0.58$

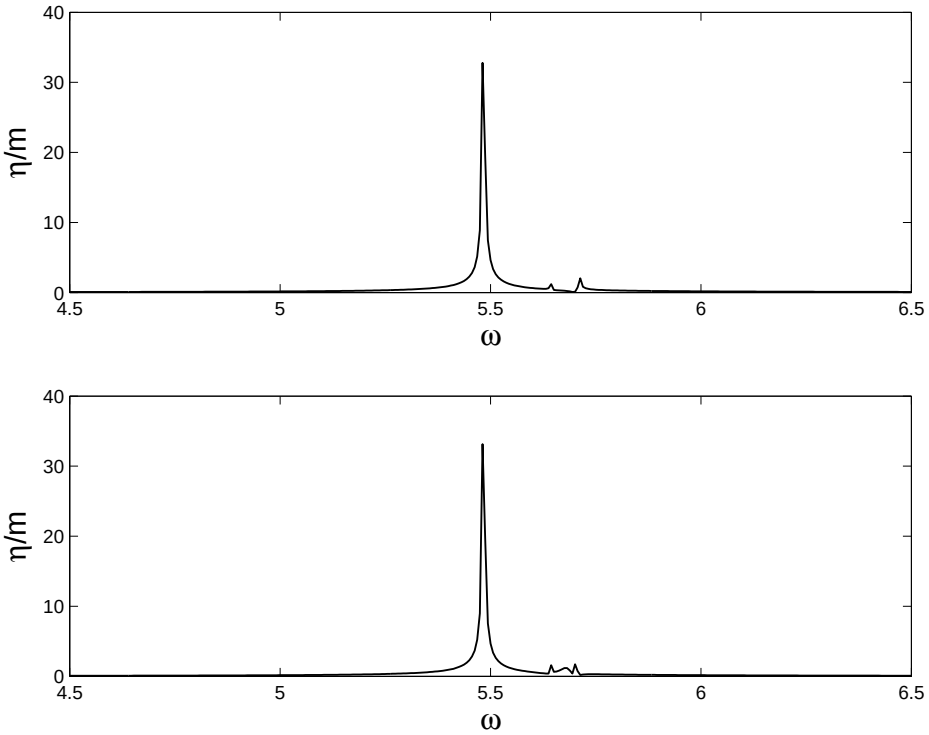

Figure 4-9: Frequency spectrum measured at the distance $x_1 = \pi/10$ (top figure) and $x_2 = \pi/2$ (bottom figure) downstream of the object. Parameters are $\mathcal{R} = 0.9$, Fr $= 0.032$, $h = 4$ and source oscillate with superposition of three frequencies: $\tau^{(1)} = 0.24$, $\tau^{(2)} = 0.49$, and $\tau^{(3)} = 0.58$

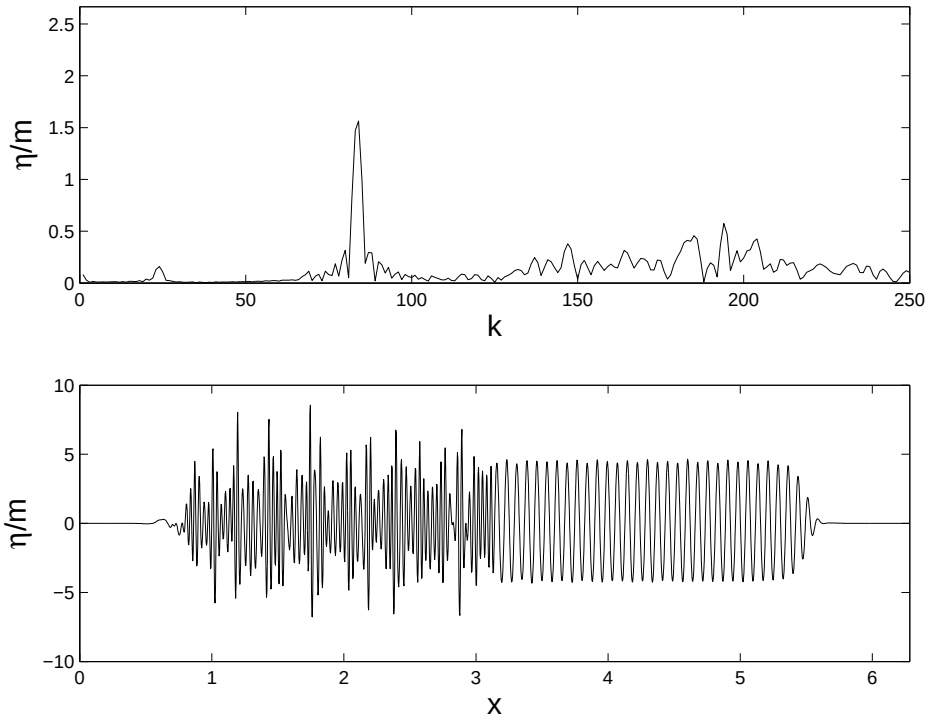

Figure 4-10: Surface spectrum and real elevation of an oscillating and translating source from nonlinear (M=3) direct simulation. Parameters are $\mathcal{R} = 0.9$, Fr $= 0.032$, $h = 4$ and source oscillate with superposition of three frequencies: $\tau^{(1)} = 0.24$, $\tau^{(2)} = 0.49$, and $\tau^{(3)} = 0.58$

transfer occurs over a distance. If we consider our two sensors, as shown in figure 4-11 near the object sensor is spiky and clearly indicate the major frequency. However, over a finite distance, the spectrum spreads over a range of frequencies and no dominant frequency is distinguishable. To see what the effect of stratification is, we also simulate the same setup with no stratification $\mathcal{R} = 1$. Figure 4-12 and 4-13 show that although nonlinearity alter the spectrum, however, the major frequency is still distinguishable from the rest.

Figure 4-14 shows the spectrum evolution as waves move away from the disturbance. Wave elevations are measured at three points respectively at $x_1 = \pi/10$, $x_2 = 3\pi/10$ and $x_3 = 7\pi/10$ from the disturbance (in physical domain respectively correspond to distances 500 m, 1.5 Km and 3.5 Km behind the ship). The spectrum at these three locations are compared for when there is no stratification ($\mathcal{R}$=1) and when stratification exist ($\mathcal{R}$=0.9). Near the ship, the spectrum is very close to linear theory prediction, however, as waves travel nonlinearities come into play. Figure 4-14 shows that the existence of stratification and resonance can significantly change the spectrum resulting in a total loss of information: the

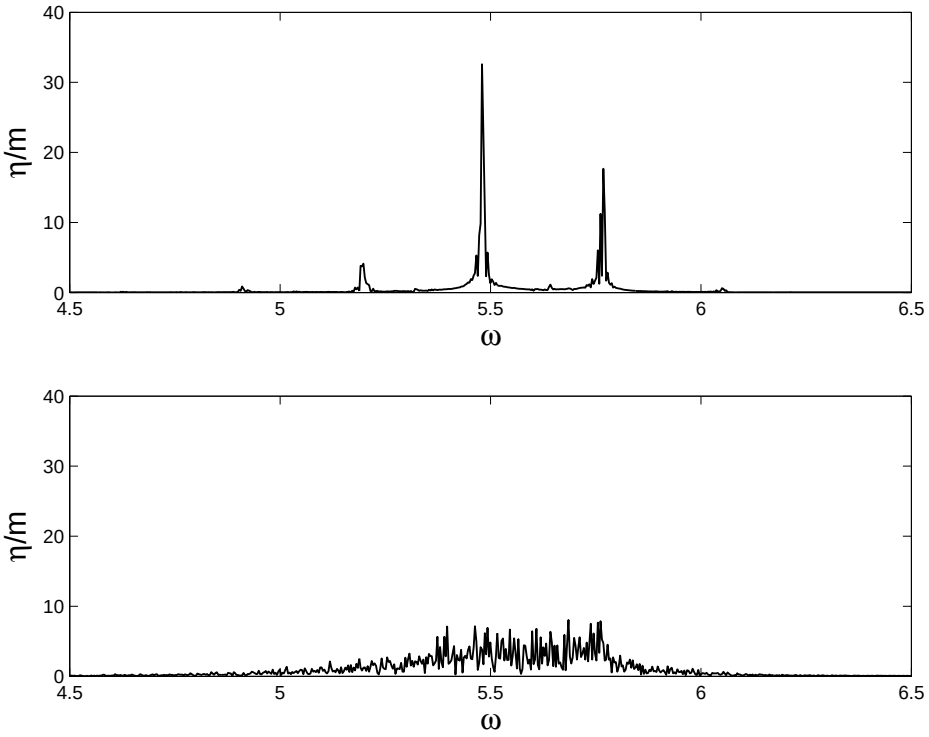

Figure 4-11: Frequency spectrum measured at the distance $x_1 = \pi/10$ (top figure) and $x_2 = \pi/2$ (bottom figure) downstream of the object. Parameters are $\mathcal{R} = 0.9$, Fr $= 0.032$, $h = 4$ and source oscillate with superposition of three frequencies: $\tau^{(1)} = 0.24$, $\tau^{(2)} = 0.49$, and $\tau^{(3)} = 0.58$

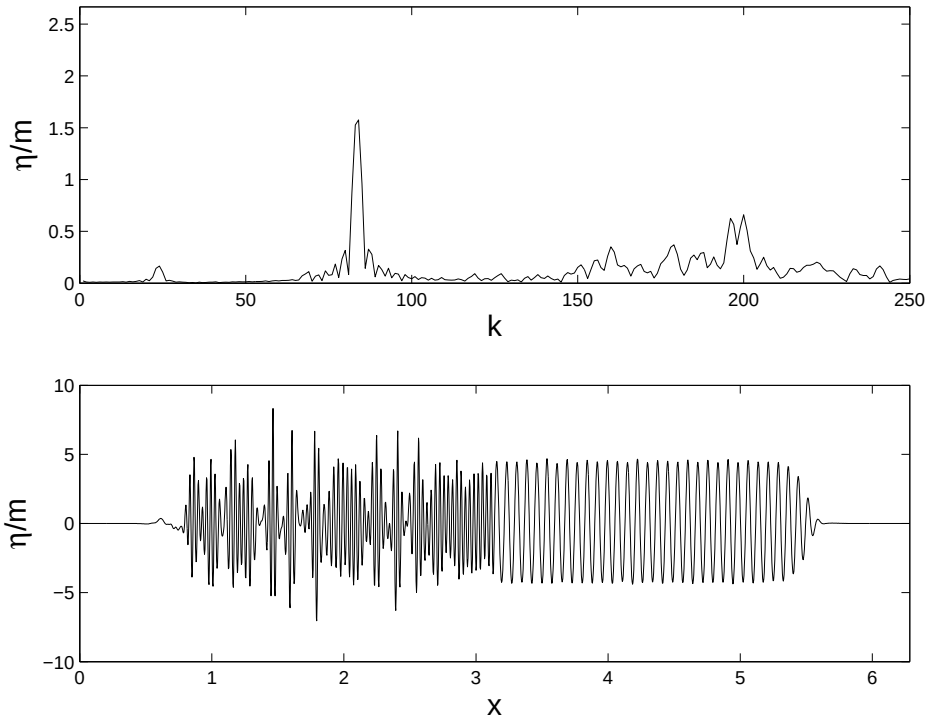

Figure 4-12: Surface spectrum and real elevation of an oscillating and translating source from nonlinear (M=3) direct simulation. Parameters are $\mathcal{R} = 1.0$, Fr $= 0.032$, $h = 4$ and source oscillate with superposition of three frequencies: $\tau^{(1)} = 0.24$, $\tau^{(2)} = 0.49$, and $\tau^{(3)} = 0.58$

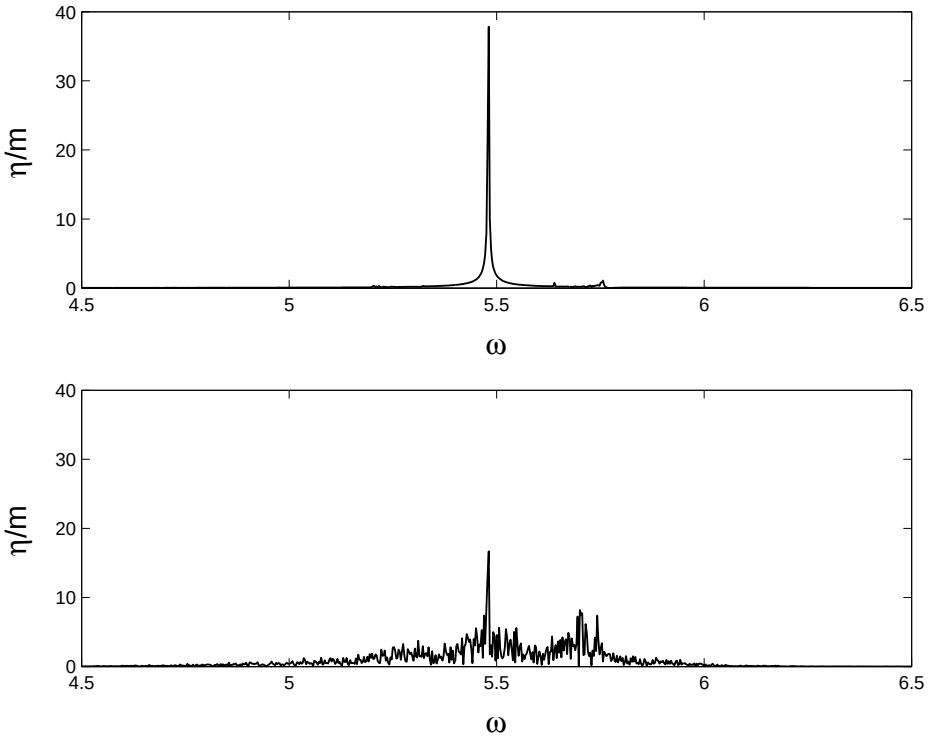

Figure 4-13: Frequency spectrum measured at the distance $x_1 = \pi/10$ (top figure) and $x_2 = \pi/2$ (bottom figure) downstream of the object. Parameters are $\mathcal{R} = 1.0,\ \mathrm{Fr} = 0.032,\ h = 4$ and source oscillate with superposition of three frequencies: $\tau^{(1)} = 0.24,\ \tau^{(2)} = 0.49$, and $\tau^{(3)} = 0.58$

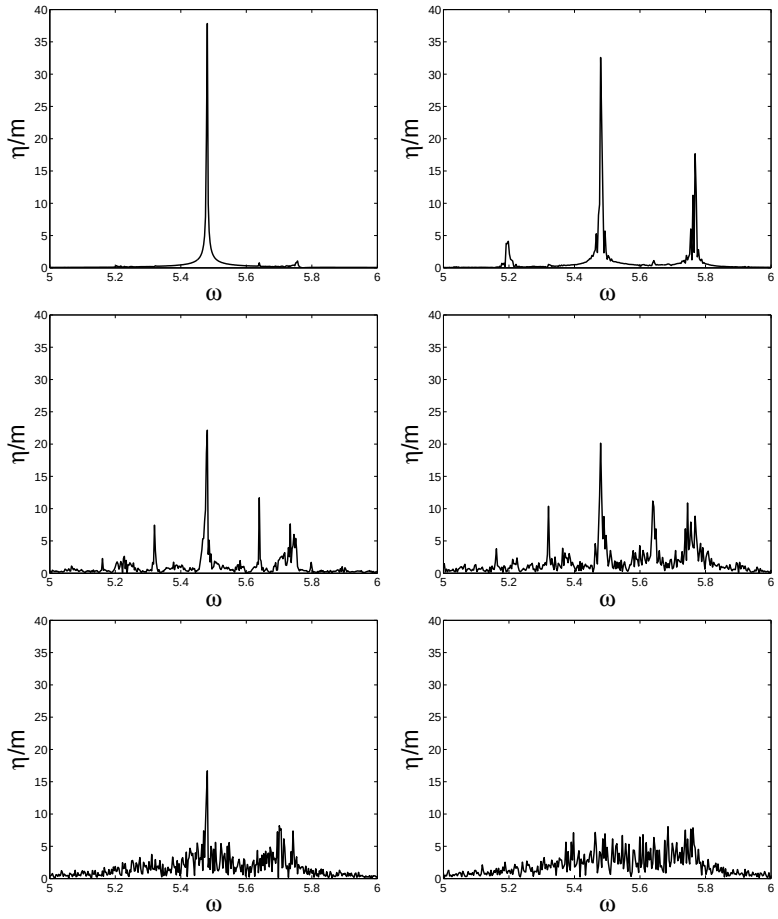

Figure 4-14: Frequency spectrum evolution over the distance measured from the disturbance for homogeneous fluid $\mathcal{R}$=1.0 (right column) and stratified flud $\mathcal{R}$=0.9 (left column). Measurements are (from top bottom) respectively at $x_1 = \pi/10$, $x_2 = 3\pi/10$ and $x_3 = 7\pi/10$ from the disturbance. Parameters are $\mathcal{F}$=0.032, h=4 and the disturbance oscillates with superposition of three frequencies: $\tau^{(1)}$=0.24, $\tau^{(2)}$=0.49, and $\tau^{(3)}$=0.58.

spectrum spreads over a band of frequencies and no dominant frequency is distinguishable

4.5 Concluding remarks

Three waves on the surface of a homogeneous fluid are known to be non-resonant. Therefore to the second order a 2D disturbance cannot resonant a new wave on a surface of a homogeneous fluid. However, triad resonance is known to exist in a two-layer density stratified fluid. We showed that triad resonance can occur between waves of a disturbance in a two-layer density stratified fluid. Many resonance cases can occur: Resonant wave can be a fast surface wave when the submarine is slowly advancing near a deep thermocline,

resonant wave can move toward the ship and vibrate the ship with its new frequency, and resonant wave can have a group velocity close to the disturbance speed, hence trail a hump of waves with the disturbance. An algorithm based on higher order spectral is developed to study the general problem of wave generation and interaction in a two-layer fluid and in the presence of a time dependent accelerating disturbance. As an example it is shown that multiple resonance may result in a complicated spectrum and loss of information.

Chapter 5

Conclusions

In part one of this thesis (chapter one and two) the generalized two-dimensional Bragg resonance of waves in a two-layer density stratified fluid over a rippled bottom is studied analytically (using perturbation theory) and numerically.

Bragg resonances obtain involving triad (class I) and quartet (class II and III) interactions at second and third order (in wave/bottom steepness) respectively in which at least one of the participant is a component of the rippled bottom. The results are a generalization of the unstratified (single layer) fluid case of Liu & Yue (1998), but, because of the possibility of internal mode waves, now admit many (new) resonance cases and combinations. These are enumerated and represented schematically in Feynman-like diagrams. In class I and II Bragg resonances only one frequency exists, while in the class III Bragg resonance, the frequency of resonant wave can be the sum or the difference of frequency of incident waves resulting in the possibility for the generation of very long or short waves. For all three classes of resonances, regular perturbation solutions are obtained which predict the resonances and the growth of the resonant transmission or reflection waves for a finite bottom patch. For very long bottom patches, regular perturbation results are not valid, and analyses involving slow-variables and multiple scales are needed (see Appendix H). This is obtained here for the case of class I resonance.

Chapter one provides the analytic basis and guidance for understanding the complex resonant interactions involving surface/internal mode waves travelling over a rippled bottom. In practice, the general problem consists of surface/internal mode waves and bottom topography containing multiple (indeed a spectrum of) components, plus resonant gener-

ated wave components, obtaining multiple resonances and resonant combinations among these components. For this general problem, a direct numerical simulation of the nonlinear evolution is needed.

To complement the perturbation analyses of chapter one, in chapter two an efficient and accurate computational method is developed for the study of general nonlinear interactions of surface/interfacial waves with variable bottom topography in a two-layer density stratified fluid. The method is based on the extension, to include interfacial waves, of a powerful high-order spectral (HOS) method originally developed for the study of nonlinear gravity wave-wave and wave-bottom interactions in a homogenous fluid. The method we developed accounts for nonlinear interactions of surface/interfacial waves with bottom ripples up to an arbitrary high order M and, as with the original HOS, achieves an exponential convergence with respect to the number of spectral modes modes N used (for the surface, interfacial and bottom), and an almost linear computational effort with respect to N and M. Systematic validation and convergence tests are performed including the directed comparison to the exact solution of a fully-nonlinear two-layer Stokes wave.

The numerical method is used to study a number of canonical problems corresponding to different classes of Bragg resonances and the results are compared to the perturbation results of chapter one for these cases. The comparisons are excellent within the region of validity of the perturbation results, deviating typically for longer interaction distance and greater wave/bottom steepness, highlighting the importance of (even) higher-order nonlinear interactions not accounted for in the theory.

As a final example, a more general but still relatively simple case is considered involving a single (two-layer) incident wave propagating over a rippled bottom containing three wavenumber components. By selecting these wavenumbers, conditions for multiple resonances obtain with the resulting evolution leading to the creation of many new Bragg transmitted/reflected waves and eventually chaotic motion after some time.

In chapter three the linear problem of wave generation by a translating pulsating point source in a two-layer density stratified fluid is studied analytically and numerically. The problem is motivated by the possibility of observing/characterizing the waves associated with ships and submarines in strong stratified waters that may be present, for example, in warm littoral zones.

From the dispersion relation, it is shown that N_w=4,6 or 8 waves can exist at the farfield

of the disturbance depending on the parameters associated with the disturbance ($\mathcal{F}$, τ, z_0) and the ocean body ($\mathcal{R}$, h). The two- and three-dimensional Green functions are obtained analytically by solving the respective boundary-value problem. The Green functions give the entire wavefield and, of special interest, the far-field amplitudes associated with the N_w waves. These amplitudes depend qualitatively on the location of the disturbance (in the upper or lower fluid), the Froude number $\mathcal{F}$ and dimensionless frequency of pulsation τ of the disturbance, and the density ratio $\mathcal{R}$ and depth ratio h of the stratified layers. These dependencies are elucidated and discussed for $\mathcal{R}$=0.2 and 0.95, the latter being typical of real oceans.

For direct simulation, a spectral-based numerical scheme is developed. The numerical scheme is capable of simulating the general problem involving one or more bodies moving/oscillating arbitrarily with time. The numerical method, of course, also provides an independent check of the theoretical results, which is performed.

In a homogeneous fluid four waves exist at the far field of a translating/oscillating disturbance. But waves in homogeneous fluid are known to be non-resonant at the second order. Many seas and oceans, however, are weakly stratified. In chapter four it is shown that in the presence of stratification triad resonance between ship-generated waves can occur. The result of this nonlinear resonance is a new wave that can affect tracing of submerged/floating objects. It is shown that the resonant wave of a disturbance can move back toward and hit the disturbance; a deeply submerged object if hit by an internal wave can generate a distinguishable surface trace, and resonance interaction can keep feeding the amplitude of co-moving disturbance waves. The Higher order spectral method (HOS) is extended to consider the effect of the current and an oscillating submerged singularity, and theoretical predictions of resonance are validated by direct simulation. It is shown via an illustrative example that multiple resonance may result in a spread spectrum and information loss.

Study of two-layer density stratified fluid has also implications in wave-mud interactions if the mud layer is considered as the lower layer. A simplified model, in which mud layer is considered as a mass-spring-damper bed is presented in Appendix G.

‘

Appendix A

Stokes wave for a two-layer fluid using Newton's iterative method

Newton's iterative method can be used to solve the system of nonlinear equations (2.2.1a) – (2.2.1h) for the nonlinear permanent wave form (Stokes wave) in a two-layer fluid over a flat horizontal bottom. For convenience, we rewrite (2.2.1a) – (2.2.1h) to refer to a coordinate system moving at the phase speed c of the wave and assume a steady solution in this moving frame:

$$\nabla^2\phi_u = 0 \qquad -h_u + \eta_\ell < z < \eta_u \tag{A.0.1a}$$

$$\nabla^2\phi_\ell = 0 \qquad -h_u - h_\ell + \eta_b < z < -h_u + \eta_\ell \tag{A.0.1b}$$

$$f_1 \equiv -c\eta_{u,x} + \eta_{u,x}\phi_{u,x} - \phi_{u,z} = 0 \qquad z = \eta_u \tag{A.0.1c}$$

$$f_2 \equiv -c\phi_{u,x} + \tfrac{1}{2}(\phi_{u,x}^2 + \phi_{u,z}^2) + g\eta_u = 0 \qquad z = \eta_u \tag{A.0.1d}$$

$$f_3 \equiv -c\eta_{\ell,x} + \eta_{\ell,x}\phi_{u,x} - \phi_{u,z} = 0 \qquad z = -h_u + \eta_\ell \tag{A.0.1e}$$

$$f_4 \equiv -c\eta_{\ell,x} + \eta_{\ell,x}\phi_{\ell,x} - \phi_{\ell,z} = 0 \qquad z = -h_u + \eta_\ell \tag{A.0.1f}$$

$$f_5 \equiv \rho_u[-c\phi_{u,x} + \tfrac{1}{2}(\phi_{u,x}^2 + \phi_{u,z}^2) + g\eta_\ell] - \rho_\ell[-c\phi_{\ell,x} + \tfrac{1}{2}(\phi_{\ell,x}^2 + \phi_{\ell,z}^2) + g\eta_\ell] = 0 \qquad z = -h_u + \eta_\ell \tag{A.0.1g}$$

$$f_6 \equiv \phi_{\ell,z} = 0 \qquad z = -h_u - h_\ell. \tag{A.0.1h}$$

The solution can be written in the general form which satisfies the respective Laplace equations and the bottom boundary condition:

$$\eta_u(x,t) = \sum_{n=1}^{N} \eta_{un} e^{ik_n x} + c.c. \ , \qquad \eta_\ell(x,t) = \sum_{n=1}^{N} \eta_{\ell n} e^{ik_n x} + c.c. \ , \tag{A.0.2a}$$

$$\phi_u(x,z,t) = \sum_{n=1}^{N} \left[\phi^c_{un} \frac{\cosh k_n(z-h_u)}{\cosh(k_n h_u)} + \phi^s_{un} \frac{\sinh k_n(z-h_u)}{\cosh k_n h_u} \right] e^{ik_n x} + c.c. \ , \tag{A.0.2b}$$

$$\phi_\ell(x,z,t) = \sum_{n=1}^{N} \phi_{\ell n} \frac{\cosh k_n(z+h_u+h_\ell)}{\cosh k_n h_\ell} e^{ik_n x} + c.c. \ . \tag{A.0.2c}$$

where N is the number of Fourier modes. The unknown modal amplitudes, η_{un}, $\eta_{\ell n}$, ϕ^c_{un}, ϕ^s_{un}, and $\phi_{\ell n}$, n=1, ..., N, and the unknown phase speed of the wave c are to be determined from the five boundary conditions on the free surface and interface.

To do that, we rewrite these boundary conditions in a symbolic form:

$$\mathbf{F}(\mathbf{X}) = \mathbf{0} \tag{A.0.3}$$

where $\mathbf{F} \equiv \{\mathbf{f_1}, \mathbf{f_2}, \mathbf{f_3}, \mathbf{f_4}, \mathbf{f_5}\}$ and the unknown vector $\mathbf{X}$ is:

$$\mathbf{X} = \{\eta_{u1}, \ldots, \eta_{uN-1}, c, \eta_{\ell 1}, \ldots, \eta_{\ell N}, \phi^c_{u1}, \ldots, \phi^c_{uN}, \phi^s_{u1}, \ldots, \phi^s_{uN}, \phi_{\ell 1}, \ldots, \phi_{\ell N}\} \ . \tag{A.0.4}$$

Finally, to complete the system, we set η_{uN}=0. Newton's iterative method is applied to solve the system of nonlinear equations, (A.0.3), for the unknown vector $\mathbf{X}$. For an initial guess, the linearized solution is used.

Appendix B

Weyl's Identity

The Green's function for the Laplace's equation ($\nabla^2\phi = 0$) is

$$G = -\frac{1}{4\pi}\frac{1}{r} \tag{B.0.1}$$

It can be shown by direct substitution that it is indeed the solution to the Laplace's equation with an impulse forcing:

$$\nabla^2 G = \delta(\mathbf{x}). \tag{B.0.2}$$

To do so, integrate the left hand side within a sphere with radius r that encompasses the origin

$$\int_V \nabla^2 G \; dV = -\frac{1}{4\pi}\int_V \nabla.(\nabla G) \; dV = \int_S \mathbf{n}.(\nabla G) \; dS = 1 \tag{B.0.3}$$

because

$$\nabla G = -\frac{1}{4\pi}\frac{\partial}{\partial r}\frac{1}{r} = \frac{1}{4\pi}\frac{1}{r^2}\hat{r}. \tag{B.0.4}$$

but

$$\int_V \delta(\mathbf{x}) = 1 \tag{B.0.5}$$

and therefore the identity is proved.

Now assume that the Fourier transform exists for $G(x, y, z)$ in the form: (derivation follows Duffy, 2004):

$$G(x,y,z) = \frac{1}{(2\pi)^3}\int_{-\infty}^{\infty}\int_{-\infty}^{\infty}\int_{-\infty}^{\infty} \tilde{G}(k,l,m)\ e^{i(kx+ly+mz)}\ dk\ dl\ dm \tag{B.0.6}$$

where

$$\tilde{G}(k,l,m) = \int_{-\infty}^{\infty}\int_{-\infty}^{\infty}\int_{-\infty}^{\infty} G(x,y,z)\ e^{-i(kx+ly+mz)}\ dx\ dy\ dz \tag{B.0.7}$$

is the Fourier transform of the Green's function. Taking the Fourier transform of both sides of equation B.0.2 we get

$$-\kappa^2\tilde{G}(k,l,m) = 1 \tag{B.0.8}$$

where $\kappa^2 = k^2 + l^2 + m^2$. Therefore

$$\tilde{G}(p,q,r) = -\frac{1}{\kappa^2} \tag{B.0.9}$$

and

$$G(x,y,z) = -\frac{1}{(2\pi)^3}\int_{-\infty}^{\infty}\int_{-\infty}^{\infty}\int_{-\infty}^{\infty} \frac{1}{\kappa^2}\ e^{i(kx+ly+mz)}\ dk\ dl\ dm \tag{B.0.10}$$

The integration in m can be evaluated using the contour integral and Residue theorem. The m-integral is

$$\int_{-\infty}^{\infty}\frac{e^{-imz}}{k^2+l^2+m^2}dr = \pi\frac{e^{-|z|\sqrt{k^2+l^2}}}{\sqrt{k^2+l^2}} \tag{B.0.11}$$

for $z < 0$ (note that z is a real variable), we have to choose the lower half plane and for $z > 0$ the upper half plane. Therefore

$$G(x,y,z) = -\frac{1}{8\pi^2}\int_{-\infty}^{\infty}\int_{-\infty}^{\infty} \frac{e^{ikx+ily-|z|\sqrt{k^2+l^2}}}{\sqrt{k^2+l^2}}\ dk\ dl \tag{B.0.12}$$

Equating this with B.0.1 we get the so called *Weyl integral*:

$$\frac{1}{r} = \frac{1}{2\pi} \int_{-\infty}^{\infty} \int_{-\infty}^{\infty} \frac{e^{ikx+ily-|z|\sqrt{k^2+l^2}}}{\sqrt{k^2+l^2}} \, dk \, dl \tag{B.0.13}$$

Appendix C

Triad wave-wave resonance Condition in a two-layer fluid

It is known that in a two-layer density stratified fluid, three waves, either two surface-mode waves and one internal-mode wave (studied first by Ball, 1964) or two internal-mode waves and one surface-mode wave (first studied by Wen, 1995*b*), can make a triad resonance. For this to happen, they must satisfy the triad resonance condition:

$$k_0 = k_1 + k_2 \tag{C.0.1}$$

$$\omega_0 = \omega_1 + \omega_2 \tag{C.0.2}$$

where $\mathcal{D}(k_i, \omega_i) = 0$ for $i = 0, 1, 2$ and $\mathcal{D}(\omega, k)$ is the two-layer dispersion relation

$$\mathcal{D}(\omega, k) = \omega^4(R + \coth kh_u \coth kh_\ell) - \omega^2 gk(\coth kh_u + \coth kh_\ell) + g^2k^2(1 - R), \tag{C.0.3}$$

where $R = \rho_u/\rho_l$ is the density ratio.

A surface-mode wave (k_{s1}) and an internal-mode wave (k_{i2}) can resonate an oppositely-traveling surface-mode wave (k_{s2}) that has a lower frequency compared to k_{s1}. The same surface-mode wave (k_{s1}) with an oppositely-traveling internal-mode wave (k_{i1}) can resonate another oppositely-traveling surface-mode wave (k_{s2}) that has a higher frequency compared to k_{s1}. These two cases, first discussed by Ball (1964), are shown graphically (two lower curves) in figure C-2-a for $R = 0.9$ and $h^* = h_\ell/h_u = 1$. For a given right-going surface-mode wave k_{s1}, the longer (shorter) second surface-mode wave k_{s2}, generates a right (left)

going internal-mode wave. Looking in depth, these two cases are basically just one: one surface-mode wave with a one internal-mode wave that travels in the same direction give an oppositely-traveling surface-mode wave with the frequency less than original surface-mode wave. Asymptotic relations for these two branches in the weak stratification ($1 - R = \epsilon^2$ and $\epsilon \ll 1$) can be obtained: in the limit of both deep layers ($kh_u \gg 1$ and $kh_l \gg 1$), both shallow layers ($kh_u \ll 1$ and $kh_l \ll 1$) and upper shallow-lower deep layer ($kh_u \ll 1$ and $kh_l \gg 1$) we have respectively

$$\frac{k_{s2}}{k_{s1}} = -1 \pm 2\epsilon, \quad \frac{k_{s2}}{k_{s1}} = -1 \pm \frac{2h^*(3+2h^*)}{(1+h^*)^2}\,\epsilon^2, \quad \frac{k_{s2}}{k_{s1}} = -1 \pm 4\epsilon\sqrt{k_{s1}h_u} \tag{C.0.4}$$

The equations for the limit of both deep layers are shown by dashed lines in figure C-2-a. Despite Ball (1964)'s claim that these two cases are the only two possible cases of resonance between two surface-mode waves and one internal-mode wave (2S-1I), we found that there are two other possibilities. Figure C-1 illustrates these two cases schematically on the dispersion relation curve. In order to have this type of resonance, the slope of at least one point on the surface-mode (outer) branch $\tan(\theta_1)$ has to be less than the slope of internal-mode curve at the origin $\tan(\theta_2)$. But the slope of dispersion relation curve is the group velocity. From shallow water theory, the group velocity of internal-mode wave at the origin is given by

$$C^*_{g(kh_u=0)} = \frac{C_g}{\sqrt{gh_u}} = \frac{\sqrt{2}}{2}\sqrt{1 + h^* - \sqrt{(1-h^*)^2 + 4Rh^*}} \tag{C.0.5}$$

where in the limit when $1 - R = \epsilon^2$

$$C^*_{g(kh_u=0)} = \epsilon\sqrt{\frac{h^*}{1+h^*}} \tag{C.0.6}$$

Group velocity for the surface-mode wave at a given wave-number in general is a complicated function of R, h^* and kh_u, but in the case of deep layers it is given by

$$C^*_{g(kh_u=0)} = \frac{1}{\sqrt{kh_u}} \tag{C.0.7}$$

obviously for

$$kh_u > \frac{1+h^*}{4h^*\epsilon^2} \tag{C.0.8}$$

(provided that $kh_u \gg 1$ and $kh_\ell \gg 1$) the group velocity condition is satisfied and we get two new resonance cases. This condition clearly states that for an arbitrary chosen density ratio (close to unity) and depth ratio, these two new resonance can be appeared provided that we choose a big enough wave-number for the incident surface-mode wave. Figure C-2-a shows these new emerged resonance cases (the solid parabola-like part). The two branches of this parabola-like function asymptotically tend to

$$\frac{k_{s2}}{k_{s1}} = 1 \pm 2\,\epsilon^2 \tag{C.0.9}$$

as shown by dashed-lines in figure C-2-a.

Figure C-2-b shows the resonance combinations when two internal-mode waves and one surface-mode wave (2I-1S) exchange energy. Comparing two branches of (2I-1S) case with the corresponding branches of (2S-1I) case, it is seen that the resultant surface-mode wave in (2I-1S) case has a much lower wave-number than the initial internal-mode waves, while in (2S-1I) case, the resultant internal-mode wave has the same order wave-number as the initial two surface-mode waves. As the density ratio R goes to zero, these two branches get close to each other and to the slope of the unity.

Again the asymptotic formula in the limit of weak stratification for both deep layers, both shallow layers and upper-shallow lower-deep layers are given respectively by

$$\frac{k_{i2}}{k_{i1}} = 1 \pm 2\epsilon^2, \quad \frac{k_{i2}}{k_{i1}} = \quad 1 \pm \frac{2h^*(3+2h^*)}{(1+h^*)^2}\,\epsilon^2, \quad \frac{k_{i2}}{k_{i1}} \quad = \quad 1 \pm 4\epsilon^2 k_{i1} h_u \tag{C.0.10}$$

The deep layer asymptotes are shown by dashed-lines in figure C-2-b. Equality of asymptotic shallow-layers formula in (2S-1I) and (2I-1s) cases can be easily seen from the dispersion relation curves since in this limit all curves are simple straight lines. Therefore, similarity between triangles forming the triad resonance exists and ratios have to be the same.

For a very very strong stratification, two new resonance cases are added to (2I-1S) cases. It can be shown that in the limit of deep layers, the condition for having these two cases is $R > 1/3$ which is not physical.

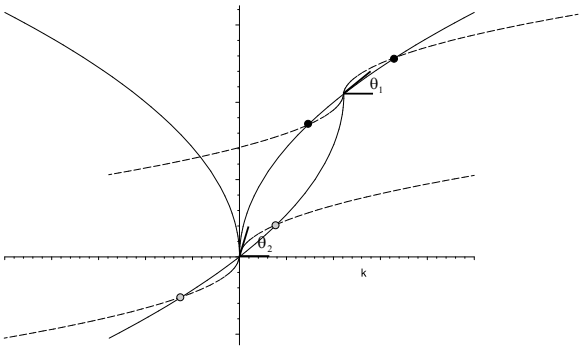

Figure C-1: Two new cases of resonance between two surface-mode waves and one internal-mode wave not considered in Ball (1964). The gray circles are equivalent of black circles at the origin. solid curve indicates the surface-mode dispersion relation and dashed curve is for internal-mode dispersion relation

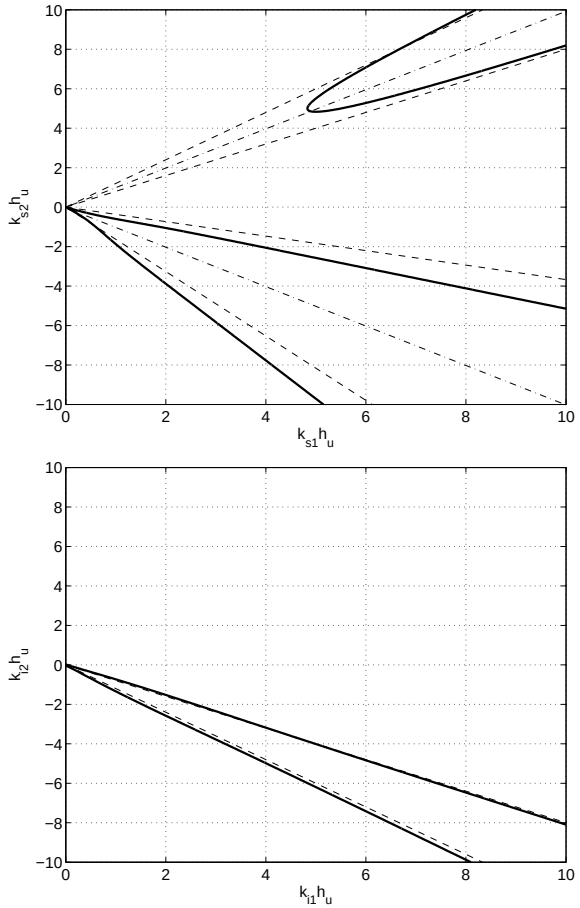

Figure C-2: Two-dimensional triad resonance in two-layer fluid. a. two surface-mode waves (k_{s1}, k_{s2}) and one internal-mode wave (either of k_{i1} or k_{i2}), b. two internal-mode waves (k_{i1}, k_{i2}) and one surface-mode wave (either of k_{s1} or k_{s2}). $R = 0.9$, $h^* = 1$.

Appendix D

Moving point source in two semi-infinite fluids

Assume a source is moving leftward with velocity U in a two semi-infinite fluids as shown in figure 1-1. Consider a coordinate system that moves with the source and originates on the undisturbed free surface right above the source. If in the moving coordinate system everything is steady then the linearized governing equations are

$$\nabla^2\phi_u = 0 \tag{D.0.1}$$

$$\nabla^2\phi_l = M\delta(z - z_0)\delta(x) \tag{D.0.2}$$

$$\phi_{u,z} = \phi_{l,z} \tag{D.0.3}$$

$$U\eta_x = \phi_{u,z} \tag{D.0.4}$$

$$R(U\phi_{u,x} + g\eta) = (U\phi_{l,x} + g\eta) \tag{D.0.5}$$

$$\nabla\phi_u \to 0 \text{ as } z \to +\infty \tag{D.0.6}$$

$$\nabla\phi_l \to 0 \text{ as } z \to -\infty \tag{D.0.7}$$

where M is the strength of the source and $R = \rho_u/\rho_l$ is the density ratio. We divide the lower layer potential ϕ_l into singularity part ϕ_l^s and the rest ϕ_l^r. The singular part is well known and is given by

$$\phi_l^s = -\frac{M}{4\pi}\frac{1}{r} \tag{D.0.8}$$

where $r = \sqrt{x^2 + y^2 + (z - z_0)^2}$. Using Weyl's integral and Fourier transform properties the total solution can be written in the form

$$\phi_u = \frac{1}{4\pi^2} \int_{-\infty}^{\infty} \int_{-\infty}^{\infty} \tilde{\phi}_u(\alpha, \beta) e^{[if - Kz]} d\alpha d\beta \tag{D.0.9}$$

$$\phi_l = \phi_l^r + \phi_l^s = \frac{1}{4\pi^2} \int_{-\infty}^{\infty} \int_{-\infty}^{\infty} \tilde{\phi}_l(\alpha, \beta) e^{[if + Kz]} d\alpha d\beta$$
$$- \frac{M}{8\pi^2} \int_{-\infty}^{\infty} \int_{-\infty}^{\infty} \frac{1}{K} e^{[if - K|z - z_0|]} d\alpha d\beta \tag{D.0.10}$$

where $K = \sqrt{\alpha^2 + \beta^2}$ and $f = \alpha x + \beta y$. The signs for z powers have been chosen so that boundary conditions D.0.6 and D.0.7 are satisfied. Substituting D.0.9 and D.0.10 into D.0.3 and D.0.5 conditions we get a linear set of equations for $\tilde{\phi}_u(\alpha, \beta)$ and $\tilde{\phi}_l(\alpha, \beta)$.

$$\tilde{\phi}_u(\alpha, \beta) = \frac{MU^2 \lambda \alpha^2}{K(Kg\gamma - U^2\alpha^2)} e^{Kz_0} \tag{D.0.11}$$

$$\tilde{\phi}_l(\alpha, \beta) = -\frac{M}{2K} \left(1 + \frac{2U^2\alpha^2\lambda}{Kg\gamma - U^2\alpha^2}\right) e^{Kz_0} \tag{D.0.12}$$

The interface elevation can be found from equation D.0.4

$$\eta(x, y) = \frac{iMU\lambda}{4\pi^2} \int_{-\infty}^{\infty} \int_{-\infty}^{\infty} \frac{\alpha e^{if + Kz_0}}{(Kg\gamma - U^2\alpha^2)} d\alpha d\beta \tag{D.0.13}$$

where $\gamma = (1 - R)/(1 + R)$ and $\lambda = 1/(1 + R)$.

Appendix E

HOS formulation for a blunt body

E.1 Introduction

Panel method converts the problem of Laplace's equation (partial differential equation) in a given domain to a linear integral equation over the boundary of the domain. To satisfy the boundary conditions, suitable number of sources/doublets have to be taken, but there is a freedom in choosing which one to take.

The panel method is capable of handling more complicated geometries than other available methods. It is also very flexible and economic (see Mason, 1995). The panel method used to be called the surface singularity method, but then using quadrilaterals to make grids on the surfaces changed its name to the panel method. The boundary element method technique is the same idea that is used in other problems governed by linear partial differential equations (see Hess, 1990).

The most important application of the panel method is in 3D problems because in 2D problems more precise methods such as mappings can be used to solve the Laplace's equation in complicated geometries. One of the important advantage of the panel method over other existing methods is that we don't need to define grid within the flow field.

The various types of implementations are

1. using different singularities (sources, doublets and vortices)

2. type of distribution of each singularity over the panel

3. the geometry of the panel

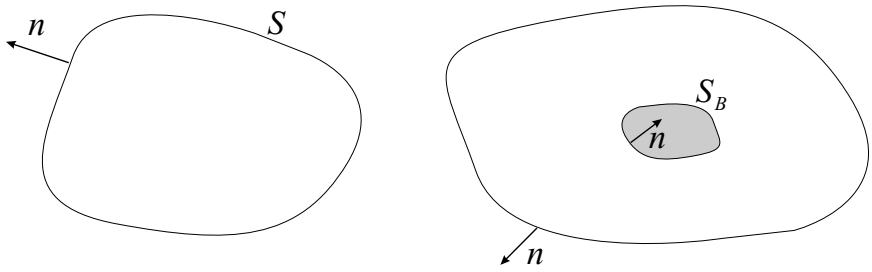

Figure E-1: The domains for derivation of the integral equation. Left is the flow in interior domain and the right picture is the flow out-side the body

E.2 Formulation

[1]For an irrotational flow we can define a potential function. If the flow is incompressible then this potential satisfies Laplace's equation [2]

$$\nabla^2\phi = 0. \tag{E.2.1}$$

Consider the divergence theorem

$$\int_S \mathbf{n} \,.\, \mathbf{q}\; dS = \int_V \nabla \,.\, \mathbf{q}\; dV \tag{E.2.2}$$

where $\mathbf{n}$ is the unit vector perpendicular to the boundary and pointing outward. Assume ϕ_1 and ϕ_2 are two solutions of the Laplace's equation and take $\mathbf{q} = \phi_1\nabla\phi_2 - \phi_2\nabla\phi_1$ in the divergence theorem, therefore

$$\int_S (\phi_1\nabla\phi_2 - \phi_2\nabla\phi_1) \,.\, \mathbf{n}\; dS = \int_V (\phi_1\nabla^2\phi_2 - \phi_2\nabla^2\phi_1)\; dV \tag{E.2.3}$$

If potentials have no singularity inside the domain V then the above integrals are equal to zero. If we assume that

$$\phi_1 = \frac{1}{r} \;\text{ and }\; \phi_2 = \Phi \tag{E.2.4}$$

where Φ is the potential of our interest, then we can express $\Phi(P)$ where P is an arbitrary point in the domain in terms of an integral over just the boundary S of the domain. Note

[1]see Katz & Plotkin (2001); Mason (1995)

[2]ϕ can not have extremum at any interior point. Extremum of ϕ and therefore extremum of pressure and velocity all occur on the boundary.

that r is being measured from P and therefore one of the chosen potentials has a singularity inside the domain of our interest. If we exclude the point P by a sphere with a radius ϵ, the flow is potential without singularity everywhere outside this small sphere and the outer boundary. mathematically

$$\int_{S-S_\epsilon} (\phi_1 \nabla\phi_2 - \phi_2 \nabla\phi_1) \,.\, \mathbf{n}\, dS = \int_S \left(\frac{1}{r}\nabla\Phi - \Phi\nabla\frac{1}{r}\right) \,.\, \mathbf{n}\, dS - \int_{S_\epsilon} \left(\frac{1}{r}\frac{\partial\Phi}{\partial r} + \frac{\Phi}{r^2}\right) dS = 0 \tag{E.2.5}$$

but in spherical coordinate $dS = r^2 \sin\theta d\theta d\varphi$ and we assume over the small sphere S_ϵ, ϕ and all its derivatives remain approximately constant. therefore, we conclude

$$\left.\frac{\partial\Phi}{\partial r}\right|_P \int r\sin\theta \; d\theta \; d\varphi + \left.\Phi\right|_P \int \sin\theta \; d\theta \; d\varphi = \int_S \left(\frac{1}{r}\nabla\Phi - \Phi\nabla\frac{1}{r}\right) \,.\, \mathbf{n}\, dS \tag{E.2.6}$$

when $r = \epsilon \to 0$, the first integral vanishes but the second integral is equal to 4π. Therefore,

$$\begin{aligned} \Phi(P) &= \frac{1}{4\pi}\int_S \left(\frac{1}{r}\nabla\Phi - \Phi\nabla\frac{1}{r}\right) \,.\, \mathbf{n}\, dS \\ &= \frac{1}{4\pi}\int_S \left(\frac{1}{r}\frac{\partial\Phi}{\partial n} - \Phi\frac{\partial}{\partial n}\frac{1}{r}\right) dS \end{aligned} \tag{E.2.7}$$

In two-dimension the coefficient $1/4\pi$ has to be replaced by $1/2\pi$. The function $\Phi(P)$ gives the value of the potential at all interior points as a function of Φ and $\partial\Phi/\partial n$ on the boundaries. All results so far are related to the interior domain (figure E-1-left). For the exterior of a domain bounded by a boundary at infinity, if we assume that the integral over that infinite boundary is equal to Φ_∞, then the same procedure gives

$$\begin{aligned} \Phi(P) &= \Phi_\infty + \frac{1}{4\pi}\int_{S_B} \left(\frac{1}{r}\nabla\Phi - \Phi\nabla\frac{1}{r}\right) \,.\, \mathbf{n}\, dS \\ &= \Phi_\infty + \frac{1}{4\pi}\int_{S_B} \left(\frac{1}{r}\frac{\partial\Phi}{\partial n} - \Phi\frac{\partial}{\partial n}\frac{1}{r}\right) dS \end{aligned} \tag{E.2.8}$$

where here P is a point outside S_B in figure E-1-right. In 3-dimension, potential of a source and a doublet are

$$\phi_s = \frac{\sigma}{4\pi r} \quad , \quad \phi_d = \frac{\mu}{4\pi}\frac{\partial}{\partial n}\frac{1}{r} \tag{E.2.9}$$

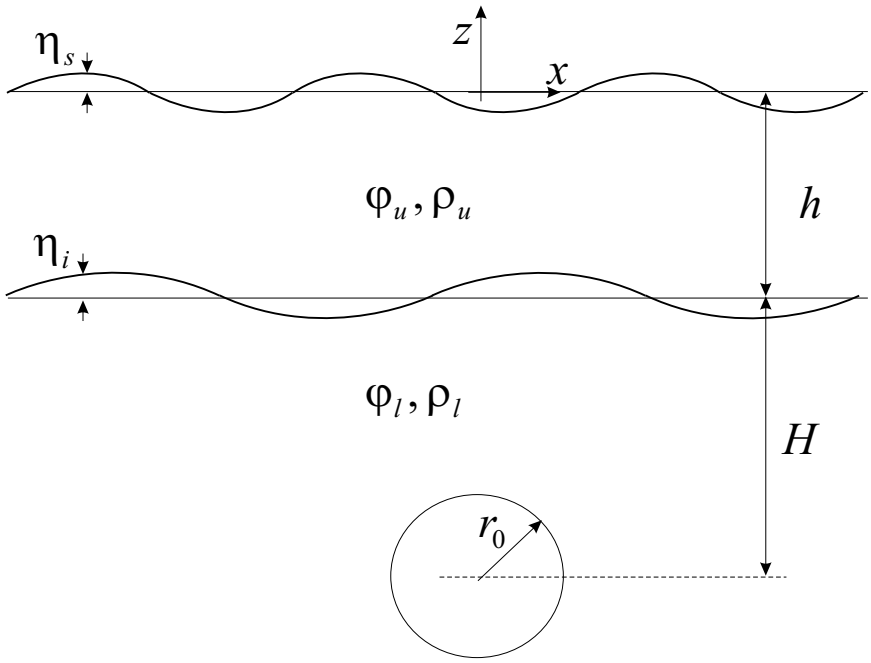

Figure E-2: The setup

Therefore equation E.2.8 can be written in the following form

$$\Phi(P) = \Phi_\infty + \frac{1}{4\pi}\int_{S_B}\left(\sigma\frac{1}{r} - \mu\frac{\partial}{\partial n}\frac{1}{r}\right)\, dS \tag{E.2.10}$$

where σ and μ are called the source and the double strengths respectively and act like a Green function. This equation states that we can find the potential outside a submerged body by a suitable distribution of point sources and doublets on the boundary. Now the problem is to find these strengths and the potential at infinity such that all boundary conditions are satisfied.

In 2-dimensional problem the potential of a source and a doublet is given by

$$\phi_s = \frac{\sigma}{2\pi}\ln r \quad , \quad \phi_d = \frac{\mu}{2\pi}\frac{\cos\theta}{r}. \tag{E.2.11}$$

The 2D version of equation E.2.10 is

$$\Phi(P) = \Phi_\infty + \frac{1}{4\pi}\int_{S_B}\left(\frac{\sigma}{2\pi}\ln r - \frac{\mu}{2\pi}\frac{\cos\theta}{r}\right)\, dS. \tag{E.2.12}$$

E.3 HOS formulation

Consider the irrotational motion of two homogeneous, incompressible, immiscible and inviscid fluids with densities ρ_u and ρ_l. Indices $_u$ and $_l$ are extensively used in this paper to indicate upper layer and lower layer respectively. The two fluid are under a free surface and separated by their interface (Fig. E-2). Surface tension is not considered. h_u is the depth of the upper layer and the lower layer is assumed to be infinitely deep. The center of the cylinder is located at the depth of H bellow the interface. The flow in each layer is described by a velocity potential $\phi_u(x,z,t)$ and $\phi_l(x,z,t)$. To formulate the problem we use a global cartesian coordinate system (x,z) with its origin located on the mean free surface, and a local cylindrical coordinate (r,θ) with its origin at the center of the submerged cylinder where $r^2 = x^2 + (z+H+h)^2$ and θ is measured counterclockwise from positive x-axis direction.

Full nonlinear governing equations are

$$\nabla^2\phi_u = 0 \qquad -h_u + \eta_i < z < \eta_s \qquad \text{(E.3.13a)}$$

$$\nabla^2\phi_l = 0 \qquad -\infty < z < -h_u + \eta_i \qquad \text{(E.3.13b)}$$

$$\eta_{s,t} + \eta_{s,x}\phi_{u,x} - \phi_{u,z} = 0 \qquad z = \eta_s \qquad \text{(E.3.13c)}$$

$$\phi_{u,t} + \tfrac{1}{2}(\phi_{u,x}^2 + \phi_{u,z}^2) + g\eta_s = 0 \qquad z = \eta_s \qquad \text{(E.3.13d)}$$

$$\eta_{i,t} + \eta_{i,x}\phi_{u,x} - \phi_{u,z} = 0 \qquad z = -h + \eta_i \qquad \text{(E.3.13e)}$$

$$\eta_{i,t} + \eta_{i,x}\phi_{l,x} - \phi_{l,z} = 0 \qquad z = -h + \eta_i \qquad \text{(E.3.13f)}$$

$$\rho_u(\phi_{u,t} + \tfrac{1}{2}(\phi_{u,x}^2 + \phi_{u,z}^2) + g\eta_i) - \rho_l(\phi_{l,t} + \tfrac{1}{2}(\phi_{l,x}^2 + \phi_{l,z}^2) + g\eta_i) = 0 \qquad z = -h + \eta_i \qquad \text{(E.3.13g)}$$

$$\nabla\phi_l \to 0 \qquad z = \to -\infty, \qquad \text{(E.3.13h)}$$

$$\phi_{l,r}(R,\theta,t) = 0 \qquad 0 \le \theta \le 2\pi. \qquad \text{(E.3.13i)}$$

where $\eta_s = \eta_s(x,t)$ and $\eta_i = \eta_i(x,t)$ are respectively surface and interface elevation and g is the gravity acceleration. the subscript $_{,X}$ means the derivative with respect to X. We

define a so called surface/interface potential

$$\phi^{S,I}(x,t) = \phi(x,\eta_{s,i}(x,t),t) \tag{E.3.14}$$

$$\phi_x^{S,I} = \phi_x + \partial_x\eta_{s,i}\ \phi_z \tag{E.3.15}$$

using this notation we can write the pressure continuity condition on the surface and interface in the form

$$\phi_{u,t}^S = \frac{1}{2}\nabla_x\phi_u^S.\nabla_x\phi_u^S + \frac{1}{2}(1+\nabla_x\eta.\nabla_x\eta){\phi_{u,z}}^2 - g\eta_s \ @\ z=\eta_s \tag{E.3.16}$$

$$\begin{aligned}(\phi_l^I - R\phi_u^I)_{,t} &= \frac{1}{2}(R\nabla_x\phi_u^I.\nabla_x\phi_u^I - \nabla_x\phi_l^I.\nabla_x\phi_l^I) \\ &+\frac{1}{2}(1+\nabla_x\eta.\nabla_x\eta)({\phi_{l,z}}^2 - R{\phi_{u,z}}^2) - g\eta(1-R)\ @\ z=-h+\eta_i\end{aligned} \tag{E.3.17}$$

We assume that ϕ_u,ϕ_l and η are $O(\epsilon)$ where ϵ is a measure of the wave steepness and is a small quantity. Expansion up to a given order M in ϵ gives

$$\phi_u(\mathbf{x},z,t) = \sum_{m=1}^{M}\phi_u^{(m)}(\mathbf{x},z,t) \tag{E.3.18}$$

$$\phi_l(\mathbf{x},z,t) = \sum_{m=1}^{M}\phi_l^{(m)}(\mathbf{x},z,t) \tag{E.3.19}$$

For 2π periodic problem in x, we represent the solution of Laplace equation in the form

$$\phi_u^{(m)}(x,z,t) = \int_{-L}^{L}\mu_s(x',t)G_{z'}(x,z;x',0)dx' + \int_{-L}^{L}\mu_{iu}(x',t)G_{z'}(x,z;x',-h)dx' \tag{E.3.20}$$

$$\phi_l^{(m)}(x,z,t) = \int_{-L}^{L}\mu_{il}(x',t)G_{z'}(x,z;x',-h)dx' + \int_{0}^{2\pi}\sigma(\theta',t)G(r,\theta;r_0,\theta')r_0d\theta' \tag{E.3.21}$$

where

$$G(x,z;x',z') = \frac{1}{2}\log\left[\sin^2\left(\frac{x-x'}{2L/\pi}\right) + \sinh^2\left(\frac{z-z'}{2L/pi}\right)\right] \tag{E.3.22}$$

and $\mu_s, \mu_{iu}, \mu il$ and σ are respectively the dipole strength on the mean surface, mean interface for the upper layer, mean interface for the lower layer and the source strength on the body boundary. The chosen form of the solution satisfies Laplace's equation and the boundary condition at the infinity. The four singularity strengths have to be found in such

a way that all other boundary conditions are satisfied. If we assume that the potential on the real free surface and the difference of the lower layer potential and the density-ratio-weighted upper layer potential is given, then we can show that by combining all boundary conditions we can get the four required equation to solve for unknown strengths and therefore the boundary value problem is solved. Having the BVP solved, the right hand side of the temporal evolution equations are known and they can be integrated to provide the information about the future of the fluid.

1. For the surface from classical HOS approach we have (close to the free surface)

$$\phi_u(x,z,t) = \sum_{m=1}^{M} \phi^{(m)}(x,z,t) = \sum_{m=1}^{M} \sum_{k=0}^{M-m} \frac{z^k}{k} \frac{\partial^k}{\partial z^k} \phi^{(m)}(x,z,t)\big|_{z=0} \tag{E.3.23}$$

assuming $\phi_u(x,\eta_s,t=0) = \phi_u^S(x)$ is given, matching the same orders gives

$$\begin{aligned} \phi_u^{(1)}(x,0,t) &= \phi_u^S, & \text{(E.3.24)} \\ \phi_u^{(m)}(x,0,t) &= -\sum_{k=1}^{m-1} \frac{\eta_s^k}{k!} \frac{\partial^k}{\partial z^k} \phi^{m-k}(x,z,t)\big|_{z=0}, \qquad m = 2,3,...,M. & \text{(E.3.25)} \end{aligned}$$

2. For the interface we define

$$\psi(x,\zeta,t) = \phi_l(x,\zeta,t) - R\ \phi_u(x,\zeta,t) \tag{E.3.26}$$

where ($\zeta = z + h_1$). expansion of ψ close to the interface gives

$$\psi(x,\zeta,t) = \sum_{m=1}^{M} \psi^{(m)}(x,\zeta,t) = \sum_{m=1}^{M} \sum_{k=0}^{M-m} \frac{\zeta^k}{k} \frac{\partial^k}{\partial \zeta^k} \psi^{(m)}(x,\zeta,t)\big|_{\zeta=0} \tag{E.3.27}$$

assuming $\psi(x,\eta_i,t=0) = \psi^I(x)$ is given, matching the same orders gives

$$\begin{aligned} \psi^{(1)}(x,0,t) &= \psi^I, & \text{(E.3.28)} \\ \psi^{(m)}(x,0,t) &= -\sum_{k=1}^{m-1} \frac{\eta_i^k}{k!} \frac{\partial^k}{\partial \zeta^k} \psi^{m-k}(x,\zeta,t)\big|_{\zeta=0}, \qquad m = 2,3,...,M. & \text{(E.3.29)} \end{aligned}$$

3. subtracting two kinematic interface condition from each other gives

$$(\phi_{u,z} - \phi_{l,z}) = \eta_x(\phi_{u,x} - \phi_{l,x}) \ @\ z = -h_1 + \eta_i \tag{E.3.30}$$

now we define another variable

$$\Phi(x,\zeta,t) = \phi_u(x,\zeta,t) - \phi_l(x,\zeta,t) \tag{E.3.31}$$

$$\Phi(x,\zeta,t) = \sum_{m=1}^{M} \Phi^{(m)}(x,\zeta,t) = \sum_{m=1}^{M}\sum_{k=0}^{M-m} \frac{\zeta^k}{k}\frac{\partial^k}{\partial\zeta^k}\Phi^{(m)}(x,\zeta,t)\big|_{\zeta=0} \tag{E.3.32}$$

and the equation simply turns to

$$\Phi_\zeta = \eta_x \Phi_x \qquad\qquad z = \eta_i \tag{E.3.33}$$

The key idea is that the right hand side starts from second order terms, and this gives the first order term of the left hand side equal to zero (linear solution). Having the first term of left hand side we can proceed to higher order and solve for unknown coefficients of the solution. Substituting the expansion gives

$$\sum_{m=1}^{M}\sum_{k=0}^{M-m} \frac{\eta_i^k}{k}\frac{\partial^{k+1}}{\partial\zeta^{k+1}}\Phi^{(m)}(x,\zeta,t)\big|_{\zeta=0} = \eta_{i,x}\sum_{m=1}^{M}\sum_{k=0}^{M-m} \frac{\eta_i^k}{k}\frac{\partial^k}{\partial\zeta^k}\Phi_x^{(m)}(x,\zeta,t)\big|_{\zeta=0} \tag{E.3.34}$$

solving for $\Phi^{(m)}$ results in

$$\Phi_z^{(1)}(x,0,t) = 0, \tag{E.3.35}$$

$$\Phi_z^{(m)}(x,0,t) = -\sum_{k=1}^{m-1} \frac{\eta_i^{k-1}}{(k-1)!}\frac{\partial^{k-1}}{\partial\zeta^{k-1}}\Phi_x^{m-k}(x,\zeta,t)\big|_{\zeta=0} - \sum_{k=1}^{m-1} \frac{\eta_i^k}{k!}\frac{\partial^{k+1}}{\partial\zeta^{k+1}}\Phi^{m-k}(x,\zeta,t)\big|_{\zeta=0}, \qquad m = 2,3,\ldots \tag{E.3.36}$$

4. The fourth equation is the no-flux (Neuman) boundary condition on the cylinder boundary.

Having this four sets of equations the problem is closed.

Appendix F

Oblique Bragg resonance

In three dimension the bottom boundary condition at the second order is

$$\phi^{(2)}_{\ell,z} = \eta_{b,x}\phi^{(1)}_{\ell,x} + \eta_{b,y}\phi^{(1)}_{\ell,y} - \eta_b\phi^{(1)}_{\ell,zz} \qquad z = -h_u - h_\ell. \tag{F.0.1}$$

Class I Bragg resonance condition in three dimension is

$$\mathbf{k} + \mathbf{k}_b = \mathbf{k}_r \tag{F.0.2}$$

$$\omega = \omega_r \tag{F.0.3}$$

We assume the incident wave is a surface mode wave with the wavenumber $\mathbf{k} = (k_s \cos\theta_s, k_s \sin\theta_s)$ where $k_s = |\mathbf{k}|$ travels over a periodic topography with the wavenumber $\mathbf{k}_b = (k_b \cos\theta_b, k_b \sin\theta_b)$ where $k_b = |\mathbf{k}_b|$:

$$\eta_b = d\cos(\mathbf{k}_b \cdot \mathbf{x}) \tag{F.0.4}$$

We chose our coordinates such that the positive x-axis is along the resonant internal-mode wave, i.e. $\mathbf{k}_r = (k_i, 0)$

$$\begin{aligned} \phi^{(2)}_{\ell,z} &= -1/2Cd(k_b k_s \cos\theta_b \cos\theta_s + k_b k_s \sin\theta_b \sin\theta_s + k_s^2)\sin(k_i x - \omega t) + \mathrm{NT} \\ &= -1/2Cd[k_b k_s \cos(\theta_b - \theta_s) + k_s^2]\sin(k_i x - \omega t) + \mathrm{NT} \end{aligned} \tag{F.0.5}$$

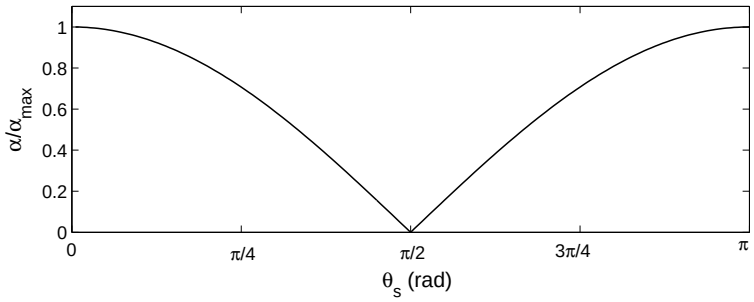

Figure F-1: variation of strength of class I Bragg resonance as a function of incident angle for h_ℓ/h_u=0.63, $\mathcal{R}$=0.85, $\omega_s^2 h_u/g$=0.96.

The magnitude of the forcing term is maximum when the absolute value of the quantity inside bracket

$$\alpha \equiv |k_b k_s \cos(\theta_b - \theta_s) + k_s^2| \tag{F.0.6}$$

is maximum. With Jamali *et al.* (2003); Hill & Foda (1998) parameters $h_u = 12.5cm$, $h_\ell = 7.9cm$, $\mathcal{R} = 0.85$, $\omega_s = 8.7s^{-1}$, figure F-1 shows the relative value of α with respect to its maximum value. It is seen that oblique class I Bragg resonance is always weaker than the normal incident (compare with Liu & Yue (1998) figure 7 or Mei *et al.* (2005) figure 15.16).

Appendix G

Wave attenuation over muddy sea floor

G.1 Introduction

Mud or cohesive sediment is a mixture of clay particles, silt, (fine) sand, organic material, sometimes gas, and water. This sediment mixture has cohesive properties because of low permeability and electrochemical attraction of clay particles and organic material. Effect of muddy sea floor is important in many real world applications:

1. Mud deposits adversely affects the navigation,
2. Unfortunately, today many mud deposits are contaminated, endangering the ecosystem and increasing the costs of dredging operations progressively,
3. Mud is also one of the controlling factors for ecological development in the water system and shapes the physical and biological lanscape. Life, feeding, breeding and growth of biological organism is highly dependent on the oxygenation of water,
4. sediment transport: erosion of beaches and accretions,
5. undermining of coastal structures,
6. silt up of navigation channels and ports.

Sediment grains are divided to two basic categories: Clastic grains resulting from the rock detrital and biogenic or calcium carbonate grains which are made up of shells or

skeletons of invertebrates. Sediments may also be categorized into cohesionless (grains usually bigger than $0.06mm$ and are held together by gravitational forces) and cohesive (mainly clay minerals held together with electrolytic forces). Rivers carrying glaciers and biogenics are the main source (90%) of total marine sediments (see Pethick 1984 Pethick (1984)). The three main resultants of weathering are rock fragments, quartz grains and clay minerals. Quartz is the main constituent of the sand deposits in beaches in the mid-latitudes and mud is the main constituent of tidal flats and estuaries.

Sediment-fluid interaction plays a major role in formation of bed-forms such as dunes, ripples and banks. when the Reynolds number of sediment particles are less than 0.1, stokes' law predicts the falling rate (settling velocity)

$$w = \frac{2(\rho_s - \rho_f)gr^2}{9\mu} \tag{G.1.1}$$

where ρ_s and ρ_f are the sediment particle and the fluid densities, g is the gravitational acceleration, r is the particle radius and μ is the fluid viscosity.

Mud on the sea bottom is a mixture of water and clay particles with 6-18% volume concentration which results is a total density of $1100 - 1300kg/m^3$. It has been observed that near muddy coasts, wind waves damp withing a distance of a few wavelengths and the wave amplitude diminishes roughly in proportion to the water depth, and breaking is less common Liu & Mei ($1993a$). However, "No systematic studies" has been done when the interaction is between the fluid and cohesive sediments or mixture of cohesive and non-cohesive sediments (Winterwerp and Van Kesteren 2004 Winterwerp & Kesteren (2004)).

Observations of Gade 1958 Gade (1958) in the Gulf of Mexico, Silvester 1974 Silvester (1974) and Macpherson 1980 Macpherson (1980) in areas off the southwest coast of India showed that waves were attenuated over a distance of a few wavelengths. In fact, Gade talks about a place named "Mud Hole" in the gulf of Mexico whit such a strong wave dissipation that fishing boats use it as a shelter during sudden storms. Viscosity is the major sink of energy in short waves (including capillary-gravity waves), while for long waves, surface processes such as wave-breaking has the major role in the dissipation process.

G.2 Review of wave-mud interaction models

G.2.1 Bottom Friction Model

Once we introduce viscosity to the water properties, the no slip boundary condition makes a boundary layer where velocity varies from zero at the bottom to the mean outer flow at the top.

Stokes' Boundary Layer

Assume a two dimensional motion of a fluid governed by Navier-Stokes equation

$$\frac{\partial u}{\partial t} + u\frac{\partial u}{\partial x} + w\frac{\partial u}{\partial z} = -\frac{1}{\rho}\frac{\partial p}{\partial x} + \nu\left(\frac{\partial^2 u}{\partial x^2} + \frac{\partial^2 u}{\partial z^2}\right) \tag{G.2.2}$$

We assume that the boundary layer is very thin compared to the horizontal length scale, i.e. $\delta/L \ll 1$ where δ is the width of the boundary layer and L is the horizontal length scale. From the continuity equation we conclude that $w = O(\delta/LU) \ll 1$ and therefore the order of magnitude of terms are

$$1 + \frac{U}{L\omega} + \frac{U}{L\omega} = \frac{P}{UL\omega\rho} + \frac{\nu}{L^2\omega} + \frac{\nu}{L^2\omega}\left(\frac{L}{\delta}\right)^2 \tag{G.2.3}$$

where we have used U and $1/\omega$ to normalize u and t respectively. Now if we assume

$$\frac{\nu}{L^2\omega} \ll \frac{U}{L\omega} \ll 1 \tag{G.2.4}$$

the Navier-Stokes equation simplifies to

$$\frac{\partial u}{\partial t} = -\frac{1}{\rho}\frac{\partial p}{\partial x} + \nu\frac{\partial^2 u}{\partial z^2} \tag{G.2.5}$$

Also from the Navier-Stokes equation in the z-direction we conclude that the pressure is constant across the boundary layer.

Just outside the boundary condition the same G.2.4 condition states that in Bernouli's equation the nonlinear terms are negligible and

$$\frac{\partial u_0}{\partial t} + \frac{1}{\rho}\frac{\partial p}{\partial x} = 0 \tag{G.2.6}$$

where u_0 is the velocity outside the boundary layer. For our case u_0 corresponds to the irrotational velocity of the wave field. Therefore

$$\frac{\partial(u-u_0)}{\partial t} = \nu \frac{\partial^2 u}{\partial z^2} \tag{G.2.7}$$

with boundary conditions

$$u \to u_0 \qquad z \to \infty \tag{G.2.8}$$

$$u = 0 \qquad z = 0 \tag{G.2.9}$$

Assume a progressive wave on the out field given by

$$u_0 = U e^{i(kx-\omega t)} \tag{G.2.10}$$

we assume a solution of the form

$$u = [U + f(z)]e^{i(kx-\omega t)} \tag{G.2.11}$$

Therefore the equation reduces to

$$f'' + \frac{i\omega}{\nu} f = 0 \tag{G.2.12}$$

The final solution is

$$u = U\left\{1 - \exp\left[-(1-i)\sqrt{\frac{\omega}{2\nu}}\right] z\right\} e^{i(kx-\omega t)} \tag{G.2.13}$$

where $\delta = \sqrt{\frac{2\nu}{\omega}}$ is the boundary layer thickness. At the leading order the solution to the boundary layer of external oscillatory flow matches with that of stokes' boundary layer for the oscillating plate.

Seabed shear stress

The amplitude of bed shear stress is given by

$$\tau_0 = \frac{1}{2} f_w \rho U^2 \tag{G.2.14}$$

where U is the amplitude of velocity near the bed, and f_w is the wave friction factor:

1. For *laminar* flow, the wave friction factor is given by the Stokes' boundary layer

$$f_w = \frac{2}{\sqrt{Re}} \tag{G.2.15}$$

   where $Re = UA/\nu$ and $A = U/\omega$.

2. For *smooth turbulent* flow, Myrhaug Myrhaug (1995) introduces the smooth bed wave friction factor

$$f_w = \frac{r}{Re^s} \qquad \text{for } Re \geq 3e5 \tag{G.2.16}$$

   with $(r, s) = (0.045, 0.175)$.

3. For *rough turbulent* flow, Myrhaug et al. D. Myrhaug (2001) proposes the following friction factor

$$f_w = c\left(\frac{A}{z_0}\right)^{-d} \tag{G.2.17}$$

   with

$$(c, d) = (18, 1) \; for \; 20 \leq A/z_0 \leq 200$$
$$(c, d) = (1.39, 0.52) \; for \; 200 \leq A/z_0 \leq 11000$$
$$(c, d) = (0.112, 0.25) \; for \; 11000 \leq A/z_0$$

   and where $z_0 = 2.5d_{50}/30$ is the bed roughness based on the median grain roughness (see D. Myrhaug & Rue (2006)).

G.2.2 Non-Newtonian Fluid Mud Model

A Newtonian fluid is a fluid for which

$$\tau = \mu\frac{\partial u}{\partial y} \tag{G.2.18}$$

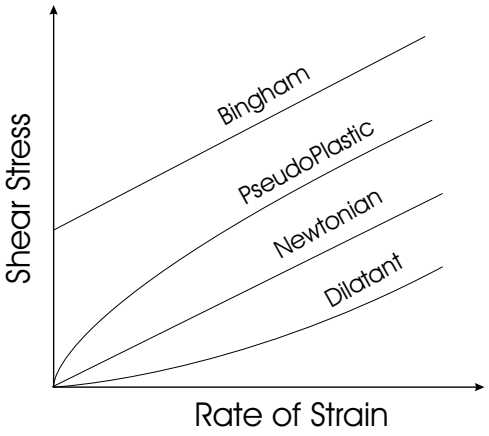

Figure G-1: Stree-rate of strain relationship for three most important classes of time-independent non-Newtonain fluids

where μ is called the Newtonian viscosity and depends only on temperature and pressure. Newtonian behavior occurs where molecular species are small, such as in all gases, and liquids and solutions of low molecular weights. A non-Newtonian fluid if a fluid for which the stress-rate of shear relation is nonlinear (see Wilkinson Wilkinson (1960)). Flow of lava, ice, mud slides, snow avalanches, debris, mucus and blood within our bodies and toothpaste are examples of non-Newtonian fluid flow.Unlike a Newtonian fluid, a visco-plastic fluid is a fluid with a yield stress. That is, the yield stress needs to be exceeded in order for the fluid to flow. Wherever the stress does not exceed the yield stress, there is no flow and this region is called the unyielded region. The region where there is flow is called the yielded region. Visco-plastic fluids can be modeled by one of the Bingham, Casson, or Herschel-Bulkley equations which all provide mathematical relations between the stress and strain-rate. Figure G-1 shows three most important types of time-independent non-Newtonian fluids.

Bi-viscous fluid is a model in which the fluid has two viscosity: it behaves like a Newtonian fluid until the shear stress is less than a yield stress τ_0. But if the shear exceeds τ_0, the behavior changes to a different viscosity fluid with a residue stress. Mathematically (Becker & Bercovici (2000))

$$\frac{1}{\mu}\tau = \frac{\partial u}{\partial y}, \qquad \tau < \tau_0 \tag{G.2.19}$$

$$\frac{1}{\mu'}\tau = \tau_0\left(\frac{1}{\mu'} - \frac{1}{\mu}\right)\operatorname{sgn}\left(\frac{\partial u}{\partial y}\right) + \frac{\partial u}{\partial y}, \quad \tau > \tau_0 \tag{G.2.20}$$

where μ and μ' are the dynamic viscosities. In the limit, when $\mu = \mu'$ the fluid is a Newtonian fluid and when $\mu \longrightarrow \infty$ the fluid is called a Bingham fluid.

The most widely used model, because of its simplicity, is the Bingham fluid model. Bingham-fluids are characterized by a yield stress. Contrary to newtonian fluids they can transmit a shear stress also without a velocity gradient. But in order to make the Bingham-fluid flowing, the driving shear stress has to be larger than the yield stress. Below this yield stress the fluid will behave almost like a solid body and above as a liquide. Examples of Bingham-fluids are tooth paste, paint, water suspensions of clay, sewage sludge, some emulsions, thickened hydrocarbon greases, and slurries of uranium oxide in nuclear reactors.

The shear-stress relation for a Bingham fluid is

$$\tau = \tau_0 + \mu \frac{\partial u}{\partial y} \tag{G.2.21}$$

For the seabed, the clay concentration normally varies in depth, therefore τ_0 and μ must be functions of the depth. Bingham rheology is not a perfect sand model because for example for flow down an incline, motion will initiate from the top for sand, but from the bottom for a Bingham fluid (Jaeger and Nagel 1992 JAEGER H.M. (1992)). Therefore it seems that the yield stress of sand is pressure dependent or in other words sand yields harder when under a heavier pressure (see Becker and Bercovici 2000 Becker & Bercovici (2000)). Also compressibility of silt is nearly 1000 times that of pure water. For mud, the compressibility of the grain skeleton is even greater (see Sleath 1984 Sleath (1984)).

The simplest model for pseudoplastic and dilatant fluids is

$$\tau = k \left(\frac{\partial u}{\partial y} \right)^n \tag{G.2.22}$$

where k is a measure of viscosity and n is a measure of nonlinearity and is less than zero and greater than zero for pseudoplastic and dilatant fluids respectively.

If elasticity is added to viscosity another group of non-Newtonian fluids emerges: Viscoelastic fluids. An example of viscoelastic fluid is the pitch. In a viscoelastic fluid, the shear stress causes the rate of the strain, and, furthermore if shear stress changes with time, then the rate of change of stress causes another rate of the strain part due to elastic

behavior of the fluid. Mathematically it means

$$\frac{\partial u}{\partial y} = \frac{\tau}{\mu} + \frac{\dot{\tau}}{G} \tag{G.2.23}$$

or

$$\tau + \lambda_1 \dot{\tau} = \mu \frac{\partial u}{\partial y} \tag{G.2.24}$$

where $\lambda_1 = \mu/G$.

Liu and Mei 1993a Liu & Mei (1993a), and Liu and Mei 1993b Liu & Mei (1993b) use shallow water assumption and Bingham fluid model for the mud to study the attenuation of long waves and solitons over a layer of relatively thick mud. They neglect the interfacial friction and suspension and use the method of characteristics to solve their hyperbolic and coupled partial differential equations. In their work evolution of a localized initial free surface displacement is studied. They observed that due to yield stress of the mud layer, the water surface becomes piecewise linear and, while radiates, leaves permanent imprints in the underlying mud layer.

Becker and Bercovici 2000 Becker & Bercovici (2000) consider the two layer model response to periodic forcing with a bi-viscous rheology. Using linear shallow water assumption, their numerical simulations showed that small scale and small wavelength spatial features although generated, but oscillate and do not form any permanent bedforms. Yet by including a pressure-dependent yield stress, permanent bedforms are excited. In a separate work, Becker and Bercovici 2001 Becker & Bercovici (2001) added the finite amplitude assumption to this model.

G.2.3 Newtonian Mud Model

Jamali (1998) studied the two-dimensional interaction of an upper inviscid layer over a viscose lower layer. For the upper inviscid layer the governing equation is the laplace's

equation:

$$\nabla^2\phi = 0, \tag{G.2.25}$$

$$\eta_{s,t} + \eta_{s,x}.\phi_{,x} = \phi_{,z} \qquad z = \eta_s \tag{G.2.26}$$

$$\phi_{,t} + \frac{1}{2}(\nabla\phi)^2 + g\zeta + p = C(t) \qquad z = \eta_s \tag{G.2.27}$$

$$\eta_{i,t} + \eta_{i,x}.\phi_{,x} = \phi_{,z} \qquad z = -h_u + \eta_i \tag{G.2.28}$$

For the lower viscous fluid we start from the Navier-Stokes equation:

$$\nabla.\mathbf{u} = 0 \tag{G.2.29}$$

$$\mathbf{u}_{,t} + \mathbf{u}.\nabla\mathbf{u} = -(1/\rho)\nabla p + \nu\nabla^2\mathbf{u} + \mathbf{F} \tag{G.2.30}$$

where ν is the kinematic viscosity and F is the external forcing term. First equation is the continuity equation and the second equation is the momentum equation. We can substitute the second term in the Navier-Stokes equation from the identity

$$\mathbf{u}.\nabla\mathbf{u} = \nabla(\frac{1}{2}\mathbf{u}^2) - \mathbf{u}\times\mathbf{w}. \tag{G.2.31}$$

Now taking the curl of the Navier-Stokes equation using the following vector identity

$$\nabla\times(\mathbf{a}\times\mathbf{b}) = \mathbf{a}\nabla.\mathbf{b} - \mathbf{b}\nabla.\mathbf{a} - (\mathbf{a}.\nabla)\mathbf{b} + (\mathbf{b}.\nabla)\mathbf{a} \tag{G.2.32}$$

noting that $\nabla\times\nabla\mathbf{G} = \nabla.\nabla\times\mathbf{G} = 0$, i.e. curl(grad)=div(curl)=0 we get the vorticity transport equation

$$\mathbf{w}_{,t} + \mathbf{u}.\nabla\mathbf{w} = \mathbf{w}.\nabla\mathbf{u} + \nu\nabla^2\mathbf{w} \tag{G.2.33}$$

which in the absence of the viscosity (last term) is called Helmholtz's equation (Saffman (1992)).

In two dimension problem we can define the stream function

$$u = \psi_z, \quad w = -\psi_x \tag{G.2.34}$$

therefore $\mathbf{w} = \nabla^2\psi\ \hat{j}$ where $\nabla = \partial_{,x}\hat{i} + \partial_{,z}\hat{k}$ is the two dimensional operator. The vorticity

transport equation reduces to the following one-dimensional equation in y-direction:

$$\nabla^2\psi_{,t} - \nu\nabla^4\psi = \psi_{,x}\nabla^2\psi_{,z} - \psi_{,z}\nabla^2\psi_{,x} \tag{G.2.35}$$

The boundary conditions at the interface can be written as

$$\eta_{i,t} + \eta_{i,x}\psi_{,z} = -\psi_{,x} \tag{G.2.36}$$

$$\tau = 0 \tag{G.2.37}$$

$$\sigma_n = -p \tag{G.2.38}$$

The first equation is the kinematic boundary condition, the second has to be satisfied because inviscid upper layer can not undergo shear and the third is the normal shear for lower viscous fluid has to be equal to the pressure at the interface.

From stress transformation rules we have

$$\sigma_{nn} = \sigma_{xx}\sin^2\theta + \sigma_{zz}\cos^2\theta - 2\sigma_{xz}\sin\theta\cos\theta \tag{G.2.39}$$

$$\tau = \sigma_{nt} = (\sigma_{xx} - \sigma_{zz})\sin\theta\cos\theta - \sigma_{xz}(\cos^2\theta - \sin^2\theta) \tag{G.2.40}$$

but for the interface

$$\tan\theta = \eta_{i,x} \Rightarrow \sin^2\theta = \frac{\eta_{i,x}^2}{1+\eta_{i,x}^2} \text{ and } \cos^2\theta = \frac{1}{1+\eta_{i,x}^2} \tag{G.2.41}$$

but for a Newtonian fluid [1] the three-dimensional stress tensor is

$$\sigma_{ij} = -p\delta_{ij} + \mu\left(\frac{\partial q_i}{\partial x_j} + \frac{\partial q_j}{\partial x_i}\right) \tag{G.2.42}$$

where q_i is the velocity in the x_i direction and $x_i = x, y, z$ for $i = 1, 2, 3$ respectively. Therefore

$$\sigma_{xx} = -p + 2\mu\psi_{xz} \tag{G.2.43}$$

$$\sigma_{yy} = -p - 2\mu\psi_{xz} \tag{G.2.44}$$

$$\sigma_{xy} = \mu(\psi_{zz} - \psi_{xx}). \tag{G.2.45}$$

[1] what if fluid is non-Newtonian?

Upon substitution into G.2.39 and G.2.40, interface boundary conditions can be written as

$$\eta_{i,t} + \eta_{i,x}\psi_{,z} = -\psi_{,x} \qquad z = -h_u + \eta_i \quad \text{(G.2.46)}$$

$$\mu(\psi_{,zz} - \psi_{,xx})(\eta_{i,x}^2 - 1) + 4\mu\psi_{,xz}\eta_{i,x} = 0 \qquad z = -h_u + \eta_i \quad \text{(G.2.47)}$$

$$(\psi_{,zz} - \psi_{,xx})\eta_{i,x} + \psi_{,xz}(1 - \eta_{i,x}^2) = 0 \qquad z = -h_u + \eta_i \quad \text{(G.2.48)}$$

Equation G.2.48 is the simplified version of equation (4.20) of Jamali (1998). The no slip [2] bottom boundary condition is

$$\psi_{,x} = \psi_{,z} = 0 \qquad z = -h_u - h_l + \eta_b \quad \text{(G.2.49)}$$

or in other words, bottom is a streamline.

Equations G.2.25-G.2.28 and G.2.35 along with G.2.46-G.2.48, and finally G.2.49 are the full governing equations and boundary conditions.

Ng (2000) considers a thin layer of viscous mud under the water surface waves. He assumes that the mud depth, the mud stokes' boundary layer thickness ($\delta = \sqrt{2\nu/\omega}$ where ν is the kinematic viscosity and ω is the frequency of the wave) and the wave amplitude are comparable with each other and much smaller than the wavelength. He starts with boundary layer equation for the mud layer and for the water layer close to the interface. He then matches the boundary layer equation with the far field inviscid fluid. He finds that the wave attenuation rate is maximum when the relative mud depth, i.e. mud depth relative to the stokes' boundary layer, is 1.55. He also shows that the mass-transport velocity of the mud increases when the mud layer thickness increases, but decreases with increase in the mud density.

Dalrymple & Liu (1978) use a linearized two-layer viscous model, and shows that the maximum attenuation occurs when the thickness of lower high-viscous layer is about 30% greater than the boundary layer thickness δ.

[2] can be easily generalized to slip and/or porous bottom

G.2.4 Viscoelastic Mud Model

The Voigt model for a viscoelastic material assumes a spring that obey the Hook's law and a dash-pot which is a piston drawn into a Newtonian fluid. Assuming an incompressible Voigt viscoelastic medium, the linearized equation of motion for small perturbations is

$$\frac{\partial^2 \mathbf{x}}{\partial t^2} = -\frac{1}{\rho}\nabla p + \nu \frac{\partial}{\partial t}\nabla^2 \mathbf{x} + \frac{G}{\rho}\nabla^2 \mathbf{x} - \mathbf{g} \tag{G.2.50}$$

where $\mathbf{x}$ is the particle displacement and G is the shear modulus of elasticity. But $\partial \mathbf{x}/\partial t = \mathbf{u}$ and if we assume that $\mathbf{x}$ and $\mathbf{u}$ both vary as $\exp(-i\sigma t)$, then the equation can be written in the following form

$$\frac{\partial \mathbf{u}}{\partial t} = -\frac{1}{\rho}\nabla p + \nu_e \nabla^2 \mathbf{u} - \mathbf{g} \tag{G.2.51}$$

where the viscoelastic parameter ν_e is

$$\nu_e = \nu + \frac{iG}{\rho\sigma} \tag{G.2.52}$$

whose real part is viscosity and its imaginary part is a measure of elasticity (see MacPherson 1980 Macpherson (1980))

The linearized Navier-Stokes equation can be expressed in terms of a velocity potential *and* a stream function. We define

$$u = -\frac{\partial \phi}{\partial x} - \frac{\partial \psi}{\partial z}, \quad v = -\frac{\partial \phi}{\partial z} + \frac{\partial \psi}{\partial x}. \tag{G.2.53}$$

The governing equations become

$$\nabla^2 \phi = 0 \tag{G.2.54}$$

$$\nu_e \nabla^2 \psi = \tfrac{\partial \psi}{\partial t} \tag{G.2.55}$$

$$p = \rho \tfrac{\partial \psi}{\partial t} - \rho g y. \tag{G.2.56}$$

with boundary conditions

$$\phi^+_{,tt} + g\phi^+_{,y} = 0 \qquad z = 0 \qquad \text{(G.2.57)}$$

$$-2\phi_{,xy} - \psi_{,yy} + \psi_{,xx} = 0 \qquad z = -h_u \qquad \text{(G.2.58)}$$

$$\eta_{i,t} = -\phi_{,y} + \psi_{,x} = -\phi^+_{,y} \qquad z = -h_u \qquad \text{(G.2.59)}$$

$$-\rho_l\phi_{,t} + \rho_l g\eta_i + 2\rho_l\nu_e(-\phi_{zz} + \psi_{,xz}) + \rho_u\phi^+_{,t} - \rho_u g\eta_i = T\eta_{i,xx} \qquad z = -h_u \qquad \text{(G.2.60)}$$

$$-\phi_x - \psi_z = 0 \qquad z = -h_u - h_l \qquad \text{(G.2.61)}$$

$$-\phi_z + \psi_x = 0 \qquad z = -h_u - h_l \qquad \text{(G.2.62)}$$

equation G.2.57 is the combined free-surface boundary condition, equation G.2.58 is the no-shear interface condition, equations G.2.59 and G.2.60 are respectively the kinematic and dynamic boundary conditions on the interface and equations G.2.61 and G.2.62 are the bottom no-slip conditions.

Macpherson also concludes that the energy dissipation is less for very long and very short waves: Long waves are spread over a large distance and short waves can not feel the bottom.

G.2.5 Mud-induced Short wave dissipation

It is known that long waves at muddy sites are attenuated in variance by an order of magnitude compared to sandy sites. Also it is known that long waves dissipate over the muddy bottom, but since short waves can not feel the bottom it was thought that they are not affected by the bottom.

Observation of Sheremet and Stone 2003 Sheremet & Stone (2003) at the Louisiana inner shelf showed that short waves (based on their definition $f \geq 0.2\ Hz$) decay much faster at the muddy site. Since this can not be explained by breaking or refractive scattering, and short waves hardly see the bottom, they attributed this damping to the interaction between fluid with a layer of resuspended mud.

During hurricane Claudette, Sheremet et al. 2005 Sheremet (2005) measured the suspended sediment concentration (SSC) on the muddy inner shelf fronting Atchafalaya Bay, Louisiana. They observed that during the storm due to resuspension of the sediment the

concentration exceeds $SSC = 0.5kg/m^3$ withing the water body. When the storm weakens, the resuspended sediments settle and within 1 mab the concentration reaches $1.7kg/m^3$. They suggest that dissipation is due to the formation of a strong stratification in the first 1 mab (meter above the bottom).

G.3 Viscoelastic bottom model

G.3.1 Approximate damping rate

we consider wave in a homogeneous fluid bounded by periodic side-boundary conditions, free surface and a visco-elastic bed. In two dimension, the governing equation for the bottom is

$$m^*\ddot{\eta}_b + b^*\dot{\eta}_b + k^*\eta_b = p(t) \tag{G.3.63}$$

where m^*, b^* and k^* are mass, damping coefficient and stiffness coefficient of the bottom per unit length per unit depth. $p(t)$ is the pressure at the mean bottom $z = -h$.

If pressure is periodic in time, say $p(t) = \tilde{p}_0 \cos(\omega t)$, the solution to this ordinary differential equation is well known

$$\eta_b = \frac{\tilde{p}_0}{[(k^* - m^*\omega^2)^2 + {b^*}^2\omega^2]^{\frac{1}{2}}} \cos(\omega t - \phi) \tag{G.3.64}$$

where the phase shift is given by

$$\phi = \tan^{-1}\left(\frac{b^*\omega}{k^* - m^*\omega^2}\right) \tag{G.3.65}$$

The power loss per unit horizontal length due to the damping of the bed is

$$P_{ow}(x,t) = b^*\ \dot{\eta}_b^2 = p(t)\ \dot{\eta}_b \tag{G.3.66}$$

and the time average power loss is given by

$$\bar{P}_{ow} = \frac{1}{2}\frac{b{\tilde{p_0}}^2\omega^2}{[(k - m\omega^2)^2 + (b\omega)^2]} \tag{G.3.67}$$

For a monochromatic progressive wave, this is the power loss per unit length. For standing

wave, the power loss is half of this value due to another averagin over the wave length that introduce a factor of one-half.

The energy contained in one wave-length of a progressive wave

$$\eta = a\sin(kx - \omega t) \tag{G.3.68}$$

$$\phi = -\frac{ag}{\omega}\frac{\cosh k(z+h)}{\cosh kh}\cos(kx - \omega t) \tag{G.3.69}$$

is

$$E_\lambda = \frac{1}{2}\rho g a^2 \lambda \tag{G.3.70}$$

or $E_w = 1/2\rho g a^2$ per unit length (see for example Debnath, 1994, section 2.2). Note that the energy of standing wave is half of propagatin wave with the same amplitude and wave number.

Pressure at the mean bottom is

$$p(x,t) = -\rho[\phi_{,t} + gz] \quad @z = -h \tag{G.3.71}$$

$$= \frac{\rho g a}{\cosh kh}\sin(kx - \omega t) + \rho g h \tag{G.3.72}$$

The first terms is the dynamic pressure due to the presense of the wave hence decreases as depth increases. At the limit when $kh \ll 1$ the hydrostatic pressure of shallow water wave is recovered. The second term is just the hydrostatic pressure due to the water column and only changes the set point of our mass-spring-damper system and therefore does not play any role in the damping process. To find the rate of amplitude decay we write

$$\frac{dE_w}{dt} = \bar{P} \quad \Rightarrow \frac{da}{dt} = -C\ a \quad \Rightarrow a = a_0 e^{-Ct} \tag{G.3.73}$$

$$C = \frac{1}{2\cosh^2 kh}\cdot\frac{\rho g b^* \omega^2}{[(k^* - m^*\omega^2)^2 + (b^*\omega)^2]} \tag{G.3.74}$$

$$= \frac{1}{2\cosh^2 kh}\cdot\frac{2\zeta\kappa\tilde{\Omega}}{[(1-\tilde{\Omega}^2)^2 + (2\zeta\tilde{\Omega})^2]}\cdot\omega \tag{G.3.75}$$

where $\kappa = \rho g/k^*$

G.3.2 Elastic Bottom

Linear Shallow Water

Governing equations are

$$(\eta_s - \eta_b)_{,t} + (hu)_{,x} = 0 \ , \tag{G.3.76}$$

$$u_{,t} + g\eta_{s,x} = 0 \ , \tag{G.3.77}$$

$$m^*\eta_{b,tt} + k^*\eta_b = -P_b \ . \tag{G.3.78}$$

where

$$P_b = \rho g(\eta_s - \eta_b) \ . \tag{G.3.79}$$

Assuming a solution in the form

$$\eta_s = \eta_{s0}e^{i(kx-\omega t)} \tag{G.3.80}$$

we get

$$\eta_b = \eta_{b0}e^{i(kx-\omega t)}, \quad u = u_0 e^{i(kx-\omega t)} \tag{G.3.81}$$

where

$$\eta_{b0} = \frac{\rho g}{m^*\omega^2 - (k^* - \rho g)}\eta_{s0} = \left(1 - \frac{ghk^2}{\omega^2}\right)\eta_{s0}, \quad u_0 = \frac{gk}{\omega} \tag{G.3.82}$$

and a dispersion relation in the form

$$\omega^4 - \omega^2\left(ghk^2 + \frac{k^*}{m^*}\right) + ghk^2\frac{k^* - \rho g}{m^*} = 0 \tag{G.3.83}$$

This dispersion relation is similar to the characteristic equation of two-degree of freedom system consists of one dimensional motion of two masses and two springs put in series. Note than we neglect the inertia effect of the fluid motion on the bottom pressure. Therefore, the term ρg changes the equivalent stiffness rather than equivalent mass of the bottom.

Figure shows the schematic behavior of solution to the dispersion relation (G.3.83) and

the amplitude ratio of the bottom to the surface at each mode and for each shallowness. The wedge shape asymptotes are the dispersion relation for the shallow water wave

$$\omega^{+}_{asymp} = k\sqrt{gh} \tag{G.3.84}$$

and the horizontal asymptote is the limiting value of the negative mode (i.e., the mode in which the displacement of the surface and the bottom are not in phase) as the shallowness kh grows and is

$$\omega^{-}_{asymp} = \sqrt{\frac{k^* - \rho g}{m^*}} \tag{G.3.85}$$

The minimum frequency of the positive mode is $\omega^{+}_{min} = \omega_b = \sqrt{k^*/m^*}$. Therefore the system frequency can not be between ω^{-}_{asymp} and ω^{+}_{min}.

In terms of dimensionless quantities this dispersion relation is cast into

$$\omega^{*4} - \omega^{*2}\left(\frac{ghk^2}{\omega_b^2} + 1\right) + \frac{ghk^2}{\omega_b^2}\left(1 - \frac{\rho g}{k^*}\right) = 0 \tag{G.3.86}$$

where $\omega^* = \omega/\omega_b$ and $\omega_b = \sqrt{k^*/m^*}$. The dimensionless dispersion relation can be manipulated to give

$$\mathcal{D} = \frac{\omega^2}{ghk^2} = 1 + \frac{\Pi^*}{\omega^{*2} - 1} \tag{G.3.87}$$

where $\Pi^* = \rho g/k^*$ is determined by the property of the fluid and the bottom. As ω^* tends to infinity, the dispersion relation of shallow water wave is regained.

Linear Finite Depth Water

The linearized governing equation for elastic bottom is

$$\nabla^2\phi = 0 \tag{G.3.88a}$$

$$\phi_{tt} + g\phi_z = 0 \quad @\ z = 0, \tag{G.3.88b}$$

$$\phi_z - \eta_{b,t} = 0 \quad @\ z = -h, \tag{G.3.88c}$$

$$m^*\eta_{b,tt} + k^*\eta_b + P_b = 0 \quad @\ z = -h, \tag{G.3.88d}$$

$$\phi_t + g\eta_b + \frac{P_b}{\rho} = 0 \quad @\ z = -h. \tag{G.3.88e}$$

where m^* and k^* are respectively mass and stiffness coefficient per unit length. The combination of the last three boundary conditions give

$$m^*\phi_{,ztt} + b^*\phi_{,zt} + (k^* - \rho g)\phi_{,z} - \rho\phi_{,tt} = 0 \quad @\ z = -h \tag{G.3.89}$$

General solution to this problem is

$$\phi = A\left(\frac{\cosh kz}{\cosh kh} + \frac{\omega^2}{gk}\cdot\frac{\sinh kz}{\cosh kh}\right)e^{i(kx-\omega t)} + c.c. \tag{G.3.90}$$

where *c.c.* denotes the complex conjugate, and,

$$\omega^4(m^*k\cosh kh + \rho\sinh kh) + \omega^2 k(k^*\cosh kh + m^*gk\sinh kh) + k^2 g(k^* - \rho g)\sinh kh = 0 \tag{G.3.91}$$

is the dispersion relation.

G.3.3 ViscoElastic Bottom

Linear Finite Depth Water

The linearized governing equation for elastic bottom is

$$\nabla^2\phi = 0 \tag{G.3.92a}$$

$$\phi_{tt} + g\phi_z = 0 \quad @\ z = 0, \tag{G.3.92b}$$

$$\phi_z - \eta_{b,t} = 0 \quad @\ z = -h, \tag{G.3.92c}$$

$$m^*\eta_{b,tt} + b^*\eta_{b,t} + k^*\eta_b + P_b = 0 \quad @\ z = -h, \tag{G.3.92d}$$

$$\phi_t + g\eta_b + \frac{P_b}{\rho} = 0 \quad @\ z = -h. \tag{G.3.92e}$$

where m^*, b^* and k^* are respectively mass, viscous damping and stiffness coefficient per unit length. The combination of the last three boundary conditions give

$$m^*\phi_{,ztt} + b^*\phi_{,zt} + (k^* - \rho g)\phi_{,z} - \rho\phi_{,tt} = 0 \quad @\ z = -h \tag{G.3.93}$$

General solution to this problem is

$$\phi = \left(Ae^{kz} + Be^{-kz}\right)e^{ikx+\omega t} \tag{G.3.94}$$

where

$$B = A\frac{1+\Omega^2}{1-\Omega^2}, \quad \Omega^2 = \frac{\omega^2}{gk} \tag{G.3.95}$$

and

$$(\Omega_r^2 + \kappa\tanh\mu)\Omega^4 + 2\zeta\ \Omega_r\ \Omega^3 + (\Omega_r^2\tanh\mu + 1)\Omega^2 \\ +2\zeta\ \Omega_r\tanh\mu\ \Omega + (1-\kappa)\tanh\mu = 0 \tag{G.3.96}$$

where

$$\Omega_r = \sqrt{\frac{m^*gk}{k^*}}, \quad \kappa = \frac{\rho g}{k^*}, \quad \zeta = \frac{b^*}{2\sqrt{k^*m^*}}, \quad \mu = kh. \tag{G.3.97}$$

is the dispersion relation. Note that when $k^* \to \infty$, i.e. when the bottom is rigid, we readily recover the simple flat bottom dispersion relation. In order to have a positive restoring force at the bottom $1-\kappa > 0$. With this, in the absence of the dissipation, we always have four (two pairs of two) imaginary frequencies for a given wave number, that means periodic waves.

When $\mu \to \infty$, the asymptotic lines are given by

$$(\Omega_\infty^2 + 1)\left[(\Omega_r^2+\kappa)\Omega_\infty^2 + 2\zeta\Omega_r\Omega_\infty + (1-\kappa)\right] = 0, \qquad \mu \to \infty. \tag{G.3.98}$$

The first parenthesis shows the asymptotic convergence of the surface-mode to the deep water wave dispersion relation while its damping goes to zero. The second parenthesis shows the asymptotic behavior of the bottom-mode in which the damping increases as depth deepens. Figure G-7 is the plot of the dispersion relation. For a critical damping ratio

$$\zeta_{cr} = \frac{1}{\Omega_r}\sqrt{(1-\kappa)(\Omega_r^2+\kappa)} \tag{G.3.99}$$

a bifurcation occurs in the bottom-mode dispersion curve where its oscillatory motion diminishes and the disturbance decays exponentially to zero. Also it was seen that as the damping increases, the surface-mode curve gets closer to the flat-bottom dispersion relation, as expected. For very shallow water when $\mu \ll 1$, the bottom-mode frequency is zero, while

the surface-mode frequency is

$$\Omega_0 = \frac{1}{\Omega_r}\left(-\zeta \pm \sqrt{\zeta^2 - 1}\right) \qquad \mu \to 0. \tag{G.3.100}$$

therefore both the damping and the oscillation frequency (if exists i.e. if $\zeta < 1$) increases as Ω_r decreases.

Surface Boundary Condition Modification

In dimensional space, equivalent system of equations

$$\nabla^2\phi = 0 \tag{G.3.101}$$

$$\left[\phi_{tt} + g\phi_z + \frac{b^*}{m^*}\phi_t + \frac{k^*}{m^*}\phi\right]_{,zztt} + \frac{\rho}{m^*}\phi_{,ztttt} + \frac{b^*g}{m^*}\phi_{,zzzt} + \frac{g(k^* - \rho g)}{m^*}\phi_{,zzz} = 0 \quad @\ z = 0, \tag{G.3.102}$$

$$\phi_z = 0 \quad @\ z = -h, \tag{G.3.103}$$

has the solution in the form

$$\phi = A\cosh k(z+h)e^{ikx+\omega t} \tag{G.3.104}$$

where (k, ω) satisfy the same dispersion relation as equation (G.3.96). The system (G.3.101) is called equivalent to the original system (G.3.92) because both have the same dispersion relation hence same qualitative behavior in time and space. The equivalent system that has flat bottom and a modified surface boundary condition (of great interest to numericians) can be written in many different forms. Here are a couple:

- 1.

$$\nabla^2\phi = 0 \tag{G.3.105}$$

$$\phi_{tt} + g\phi_z = \mathcal{F} \quad @\ z = 0, \tag{G.3.106}$$

$$\phi_z = 0 \quad @\ z = -h, \tag{G.3.107}$$

where

$$\mathcal{F} = \phi_{tt} + g\phi_z + \left[\phi_{tt} + g\phi_z + \frac{b^*}{m^*}\phi_t + \frac{k^*}{m^*}\phi\right]_{,zztt} + \frac{\rho}{m^*}\phi_{,ztttt} + \frac{b^* g}{m^*}\phi_{,zzzt} + \frac{g(\rho g - k^*)\rho}{m^*}\phi_{,zzz} \tag{G.3.108}$$

- 2.

  Using equation (G.3.146) assumptions the surface boundary condition in dimensionless variables becomes

$$\left[\phi_{tt} + \frac{1}{\mu^2}\phi_z + b^\dagger\phi_t + k^\dagger\phi\right]_{,zztt} + \rho^\dagger\phi_{,ztttt} + \frac{b^\dagger}{\mu^2}\phi_{,zzzt} + \left(\frac{\rho^\dagger}{\mu^4} - \frac{k^\dagger}{\mu^2}\right)\phi_{,zzz} = 0 \quad @\ z = 0, \tag{G.3.109}$$

where

$$\rho^\dagger = \frac{\rho h}{m^*}, \quad b^\dagger = \frac{b^*}{m^* k\sqrt{gh}}, \quad k^\dagger = \frac{k^*}{m^* k^2 gh}, \quad \mu = kh. \tag{G.3.110}$$

Under the condition of heavy bottom $\rho^\dagger \ll 1$, weakly deep water $\mu^{-4} \ll 1$ and weak damping and stiffness $b^{\dagger 2} \ll 1, k^{\dagger 2} \ll 1$, the term outside the bracket can be neglected. The assumption of weakly deep water suggests to change the dimensionless time scale to

$$t' = \sqrt{gk}t \tag{G.3.111}$$

under this assumption the dimensionless free surface condition becomes

$$\left[\phi_{tt} + \frac{1}{\mu}\phi_z + b^\dagger\phi_t + k^\dagger\phi\right]_{,zztt} + \rho^\dagger\phi_{,ztttt} + \frac{b^\dagger}{\mu}\phi_{,zzzt} + \left(\frac{\rho^\dagger}{\mu^2} - \frac{k^\dagger}{\mu}\right)\phi_{,zzz} = 0 \quad @\ z = 0, \tag{G.3.112}$$

where

$$\rho^\dagger = \frac{\rho h}{m^*}, \quad b^\dagger = \frac{b^*}{m^*\sqrt{kg}}, \quad k^\dagger = \frac{k^*}{m^* kg}, \quad \mu = kh. \tag{G.3.113}$$

The conditions change to: $\rho^\dagger \ll 1$, $\mu^{-2} \ll 1$, $b^{\dagger 2} \ll 1$ and $k^{\dagger 2} \ll 1$. Under these conditions we have to have

$$\phi_{tt} + \frac{1}{\mu}\phi_z + b^\dagger \phi_t + k^\dagger \phi = 0 \quad @\ z = 0, \tag{G.3.114}$$

Note that in equation (G.3.109) there is a double vertical derivative and we have already assumed exponential behavior in space and time. The governing equations in dimensional form become

$$\nabla^2 \phi = 0 \tag{G.3.115}$$

$$\phi_{tt} + g\phi_z = -\frac{b^*}{m^*}\phi_t - \frac{k^*}{m^*}\phi \quad @\ z = 0, \tag{G.3.116}$$

$$\phi_z = 0 \quad @\ z = -h, \tag{G.3.117}$$

For a periodic wave in deep water, if the effect of the bottom is small then

$$\phi = -\frac{1}{\omega^2}\phi_{tt} \approx -\frac{1}{gk}\phi_{tt} \tag{G.3.118}$$

therefore

$$\nabla^2 \phi = 0 \tag{G.3.119}$$

$$\phi_{tt} + g\phi_z = -\frac{b^*}{m^*}\phi_t + \frac{k^*}{m^* gk}\phi_{tt} \quad @\ z = 0, \tag{G.3.120}$$

$$\phi_z = 0 \quad @\ z = -h, \tag{G.3.121}$$

The modified HOS code now is based on the following two evolution equations:

$$\eta_t + \eta_x \phi_x^S - (1 + \eta_x^2)\phi_z(x, \eta, t) = 0 \tag{G.3.122}$$

$$\phi_t^S + g\eta + \frac{1}{2}\phi_x^{S2} - \frac{1}{2}(1 + \eta_x^2)\phi_z^2(x, \eta, t) + \frac{b^*}{m^*}\phi - \frac{k^*}{m^* gk}\phi_t = 0 \tag{G.3.123}$$

the second equation can be simplified as

$$\phi_t^S \left(1 - \frac{k^*}{m^* gk}\right) + g\eta + \frac{1}{2}\phi_x^{S2} - \frac{1}{2}(1 + \eta_x^2)\phi_z^2(x, \eta, t) + \frac{b^*}{m^*}\phi = 0 \tag{G.3.124}$$

- 3.

The following boundary value problem has the same dispersion relation as the surface wave over mass-spring-damper topography (equation G.3.96)

$$\nabla^2\phi = 0 \tag{G.3.125}$$

$$\phi_{tt} + g(1-A)\phi_z + \sqrt{\frac{g}{k}}\frac{1}{\Omega}\frac{BA}{B+1}\phi_{zt} \quad @\ z = 0, \tag{G.3.126}$$

$$\phi_z = 0 \quad @\ z = -h, \tag{G.3.127}$$

where

$$A = \kappa\frac{1-\Omega^4}{1+\Omega_r^2\Omega^2}, \quad B = \frac{2\zeta\Omega_r\Omega}{1+\Omega_r^2\Omega^2}$$

$$\Omega_r = \sqrt{\frac{m^*gk}{k^*}}, \quad \kappa = \frac{\rho g}{k^*}, \quad \zeta = \frac{b^*}{2\sqrt{gk}}, \quad \Omega = \frac{\omega}{\sqrt{gk}}$$

If $\zeta \ll 1$ we can find an approximate Ω from equation (G.3.96) by setting $\zeta = 0$.

- 4.

  The most robust but less beautiful way of dealing with this problem is to introduce the following boundary value problem

$$\nabla^2\phi = 0 \tag{G.3.128}$$

$$\phi_{tt} + g(1+\alpha)\phi_z + \beta\sqrt{gk}\phi_t \quad @\ z = 0, \tag{G.3.129}$$

$$\phi_z = 0 \quad @\ z = -h, \tag{G.3.130}$$

If the surface-mode solution of the dispersion relation equation (G.3.96) is given by

$$\Omega_s = a \pm ib \tag{G.3.131}$$

then

$$\alpha = \frac{a^2+b^2}{\tanh\mu} - 1, \quad \beta = -2a. \tag{G.3.132}$$

α, β are complicated functions of the wave-number but can be calculated beforehand and put into the HOS code as an initial data. As Ω_r increases from zero, α decreases uniformly, but β first increases and then decreases to zero. Increase in ζ gives rise to

decrease in α and increase in β. Decrease in κ decreases α but does not change β a lot.

The modified HOS code now is based on the following two evolution equations:

$$\eta_t + \eta_x \phi_x^S - (1+\eta_x^2)\phi_z(x,\eta,t) = 0 \tag{G.3.133}$$

$$\phi_t^S + g(1+\alpha)\eta + \frac{1}{2}\phi_x^{S2} - \frac{1}{2}(1+\eta_x^2)\phi_z^2(x,\eta,t) + \beta\sqrt{gk}\phi = 0 \tag{G.3.134}$$

figure G-10 shows HOS simulation of monochromatic incident wave over a mass-spring-damper bottom. The rate of decay strongly depends on Ω_r, ζ and μ but does not vary much with κ.

Linear Shallow Water

Governing equations are (see also Kevorkian & Yu, 1989; Chubarov *et al.*, 2005)

$$(\eta_s - \eta_b)_{,t} + (hu)_{,x} = 0 \ , \tag{G.3.135}$$

$$u_{,t} + g\eta_{s,x} = 0 \ , \tag{G.3.136}$$

$$m^*\eta_{b,tt} + b^*\eta_{b,t} + k^*\eta_b = -P_b \ . \tag{G.3.137}$$

where

$$P_b = \rho g(\eta_s - \eta_b) \ . \tag{G.3.138}$$

canceling the velocity from the equations above we end up getting the following fourth order partial differntial equation

$$\eta_{b,tttt} - gh\eta_{b,ttxx} + \frac{b^*}{m^*}(\eta_{b,ttt} - gh\eta_{b,txx}) + \frac{k^*}{m^*}\eta_{b,tt} + gh\left(\frac{\rho g - k^*}{m^*}\right)\eta_{b,xx} = 0 \tag{G.3.139}$$

Assume a solution of the form

$$\eta_b = \eta_{b0} e^{ikx} e^{\omega t} \tag{G.3.140}$$

where k is the real wave-number and ω can be a general complex number. We must have

$$\eta_s = \eta_{s0} e^{ikx} e^{\omega t} \tag{G.3.141}$$

where upon substitution into the governing differential equation gives

$$\frac{\eta_{b0}}{\eta_{s0}} = 1 + \frac{ghk^2}{\omega^2} \, . \tag{G.3.142}$$

with the dimensionless dispersion relation in the form

$$\omega^{*4} + 2\zeta\omega^{*3} + (1 + \Pi_1)\omega^{*2} - 2\Pi_1\zeta\omega^* + \Pi_1(1 - \Pi_2) = 0 \tag{G.3.143}$$

where

$$\zeta = \frac{b^*}{2\sqrt{m^* k^*}} \, , \quad \Pi_1 = \frac{ghk^2}{\omega_b^2} \, , \quad \Pi_2 = \frac{\rho g}{k^*} \, , \quad \omega_b = \sqrt{\frac{k^*}{m^*}} \, . \tag{G.3.144}$$

If $-\infty < x < \infty$ and we start with a uniform sinusoidal perturbation on the surface, then k has to stay real. For a quartic equation, the necessary condition for a stable equation, i.e. equation that all its roots lie on the left half plane of the complex plane, is that all its coefficients have the same sign (see Seroul, 2000). In our quartic dispersion relation the sign of the linear term is opposite of the sign of the quadratic and the cubic term.

For the damping coefficient less than the critical damping, i.e., $\zeta < \zeta_{cr}$, there can be an oscillatory motion along with the exponential decay, while for $\zeta > \zeta_{cr}$, the initial condition decays to zero without any complete oscillation. Note that ζ_{cr} is the *minimum* critical damping along which system behavior changes. Due to the nonlinearity, for some values of Π_1 and Π_2 if damping increases enough oscillatory motion can be seen again. Critical damping ζ_{cr} is a function of Π_1, Π_2 and is shown in figure G-4. Figure G-5 discusses the dependence of the root configuration on Π_2 in the complex plane.

Solution to the dispersion relation for $\Pi_2 = \zeta = 1.5$ is shown in figure G-6. The vertical axis is the dimensionless frequency and the horizontal axis can be considered as the square of dimensionless wave-number. For very long waves, there are three stable real roots. Therefore such a configuration decays to zero without any oscillation. At the bifurcation point $\Pi_1^b \cong 0.47$ two of real stable roots disappear and a pair of complex conjugate roots

emerge (dashed line). The imaginary part of this root (the branch of the dashed-line above zero) shows the frequency of vibration and the real part (dashed-line below zero) shows the exponential of the decay. Note that one weak stable real root survives in the entire domain.

Nonlinear Shallow Water

Liu (2006) studies the decay of solitons over a mud bottom whose dissipation effect is assume to appear as a bottom friction-like term in the momentum equation of Boussinesq shallow water wave equation.

Governing equations are

$$\nabla^2\phi = 0 \qquad -h(x,t) < z < \eta_s \tag{G.3.145a}$$

$$\eta_{s,t} + \eta_{s,x}\phi_{,x} = \phi_{,z} \qquad z = \eta_s \tag{G.3.145b}$$

$$\phi_{,t} + \tfrac{1}{2}(\nabla\phi)^2 + g\eta_s = 0 \qquad z = \eta_s \tag{G.3.145c}$$

$$-h_{,t} - h_{,x}\phi_{,x} = \phi_{,z} \qquad z = -h(x,t) \tag{G.3.145d}$$

where $-h = -h_0 + \eta_b$ and h_0 is the average bottom depth. The following scales are introduced to dimensionless the governing equations

$$\begin{aligned} &x' = kx, \quad z' = \frac{z}{h_0}, \quad t' = k\sqrt{gh_0}t, \quad \eta_s' = \frac{\eta_s}{a}, \quad \eta_b' = \frac{\eta_b}{a}, \\ &\phi' = \frac{kh_0}{a\sqrt{gh_0}}\phi, \quad h' = \frac{h}{h_0}, \quad P' = \frac{P}{\rho g h_0} \end{aligned} \tag{G.3.146}$$

where k, a and g are respectively the characteristic wave-number, characteristic amplitude and the acceleration gravity and P is the pressure. Upon substitution into the governing equation, after dropping prims we get

$$\mu^2\phi_{,xx} + \phi_{,zz} = 0 \qquad -h < z < \epsilon\eta_s \tag{G.3.147a}$$

$$\mu^2(\eta_{s,t} + \epsilon\eta_{s,x}\phi_{,x}) = \phi_{,z} \qquad z = \epsilon\eta_s \tag{G.3.147b}$$

$$\mu^2(\phi_{,t} + \eta_s) + \tfrac{1}{2}\epsilon(\mu^2\phi_{,x}^2 + \phi_z^2) = 0 \qquad z = \epsilon\eta_s \tag{G.3.147c}$$

$$-\mu^2(h_{,t} + \epsilon h_{,x}\phi_{,x}) = \phi_{,z} \qquad z = -h \tag{G.3.147d}$$

where

$$\mu \equiv kh_0 \ll 1, \quad \epsilon \equiv \frac{a}{h_0} \ll 1 \tag{G.3.148}$$

are indicators of the shallowness and the nonlinearity respectively. The ratio of nonlinearity to the shallowness

$$U_r = \frac{\epsilon}{\mu^2} \tag{G.3.149}$$

is called the Ursell's number. We assume a solution in the form

$$\phi = \sum_0^\infty [z + h(x,t)]^n \phi_n(x,y) \tag{G.3.150}$$

From Laplace's equation i.e., equation (G.3.147a) we have

$$\phi_{n+2} = -\mu^2 \frac{\phi_{n,xx} + 2(n+1)h_{,x}\phi_{n+1,x} + (n+1)h_{,xx}\phi_{n+1}}{(n+1)(n+2)[1+\mu^2 h_{,x}^2]} \tag{G.3.151}$$

and the boundary condition equation (G.3.147d) gives

$$\phi_1 = -\frac{1}{U_r} \frac{h_{,t} + \epsilon h_{,x}\phi_{0,x}}{1+\mu^2 h_{,x}^2} \tag{G.3.152}$$

Assuming $U_r = O(1)$ and $h = 1 - \mu^\alpha \eta_b(x,t)$ where $\alpha \geq 1$, we conclude $O(h_{,x} = O(h_{,x}) = O(\mu^\alpha) \ll 1$ after some algebra we get to the final equations correct to the order of $O(\mu^2) = O(\epsilon)$:

$$\mathcal{H}_{,t} + \epsilon(\mathcal{H}\bar{u})_{,x} = 0 \tag{G.3.153}$$

$$\bar{u}_{,t} + \epsilon \bar{u}\bar{u}_{,x} + \eta_{s,x} - \frac{\mu^2}{3}\bar{u}_{,xxt} + f(x,t) = 0 \tag{G.3.154}$$

$$P = (\epsilon\eta_s - z) + O(\epsilon\mu^\alpha) \tag{G.3.155}$$

where

$$\mathcal{H} = h + \epsilon\eta_s, \qquad \bar{u} = \frac{1}{\mathcal{H}} \int_{-h}^{\epsilon\eta_s} \phi_{,x} dz \tag{G.3.156}$$

are the total depth from the free surface and the depth average velocity, and

$$\begin{aligned} f(x,t) &= \frac{1}{U_r}\left[h_{,x}h_{,tt} + \frac{1}{2}\mathcal{H}_{,t}h_{,xt} - \frac{1}{2}\mathcal{H}h_{,xtt} - \mathcal{H}_{,x}h_{,tt}\right] \\ &= \frac{1}{2U_r}\left[\mu^{\alpha}\eta_{b,xtt} + \mu^{2\alpha}(\eta_{b,t}\eta_{b,xt} - \eta_b\eta_{b,xtt})\right] \end{aligned} \tag{G.3.157}$$

when the bottom is not a function of time, equations (G.3.153) and (G.3.154) reduce to equations (12.1.47) and (12.1.48) of Mei *et al.* (2005) with the assumption of small amplitude topography. Close to the bottom, the error in the pressure term drops to $O(\epsilon\mu^{2\alpha})$.

Assuming $\alpha = 2$, i.e., the bottom variation is as big as the surface perturbations, we can combine equations (G.3.153) and (G.3.154) to get

$$\eta_{s,tt} - \eta_{s,xx} - \frac{1}{U_r}\eta_{b,tt} = \epsilon\left\{(uu_x)_{,x} - (\eta_s u)_{,xt}\right\} + \mu^2\left\{(\eta_b u)_{,xt} - \frac{1}{3}u_{,xxxt} + \frac{1}{2U_r}\eta_{b,xxtt}\right\} \tag{G.3.158}$$

the bottom governing equation in the dimensional space is

$$m^*\eta_{b,tt} + b^*\eta_{b,t} + k^*\eta_b = -P = \rho g(\eta_s - \eta_b) \tag{G.3.159}$$

where m^*, b^* and k^* are respectively mass, damping coefficient and stiffness coefficient per unit area in a three dimensional problem. Note that we assume η_b is measured from the equilibrium position of the bottom where spring resists the pressure of still water $\rho g h_0$. In dimensionless form

$$\alpha_1\eta_{b,tt} + \alpha_2\eta_{b,t} + (\alpha_3 - 1)\eta_b = -\eta_s \tag{G.3.160}$$

where

$$\alpha_1 = \mu\frac{km^*}{\rho}, \quad \alpha_2 = \mu\frac{b^*}{\rho\sqrt{gh}}, \quad \alpha_3 = \frac{k^*}{\rho g}. \tag{G.3.161}$$

Now we introduce two space variables x and $X = \mu^2 x$ and expand η_s, η_b and u in power

series as follows

$$\eta_s(x,X;t) = \eta_{s0} + \mu^2\eta_{s1} + O(\mu^4) \quad \text{(G.3.162)}$$

$$\eta_b(x,X;t) = \eta_{b0} + \mu^2\eta_{b1} + O(\mu^4) \quad \text{(G.3.163)}$$

$$u(x,X;t) = u_0 + \mu^2 u_1 + O(\mu^4) \quad \text{(G.3.164)}$$

upon substitution into equation G.3.158, the perturbation equations are obtained

$$\eta_{s0,tt} - \eta_{s0,xx} - \frac{1}{U_r}\eta_{b0,tt} = 0 \quad \text{(G.3.165)}$$

$$\eta_{s1,tt} - \eta_{1,xx} - \frac{1}{U_r}\eta_{b1,tt} = \epsilon\left\{(u_0u_{0,x})_{,x} - (\eta_{s0}u_0)_{,xt}\right\} + \mu^2\left\{2\eta_{s0,xX} + (\eta_{b0}u)_{,xt} - \frac{1}{3}u_{0,xxxt} + \frac{1}{2U_r}\eta_{b0,xxtt}\right\} \quad \text{(G.3.166)}$$

Using equation (G.3.160) zeroth order equation (G.3.165) can be written in terms of a single variable η_{b0}

$$\alpha_1(\eta_{b0,tttt} - \eta_{b0,ttxx}) + \alpha_2(\eta_{b0,tt} - \eta_{b0,xx})_{,t} + (\alpha_3 - 1 + {U_r}^{-1})\eta_{b0,tt} - (\alpha_3 - 1)\eta_{b0,xx} = 0 \quad \text{(G.3.167)}$$

moving back to the physical domain and multiplying the equation by $k^2g^2h\rho/m^*$, we get equation G.3.139 that can be cast into a more meaningful physical dimensionless groups and discusses.

Cese I: Elastic Bottom

If the damping coefficient is zero, the solution to the linear problem is given by equations (G.3.80) and (G.3.81) where (k,ω) should satisfy the dispersion relation (G.3.83). In dimensionless format we get

$$\eta_{s0} = \eta_{s0}^0 e^{i(kx-\omega t)}, \quad \eta_{b0}^0 = \left(1 - \frac{1}{c^2}\right)\eta_{s0}^0, \quad u_0^0 = \frac{1}{c}\eta_{s0}^0 \quad \text{(G.3.168)}$$

where $c = \omega/(k\sqrt{gh})$ is the dimensionless wave speed and $a\sqrt{gh}/h$ is used to nondimen-

sionlize the velocity u. Therefore

$$\eta_{s0} = \zeta(\sigma), \quad \eta_{b0} = \left(1 - \frac{1}{c^2}\right)\zeta(\sigma), \quad u_0 = \frac{1}{c}\zeta(\sigma) \tag{G.3.169}$$

where $\sigma = x - ct$.

Since the dispersion relation (G.3.83) is a nonlinear equation, in general, $(2k, 2\omega)$ do not satisfy it. Therefore the nonlinear terms on the right hand side of the first order governing equation G.3.166 do not resonate first order solution while linear terms do. To avoid unbounded resonance for η_{s1} we must have

$$2\eta_{s0,xX} - \frac{1}{3}u_{0,xxxt} + \frac{1}{2U_r}\eta_{b0,xxtt} = 0 \tag{G.3.170}$$

Taking one integration with respect to x and substituting from equation (G.3.169), we end up getting

$$\zeta_{,X} + \beta\zeta_{,\sigma\sigma\sigma} = 0 \tag{G.3.171}$$

$$\beta = \frac{1}{6} + \frac{1}{4U_r}(c^2 - 1) \tag{G.3.172}$$

Assuming a periodic solution both in time and space in the form

$$\zeta = \zeta_0 e^{i(k^* X + \omega^* \sigma)} \tag{G.3.173}$$

we get the dispersion relation for the envelope

$$k^* = \beta\omega^{*3} \tag{G.3.174}$$

For $c^2 < 1 - \frac{2U_r}{3}$, the envelope moves in the same direction that the original wave is moving while for higher values it moves in the opposite direction.

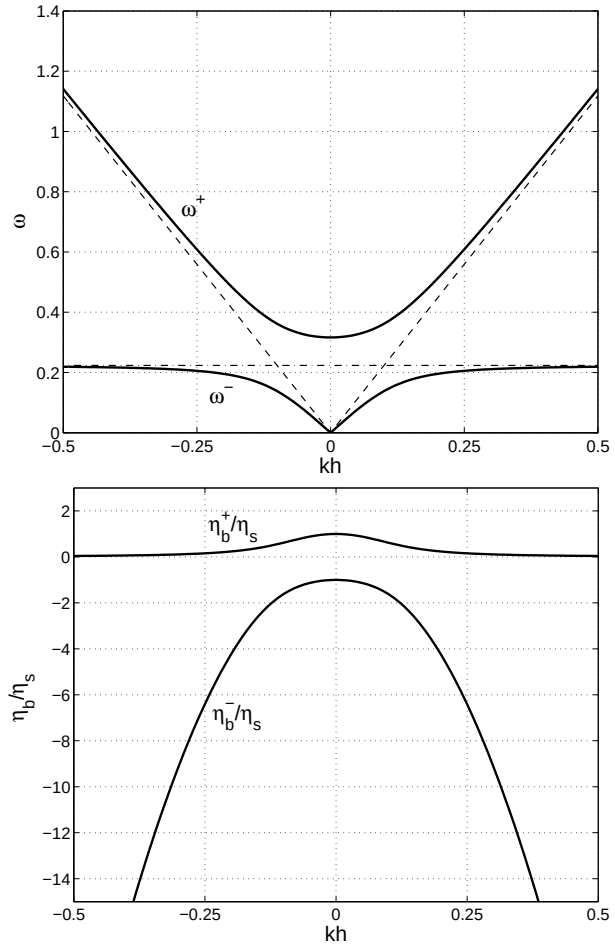

(a) (b)

Figure G-2: (a) Schematic representation of the dispersion relation curves for a wave over mass-spring bottom , (b)the ratio of the bottom amplitude to the surface amplitude. superscript + specifies the case where surface and bottom elevations are in phase.

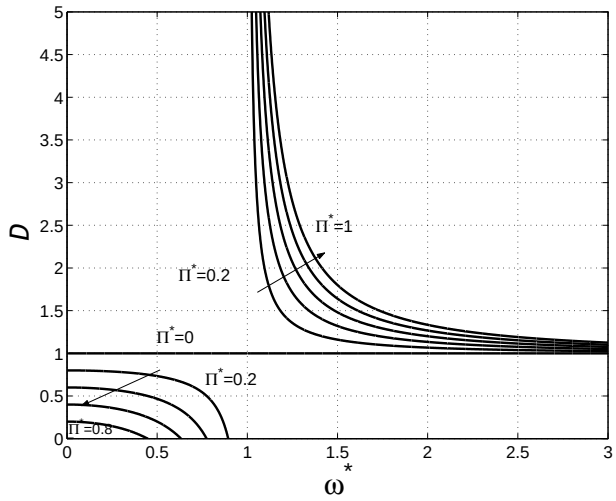

Figure G-3: dimensionless mass-spring bottom dispersion relation.

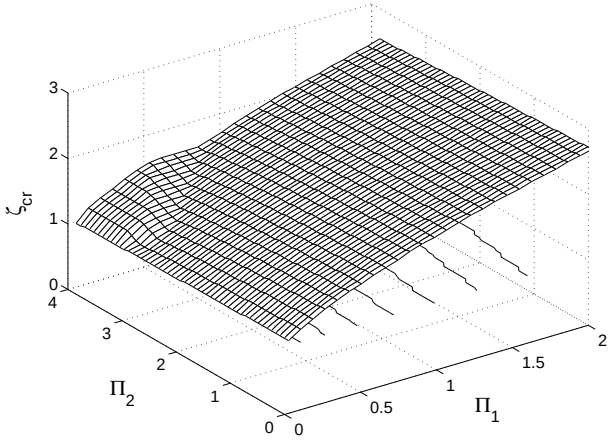

Figure G-4: Critical damping as a function of $\Pi_1 = ghk^2/\omega_b^2$ and $\Pi_2 = \rho g/k^*$

.

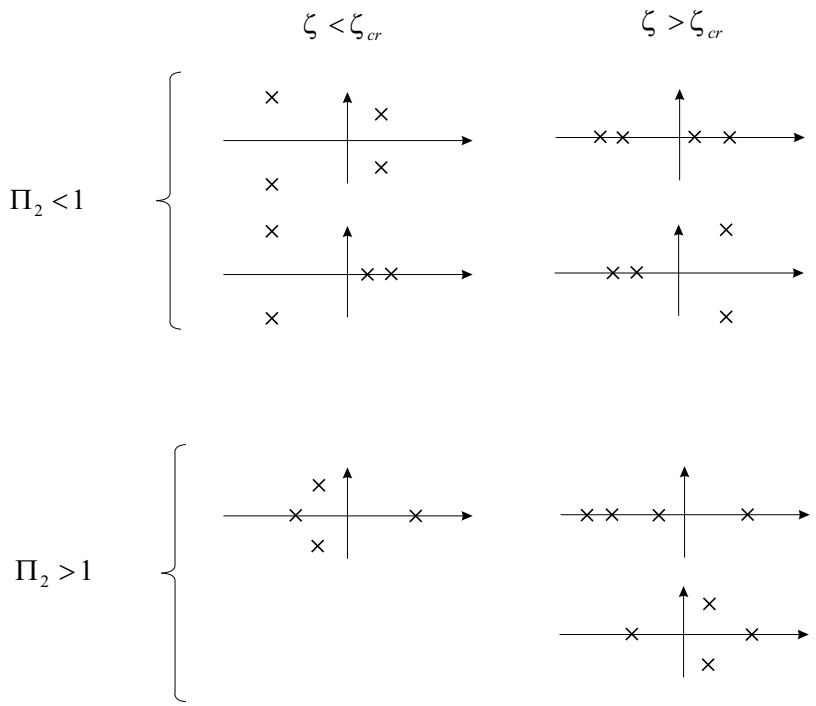

Figure G-5: Root configuration of the dimensionless dispersion relation

.

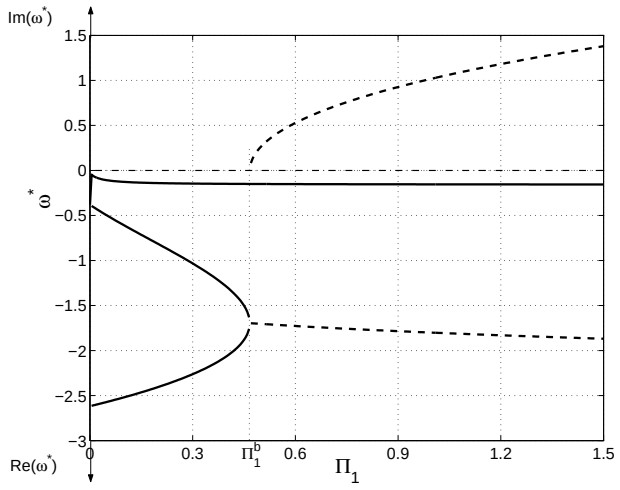

Figure G-6: Dispersion relation for water waves over a visco-elastic bed for $\Pi_2 = \zeta = 1.5$. Solid lines show the real roots and dashed lines are for real and imaginary parts of the complex root

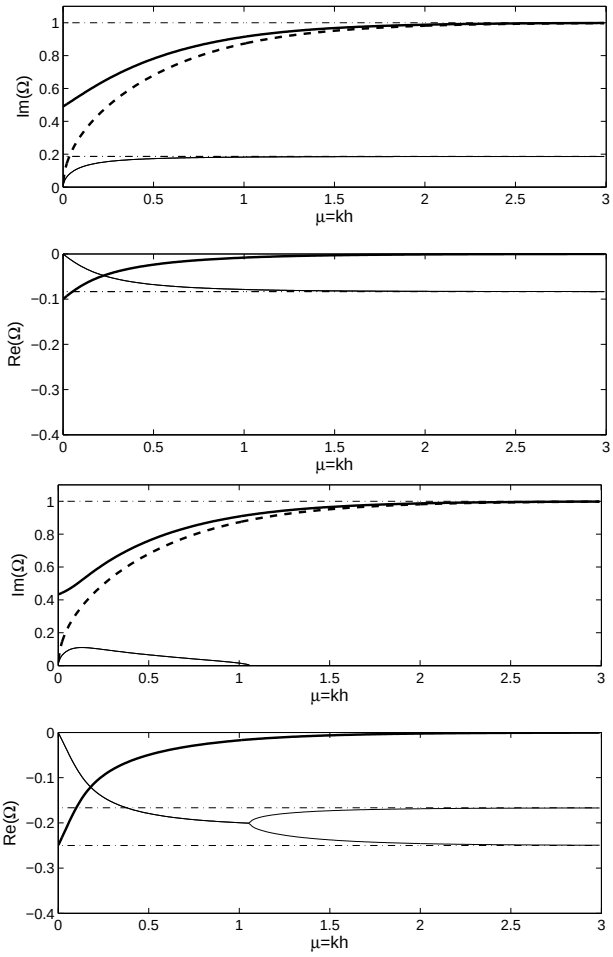

(a) (b)

Figure G-7: Variation of dimensionless frequency as a function of shallowness in a wave over mass-spring-damper bottom. Parameters are $\kappa = 0.8$, $\Omega_r = 2$ and (a). $\zeta = 0.2 < \zeta_{cr} = 0.49$, (b). $\zeta = 0.5 > \zeta_{cr}$. Data plotted are surface-mode (thick solid line), bottom mode (light solid line), flat bottom dispersion relation (dash line) and asymptotic deep water values (equation G.3.98, dash-dot line)

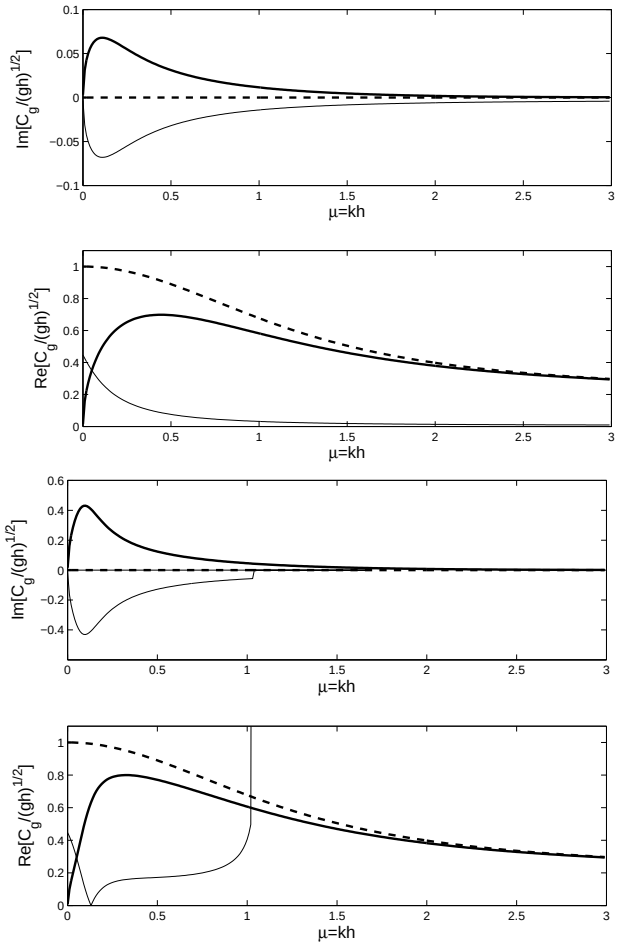

(a) (b)

Figure G-8: Variation of dimensionless group velocity as a function of shallowness in a wave over mass-spring-damper bottom. Parameters are $\kappa = 0.8$, $\Omega_r = 2$ and (a). $\zeta = 0.2 < \zeta_{cr} = 0.49$, (b). $\zeta = 0.5 > \zeta_{cr}$. Data plotted are surface-mode (thick solid line), bottom mode (light solid line), flat bottom dispersion relation (dash line) and asymptotic deep water values (equation G.3.98, dash-dot line)

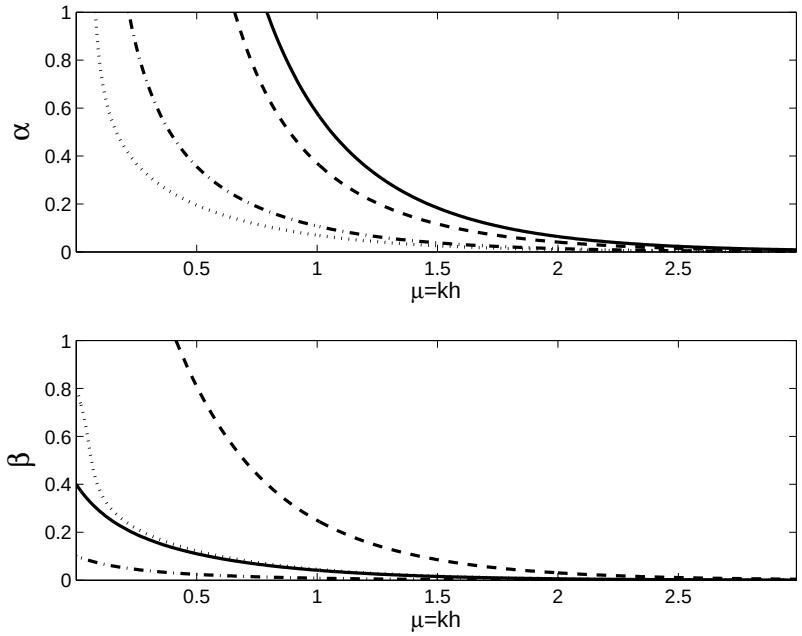

Figure G-9: Behavior of the coefficients α and β (equation G.3.132) as functions of the shallowness. Data plotted are for $\kappa = 0.9$, and, $\Omega_r = 0.5, \zeta = 0.1$ (solid line); $\Omega_r = 0.5, \zeta = 0.8$ (dash line); $\Omega_r = 2, \zeta = 0.1$ (dash-dot line); $\Omega_r = 2, \zeta = 0.8$ (dot line).

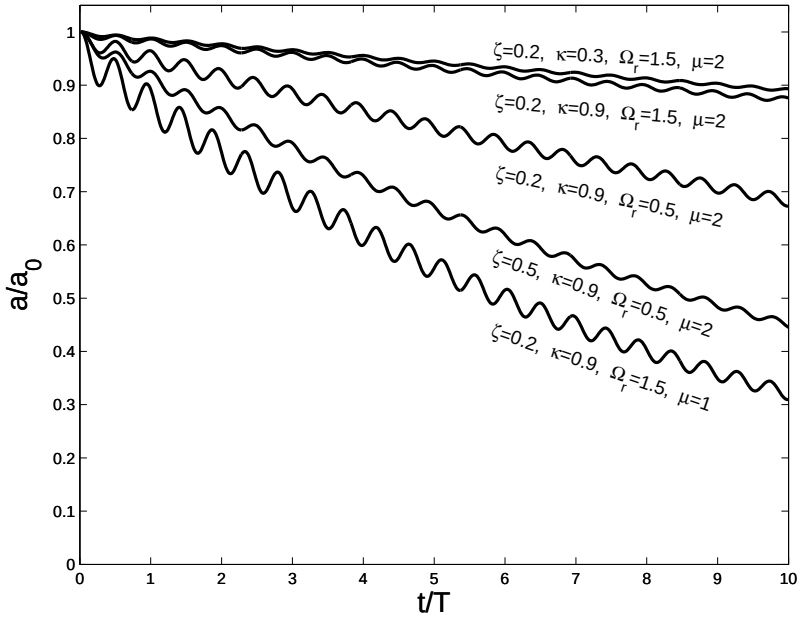

Figure G-10: HOS simulation of monochromatic incident wave as it passes over a mass-spring-damper bottom. Oscillations occur due to the mismatch of the incident wave dispersion relation and the over-deformable-topography dispersion relation.

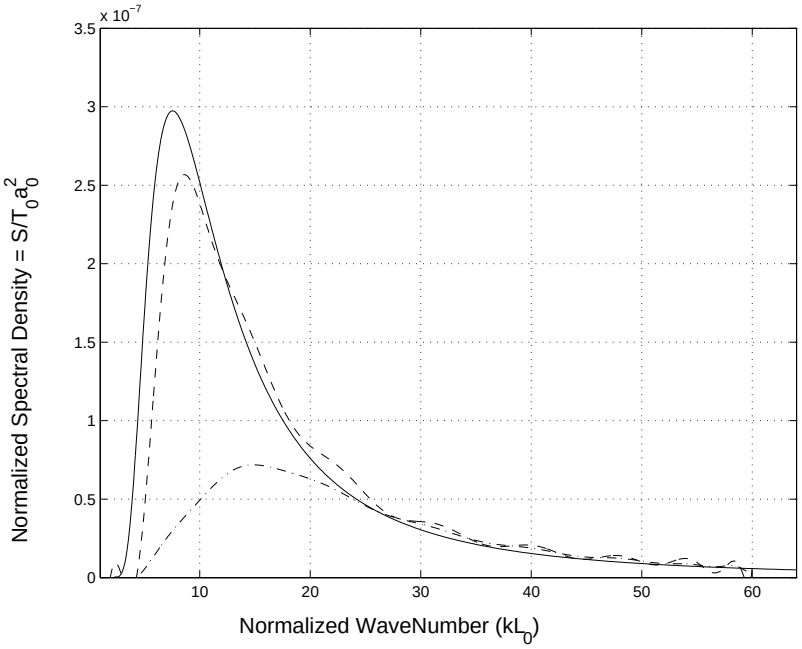

Figure G-11: PM spectrum decay for $U_{19.5} = 10$. The solid line is the initial spectrum, dash line is the spectrum in the absence of the bottom effect after $t = 100T$ where T is the period of shortest wave and dash-dot line is the spectrum after $t = 20T$ when the bottom parameters are $\kappa = 0.9, \Omega_r = 1.5, \zeta = 0.1$.

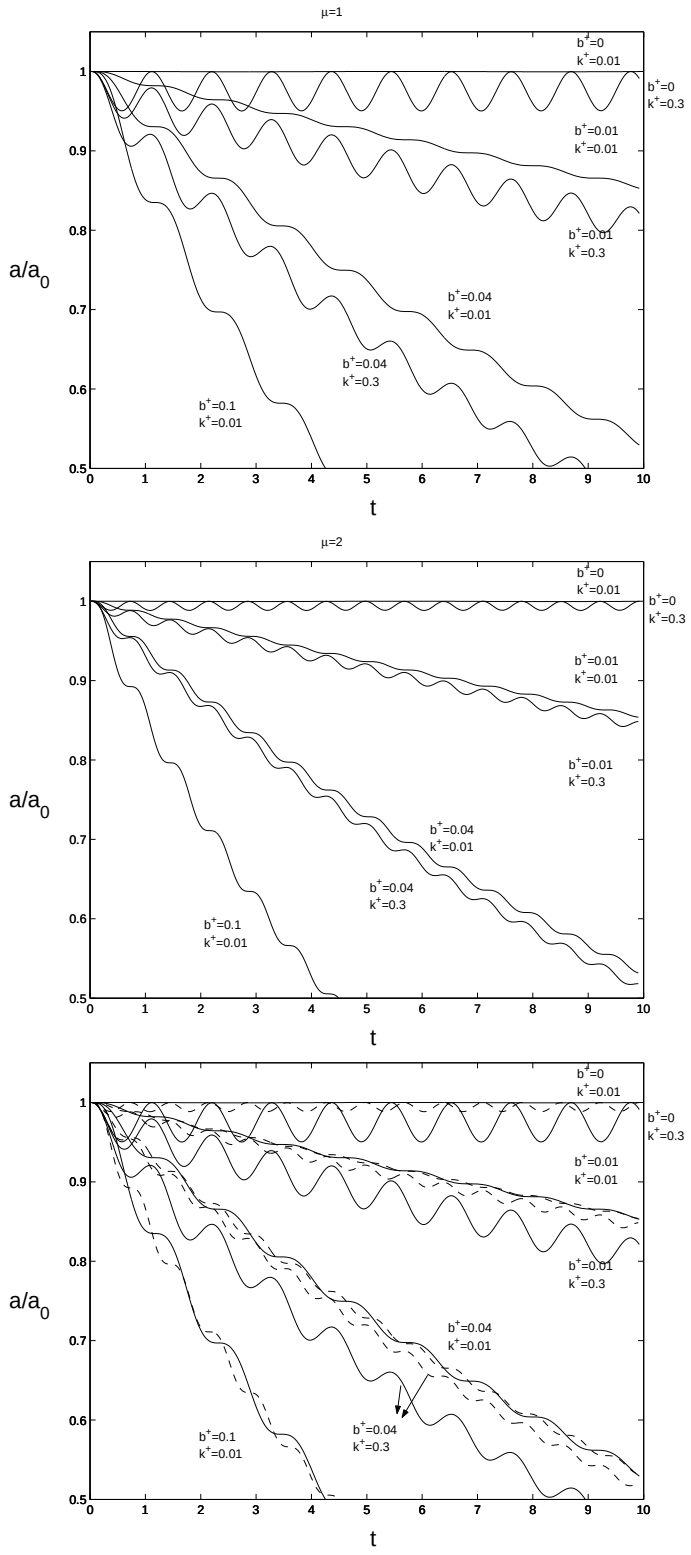

Figure G-12: Time history of amplitude of an incident wave for different dimensionless damping coefficient and stiffness.(a) $\mu = kh = 1$, (b)$\mu = kh = 2$.

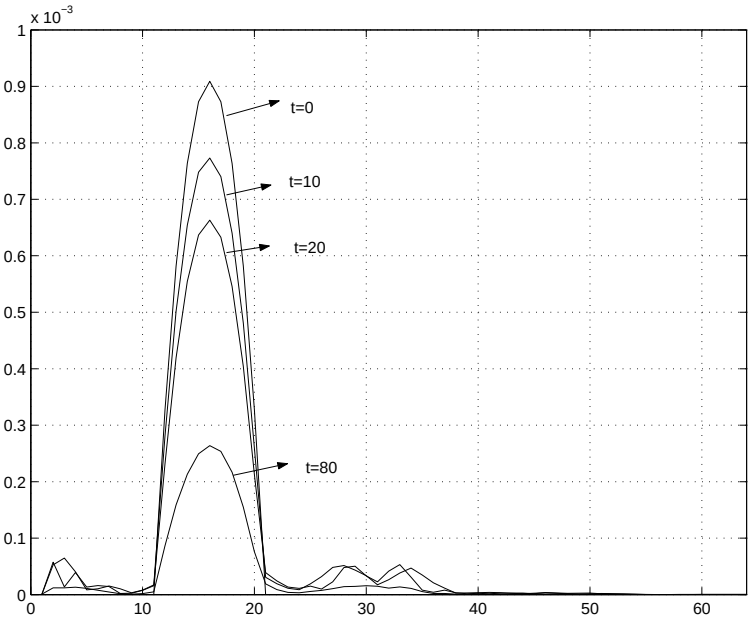

Figure G-13: Broad Spectrum over a visco-elastic bottom: $b^{\dagger} = 0.01$, $k^{\dagger} = 0.01$

Appendix H

Regular Perturbation vs Multiple Scales: Schematic Representation of the Difference

Many of nowadays most important problems in physics, engineering and applied mathematics involve difficulties that prevent us from finding exact closed-form solutions. These difficulties include (but certainly not limited to) complex nonlinear governing partial or ordinary differential equation, complex and variable coefficients and compound boundary conditions that may apply on known or unknown boundaries. In the case of water waves for example the boundary condition is applied on a surface that itself is a part of the solution to the governing partial differential equation. To overcome these issues we need to use either a theoretical approximation tool or a suitable computational technique to get a numerical solution. The most important and widely used theoretical approximation technique is the "systematic method of perturbation", aka asymptotic expansion, with respect to a small parameter. In the case of the water wave problem this small parameter can be the steepness or the shallowness. Perturbation techniques assume that the solution to the full problem can be expressed by a zeroth degree term plus a series of corrections with each term much much smaller that the previous term. Hence the full solution to the original problem is well approximated by the first few terms of this asymptotic expansion.

Assume a governing equation (including boundary conditions) in the form

$$\mathcal{L}(\phi) = 0 \tag{H.0.1}$$

where $\mathcal{L}$ is a nonlinear ordinary or partial operator. Now we assume that the solution to this problem, ϕ_s can be expressed by the sum of the first few terms of a perturbation expansion:

$$\phi_s = \epsilon\phi_1 + \epsilon^2\phi_2 + \epsilon^3\phi_3 + \cdots \tag{H.0.2}$$

where ϵ is the small parameter of the problem and $\phi_1, \phi_2, \phi_3, \cdots$ are $O(1)$ quantities. Upon substitution into the governing equation and collecting same order terms, we usually can order the equation into the following format

$$\mathcal{L} \equiv \epsilon L(\phi_1) + \epsilon^2\{L(\phi_2) - \mathcal{F}(\phi_1)\} + \epsilon^3\{L(\phi_3) - \mathcal{G}(\phi_1, \phi_2)\} + \cdots \tag{H.0.3}$$

where L is a linear operator and $\mathcal{F}, \mathcal{G}$ are nonlinear functions of their arguments. Now setting the governing equation equal to zero, from mathematics we have to have all orders identically zero, i.e.

$$L(\phi_1) = 0, \tag{H.0.4}$$

$$L(\phi_2) = \mathcal{F}(\phi_1), \tag{H.0.5}$$

$$L(\phi_3) = \mathcal{G}(\phi_1, \phi_2), \tag{H.0.6}$$

$$L(\phi_4) = \cdots \tag{H.0.7}$$

The first equation is a linear homogeneous equation and in most problems can be solved easily. The solution to the first equation, however, provides the argument for the right-hand side of the second equation converting it to a linear non-homogenous problem with a known right-hand side that again can be solved. The solution to the second equation provide the argument(s) for the third equation and so on. Following this sequence all perturbation terms can be computed. Figure H-1 shows the schematic representation of this procedure.

The difficulty with the regular perturbation theory is that it breaks down for strong interactions. If we look at the energy flow in figure H-1, it is seen that ϕ_1 provides forcing for the second order term, i.e. ϕ_2. Therefore under suitable conditions ϕ_2 starts to grow.

Conservation of energy dictates that ϕ_1 has to decay. But regular perturbation theory never corrects the ϕ_1 term. In other words there is no such a mechanism for ϕ_2 to affect the value of ϕ_1. Therefore, although for the short interaction and as long as ϕ_2 is much smaller that ϕ_1 regular perturbation predicts a very good behavior, for a longer interaction and if ϕ_2 grows and becomes comparable to ϕ_1 the result of regular perturbation is not valid anymore. In most ϕ_1 keeps on feeding ϕ_2 and therefore ϕ_2 grows indefinitely.

Multiple scales, on the other hand, overcomes this issue by taking into account more than once scale of variation. In multiple scale it is assumed that the solution has *fast* scale behavior and *slow* scale behavior. These two (or in principal they can be many) behaviors are independent of each other in early stages of development, but slowly affect each other. Mathematically speaking in Multiple Scale method the asymptotic expansion is the same as the regular perturbation expansion:

$$\phi_s = \epsilon\phi_1 + \epsilon^2\phi_2 + \epsilon_3\phi_3 + \cdots \tag{H.0.8}$$

with the difference that now the solution is a function of both fast and slow variables

$$\phi_1 = \phi_1(x, t, \bar{x} = \epsilon x, \bar{t} = \epsilon t, \hat{x} = \epsilon^2 x, \hat{t} = \epsilon^2 t, \cdots) \tag{H.0.9}$$

upon substitution into the governing equation similar set of equations, but with different right-hand sides, will be obtained

$$L(\phi_1) = 0, \tag{H.0.10}$$

$$L(\phi_2) = \mathcal{H}(\phi_1), \tag{H.0.11}$$

$$L(\phi_3) = \cdots \tag{H.0.12}$$

Now if we write down the solvability condition for ϕ_2 (i.e. prevent ϕ_2 to grow indefinitely) we get a solution for ϕ_1 that is valid over long interaction time and distance. Note that in regular perturbation since we do not let two time scale variation, such a solvability condition does not lead to a solution for ϕ_1.

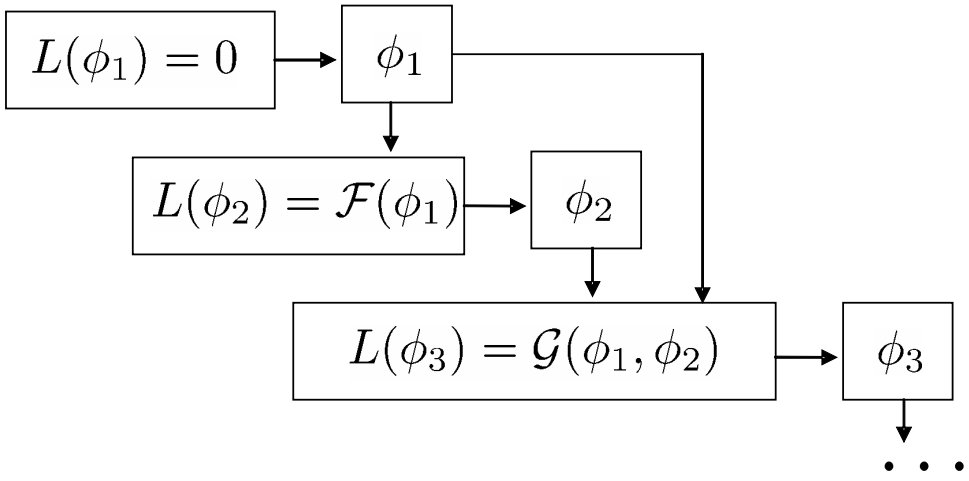

Figure H-1: Schematic representation of regular perturbation technique procedure.

Bibliography

Akylas, T. R. 1984*a* On the excitation of long nonlinear water waves by a moving pressure distribution. *J. Fluid Mech.* **141**, 455–466.

Akylas, T. R. 1984*b* On the excitation of nonlinear water waves by a moving pressure distribution oscillating at resonant frequency. *Phys. Fluids* **27** (12), 2803–2807.

Alam, Mohammad-Reza 2008 Interaction of waves in a two-layer density stratified fluid. PhD thesis, Massachusetts Institute of Technology, Cambridge, MA, USA.

Ardhuin, Fabrice & Herbers, T.H.C. 2002 Bragg scattering of random surface gravity waves by irregular seabed topography. *J. Fluid Mech.* **451**, 1–33.

Ardhuin, Fabrice & Magne, Rudy 2007 Scattering of surface gravity waves by bottom topography with a current. *J. Fluid Mech.* **576**, 235–264.

Argyris, John, Faust, Gunter & Haase, Maria 1994 *An exploration of chaos*. Amsterdam: North-Holland Publishing Co., an introduction for natural scientists and engineers, Translated from the German manuscript by Prudence Lawday.

Avital, E. & Miloh, T. 1994 On the determination of density profiles in stratified seas from kinematical patterns of ship-induced internal waves. *J. Ship Research* **38** (4), 308–318.

Avital, E. & Miloh, T. 1999 On an inverse problem of ship-induced internal waves. *Ocean Engineering* **26** (2), 99–110.

Baines, P. G. 1997 Topographic Effects in Stratified Flows. In *Cambridge Monographs on Mechanics* (ed. G. K. Batchelor & L. B. Freud). Cambridge University Press.

Ball, F. 1964 Energy transfer between external and internal gravity waves. *J. Fluid Mech.* **19**, 465–478.

Becker, Janet M. & Bercovici, David 2000 Permanent bedforms in a theoretical model of wave-sea-bed interactions. *Nonlinear processes in geophysics* **7**, 31–35.

Becker, Janet M. & Bercovici, David 2001 Pattern formation on the interface of a two-layer fluid: bi-viscous lower layer. *wave motion* **34**, 431–452.

Belzons, M., Guazzelli, E. & Parodi, O. 1988 Gravity-waves on a rough bottom - experimental-evidence of one-dimensional localization. *J. Fluid Mech.* **186**, 539–558.

Boegman, L., Imberger, J., Ivey, GN & Antenucci, JP 2003 High-frequency internal waves in large stratified lakes. *Limnology and Oceanography* **48** (2), 895–919.

Chen, Yongze & Liu, Philip L.-F. 1996 On interfacial waves over random topography. *Wave Motion* **24** (2), 169–184.

Choi, Wooyoung 2000 Modeling of strongly nonlinear internal waves in a multilayer system. In *Fifth International Symposium on Stratified Flows*. University of British Columbia, Vancouver.

Choi, Wooyoung & Camassa, Roberto 1996 Weakly nonlinear internal waves in a two-fluid system. *J. Fluid Mech.* **313**, 83–103.

Choi, Wooyoung & Camassa, Roberto 1999 Fully nonlinear internal waves in a two-fluid system. *J. Fluid Mech.* **396**, 1–36.

Chubarov, L. B., Eletskii, S. V., Fedotova, Z. I. & Khakimzyanov, G. S. 2005 Simulation of surface waves generation by an underwater landslide. *Russian J. Numer. Anal. Math. Modelling* **20** (5), 425–437.

Craik, Alex D. D. 1988 *Wave interactions and fluid flows*. Cambridge: Cambridge University Press.

Crapper, G. D. 1967 Ship waves in a stratified ocean. *J. Fluid Mech.* **29**, 667–672.

D. Myrhaug, L.E. Holmedal & Rue, H. 2006 Erosion and deposition of mud beneath random waves. *Coastal Engineering* **53**, 793–797.

D. Myrhaug, L.E. Holmedal, R.R. Simons R.D. McIver 2001 Bottom friction in random waves plus current flow. *Coastal Engineering* **43**, 75–92.

Dagan, G. & Miloh, T. 1982 Free-surface flow past oscillating singularities at resonant-frequency. *Journal Of Fluid Mechanics* **120**, 139–154.

Dalrymple, Robert A & Liu, Philip L.-F. 1978 Waves over soft muds: A two-layer fluid model. *Journal of Physical Oceanography* **8**, 1121–1131.

Davies, A.G. 1982 The reflection of wave energy by undulation on the seabed. *Dyn. Atmos. Oceans* **6**, 207–232.

Debnath, L. 1971 On transient developement of surface waves due to two dimensional sources. *Acta Mech.* **11**, 185–202.

Debnath, Lokenath 1994 *Nonlinear water waves*. Boston, MA: Academic Press Inc.

Dias, F. & Vanden-Broeck, J.-M. 2003 On internal fronts. *J. Fluid Mech.* **479**, 145–154.

Dommermuth, Douglas G & Yue, Dick K P 1987 A higher-order spectral method for the study of nonlinear gravity waves. *J. Fluid Mech.* **184**, 267–288.

Dommermuth, Douglas G & Yue, Dick K P 1988 The nonlinear three-dimensional waves generated by a moving surface disturbance. *17th Symposium on Naval Hydrodynamics* .

Duffy, Dean G. 2004 *Transform methods for solving partial differential equations*, 2nd edn. Chapman & Hall/CRC, Boca Raton, FL.

D′yachenko, A. I. & Zakharov, V. E. 1994 Is free-surface hydrodynamics an integrable system? *Phys. Lett. A* **190** (2), 144–148.

Ekman, V.W. 1904 On dead-water. norw. n. polar exped. 1893-1896: Sci. results. *Christiania* **XV**.

Faltinsen, O.M. 1993 *Sea Loads on Ships and Offshore Structures*. Cambridge University Press.

Farmer, D & Armi, L 1999 The generation and trapping of solitary waves over topography. *Science* **283 (5399)**, 188–190.

Forbes, L.K. 1988 critical free-surface flow over a semi-circular obstruction. *journal of engineering mathematics* **22**, 3–13.

Forbes, L. K. 1989 Two-layer critical flow over a semi-circular obstruction. *J. Engrg. Math.* **23** (4), 325–342.

Gade, H.G. 1958 Effects of a non-rigid, impremeable bottom on plane surface waves in shallow water. *Journal of Marine Research* **16**, 61–82.

Garrett, C. & Munk, W. 1975 Space-time scales of internal waves: A progress report. *Journal of Geophysical Research* **80** (C3), 291–298.

Gaster, M. 1962 A note on the relation between temporally-increasing and spatially-increasing disturbances in hydrodynamic stability. *J. Fluid Mech.* **14**, 222–224.

Gaudiosi, G. 1996 Offshore wind energy in the world context. *Renewable Energy* **9** (1), 899–904.

Goda, Y. & Suzuki, Y. 1976 Estimation of incident and reflected waves in random wave experiments. *Proc. of 15th coastal engng conference, Honolulu, Hawaii* pp. 828–845.

Gorodtsov, VA 1993 Radiation of internal gravitational waves in the case of uniform motion of sources of variable amplitude (the plane problem). *Journal of Applied Mechanics and Technical Physics* **34** (5), 653–660.

Grue, John 2005 Generation, propagation, and breaking of internal solitary waves. *Chaos* **15** (3), 037110, 14.

Guazzelli, Elisabeth, Rey, Vincent & Belzons, Max 1991 Higher-order bragg reflection of gravity surface waves by periodic beds. *Journal of Fluid Mechanics Digital Archive* **245** (-1), 301–317.

Harris, G. 1986 *Phytoplanton Ecology: Structure, Function, and Fluctuation*. Chapman and Hall, New York.

Haskind, M. D. 1954 On the motion with waves of heavy fluid (in russian). *Prikl. Mat. Mekh.* **18**, 15–26.

Hasselmann, K. 1966 Feynman diagrams and interaction rules of wave-wave scattering processes **4** (1), 1–32.

Havelock, T. H. 1908 The propagation of groups of waves in dispersive media with application to waves on water produced by a traveling disturbance. *Proc. Roy. Soc.* **A82**, 398–430.

Havelock, T. H. 1964 *The propagation of disturbances in dispersive media*. Stechert-Hafner, Inc., New York.

Heathershaw, A. D. & Davies, A.G. 1985 Resonant wave reflection by transverse bedforms and its relation to beaches and offshore bars. *Mar. Geol.* **62**, 321–338.

Hess, J. L. 1990 Panel methods in computational fluid dynamics. *Annual Review of Fluid Mechanics* **22**, 255–274.

Hill, D.F. 2004 Weakly nonlinear cubic interaction between surface waves and interfacial waves: an analytic solution. *Phys. Fluids* **16** (3), 839–842.

Hill, D.F. & Foda, M.A. 1996 Subharmonic resonance of short internal standing waves by progressive surface waves. *J. Fluid Mech.* **321**, 217–233.

Hill, D. F. & Foda, M. A. 1998 Subharmonic resonance of oblique interfacial waves by a progressive surface wave. *R. Soc. Lond. Proc. Ser. A Math. Phys. Eng. Sci.* **454** (1972), 1129–1144.

Hudimac, Albert A. 1961 Ship waves in a stratified ocean. *J. Fluid Mech.* **11**, 229–243.

J. Zhang, K. Hong & Yue, D.K.P. 1993 Effects of wavelength ratio on wave-mode modeling. *J. Fluid Mech.* **248**, 107–127.

JAEGER H.M., NAGEL S.R. 1992 Physics of the granular state. *science* **255**, 1523–1531.

Jamali, Mirmosadegh 1998 Surface wave interaction with with oblique internal waves. PhD thesis, The University of British Columbia, Vancouver, Canada.

Jamali, Mirmosadegh, Lawrence, Gregory A. & Seymour, Brian 2003 A note on the resonant interaction between a surface wave and two interfacial waves. *J. Fluid Mech.* **491**, 1–9.

Katz, Joseph & Plotkin, Allen 2001 *Low-Speed Aerodynamics*. Cambridge University Press.

Kelvin, L. 1905 Deep sea ship waves. *Proc. Roy. Soc. Edinb.* **25**, 1060–1084.

Kevorkian, J. & Yu, J. 1989 Passage through the critical Froude number for shallow-water waves over a variable bottom. *J. Fluid Mech.* **204**, 31–56.

Kirby, James T. 1986 A general wave equation for waves over rippled beds. *J. Fluid Mech.* **162**, 171–186.

Lamb, H. 1932 *Hydrodynamics*. Dover.

Liu, Ko-Fei & Mei, Chiang C. 1993*a* Long waves in shallow water over a layer of Bingham-plastic fluid-mud. I. Physical aspects. *Internat. J. Engrg. Sci.* **31** (1), 125–144.

Liu, Ko-Fei & Mei, Chiang C. 1993*b* Long waves in shallow water over a layer of Bingham-plastic fluid-mud. II. Mathematical derivation of long wave equations. *Internat. J. Engrg. Sci.* **31** (1), 145–155.

Liu, Philip L.-F. 2006 The sea bed dissipative mechanisms and their effects on long wave dissipation. In *Proceedings of the 28th Ocean Engineering Conference in Taiwan, National Sun Yat-Sen University, November 2006*, pp. 15–23.

Liu, Yuming & Yue, Dick K. P. 1993 On the solution near the critical frequency for an oscillating and translating body in or near a free surface. *J. Fluid Mech.* **254**, 251–266.

Liu, Yuming & Yue, Dick K. P. 1998 On generalized Bragg scattering of surface waves by bottom ripples. *J. Fluid Mech.* **356**, 297–326.

Lu, D. Q. & Chwang, Allen T. 2005 Interfacial waves due to a singularity in a system of two semi-infinite fluids. *Phys. Fluids* **17** (10), 102107, 9.

Maas, Leo & van Haren, Hans 2004 Is fair- weather drowning caused by dead water? *Technical Report* .

Macpherson, Hugh 1980 The attenuation of water waves over a nonrigid bed. *J. Fluid Mech.* **97** (4), 721–742.

Mason, W. H. 1995 Applied computational aerodynamics. An electronic version of the class notes.

McCauley, Jr., Joseph L. 1979 Phase space quantisation of interacting vortices in two dimensions. *J. Phys. A* **12** (11), 1999–2013.

McIver, P. 1984 Wave forces on arrays of floating bodies. *Journal of Engineering Mathematics* **18** (4), 273–285.

McKee, W. D. 1996 Bragg resonances in two-layer fluid. *J. Austral. Math. Soc. Ser. B* **37** (3), 334–345.

Mei, Chiang C. 1985 Resonant reflection of surface water waves by periodic sandbars. *J. Fluid Mech.* **152**, 315–335.

Mei, Chiang C., Stiassnie, Michael & Yue, Dick K.-P. 2005 *Theory and applications of ocean surface waves. Part 1,2*, *Advanced Series on Ocean Engineering*, vol. 23. World Scientific Publishing Co. Pte. Ltd., Hackensack, NJ, linear and Nonlinear aspects.

Melville, W. K. & Helfrich, Karl R. 1987 Transcritical two-layer flow over topography. *J. Fluid Mech.* **178**, 31–52.

Mielke, Alexander 1986 Steady flows of inviscid fluids under localized perturbations. *J. Differential Equations* **65** (1), 89–116.

Mowbray, D. E. & Rarity, B. S. H. 1967 A theoretical and experimental investigation of the phase configuration of internal waves of small amplitude in a density stratified fluid. *Journal of Fluid Mechanics* **28**, 1–16.

Myrhaug, D. 1995 Bottom friction beneath random waves. *Coastal Engineering* **24**, 259–273.

Nansen, Fridtjof 1969 The norwegian north polar expedition 1893-1896: Scientific results **V**.

Ng, Chiu-On 2000 Water waves over a muddy bed: a two-layer stokes' boundary layer model. *coastal engineering* **40**, 221–242.

Nycander, Jonas 2006 Tidal generation of internal waves from a periodic array of steep ridges. *J. Fluid Mech.* **567**, 415–432.

Palm, Enok & Grue, John 1999 On the wave field due to a moving body performing oscillations in the vicinity of the critical frequency. *J. Engrg. Math.* **35** (1-2), 219–232, ocean mechanics.

Pethick, John 1984 *An introduction to coastal geomorphology*. Edward Arnold.

Pramanik, AK 1974 Waves due to a moving oscillatory surface pressure in a stratified fluid. *Trans. ASME. J. Appl. Mech* **41**, 571.

Q. Zhu, A.A. TJavaras, Y. Liu D.K.P. Yue & Triantafyllou, M.S. 1999 Mechanics of nonlinear short-wave generation by a moored near-surface buoy. *J. Fluid Mech.* **381**, 305–335.

Saffman, P. G. 1992 *Vortex dynamics*. New York: Cambridge University Press.

Seroul, R. 2000 Stable polynomials. In *Programming for Mathematicians*, pp. 280–286. Springer-Verlag.

Sha, Huyun & Vanden-Broeck, J.-M. 1993 Two-layer flows past a semicircular obstruction. *physics of fluids* **5 (11)**, 2661–2668.

Sharman, R. D. & Wurtele, M. G. 1983 Ship waves and lee waves. *J. Atmospheric Sci.* **40** (2), 396–427.

Shen, H. & He, Y.J. 2005 Study internal waves in north west of south china sea by satellite images. *Geoscience and Remote Sensing Symposium, 2005. IGARSS'05. Proceedings. 2005 IEEE International* **4**.

Sheremet, A. & Stone, G. W. 2003 Observation of nearshore wave dissipation over muddy sea beds. *Journal of Geophysical Research* **108** (C11), 21(1–11).

Sheremet, A., Mehta-A.J. Liu B. Stone G.W. 2005 Wave-sediment interaction on a muddy inner shelf during hurricane claudette. *ESTUARINE COASTAL AND SHELF SCIENCE* **63** (1-2), 225–233.

Silvester, R. 1974 *Coastal Engineering, Vol. 1*. Elsevier.

Simon, MJ 1982 Multiple scattering in arrays of axisymmetric wave-energy devices. Part 1. A matrix method using a plane-wave approximation. *Journal of Fluid Mechanics Digital Archive* **120**, 1–25.

Sleath, J.F.A. 1984 *Sea Bed Mechanics*. John Wiley & sons.

Stevenson, T. N. & Thomas, N. H. 1969 2-dimensional internal waves generated by a travelling oscillating cylinder. *J. Fluid Mech.* **36**, 505–511.

Thorne, R. C. 1953 Multipole expansions in the theory of surface waves. *Proc. Cambridge Philos. Soc.* **49**, 707–716.

Thorpe, SA, Keen, JM, Jiang, R. & Lemmin, U. 1996 High-Frequency Internal Waves in Lake Geneva. *Philosophical Transactions: Mathematical, Physical and Engineering Sciences* **354** (1705), 237–257.

Tsai, Wu-ting & Yue, Dick K. P. 1996 Computation of nonlinear free-surface flows. In *Annual review of fluid mechanics, Vol. 28*, pp. 249–278. Palo Alto, CA: Annual Reviews.

Veletsos, AS & Shivakumar, P. 1993 Sloshing response of layered liquids in rigid tanks. *Tech. Rep.*. BNL–52378, Brookhaven National Lab., Upton, NY (United States).

Voitsenya, V. S. 1958 The two dimensional problem of the oscillations of a body under the surface of separation of two fluids (russian). *Prikladnaia matematika i mekhanika = Applied mathematics and mechanics* **22** (8), 789–803.

Wehausen, John V. & Laitone, Edmund V. 1960 Surface waves. In *Handbuch der Physik, Vol. 9, Part 3*, pp. 446–778. Berlin: Springer-Verlag.

Wei, Gang, Le, Jia Chun & Dai, Shi Qiang 2003 Surface effects of internal wave generated by a moving source in a two-layer fluid of finite depth. *Appl. Math. Mech.* **24** (9), 906–918.

Wei, Gang, Lu, Dongqiang & Dai, Shiqiang 2005 Waves induced by a submerged moving dipole in a two-layer fluid of finite depth. *Acta Mechanica Sinica* **21** (1), 24–31.

Wen, Feng 1995*a* Resonant generation of internal waves on the soft sea bed by a surface water wave. *Phys. Fluids* **7** (8), 1915–1922.

Wen, Feng 1995*b* Resonant generation of internal waves on the soft sea bed by a surface water wave. *Phys. Fluids* **7** (8), 1915–1922.

Wilkinson, W. L. 1960 *Non-Newtonian fluids: Fluid mechanics, mixing and heat transfer*. New York: Pergamon Press.

Winterwerp, Johan C. & Kesteren, Walther G. M. Van 2004 Introduction to the Physics of Cohesive Sediment in the Marine Environment. In *Development in sedimentology* (ed. T. Van Loon). Elsevier.

Wu, G 2004 Direct simulation and deterministic prediction of large-scale nonlinear ocean wave-field. *Ph.D Thesis, Massachusetts Institute of Technology, USA* .

Y. Liu, D.G. Dommermuth & Yue, D.K.P. 1992 A higher-order spectral method for nonlinear wave-body interactions. *J. Fluid Mech.* **245**, 115–136.

Yeung, R. W. & Nguyen, T. C. 1999 Waves generated by a moving source in a two-layer ocean of finite depth. *J. Engrg. Math.* **35** (1-2), 85–107, ocean mechanics.

Zakharov, V.E. 1968 Stability of periodic waves of finite amplitude on the surface of deep fluid. *J. Appl. Mech. Tech. Phys.* **2**, 190–194.